

CREEP OF HI-NICALON™ S CERAMIC FIBER TOWS AT 1000°C IN AIR AND IN SILICIC ACID-SATURATED STEAM

THESIS

Brian G. Kroeger, Capt, USAF

AFIT-ENY-MS-18-M-271

DEPARTMENT OF THE AIR FORCE
AIR UNIVERSITY

AIR FORCE INSTITUTE OF TECHNOLOGY

Wright-Patterson Air Force Base, Ohio

DISTRIBUTION STATEMENT A:
APPROVED FOR PUBLIC RELEASE; DISTRIBUTION UNLIMITED.

The views expressed in this thesis are those of the author and do not reflect the official policy or position of the United States Air Force, Department of Defense, or the United States Government. This material is declared a work of the U.S. Government and is not subject to copyright protection in the United States.

AFIT-ENY-18-M-271

CREEP OF HI-NICALON™ S CERAMIC FIBER TOWS AT 1000°C IN AIR AND IN SILICIC ACID-SATURATED STEAM

THESIS

Presented to the Faculty

Department of Aeronautics and Astronautics

Graduate School of Engineering and Management

Air Force Institute of Technology

Air University

Air Education and Training Command

In Partial Fulfillment of the Requirements for the

Degree of Master of Science in Aeronautical Engineering

Brian G. Kroeger, BSME, MSPM

Capt, USAF

March 2018

DISTRIBUTION STATEMENT A.
APPROVED FOR PUBLIC RELEASE; DISTRIBUTION UNLIMITED.

AFIT-ENY-18-M-271

CREEP OF HI-NICALON™ S CERAMIC FIBER TOWS AT 1000°C IN AIR AND IN SILICIC ACID-SATURATED STEAM

Brian G. Kroeger, BSME, MSPM
Capt, USAF

Committee Membership:

Dr. Marina B. Ruggles-Wrenn
Chair

Dr. Randall S. Hay
Member

Dr. Thomas Eason, III
Member

AFIT-ENY-18-M-271

Abstract

Advanced SiC/SiC ceramic matrix composites (CMCs) are being considered for a variety of applications. Of interest is their ability to withstand exposure to high temperature in an aggressive oxidizing environment. The presence of steam creates such an environment. As steam traverses across a SiC/SiC composite and through cracks in the SiC matrix, it becomes saturated with silicic acid, $Si(OH)_4$. It is essential to understand the long-term impacts and durability of SiC/SiC CMCs that have been exposed to such a demanding environment. The present research investigated creep of Hi-Nicalon™ S SiC fibers at 1000°C in air and in silicic acid saturated steam. The fiber tow consists of 500 fiber filaments with an average diameter of 12 μm. Creep tests were conducted in tension using a dead weight creep test setup. Creep stresses ranged from 3.5 to 800 MPa in air and from 3.5 to 500 MPa in silicic acid saturated steam. Creep run-out was defined as 100 hours under load. Creep run-out was achieved at stresses of 500 MPa in air and 300 MPa in saturated steam. Both primary and secondary creep regimes were observed in all tests with the transition to secondary creep occurring early in the lifetime of each test. Steady-state creep rates were found for each test. The steady-state creep rates in saturated steam were approximately an order of magnitude larger than those in air. Passive oxidation was found on the fibers tested in both environments using scanning electron microscopy (SEM). No evidence was found of active oxidation.

Acknowledgments

I would like to thank my advisor, Dr. Marina Ruggles-Wrenn. She guided me through the thesis process and provided me technical advice. Most importantly she always made time to answer any questions that I had along the way. I never would have collected all my data in the laboratory without the help and guidance of J.S., M.R., J.D. and K.L. They provided training on all equipment and were always available to troubleshoot issues. K.C. and T.C. spent hours training and helping me acquire prepare samples for the SEM and helping me acquire all the images taken. Dr. R.H. always found time to answer question, help analyze the SEM images and guided me through relevant research material. I would like to thank my parents for always being there for me and pushing me to better myself. Last but not least I would like to thank my wife, her love and support has helped me the past 18 months and I am eternally grateful that I had you by my side. She encouraged me to pursue my goals and I never would have accomplished this degree without her.

Brian G. Kroeger

Table of Contents

Abstract i
Table of Contents iii
List of Figures v
List of Tables xxx
I. Introduction and Background 1
1.1 Ceramic Matrix Composites 3
1.2 Silicon Carbide (SiC) Fibers - General Characteristics 7
1.3 Nicalon™ Fiber 8
1.4 Hi-Nicalon™ Fiber 11
1.5 Hi-Nicalon™ S Fiber 11
1.6 Creep 13
1.7 Previous Work 16
II. Material and Test Specimen 24
2.1 Material 24
2.2 Test Specimen 25
2.3 Experimental Facility 30
2.4 Temperature Profiles 36
2.5 Engineering Strain Measurement 38
III. Results and Discussion 41
3.1 Monotonic Tension Tests of Hi-Nicalon™ S Fiber Tows at 23°C 41
3.2 Creep of Hi-Nicalon™ S Fiber Tows at 1000°C 43
3.3 Post-Test Microstructural Analysis of Hi-Nicalon™ S Fiber Tows 58
IV. Conclusions and Recommendations 71

4.1 Conclusions 71
4.2 Recommendations for Future Research 72
Appendix A. Polished Fiber Cross Section Preparation for SEM 74
Appendix B. Representative SEM Fracture Surface Images 81
Appendix C. Representative SEM Polished Cross Section Images 160
Bibliography 209

List of Figures

Figure 1 - Strength to weight ratio as a function of temperature 2

Figure 2 - Notional comparison of stress-strain behaviors exhibited by a monolithic ceramic and a continuous-fiber ceramic matrix composite 4

Figure 3 - Microstructural design philosophies for enabling crack deflection in continuous-fiber ceramic composites 6

Figure 4 - Yajima production process for SiC-based fibers.. 8

Figure 5 - PCS precursor arraigned in a hexagonal, β-SiC pattern 9

Figure 6 - Production process of SiC fibers from PCS Precursor. 12

Figure 7 - Microstructure schematic of Nicalon™, Hi-Nicalon™, and Hi-Nicalon™ S fibers. .. 13

Figure 8 - Three regions of creep deformation: Primary, Secondary, and Tertiary 14

Figure 9 - A solid model of the three fiberglass tab configuration 26

Figure 10 – Fiberglass tab layout with edges filed down for creep testing. 27

Figure 11 – Test specimen preparation board.. 28

Figure 12 – Test specimen preparation process for creep testing. 29

Figure 13 – Test specimens prepared for monotonic and creep tension testing. 30

Figure 14 - Fiber tow specimen mounted in the creep testing rig 33

Figure 15 – Dead weight tensile creep test facility configured for saturated steam tests.. 34

Figure 16 - Alumina tube used for steam saturation with silica wool. 35

Figure 17 – Sacrificial silica wool inserted into the alumina tube 35

Figure 18 - Temperature profile obtained in laboratory air at 1000°C. 37

Figure 19 - Temperature profile obtained in saturated steam at 1000°C. 37

Figure 20 – Representative stress versus strain curve for Hi-Nicalon™ S fiber tows in laboratory air at 23°C 43

Figure 21 - Creep strain vs. time for Hi-Nicalon™ S fiber tows at 1000°C in laboratory air..... 46

Figure 22 - Creep strain vs. time for Hi-Nicalon™ S fiber tows at 1000°C in saturated steam... 47

Figure 23 - Creep strain vs. time for Hi-Nicalon™ S fiber tows at 1000°C in saturated steam... 47

Figure 24 - Steady-state creep rate vs. applied stress for Hi-Nicalon™ S fiber tows at 1000°C in laboratory air, steam and silicic-acid saturated steam. Results from Shillig [43] in air and steam are included for comparison. 49

Figure 25 - Creep stress vs. time to rupture for Hi-Nicalon™ S fiber tows at 1000°C in air, steam and saturated steam. Data at 1000°C in air and steam from Shillig [43] is included. Arrow indicates specimen failure did not occur when test was terminated..... 50

Figure 26 - Steady-state creep rate vs. applied stress for Hi-Nicalon™ S fiber tows at 800°C, 900°C and 1000°C in laboratory air and steam. Results from Shillig [43], Robertson [7], and Mitchell [46] are included for comparison..... 51

Figure 27 - Steady-state creep rate vs. applied stress for Hi-Nicalon™ S fiber tows at 800°C, 900°C and 1000°C in laboratory air and saturated steam. Results from Shillig [43], Robertson [7], and Mitchell [46] are included for comparison. 52

Figure 28 - Steady-state creep rate vs. applied stress for Hi-Nicalon™ S fiber tows at 800°C, 900°C and 1000°C in steam and saturated steam. Results from Shillig [43], Robertson [7], and Mitchell [46] are included for comparison..... 53

Figure 29 - Steady-state creep rate vs. applied stress for Hi-Nicalon™ S fiber tows at 800°C, 900°C and 1000°C in laboratory air, steam and saturated steam. Results from Shillig [43], Robertson [7], and Mitchell [46] are included for comparison..... 54

Figure 30 - Creep stress vs. time to rupture for Hi-Nicalon S fiber tows at 800°C, 900°C and 1000°C in laboratory air and steam. Results from Shillig [43], Robertson [7], and Mitchell [46] are included for comparison. 55

Figure 31 - Creep stress vs. time to rupture for Hi-Nicalon S fiber tows at 800°C, 900°C and 1000°C in laboratory air and saturated steam. Results from Shillig [43], Robertson [7], and Mitchell [46] are included for comparison..... 55

Figure 32- Creep stress vs. time to rupture for Hi-Nicalon S fiber tows at 800°C, 900°C and 1000°C in laboratory air, steam and saturated steam. Results from Shillig [43], Robertson [7], and Mitchell [46] are included for comparison. 57

Figure 33 - Quanta 650 scanning electron microscope (SEM) in the Air Force Research Laboratory (AFRL) Materials and Manufacturing Directorate. 59

Figure 34 - EMS 150T ES coating machine in the Air Force Research Laboratory (AFRL) Materials and Manufacturing Directorate. 60

Figure 35 - Representative fiber from Hi-Nicalon™ S fiber tow specimen subjected to 353 MPa at 1000°C in silicic acid-saturated steam for 52.53 h. Oxide scale is visible. 62

Figure 36 - SEM micrograph of the Hi-Nicalon™ S specimen “Steam 9” examining the fracture surface of a fiber subjected to creep in in silicic acid-saturated steam (σ_{cr} = 353 MPa, t_f = 52.53 h). Note oxide scale growth across the fracture surface. 63

Figure 37 - SEM micrograph of the Hi-Nicalon™ S specimen “Air 10” examining the fracture surface of a fiber subjected to creep in air (σ_{cr} = 800 MPa, t_f = 31.0 h)..... 64

Figure 38 - SEM micrograph of the Hi-Nicalon™ S specimen “Steam 10” examining the fracture surface of a fiber subjected to creep in in silicic acid-saturated steam (σ_{cr} = 450 MPa, t_f = 0.96 h). Note signs of saturated steam exposure (silica deposition). 65

Figure 39 - Representative fiber from Hi-Nicalon™ S fiber tow specimen subjected to 800 MPa at 1000°C in laboratory air for 31.0 h. The dark line along the fiber tow is indicative of contact between fibers..... 66

Figure 40 - SEM micrograph of the Hi-Nicalon™ S specimen “Steam 5” examining the fracture surface of a fiber subjected to creep in in silicic acid-saturated steam (σ_{cr} = 400 MPa, t_f = 30.83 h). Note defined silica amorphous and crystallized scale growth. 67

Figure 41 - SEM electron backscatter deflection micrograph of the Hi-Nicalon™ S specimen “Air 10” examining the cross section of the of a fiber tested in creep in air (σ_{cr} = 800 MPa, t_f = 31.0 h). 69

Figure 42 – Fibers cut and placed in two-part epoxy..... 74

Figure 43 – Fiber segments were coated with two-part epoxy. Segments were transferred between finger tips to ensure full and even coating of epoxy..... 75

Figure 44 – Fiber segment placed in tubing and shrunk on a hotplate. 76

Figure 45 – Fibers sliced into small pieces. 76

Figure 46 – Mounting fibers on Teflon disc and coating with two-part epoxy. 77

Figure 47 – Order for mounting sample to a glass stub using crystal bond. 78

Figure 48 – Tripod securing glass stub and sample for polishing. 79

Figure 49 – Grinding sample to desired height using 120 μm pad. 80

Figure 50- SEM micrograph of the Hi-Nicalon™ S specimen "Air 3" examining the fracture surface of a fiber (σ_{cr} = 700 MPa, t_f = 62.50 h). 81

Figure 51 - SEM micrograph of the Hi-Nicalon™ S specimen "Air 3" examining features on the fracture surface of a fiber (σ_{cr} = 700 MPa, t_f = 62.50 h). Note pores in fiber were likely were crack initiated. 81

Figure 52 - SEM micrograph of the Hi-Nicalon™ S specimen "Air 3" examining the fracture surface of a fiber (σ_{cr} = 700 MPa, t_f = 62.50 h). Note longitudinal fiber-fiber contact. 82

Figure 53 - SEM electron backscatter deflection micrograph of the Hi-Nicalon™ S specimen "Air 3" examining the fracture surface of a fiber (σ_{cr} = 700 MPa, t_f = 62.50 h). 82

Figure 54 - SEM micrograph of the Hi-Nicalon™ S specimen "Air 3" examining the fracture surface of a fiber (σ_{cr} = 700 MPa, t_f = 62.50 h). 83

Figure 55 - SEM electron backscatter deflection micrograph of the Hi-Nicalon™ S specimen "Air 3" examining the fracture surface of a fiber (σ_{cr} = 700 MPa, t_f = 62.50 h). 83

Figure 56 - SEM micrograph of the Hi-Nicalon™ S specimen "Air 3" examining features on the fracture surface of a fiber (σ_{cr} = 700 MPa, t_f = 62.50 h). 84

Figure 57 - SEM electron backscatter deflection micrograph of the Hi-Nicalon™ S specimen "Air 3" examining features on the fracture surface of a fiber (σ_{cr} = 700 MPa, t_f = 62.50 h). 84

Figure 58 - SEM micrograph of the Hi-Nicalon™ S specimen "Air 3" examining features on the fracture surface of a fiber (σ_{cr} = 700 MPa, t_f = 62.50 h). 85

Figure 59 - SEM electron backscatter deflection micrograph of the Hi-Nicalon™ S specimen "Air 3" examining features on the fracture surface of a fiber (σ_{cr} = 700 MPa, t_f = 62.50 h). 85

Figure 60 - SEM micrograph of the Hi-Nicalon™ S specimen "Air 3" examining the fracture surface of a fiber (σ_{cr} = 700 MPa, t_f = 62.50 h). 86

Figure 61 - SEM electron backscatter deflection micrograph of the Hi-Nicalon™ S specimen "Air 3" examining the fracture surface of a fiber (σ_{cr} = 700 MPa, t_f = 62.50 h)..... 86

Figure 62 - SEM micrograph of the Hi-Nicalon™ S specimen "Air 3" examining features on the fracture surface of a fiber (σ_{cr} = 700 MPa, t_f = 62.50 h). 87

Figure 63 - SEM electron backscatter deflection micrograph of the Hi-Nicalon™ S specimen "Air 3" examining features on the fracture surface of a fiber (σ_{cr} = 700 MPa, t_f = 62.50 h). 87

Figure 64 - SEM micrograph of the Hi-Nicalon™ S specimen "Air 3" examining the fracture surface of a fiber (σ_{cr} = 700 MPa, t_f = 62.50 h). Note signs of longitudinal fiber-fiber contact and pores in the fiber. 88

Figure 65 - SEM electron backscatter deflection micrograph of the Hi-Nicalon™ S specimen "Air 3" examining the fracture surface of a fiber (σ_{cr} = 700 MPa, t_f = 62.50 h). Note signs of longitudinal fiber-fiber contact. 88

Figure 66 - SEM micrograph of the Hi-Nicalon™ S specimen "Air 3" examining features on the fracture surface of a fiber (σ_{cr} = 700 MPa, t_f = 62.50 h). 89

Figure 67 - SEM micrograph of the Hi-Nicalon™ S specimen "Air 3" examining features on the fracture surface of a fiber (σ_{cr} = 700 MPa, t_f = 62.50 h). 89

Figure 68 - SEM micrograph of the Hi-Nicalon™ S specimen "Air 3" examining defects near the fracture surface of a fiber (σ_{cr} = 700 MPa, t_f = 62.50 h). Note these defects are likely where crack initiated. 90

Figure 69 - SEM electron backscatter deflection micrograph of the Hi-Nicalon™ S specimen "Air 3" examining defects near the fracture surface of a fiber (σ_{cr} = 700 MPa, t_f = 62.50 h). Note these defects are likely where crack initiated. 90

Figure 70 - SEM micrograph of the Hi-Nicalon™ S specimen "Air 3" examining the fracture surface of a fiber (σ_{cr} = 700 MPa, t_f = 62.50 h). 91

Figure 71 - SEM electron backscatter deflection micrograph of the Hi-Nicalon™ S specimen "Air 3" examining features on the fracture surface of a fiber (σ_{cr} = 700 MPa, t_f = 62.50 h). 91

Figure 72 - SEM micrograph of the Hi-Nicalon™ S specimen "Air 3" examining the fracture surface of a fiber (σ_{cr} = 700 MPa, t_f = 62.50 h). 92

Figure 73 - SEM electron backscatter deflection micrograph of the Hi-Nicalon™ S specimen "Air 3" examining the fracture surface of a fiber (σ_{cr} = 700 MPa, t_f = 62.50 h)..... 92

Figure 74 - SEM micrograph of the Hi-Nicalon™ S specimen "Air 3" examining features on the fracture surface of a fiber (σ_{cr} = 700 MPa, t_f = 62.50 h). 93

Figure 75 - SEM electron backscatter deflection micrograph of the Hi-Nicalon™ S specimen "Air 3" examining features on the fracture surface of a fiber (σ_{cr} = 700 MPa, t_f = 62.50 h). 93

Figure 76 - SEM micrograph of the Hi-Nicalon™ S specimen "Air 3" examining features on the fracture surface of a fiber (σ_{cr} = 700 MPa, t_f = 62.50 h). 94

Figure 77 - SEM electron backscatter deflection micrograph of the Hi-Nicalon™ S specimen "Air 3" examining features on the fracture surface of a fiber (σ_{cr} = 700 MPa, t_f = 62.50 h). 94

Figure 78 - SEM micrograph of the Hi-Nicalon™ S specimen "Air 3" examining the fracture surface of a fiber (σ_{cr} = 700 MPa, t_f = 62.50 h). 95

Figure 79 - SEM electron backscatter deflection micrograph of the Hi-Nicalon™ S specimen "Air 3" examining the fracture surface of a fiber (σ_{cr} = 700 MPa, t_f = 62.50 h)..... 95

Figure 80 - SEM micrograph of the Hi-Nicalon™ S specimen "Air 3" examining the fracture surface of a fiber (σ_{cr} = 700 MPa, t_f = 62.50 h). 96

Figure 81 - SEM electron backscatter deflection micrograph of the Hi-Nicalon™ S specimen "Air 3" examining the fracture surface of a fiber (σ_{cr} = 700 MPa, t_f = 62.50 h)..... 96

Figure 82 - SEM micrograph of the Hi-Nicalon™ S specimen "Air 3" examining the fracture surface of a fiber (σ_{cr} = 700 MPa, t_f = 62.50 h). 97

Figure 83 - SEM electron backscatter deflection micrograph of the Hi-Nicalon™ S specimen "Air 3" examining the fracture surface of a fiber (σ_{cr} = 700 MPa, t_f = 62.50 h)..... 97

Figure 84 - SEM micrograph of the Hi-Nicalon™ S specimen “Air 3” examining the fracture surface of a fiber (σ_{cr} = 700 MPa, t_f = 62.50 h)..... 98

Figure 85 - SEM electron backscatter deflection micrograph of the Hi-Nicalon™ S specimen “Air 3” examining the fracture surface of a fiber (σ_{cr} = 700 MPa, t_f = 62.50 h)..... 98

Figure 86 - SEM micrograph of the Hi-Nicalon™ S specimen “Air 3” examining the fracture surface of a fiber (σ_{cr} = 700 MPa, t_f = 62.50 h)..... 99

Figure 87 - SEM electron backscatter deflection micrograph of the Hi-Nicalon™ S specimen “Air 3” examining the fracture surface of a fiber (σ_{cr} = 700 MPa, t_f = 62.50 h)..... 99

Figure 88 - SEM micrograph of the Hi-Nicalon™ S specimen “Air 3” examining the fracture surface of a fiber (σ_{cr} = 700 MPa, t_f = 62.50 h)..... 100

Figure 89 - SEM electron backscatter deflection micrograph of the Hi-Nicalon™ S specimen “Air 3” examining the fracture surface of a fiber (σ_{cr} = 700 MPa, t_f = 62.50 h)..... 100

Figure 90 - SEM micrograph of the Hi-Nicalon™ S specimen “Air 10” examining the fracture surface of a fiber (σ_{cr} = 800 MPa, t_f = 31.0 h)..... 101

Figure 91 - SEM electron backscatter deflection micrograph of the Hi-Nicalon™ S specimen “Air 10” examining the fracture surface of a fiber (σ_{cr} = 800 MPa, t_f = 31.0 h)..... 101

Figure 92 - SEM micrograph of the Hi-Nicalon™ S specimen “Air 10” examining the fracture surface of a fiber (σ_{cr} = 800 MPa, t_f = 31.0 h)..... 102

Figure 93 - SEM electron backscatter deflection micrograph of the Hi-Nicalon™ S specimen “Air 10” examining the fracture surface of a fiber (σ_{cr} = 800 MPa, t_f = 31.0 h)..... 102

Figure 94 - SEM micrograph of the Hi-Nicalon™ S specimen “Air 10” examining the fracture surface of a fiber (σ_{cr} = 800 MPa, t_f = 31.0 h)..... 103

Figure 95 - SEM electron backscatter deflection micrograph of the Hi-Nicalon™ S specimen “Air 10” examining the fracture surface of a fiber (σ_{cr} = 800 MPa, t_f = 31.0 h)..... 103

Figure 96 - SEM micrograph of the Hi-Nicalon™ S specimen “Air 10” examining the fracture surface of a fiber (σ_{cr} = 800 MPa, t_f = 31.0 h)..... 104

Figure 97 - SEM electron backscatter deflection micrograph of the Hi-Nicalon™ S specimen “Air 10” examining the fracture surface of a fiber (σ_{cr} = 800 MPa, t_f = 31.0 h)..... 104

Figure 98 - SEM micrograph of the Hi-Nicalon™ S specimen “Air 10” examining the fracture surface of a fiber (σ_{cr} = 800 MPa, t_f = 31.0 h). Note signs of longitudinal fiber contact. 105

Figure 99 - SEM electron backscatter deflection micrograph of the Hi-Nicalon™ S specimen “Air 10” examining the fracture surface of a fiber (σ_{cr} = 800 MPa, t_f = 31.0 h)..... 105

Figure 100 - SEM micrograph of the Hi-Nicalon™ S specimen “Air 10” examining the fracture surface of a fiber (σ_{cr} = 800 MPa, t_f = 31.0 h)..... 106

Figure 101 - SEM electron backscatter deflection micrograph of the Hi-Nicalon™ S specimen “Air 10” examining the fracture surface of a fiber (σ_{cr} = 800 MPa, t_f = 31.0 h)..... 106

Figure 102 - SEM micrograph of the Hi-Nicalon™ S specimen “Air 10” examining the fracture surface of a fiber (σ_{cr} = 800 MPa, t_f = 31.0 h). Note signs longitudinal fiber contact. .. 107

Figure 103 - SEM electron backscatter deflection micrograph of the Hi-Nicalon™ S specimen “Air 10” examining the fracture surface of a fiber (σ_{cr} = 800 MPa, t_f = 31.0 h)..... 107

Figure 104 - SEM micrograph of the Hi-Nicalon™ S specimen “Air 10” examining the fracture surface of a fiber (σ_{cr} = 800 MPa, t_f = 31.0 h)..... 108

Figure 105 - SEM electron backscatter deflection micrograph of the Hi-Nicalon™ S specimen “Air 10” examining the fracture surface of a fiber (σ_{cr} = 800 MPa, t_f = 31.0 h)..... 108

Figure 106 - SEM micrograph of the Hi-Nicalon™ S specimen “Steam 9” examining the fracture surface of a fiber (σ_{cr} = 353 MPa, t_f = 52.53 h). Note the silica scale ring and growth along facture surface. 109

Figure 107 - SEM electron backscatter deflection micrograph of the Hi-Nicalon™ S specimen “Steam 9” examining the fracture surface of a fiber (σ_{cr} = 353 MPa, t_f = 52.53 h)..... 109

Figure 108 - SEM micrograph of the Hi-Nicalon™ S specimen “Steam 9” examining the fracture surface of a fiber (σ_{cr} = 353 MPa, t_f = 52.53 h). Note the silica scale ring and growth along facture surface. 110

Figure 109 - SEM electron backscatter deflection micrograph of the Hi-Nicalon™ S specimen “Steam 9” examining the fracture surface of a fiber (σ_{cr} = 353 MPa, t_f = 52.53 h). Note the silica scale ring and growth along facture surface. 110

Figure 110 - SEM micrograph of the Hi-Nicalon™ S specimen “Steam 9” examining the fracture surface of a fiber (σ_{cr} = 353 MPa, t_f = 52.53 h). Note the defined silica scale ring and growth along facture surface. 111

Figure 111 - SEM electron backscatter deflection micrograph of the Hi-Nicalon™ S specimen “Steam 9” examining the fracture surface of a fiber (σ_{cr} = 353 MPa, t_f = 52.53 h). Note the defined silica scale ring and growth along facture surface. 111

Figure 112 - SEM micrograph of the Hi-Nicalon™ S specimen “Steam 9” examining the fracture surface of a fiber (σ_{cr} = 353 MPa, t_f = 52.53 h). Note defined silica scale growth. 112

Figure 113 - SEM electron backscatter deflection micrograph of the Hi-Nicalon™ S specimen “Steam 9” examining the fracture surface of a fiber (σ_{cr} = 353 MPa, t_f = 52.53 h). Note defined silica scale growth. 112

Figure 114 - SEM micrograph of the Hi-Nicalon™ S specimen “Steam 9” examining the fracture surface of a fiber (σ_{cr} = 353 MPa, t_f = 52.53 h). Note defined silica scale growth. 113

Figure 115 - SEM electron backscatter deflection micrograph of the Hi-Nicalon™ S specimen “Steam 9” examining the fracture surface of a fiber (σ_{cr} = 353 MPa, t_f = 52.53 h). Note defined silica scale growth. 113

Figure 116 - SEM micrograph of the Hi-Nicalon™ S specimen “Steam 9” examining the fracture surface of a fiber (σ_{cr} = 353 MPa, t_f = 52.53 h). Note defined silica scale growth. 114

Figure 117 - SEM electron backscatter deflection micrograph of the Hi-Nicalon™ S specimen “Steam 9” examining the fracture surface of a fiber (σ_{cr} = 353 MPa, t_f = 52.53 h). Note defined silica scale growth. 114

Figure 118 - SEM micrograph of the Hi-Nicalon™ S specimen “Steam 9” examining the fracture surface of a fiber (σ_{cr} = 353 MPa, t_f = 52.53 h). Note defined silica amorphous and crystallized scale growth. 115

Figure 119 - SEM electron backscatter deflection micrograph of the Hi-Nicalon™ S specimen “Steam 9” examining the fracture surface of a fiber (σ_{cr} = 353 MPa, t_f = 52.53 h). Note defined silica amorphous and crystallized scale growth. 115

Figure 120 - SEM micrograph of the Hi-Nicalon™ S specimen “Steam 9” examining the fracture surface of a fiber (σ_{cr} = 353 MPa, t_f = 52.53 h). Note defined silica scale growth. 116

Figure 121 - SEM electron backscatter deflection micrograph of the Hi-Nicalon™ S specimen "Steam 9" examining the fracture surface of a fiber (σ_{cr} = 353 MPa, t_f = 52.53 h). Note defined silica scale growth. 116

Figure 122 - SEM micrograph of the Hi-Nicalon™ S specimen "Steam 9" examining the fracture surface of a fiber (σ_{cr} = 353 MPa, t_f = 52.53 h). Note defined silica scale growth. 117

Figure 123 - SEM electron backscatter deflection micrograph of the Hi-Nicalon™ S specimen "Steam 9" examining the fracture surface of a fiber (σ_{cr} = 353 MPa, t_f = 52.53 h). Note defined silica scale growth. 117

Figure 124 - SEM micrograph of the Hi-Nicalon™ S specimen "Steam 9" examining the fracture surface of a fiber (σ_{cr} = 353 MPa, t_f = 52.53 h). Note defined silica scale growth. 118

Figure 125 - SEM electron backscatter deflection micrograph of the Hi-Nicalon™ S specimen "Steam 9" examining the fracture surface of a fiber (σ_{cr} = 353 MPa, t_f = 52.53 h). Note defined silica scale growth. 118

Figure 126 - SEM micrograph of the Hi-Nicalon™ S specimen "Steam 9" examining the fracture surface of a fiber (σ_{cr} = 353 MPa, t_f = 52.53 h). Note defined silica amorphous and crystallized scale growth. 119

Figure 127 - SEM electron backscatter deflection micrograph of the Hi-Nicalon™ S specimen "Steam 9" examining the fracture surface of a fiber (σ_{cr} = 353 MPa, t_f = 52.53 h). Note defined silica amorphous and crystallized scale growth. 119

Figure 128 - SEM micrograph of the Hi-Nicalon™ S specimen "Steam 9" examining the fracture surface of a fiber (σ_{cr} = 353 MPa, t_f = 52.53 h). Note oxide scale growth across the fracture surface. 120

Figure 129 - SEM electron backscatter deflection micrograph of the Hi-Nicalon™ S specimen "Steam 9" examining the fracture surface of a fiber (σ_{cr} = 353 MPa, t_f = 52.53 h). Note oxide scale growth across the fracture surface. 120

Figure 130 - SEM micrograph of the Hi-Nicalon™ S specimen "Steam 9" examining the fracture surface of a fiber (σ_{cr} = 353 MPa, t_f = 52.53 h). Note defined silica scale growth. 121

Figure 131 - SEM electron backscatter deflection micrograph of the Hi-Nicalon™ S specimen "Steam 9" examining the fracture surface of a fiber (σ_{cr} = 353 MPa, t_f = 52.53 h). Note defined silica scale growth. 121

Figure 132 - SEM micrograph of the Hi-Nicalon™ S specimen “Steam 9” examining the fracture surface of a fiber (σ_{cr} = 353 MPa, t_f = 52.53 h). Note defined silica scale growth. 122

Figure 133 - SEM electron backscatter deflection micrograph of the Hi-Nicalon™ S specimen “Steam 9” examining the fracture surface of a fiber (σ_{cr} = 353 MPa, t_f = 52.53 h). Note defined silica scale growth. 122

Figure 134 - SEM micrograph of the Hi-Nicalon™ S specimen “Steam 9” examining features on the fracture surface of a fiber (σ_{cr} = 353 MPa, t_f = 52.53 h). Note silica scale is chipping off the fiber. 123

Figure 135 - SEM electron backscatter deflection micrograph of the Hi-Nicalon™ S specimen “Steam 9” examining features on the fracture surface of a fiber (σ_{cr} = 353 MPa, t_f = 52.53 h). Note silica scale is chipping off the fiber. 123

Figure 136 - SEM micrograph of the Hi-Nicalon™ S specimen “Steam 9” examining the fracture surface of a fiber (σ_{cr} = 353 MPa, t_f = 52.53 h). Note defined silica scale growth. 124

Figure 137 - SEM electron backscatter deflection micrograph of the Hi-Nicalon™ S specimen “Steam 9” examining the fracture surface of a fiber (σ_{cr} = 353 MPa, t_f = 52.53 h). Note defined silica scale growth. 124

Figure 138 - SEM micrograph of the Hi-Nicalon™ S specimen “Steam 9” examining the fracture surface of a fiber (σ_{cr} = 353 MPa, t_f = 52.53 h). Note defined silica scale growth. 125

Figure 139 - SEM electron backscatter deflection micrograph of the Hi-Nicalon™ S specimen “Steam 9” examining the fracture surface of a fiber (σ_{cr} = 353 MPa, t_f = 52.53 h). Note defined silica scale growth. 125

Figure 140 - SEM micrograph of the Hi-Nicalon™ S specimen “Steam 5” examining the fracture surface of a fiber (σ_{cr} = 400MPa, t_f = 30.83 h). Note defined silica amorphous and crystallized scale growth. 126

Figure 141 - SEM electron backscatter deflection micrograph of the Hi-Nicalon™ S specimen “Steam 5” examining the fracture surface of a fiber (σ_{cr} = 400 MPa, t_f = 30.83 h). Note defined silica amorphous and crystallized scale growth. 126

Figure 142 - SEM micrograph of the Hi-Nicalon™ S specimen “Steam 5” examining the fracture surface of a fiber (σ_{cr} = 400 MPa, t_f = 30.83 h). Note defined silica scale growth. 127

Figure 143 - SEM electron backscatter deflection micrograph of the Hi-Nicalon™ S specimen "Steam 5" examining the fracture surface of a fiber (σ_{cr} = 400 MPa, t_f = 30.83 h). Note defined silica scale growth. 127

Figure 144 - SEM micrograph of the Hi-Nicalon™ S specimen "Steam 5" examining the fracture surface of a fiber (σ_{cr} = 400 MPa, t_f = 30.83 h). Note defined silica amorphous and crystallized scale growth. 128

Figure 145 - SEM electron backscatter deflection micrograph of the Hi-Nicalon™ S specimen "Steam 5" examining the fracture surface of a fiber (σ_{cr} = 400 MPa, t_f = 30.83 h). Note defined silica amorphous and crystallized scale growth. 128

Figure 146 - SEM micrograph of the Hi-Nicalon™ S specimen "Steam 5" examining the fracture surface of a fiber (σ_{cr} = 400 MPa, t_f = 30.83 h). Note defined silica amorphous and crystallized scale growth. 129

Figure 147 - SEM electron backscatter deflection micrograph of the Hi-Nicalon™ S specimen "Steam 5" examining the fracture surface of a fiber (σ_{cr} = 400 MPa, t_f = 30.83 h). Note defined silica amorphous and crystallized scale growth. 129

Figure 148 - SEM micrograph of the Hi-Nicalon™ S specimen "Steam 5" examining the fracture surface of a fiber (σ_{cr} = 400 MPa, t_f = 30.83 h). Note defined silica amorphous and crystallized scale growth. 130

Figure 149 - SEM electron backscatter deflection micrograph of the Hi-Nicalon™ S specimen "Steam 5" examining the fracture surface of a fiber (σ_{cr} = 400 MPa, t_f = 30.83 h). Note defined silica amorphous and crystallized scale growth. 130

Figure 150 - SEM micrograph of the Hi-Nicalon™ S specimen "Steam 5" examining the fracture surface of a fiber (σ_{cr} = 400 MPa, t_f = 30.83 h). Note defined silica scale growth. 131

Figure 151 - SEM electron backscatter deflection micrograph of the Hi-Nicalon™ S specimen "Steam 5" examining the fracture surface of a fiber (σ_{cr} = 400 MPa, t_f = 30.83 h). Note defined silica scale growth. 131

Figure 152 - SEM micrograph of the Hi-Nicalon™ S specimen "Steam 5" examining the fracture surface of a fiber (σ_{cr} = 400 MPa, t_f = 30.83 h). Note defined silica scale growth. 132

Figure 153 - SEM electron backscatter deflection micrograph of the Hi-Nicalon™ S specimen "Steam 5" examining the fracture surface of a fiber (σ_{cr} = 400 MPa, t_f = 30.83 h). Note defined silica scale growth. 132

Figure 154 - SEM micrograph of the Hi-Nicalon™ S specimen “Steam 5” examining the fracture surface of a fiber (σ_{cr} = 400 MPa, t_f = 30.83 h). Note defined silica scale growth. 133

Figure 155 - SEM electron backscatter deflection micrograph of the Hi-Nicalon™ S specimen “Steam 5” examining the fracture surface of a fiber (σ_{cr} = 400 MPa, t_f = 30.83 h). Note defined silica scale growth. 133

Figure 156 - SEM micrograph of the Hi-Nicalon™ S specimen “Steam 5” examining the fracture surface of a fiber (σ_{cr} = 400 MPa, t_f = 30.83 h). Note defined silica amorphous and crystallized scale growth. 134

Figure 157 - SEM electron backscatter deflection micrograph of the Hi-Nicalon™ S specimen “Steam 5” examining the fracture surface of a fiber (σ_{cr} = 400 MPa, t_f = 30.83 h). Note defined silica amorphous and crystallized scale growth. 134

Figure 158 - SEM micrograph of the Hi-Nicalon™ S specimen “Steam 10” examining features on the fracture surface of a fiber (σ_{cr} = 450 MPa, t_f = 0.96 h). 135

Figure 159 - SEM electron backscatter deflection micrograph of the Hi-Nicalon™ S specimen “Steam 10” examining features on the fracture surface of a fiber (σ_{cr} = 450 MPa, t_f = 0.96 h). 135

Figure 160 - SEM micrograph of the Hi-Nicalon™ S specimen “Steam 10” examining features on the fracture surface of a fiber (σ_{cr} = 450 MPa, t_f = 0.96 h). 136

Figure 161 - SEM electron backscatter deflection micrograph of the Hi-Nicalon™ S specimen “Steam 10” examining features on the fracture surface of a fiber (σ_{cr} = 450 MPa, t_f = 0.96 h). 136

Figure 162 - SEM micrograph of the Hi-Nicalon™ S specimen “Steam 10” examining the fracture surface of a fiber (σ_{cr} = 450 MPa, t_f = 0.96 h). 137

Figure 163 - SEM electron backscatter deflection micrograph of the Hi-Nicalon™ S specimen “Steam 10” examining the fracture surface of a fiber (σ_{cr} = 450 MPa, t_f = 0.96 h)..... 137

Figure 164 - SEM micrograph of the Hi-Nicalon™ S specimen “Steam 10” examining the fracture surface of a fiber (σ_{cr} = 450 MPa, t_f = 0.96 h). 138

Figure 165 - SEM electron backscatter deflection micrograph of the Hi-Nicalon™ S specimen “Steam 10” examining the fracture surface of a fiber (σ_{cr} = 450 MPa, t_f = 0.96 h)..... 138

Figure 166 - SEM micrograph of the Hi-Nicalon™ S specimen “Steam 10” examining the fracture surface of a fiber (σ_{cr} = 450 MPa, t_f = 0.96 h). 139

Figure 167 - SEM electron backscatter deflection micrograph of the Hi-Nicalon™ S specimen “Steam 10” examining the fracture surface of a fiber (σ_{cr} = 450 MPa, t_f = 0.96 h)..... 139

Figure 168 - SEM micrograph of the Hi-Nicalon™ S specimen “Steam 10” examining the fracture surface of a fiber (σ_{cr} = 450 MPa, t_f = 0.96 h). 140

Figure 169 - SEM electron backscatter deflection micrograph of the Hi-Nicalon™ S specimen “Steam 10” examining the fracture surface of a fiber (σ_{cr} = 450 MPa, t_f = 0.96 h)..... 140

Figure 170 - SEM micrograph of the Hi-Nicalon™ S specimen “Steam 10” examining the fracture surface of a fiber (σ_{cr} = 450 MPa, t_f = 0.96 h). 141

Figure 171 - SEM electron backscatter deflection micrograph of the Hi-Nicalon™ S specimen “Steam 10” examining the fracture surface of a fiber (σ_{cr} = 450 MPa, t_f = 0.96 h)..... 141

Figure 172 - SEM micrograph of the Hi-Nicalon™ S specimen “Steam 10” examining features on the fracture surface of a fiber (σ_{cr} = 450 MPa, t_f = 0.96 h). 142

Figure 173 - SEM electron backscatter deflection micrograph of the Hi-Nicalon™ S specimen “Steam 10” examining features on the fracture surface of a fiber (σ_{cr} = 450 MPa, t_f = 0.96 h). 142

Figure 174 - SEM micrograph of the Hi-Nicalon™ S specimen “Steam 10” examining the fracture surface of a fiber (σ_{cr} = 450 MPa, t_f = 0.96 h). 143

Figure 175 - SEM electron backscatter deflection micrograph of the Hi-Nicalon™ S specimen “Steam 10” examining the fracture surface of a fiber (σ_{cr} = 450 MPa, t_f = 0.96 h)..... 143

Figure 176 - SEM micrograph of the Hi-Nicalon™ S specimen “Steam 10” examining the fracture surface of a fiber (σ_{cr} = 450 MPa, t_f = 0.96 h). 144

Figure 177 - SEM electron backscatter deflection micrograph of the Hi-Nicalon™ S specimen “Steam 10” examining the fracture surface of a fiber (σ_{cr} = 450 MPa, t_f = 0.96 h)..... 144

Figure 178 - SEM micrograph of the Hi-Nicalon™ S specimen “Steam 10” examining the fracture surface of a fiber (σ_{cr} = 450 MPa, t_f = 0.96 h). 145

Figure 179 - SEM electron backscatter deflection micrograph of the Hi-Nicalon™ S specimen "Steam 10" examining the fracture surface of a fiber (σ_{cr} = 450 MPa, t_f = 0.96 h)..... 145

Figure 180 - SEM micrograph of the Hi-Nicalon™ S specimen "Steam 10" examining the fracture surface of a fiber (σ_{cr} = 450 MPa, t_f = 0.96 h). Note signs of saturated steam exposure (silica deposition). 146

Figure 181 - SEM electron backscatter deflection micrograph of the Hi-Nicalon™ S specimen "Steam 10" examining the fracture surface of a fiber (σ_{cr} = 450 MPa, t_f = 0.96 h)..... 146

Figure 182 - SEM micrograph of the Hi-Nicalon™ S specimen "Steam 10" examining the fracture surface of a fiber (σ_{cr} = 450 MPa, t_f = 0.96 h). Note signs of saturated steam exposure (silica deposition). 147

Figure 183 - SEM micrograph of the Hi-Nicalon™ S specimen "Steam 6" examining the fracture surface of a fiber (σ_{cr} = 500 MPa, t_f = 0.02 h). Note signs of saturated steam exposure (silica deposition). 147

Figure 184 - SEM micrograph of the Hi-Nicalon™ S specimen "Steam 6" examining the fracture surface of a fiber (σ_{cr} = 500 MPa, t_f = 0.02 h). Note signs of saturated steam exposure (silica deposition) and signs of fiber-fiber contact. 148

Figure 185 - SEM micrograph of the Hi-Nicalon™ S specimen "Steam 6" examining features on the fracture surface of a fiber (σ_{cr} = 500 MPa, t_f = 0.02 h). Note signs of saturated steam exposure (silica deposition). 148

Figure 186 - SEM micrograph of the Hi-Nicalon™ S specimen "Steam 6" examining features on the fracture surface of a fiber (σ_{cr} = 500 MPa, t_f = 0.02 h). 149

Figure 187 - SEM micrograph of the Hi-Nicalon™ S specimen "Steam 6" examining the fracture surface of a fiber (σ_{cr} = 500 MPa, t_f = 0.02 h). Note signs of fiber-fiber contact. 149

Figure 188 - SEM micrograph of the Hi-Nicalon™ S specimen "Steam 6" examining features on the fracture surface of a fiber (σ_{cr} = 500 MPa, t_f = 0.02 h). Note signs of fiber-fiber contact. 150

Figure 189 - SEM micrograph of the Hi-Nicalon™ S specimen "Steam 6" examining the fracture surfaces four fibers (σ_{cr} = 500 MPa, t_f = 0.02 h). Note signs of saturated steam exposure (silica deposition) signs of fiber-fiber contact. 150

Figure 190 - SEM micrograph of the Hi-Nicalon™ S specimen “Steam 6” examining the fracture surface of a fiber (σ_{cr} = 500 MPa, t_f = 0.02 h). Note signs of saturated steam exposure (silica deposition). 151

Figure 191 - SEM micrograph of the Hi-Nicalon™ S specimen “Steam 6” examining the fracture surface of a fiber (σ_{cr} = 500 MPa, t_f = 0.02 h). Note signs of saturated steam exposure (silica deposition). 151

Figure 192 - SEM micrograph of the Hi-Nicalon™ S specimen “Steam 6” examining the fracture surface of a fiber (σ_{cr} = 500 MPa, t_f = 0.02 h). Note signs of saturated steam exposure (silica deposition). 152

Figure 193 - SEM micrograph of the Hi-Nicalon™ S specimen “Steam 6” examining features on the fracture surface of a fiber (σ_{cr} = 500 MPa, t_f = 0.02 h). Note signs of saturated steam exposure (silica deposition/dewetting). 152

Figure 194 - SEM micrograph of the Hi-Nicalon™ S specimen “Steam 6” examining the fracture surface of a fiber (σ_{cr} = 500 MPa, t_f = 0.02 h). Note signs of saturated steam exposure (silica deposition). 153

Figure 195 - SEM micrograph of the Hi-Nicalon™ S specimen “Steam 6” examining the fracture surface of a fiber (σ_{cr} = 500 MPa, t_f = 0.02 h). Note signs of saturated steam exposure (silica deposition). 153

Figure 196 - SEM micrograph of the Hi-Nicalon™ S specimen “Steam 6” examining the fracture surface of a fiber (σ_{cr} = 500 MPa, t_f = 0.02 h). Note signs of saturated steam exposure (silica deposition). 154

Figure 197 - SEM micrograph of the Hi-Nicalon™ S specimen “Steam 6” examining the fracture surface of a fiber (σ_{cr} = 500 MPa, t_f = 0.02 h). Note signs of saturated steam exposure (silica deposition). 154

Figure 198 - SEM micrograph of the Hi-Nicalon™ S specimen “Steam 6” examining the fracture surface of a fiber (σ_{cr} = 500 MPa, t_f = 0.02 h). Note signs of saturated steam exposure (silica deposition). 155

Figure 199 - SEM micrograph of the Hi-Nicalon™ S specimen “Steam 6” examining silica deposition near a fiber (σ_{cr} = 500 MPa, t_f = 0.02 h). 155

Figure 200 - SEM micrograph of the Hi-Nicalon™ S specimen “Steam 6” examining the fracture surface of a fiber (σ_{cr} = 500 MPa, t_f = 0.02 h). Note signs of saturated steam exposure (dewetting). 156

Figure 201 - SEM micrograph of the Hi-Nicalon™ S specimen “Steam 6” examining the fracture surface of a fiber (σ_{cr} = 500 MPa, t_f = 0.02 h). Note signs of saturated steam exposure (silica deposition/dewetting). 156

Figure 202 - SEM micrograph of the Hi-Nicalon™ S specimen “Steam 6” examining the fracture surface of a fiber (σ_{cr} = 500 MPa, t_f = 0.02 h). Note possible oxide scale growth. 157

Figure 203 - SEM micrograph of the Hi-Nicalon™ S specimen “Steam 6” examining the fracture surface of a fiber (σ_{cr} = 500 MPa, t_f = 0.02 h). 157

Figure 204 - SEM micrograph of the Hi-Nicalon™ S specimen “Steam 6” examining the fracture surface of a fiber (σ_{cr} = 500 MPa, t_f = 0.02 h). Note signs of saturated steam exposure (silica deposition). 158

Figure 205 - SEM micrograph of the Hi-Nicalon™ S specimen “Steam 6” examining the fracture surfaces of six fibers (σ_{cr} = 500 MPa, t_f = 0.02 h). Note signs of saturated steam exposure (silica deposition). 158

Figure 206 - SEM micrograph of the Hi-Nicalon™ S specimen “Steam 6” examining the fracture surfaces of six fibers (σ_{cr} = 500 MPa, t_f = 0.02 h). Note signs of saturated steam exposure (silica deposition). 159

Figure 207 - SEM micrograph of the Hi-Nicalon™ S specimen “Air 7” examining the cross section at the midpoint of a fiber (σ_{cr} = 300 MPa, t_f = 100 h). 160

Figure 208 - SEM electron backscatter deflection micrograph of the Hi-Nicalon™ S specimen “Air 7” examining the cross section at the midpoint of a fiber (σ_{cr} = 300 MPa, t_f = 100 h). 160

Figure 209 - SEM micrograph of the Hi-Nicalon™ S specimen “Air 7” examining the cross section at the midpoint of a fiber (σ_{cr} = 300 MPa, t_f = 100 h). 161

Figure 210 - SEM electron backscatter deflection micrograph of the Hi-Nicalon™ S specimen “Air 7” examining the cross section at the midpoint of a fiber (σ_{cr} = 300 MPa, t_f = 100 h). 161

Figure 211 - SEM micrograph of the Hi-Nicalon™ S specimen “Air 7” examining the cross section at the midpoint of a fiber (σ_{cr} = 300 MPa, t_f = 100 h). 162

Figure 212 - SEM electron backscatter deflection micrograph of the Hi-Nicalon™ S specimen “Air 7” examining the cross section at the midpoint of a fiber (σ_{cr} = 300 MPa, t_f = 100 h). 162

Figure 213 - SEM micrograph of the Hi-Nicalon™ S specimen “Air 7” examining a portion of the cross section at the midpoint of a fiber (σ_{cr} = 300 MPa, t_f = 100 h). 163

Figure 214 - SEM electron backscatter deflection micrograph of the Hi-Nicalon™ S specimen “Air 7” examining a portion of the cross section at the midpoint of a fiber (σ_{cr} = 300 MPa, t_f = 100 h). 163

Figure 215 - SEM micrograph of the Hi-Nicalon™ S specimen “Air 7” examining the cross section at the midpoint of a fiber (σ_{cr} = 300 MPa, t_f = 100 h). 164

Figure 216 - SEM electron backscatter deflection micrograph of the Hi-Nicalon™ S specimen “Air 7” examining the cross section at the midpoint of a fiber (σ_{cr} = 300 MPa, t_f = 100 h). 164

Figure 217 - SEM micrograph of the Hi-Nicalon™ S specimen “Air 7” examining the cross section at the midpoint of a fiber (σ_{cr} = 300 MPa, t_f = 100 h). 165

Figure 218 - SEM electron backscatter deflection micrograph of the Hi-Nicalon™ S specimen “Air 7” examining the cross section at the midpoint of a fiber (σ_{cr} = 300 MPa, t_f = 100 h). 165

Figure 219 - SEM micrograph of the Hi-Nicalon™ S specimen “Air 7” examining the cross section at the midpoint of a fiber (σ_{cr} = 300 MPa, t_f = 100 h). 166

Figure 220 - SEM electron backscatter deflection micrograph of the Hi-Nicalon™ S specimen “Air 7” examining the cross section at the midpoint of a fiber (σ_{cr} = 300 MPa, t_f = 100 h). 166

Figure 221 - SEM micrograph of the Hi-Nicalon™ S specimen “Air 11” examining the cross section at the midpoint of a fiber (σ_{cr} = 500 MPa, t_f = 100 h). 167

Figure 222 - SEM electron backscatter deflection micrograph of the Hi-Nicalon™ S specimen “Air 11” examining the cross section at the midpoint of a fiber (σ_{cr} = 500 MPa, t_f = 100 h). 167

Figure 223 - SEM micrograph of the Hi-Nicalon™ S specimen “Air 11” examining the cross section at the midpoint of a fiber (σ_{cr} = 500 MPa, t_f = 100 h). 168

Figure 224 - SEM electron backscatter deflection micrograph of the Hi-Nicalon™ S specimen “Air 11” examining the cross section at the midpoint of a fiber (σ_{cr} = 500 MPa, t_f = 100 h). 168

Figure 225 - SEM micrograph of the Hi-Nicalon™ S specimen “Air 11” examining the cross section at the midpoint of a fiber (σ_{cr} = 500 MPa, t_f = 100 h). 169

Figure 226 - SEM electron backscatter deflection micrograph of the Hi-Nicalon™ S specimen “Air 11” examining the cross section at the midpoint of a fiber (σ_{cr} = 500 MPa, t_f = 100 h). 169

Figure 227 - SEM micrograph of the Hi-Nicalon™ S specimen “Air 11” examining the cross section at the midpoint of a fiber (σ_{cr} = 500 MPa, t_f = 100 h). 170

Figure 228 - SEM electron backscatter deflection micrograph of the Hi-Nicalon™ S specimen “Air 11” examining the cross section at the midpoint of a fiber (σ_{cr} = 500 MPa, t_f = 100 h). 170

Figure 229 - SEM micrograph of the Hi-Nicalon™ S specimen “Air 11” examining the cross section at the midpoint of a fiber (σ_{cr} = 500 MPa, t_f = 100 h). 171

Figure 230 - SEM electron backscatter deflection micrograph of the Hi-Nicalon™ S specimen “Air 11” examining the cross section at the midpoint of a fiber (σ_{cr} = 500 MPa, t_f = 100 h). 171

Figure 231 - SEM micrograph of the Hi-Nicalon™ S specimen “Air 11” examining the cross section at the midpoint of a fiber (σ_{cr} = 500 MPa, t_f = 100 h). 172

Figure 232 - SEM electron backscatter deflection micrograph of the Hi-Nicalon™ S specimen “Air 11” examining the cross section at the midpoint of a fiber (σ_{cr} = 500 MPa, t_f = 100 h). 172

Figure 233 - SEM micrograph of the Hi-Nicalon™ S specimen “Air 3” examining the cross section at the lower portion of a fiber (σ_{cr} = 700 MPa, t_f = 62.5 h). 173

Figure 234 - SEM electron backscatter deflection micrograph of the Hi-Nicalon™ S specimen “Air 3” examining the cross section of the lower portion of a fiber (σ_{cr} = 700 MPa, t_f = 62.5 h). 173

Figure 235 - SEM micrograph of the Hi-Nicalon™ S specimen “Air 3” examining the cross section of the lower portion of a fiber (σ_{cr} = 700 MPa, t_f = 62.5 h)..... 174

Figure 236 - SEM electron backscatter deflection micrograph of the Hi-Nicalon™ S specimen “Air 3” examining the cross section of the lower portion of a fiber (σ_{cr} = 700 MPa, t_f = 62.5 h). 174

Figure 237 - SEM micrograph of the Hi-Nicalon™ S specimen “Air 3” examining the cross section of the lower portion of a fiber (σ_{cr} = 700 MPa, t_f = 62.5 h)..... 175

Figure 238 - SEM electron backscatter deflection micrograph of the Hi-Nicalon™ S specimen “Air 3” examining the cross section of the lower portion of a fiber (σ_{cr} = 700 MPa, t_f = 62.5 h). 175

Figure 239 - SEM micrograph of the Hi-Nicalon™ S specimen “Air 3” examining the cross section of the lower portion of a fiber (σ_{cr} = 700 MPa, t_f = 62.5 h)..... 176

Figure 240 - SEM electron backscatter deflection micrograph of the Hi-Nicalon™ S specimen “Air 3” examining the cross section of the lower portion of a fiber (σ_{cr} = 700 MPa, t_f = 62.5 h). 176

Figure 241 - SEM micrograph of the Hi-Nicalon™ S specimen “Air 3” examining the cross section of the lower portion of a fiber (σ_{cr} = 700 MPa, t_f = 62.5 h)..... 177

Figure 242 - SEM electron backscatter deflection micrograph of the Hi-Nicalon™ S specimen “Air 3” examining the cross section of the lower portion of a fiber (σ_{cr} = 700 MPa, t_f = 62.5 h). 177

Figure 243 - SEM micrograph of the Hi-Nicalon™ S specimen “Air 10” examining the cross section of the lower portion of a fiber (σ_{cr} = 800 MPa, t_f = 31.0 h)..... 178

Figure 244 - SEM electron backscatter deflection micrograph of the Hi-Nicalon™ S specimen “Air 10” examining the cross section of the lower portion of a fiber (σ_{cr} = 800 MPa, t_f = 31.0 h). 178

Figure 245 - SEM micrograph of the Hi-Nicalon™ S specimen “Air 10” examining the cross section of the lower portion of a fiber (σ_{cr} = 800 MPa, t_f = 31.0 h)..... 179

Figure 246 - SEM electron backscatter deflection micrograph of the Hi-Nicalon™ S specimen “Air 10” examining the cross section of the lower portion of a fiber (σ_{cr} = 800 MPa, t_f = 31.0 h). 179

Figure 247 - SEM micrograph of the Hi-Nicalon™ S specimen “Air 10” examining the cross section of the lower portion of a fiber (σ_{cr} = 800 MPa, t_f = 31.0 h)..... 180

Figure 248 - SEM electron backscatter deflection micrograph of the Hi-Nicalon™ S specimen “Air 10” examining the cross section of the lower portion of a fiber (σ_{cr} = 800 MPa, t_f = 31.0 h). 180

Figure 249 - SEM micrograph of the Hi-Nicalon™ S specimen “Air 10” examining the cross section of the lower portion of a fiber (σ_{cr} = 800 MPa, t_f = 31.0 h)..... 181

Figure 250 - SEM electron backscatter deflection micrograph of the Hi-Nicalon™ S specimen “Air 10” examining the cross section of the lower portion of a fiber (σ_{cr} = 800 MPa, t_f = 31.0 h). 181

Figure 251 - SEM micrograph of the Hi-Nicalon™ S specimen “Air 10” examining the cross section of the lower portion of a fiber (σ_{cr} = 800 MPa, t_f = 31.0 h)..... 182

Figure 252 - SEM electron backscatter deflection micrograph of the Hi-Nicalon™ S specimen “Air 10” examining the cross section of the lower portion of a fiber (σ_{cr} = 800 MPa, t_f = 31.0 h). 182

Figure 253 - SEM micrograph of the Hi-Nicalon™ S specimen “Air 10” examining the cross section of the lower portion of a fiber (σ_{cr} = 800 MPa, t_f = 31.0 h)..... 183

Figure 254 - SEM electron backscatter deflection micrograph of the Hi-Nicalon™ S specimen “Air 10” examining the cross section of the lower portion of a fiber (σ_{cr} = 800 MPa, t_f = 31.0 h). 183

Figure 255 - SEM micrograph of the Hi-Nicalon™ S specimen “Air 10” examining the cross section of the upper portion of a fiber (σ_{cr} = 800 MPa, t_f = 31.0 h)..... 184

Figure 256 - SEM electron backscatter deflection micrograph of the Hi-Nicalon™ S specimen “Air 10” examining the cross section of the upper portion of a fiber (σ_{cr} = 800 MPa, t_f = 31.0 h). 184

Figure 257 - SEM micrograph of the Hi-Nicalon™ S specimen “Air 10” examining the cross section of the upper portion of a fiber (σ_{cr} = 800 MPa, t_f = 31.0 h)..... 185

Figure 258 - SEM electron backscatter deflection micrograph of the Hi-Nicalon™ S specimen “Air 10” examining the cross section of the upper portion of a fiber (σ_{cr} = 800 MPa, t_f = 31.0 h). 185

Figure 259 - SEM micrograph of the Hi-Nicalon™ S specimen “Air 10” examining the cross section of the upper portion of a fiber (σ_{cr} = 800 MPa, t_f = 31.0 h)..... 186

Figure 260 - SEM electron backscatter deflection micrograph of the Hi-Nicalon™ S specimen “Air 10” examining the cross section of the upper portion of a fiber (σ_{cr} = 800 MPa, t_f = 31.0 h). 186

Figure 261 - SEM micrograph of the Hi-Nicalon™ S specimen “Air 10” examining the cross section of the upper portion of a fiber (σ_{cr} = 800 MPa, t_f = 31.0 h)..... 187

Figure 262 - SEM electron backscatter deflection micrograph of the Hi-Nicalon™ S specimen “Air 10” examining the cross section of the upper portion of a fiber (σ_{cr} = 800 MPa, t_f = 31.0 h). 187

Figure 263 - SEM micrograph of the Hi-Nicalon™ S specimen “Air 10” examining the cross section of the upper portion of a fiber (σ_{cr} = 800 MPa, t_f = 31.0 h)..... 188

Figure 264 - SEM electron backscatter deflection micrograph of the Hi-Nicalon™ S specimen “Air 10” examining the cross section of the upper portion of a fiber (σ_{cr} = 800 MPa, t_f = 31.0 h). 188

Figure 265 - SEM micrograph of the Hi-Nicalon™ S specimen “Air 10” examining the cross section of the upper portion of a fiber (σ_{cr} = 800 MPa, t_f = 31.0 h)..... 189

Figure 266 - SEM electron backscatter deflection micrograph of the Hi-Nicalon™ S specimen “Air 10” examining the cross section of the upper portion of a fiber (σ_{cr} = 800 MPa, t_f = 31.0 h). 189

Figure 267 - SEM micrograph of the Hi-Nicalon™ S specimen “Air 10” examining the cross section of the upper portion of a fiber (σ_{cr} = 800 MPa, t_f = 31.0 h)..... 190

Figure 268 - SEM electron backscatter deflection micrograph of the Hi-Nicalon™ S specimen “Air 10” examining the cross section of the upper portion of a fiber (σ_{cr} = 800 MPa, t_f = 31.0 h). 190

Figure 269 - SEM micrograph of the Hi-Nicalon™ S specimen “Steam 2” examining the cross section at the midpoint of a fiber (σ_{cr} = 3.5 MPa, t_f = 100 h). 191

Figure 270 - SEM electron backscatter deflection micrograph of the Hi-Nicalon™ S specimen “Steam 2” examining the cross section at the midpoint of a fiber (σ_{cr} = 3.5 MPa, t_f = 100 h). 191

Figure 271 - SEM micrograph of the Hi-Nicalon™ S specimen “Steam 2” examining the cross section at the midpoint of a fiber (σ_{cr} = 3.5 MPa, t_f = 100 h). 192

Figure 272 - SEM electron backscatter deflection micrograph of the Hi-Nicalon™ S specimen “Steam 2” examining the cross section at the midpoint of a fiber (σ_{cr} = 3.5 MPa, t_f = 100 h). 192

Figure 273 - SEM micrograph of the Hi-Nicalon™ S specimen “Steam 2” examining the cross section at the midpoint of a fiber (σ_{cr} = 3.5 MPa, t_f = 100 h). 193

Figure 274 - SEM electron backscatter deflection micrograph of the Hi-Nicalon™ S specimen “Steam 2” examining the cross section at the midpoint of a fiber (σ_{cr} = 3.5 MPa, t_f = 100 h). 193

Figure 275 - SEM micrograph of the Hi-Nicalon™ S specimen “Steam 2” examining the cross section at the midpoint of a fiber (σ_{cr} = 3.5 MPa, t_f = 100 h). 194

Figure 276 - SEM electron backscatter deflection micrograph of the Hi-Nicalon™ S specimen “Steam 2” examining the cross section at the midpoint of a fiber (σ_{cr} = 3.5 MPa, t_f = 100 h). 194

Figure 277 - SEM micrograph of the Hi-Nicalon™ S specimen “Steam 2” examining the cross section at the midpoint of a fiber (σ_{cr} = 3.5 MPa, t_f = 100 h). 195

Figure 278 - SEM electron backscatter deflection micrograph of the Hi-Nicalon™ S specimen “Steam 2” examining the cross section at the midpoint of a fiber (σ_{cr} = 3.5 MPa, t_f = 100 h). 195

Figure 279 - SEM micrograph of the Hi-Nicalon™ S specimen “Steam 2” examining the cross section at the midpoint of a fiber (σ_{cr} = 3.5 MPa, t_f = 100 h). 196

Figure 280 - SEM electron backscatter deflection micrograph of the Hi-Nicalon™ S specimen “Steam 2” examining the cross section at the midpoint of a fiber (σ_{cr} = 3.5 MPa, t_f = 100 h). 196

Figure 281 - SEM micrograph of the Hi-Nicalon™ S specimen “Steam 5” examining the cross section the lower portion of a fiber (σ_{cr} = 400 MPa, t_f = 30.83 h). 197

Figure 282 - SEM electron backscatter deflection micrograph of the Hi-Nicalon™ S specimen “Steam 5” examining the cross section the lower portion of a fiber (σ_{cr} = 400 MPa, t_f = 30.83 h). 197

Figure 283 - SEM micrograph of the Hi-Nicalon™ S specimen “Steam 5” examining the cross section the lower portion of a fiber (σ_{cr} = 400 MPa, t_f = 30.83 h). 198

Figure 284 - SEM electron backscatter deflection micrograph of the Hi-Nicalon™ S specimen “Steam 5” examining the cross section the lower portion of a fiber (σ_{cr} = 400 MPa, t_f = 30.83 h). 198

Figure 285 - SEM micrograph of the Hi-Nicalon™ S specimen “Steam 5” examining the cross section the lower portion of a fiber (σ_{cr} = 400 MPa, t_f = 30.83 h). 199

Figure 286 - SEM electron backscatter deflection micrograph of the Hi-Nicalon™ S specimen “Steam 5” examining the cross section the lower portion of a fiber (σ_{cr} = 400 MPa, t_f = 30.83 h). 199

Figure 287 - SEM micrograph of the Hi-Nicalon™ S specimen “Steam 5” examining the cross section the lower portion of a fiber (σ_{cr} = 400 MPa, t_f = 30.83 h). 200

Figure 288 - SEM electron backscatter deflection micrograph of the Hi-Nicalon™ S specimen “Steam 5” examining the cross section the lower portion of a fiber (σ_{cr} = 400 MPa, t_f = 30.83 h). 200

Figure 289 - SEM micrograph of the Hi-Nicalon™ S specimen “Steam 5” examining the cross section the lower portion of a fiber (σ_{cr} = 400 MPa, t_f = 30.83 h). 201

Figure 290 - SEM electron backscatter deflection micrograph of the Hi-Nicalon™ S specimen “Steam 5” examining the cross section the lower portion of a fiber (σ_{cr} = 400 MPa, t_f = 30.83 h). 201

Figure 291 - SEM micrograph of the Hi-Nicalon™ S specimen “Steam 5” examining the cross section the lower portion of a fiber (σ_{cr} = 400 MPa, t_f = 30.83 h). 202

Figure 292 - SEM electron backscatter deflection micrograph of the Hi-Nicalon™ S specimen “Steam 5” examining the cross section the lower portion of a fiber (σ_{cr} = 400 MPa, t_f = 30.83 h). 202

Figure 293 - SEM micrograph of the Hi-Nicalon™ S specimen “Steam 5” examining the cross section the lower portion of a fiber (σ_{cr} = 400 MPa, t_f = 30.83 h). 203

Figure 294 - SEM electron backscatter deflection micrograph of the Hi-Nicalon™ S specimen “Steam 5” examining the cross section the lower portion of a fiber (σ_{cr} = 400 MPa, t_f = 30.83 h). 203

Figure 295 - SEM micrograph of the Hi-Nicalon™ S specimen “Steam 5” examining the cross section the lower portion of a fiber (σ_{cr} = 400 MPa, t_f = 30.83 h). 204

Figure 296 - SEM electron backscatter deflection micrograph of the Hi-Nicalon™ S specimen “Steam 5” examining the cross section the lower portion of a fiber (σ_{cr} = 400 MPa, t_f = 30.83 h). 204

Figure 297 - SEM micrograph of the Hi-Nicalon™ S specimen “Steam 5” examining the cross section the lower portion of a fiber (σ_{cr} = 400 MPa, t_f = 30.83 h). 205

Figure 298 - SEM electron backscatter deflection micrograph of the Hi-Nicalon™ S specimen “Steam 5” examining the cross section the lower portion of a fiber (σ_{cr} = 400 MPa, t_f = 30.83 h). 205

Figure 299 - SEM micrograph of the Hi-Nicalon™ S specimen “Steam 5” examining the cross section the lower portion of a fiber (σ_{cr} = 400 MPa, t_f = 30.83 h). 206

Figure 300 - SEM electron backscatter deflection micrograph of the Hi-Nicalon™ S specimen “Steam 5” examining the cross section the lower portion of a fiber (σ_{cr} = 400 MPa, t_f = 30.83 h). 206

Figure 301 - SEM micrograph of the Hi-Nicalon™ S specimen “Steam 5” examining the cross section the lower portion of a fiber (σ_{cr} = 400 MPa, t_f = 30.83 h). 207

Figure 302 - SEM electron backscatter deflection micrograph of the Hi-Nicalon™ S specimen “Steam 5” examining the cross section the lower portion of a fiber (σ_{cr} = 400 MPa, t_f = 30.83 h). 207

Figure 303 - SEM micrograph of the Hi-Nicalon™ S specimen “Steam 5” examining the cross section the lower portion of a fiber (σ_{cr} = 400 MPa, t_f = 30.83 h). 208

Figure 304 - SEM micrograph of the Hi-Nicalon™ S specimen “Steam 5” examining the cross section the lower portion of a fiber (σ_{cr} = 400 MPa, t_f = 30.83 h). 208

List of Tables

Table 1 - Characteristics of different classes of CMCs.. 4

Table 2 - Details of manufacture, elemental composition and approximate cost of all three generations of SiC based fibers..... 10

Table 3 - Properties and compositions of silicon-based fibers 10

Table 4 - Creep mechanisms in fine grain ceramic polycrystals 16

Table 5 - Typical properties of Hi-Nicalon™ S fiber tow..... 25

Table 6 - Fiberglass tab dimensions..... 26

Table 7 - Effective gauge lengths of Hi-Nicalon™ S fibers at 1000°C..... 41

Table 8 – Results of the monotonic tension tests of Hi-Nicalon™ S fiber tows in air at 23°C.... 42

Table 9 - Summary of tensile creep test results for Hi-Nicalon™ S fiber tows at 1000°C in laboratory air and in silicic acid-saturated steam..... 44

Table 10 - Hi-Nicalon™ S specimens prepared for analysis in the scanning electron microscope. 61

Table 11 – Predictions of oxide scale thickness for test conditions obtained using Deal-Grove kinetics. 68

I. Introduction and Background

Technological advancements of materials have led to revolutions and have defined eras in history, such as the Stone Age, Bronze Age and Iron ages. With all the research and progress in the area of combining materials in such a way that their combination is better than the sum, some say we are in the midst of the "Composite Age" [1].

A composite, is a material that has a chemically and/or physically distinct phase distributed within a continuous phase [2]. The history of composites dates all the way back to ancient Egypt, where straw was baked in clay to strengthen bricks [3]. Today, composites are being used in a variety of applications ranging from metal rods or rebar employed to reinforce concrete. Polymer Matrix Composites (PMCs) have successfully combined two phases to generate a high-strength, lightweight material used in aerospace, aircraft, automotive, marine, energy, infrastructure, biomedical and recreational (sports) applications [4]. However, PMCs do not retain their strength at elevated temperatures. In the case of high-temperature applications, traditional metals, alloys, and PMCs cannot provide the requisite strength at elevated temperatures. Figure 3 below depicts the strength of various engineering materials versus temperature [5]. Consequently, considerable research has been done over the last 50 years to produce a material that can maintain its strength and stiffness at elevated temperatures [6].

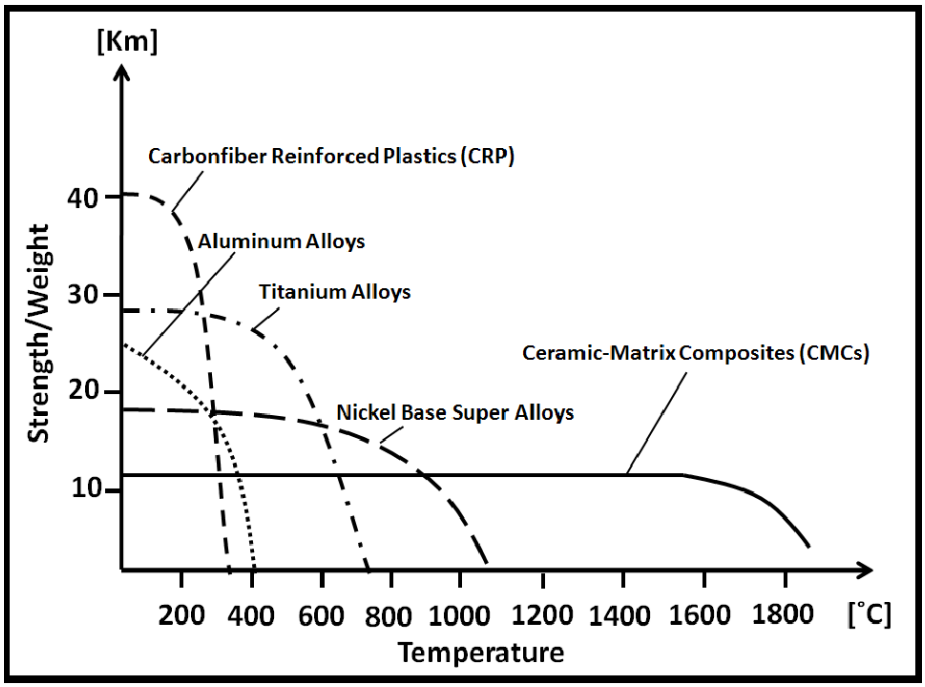


Figure 1 - Strength to weight ratio as a function of temperature. Reproduced from [5], pg. 410, Figure 1, Copyright © 2004, with permission from Elsevier.

Structural ceramics are brittle materials that exhibit high strength and stiffness at elevated temperatures while also possessing low density. However, ceramics are also known to lack toughness and damage tolerance, and to fail catastrophically. Ceramic matrix composites (CMCs) were designed to specifically to combat these undesirable traits. While the CMCs generally consist of brittle constituents (e.g. ceramic fibers and ceramic matrix), they exhibit toughness, flaw tolerance and are capable of a non-catastrophic failure mode. The damage-tolerant behavior and a "graceful" failure mode of the CMCs are achieved through the weak fiber/matrix interphase. A properly designed fiber/matrix interphase serves to dissipate the energy of the crack front moving through the material and to deflect the cracks around the load-

bearing fibers. In the CMC the deformation proceeds through damage associated with matrix cracking, and debonding and sliding along the fiber-matrix interfaces. While both fiber and matrix are brittle materials that fail catastrophically, the CMC exhibits “inelastic” deformation and fails gracefully.

1.1 Ceramic Matrix Composites

As mentioned above, monolithic ceramics are brittle and lack a mechanism to absorb energy. Hence, they fail catastrophically without warning. For this reason, much research in the second half of the 20th century was directed towards developing CMCs that exhibit toughness, tolerance to the presence of cracks and defects and a graceful failure mode [2]. Continuous Fiber Ceramic Composites (CFCCs) are CMCs reinforced with fibers that run the entire length of the composite. CFCCs have better toughness characteristics than both monolithic ceramics and the discontinuous fiber ceramic composites (DFCCs, typically reinforced with particulates, platelets or whiskers) [2]. This desirable behavior of the CFCCs is typically achieved by means of a properly designed weak fiber/matrix interphase or by means of an exceptionally weak porous matrix [7]. Figure 2 shows a schematic representation of tensile stress-strain curves for a monolithic ceramic and for a CFCC. A monolithic ceramic has higher stiffness than a CFCC, but it also fails abruptly in a catastrophic manner. Table 1 compares characteristics of the three different classes of composites: carbon-carbon composites, CMCs reinforced with continuous fibers and the CMCs with discontinuous forms of reinforcement [3].

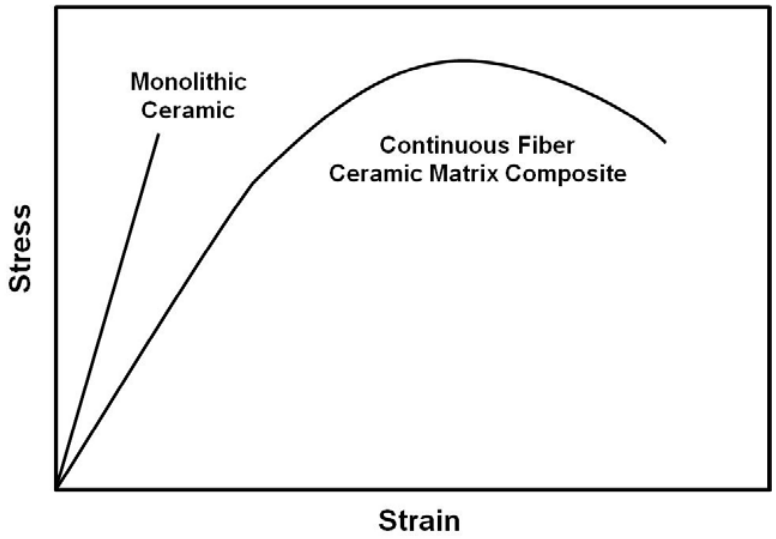


Figure 2 - Notional comparison of stress-strain behaviors exhibited by a monolithic ceramic and a continuous-fiber ceramic matrix composite. Reproduced from Armani [8].

Table 1 - Characteristics of different classes of CMCs. Reproduced from [3], pg. 44, Table 2.1.

Carbon-Carbon	Continuous CMCs	Discontinuous CMCs
Exceptional High Temp Mech Properties	Excellent High Temp Mech. Properties	Excellent High Temp Mech Properties
High Specific Strength and Stiffness High Fracture Toughness	High Specific Strength and Stiffness High Fracture Toughness	High Specific Strength and Stiffness Higher Useful Strengths.
Dimensional Stability Low Thermal Expansion	Dimensional Stability Low Thermal Expansion	Fracture Toughness Good but Inferior to Continuous CMCs
High Thermal Shock Resistance Graceful Failure Modes	Good Thermal Shock Resistance Graceful Failure Mode	Thermal Shock Resistance Inferior to Continuous CMCs
Tailorable Properties Machinability Poor Oxidation Resistance	Oxidation Resistance Machining More Difficult Processing More Complicated and Expensive	Amenable to Cheaper Conventional Processes Machining Expensive

Figure 3 schematically depicts three microstructural design concepts enabling damage-tolerant behavior and non-catastrophic mode of failure in CFCCs [7]. The three microstructural design philosophies in Figure 3 promote uncorrelated fiber failure resulting in energy dissipation

and subsequent fiber pull-out. The first design approach employs a fiber coating (typically C and BN) to form a weak fiber/matrix interface. This design path is typically used to fabricate dense-matrix CFCCs such as SiC/SiC CFCCs. The second design approach, typically employed when fabricating oxide/oxide CFCCs, relies on porous matrix for crack deflection and toughness. In this case no coating is applied to the fibers. The third design approach show in Figure 3 utilized fugitive coatings. After composite has been manufactured, these coatings are volatized by oxidation leaving a gap at the fiber/matrix interface.

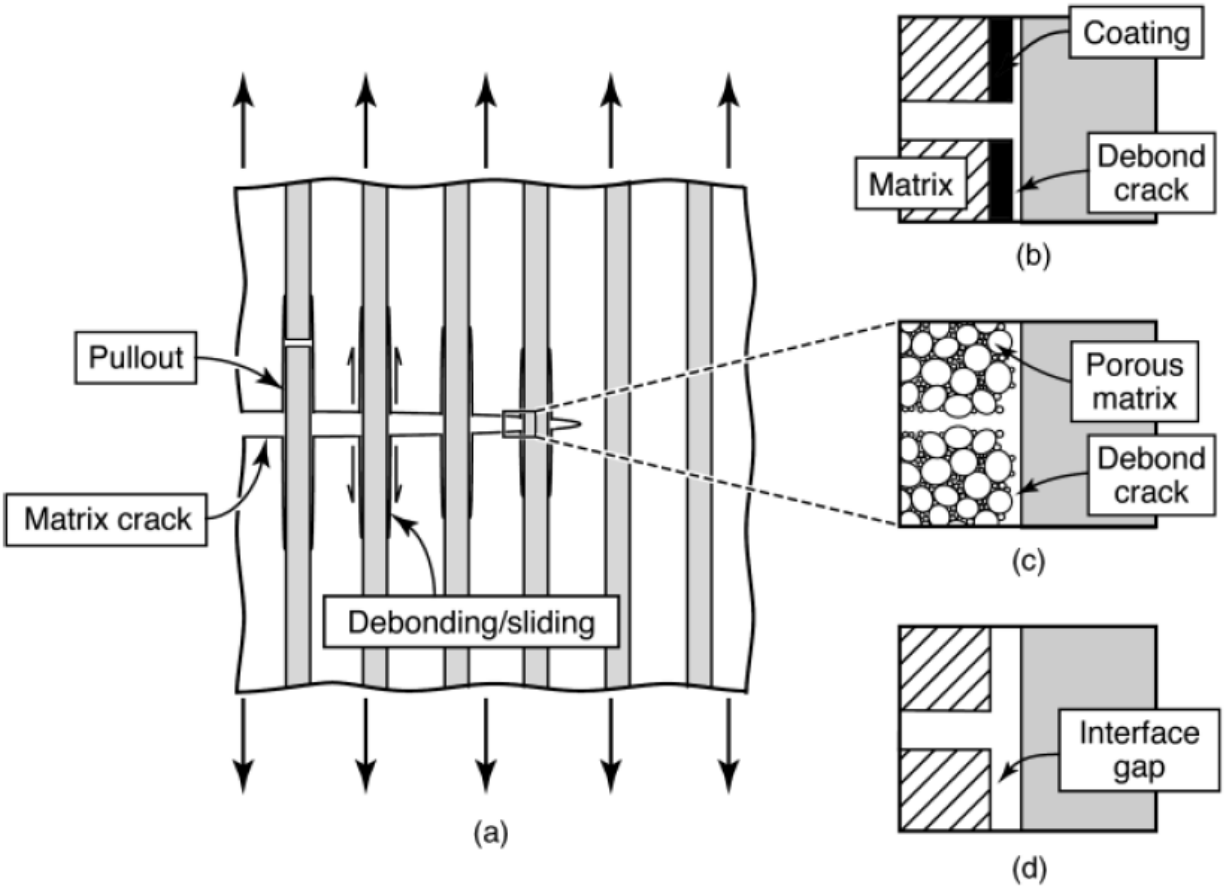


Figure 3 - Microstructural design philosophies for enabling crack deflection in continuous-fiber ceramic composites. F.W. Zok, John Wiley & Sons [9].

Of particular interest are SiC fiber-reinforced SiC matrix composites. These materials combine low density with high strength and fracture toughness at high temperatures. However, both SiC fibers and SiC-based matrix materials are intrinsically prone to oxidation. As a result, SiC/SiC experience oxidation embrittlement when exposed to oxidizing environments at elevated temperature. Oxidation embrittlement takes place when oxygen enters through the matrix cracks

and attacks the fibers and the fiber coatings. Oxidative degradation of fibers and fiber coatings is accelerated in moisture-containing environments. Because fibers play a key load-bearing role, oxidative degradation of the fibers leads to degradation of mechanical properties and performance of the overall composite. Thus, a thorough understanding of fiber behavior in oxidizing environments is critical to gaining insight into the effects of oxidation on mechanical properties of SiC/SiC composites.

1.2 Silicon Carbide (SiC) Fibers - General Characteristics

The production process for Silicon Carbide (SiC) fibers was developed in the 1960s. SiC fiber is made by a Chemical Vapor Deposition (CVD) process onto a tungsten or carbon substrate. The substrate is heated to about 1300°C. Early methods of producing SiC fiber resulted in a very thick filament of 100 to 140 μm in diameter. This was an inflexible fiber that could only be used to reinforce metal matrix composites (MMCs) and intermetallics [10]. Yajima [11] developed an alternative method of producing a smaller diameter SiC fiber by utilizing a polymer precursor. The steps in this method include melt spinning a polymer into a fiber, crosslinking the fiber by curing and pyrolyzing [11]. A diagram of the Yajima process is depicted in the Figure 4. Using the new method, fibers of approximately 10 μm diameter could now be produced. These smaller diameter fibers could be woven into plies and used in CMCs [6].

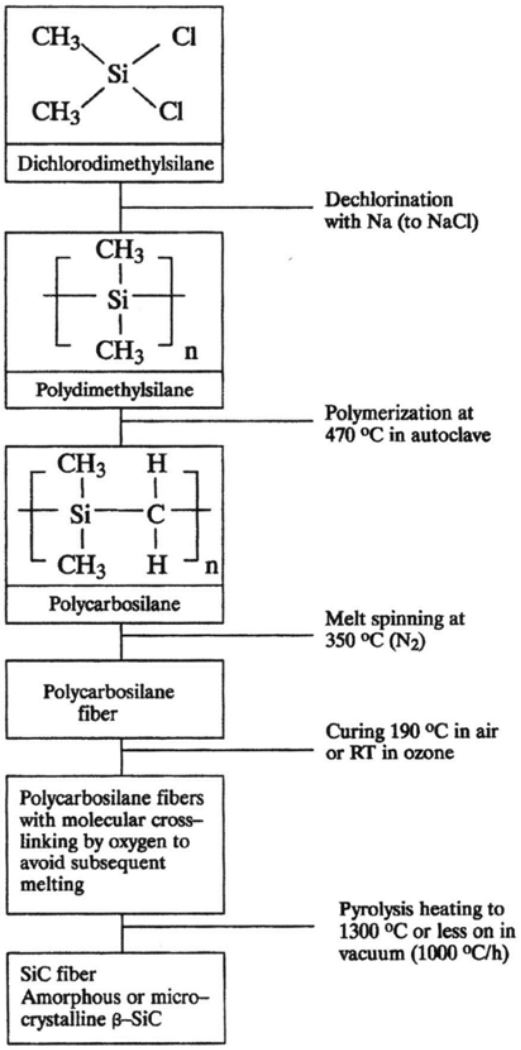


Figure 4 - Yajima production process for SiC-based fibers. Reprinted by permission from Springer US, Ceramic Matrix Composites: Ceramic reinforcements by K. K. Chawla [2], Copyright ©1993.

1.3 Nicalon™ Fiber

Production of 100 series Nicalon™ fibers began in 1980 by Nippon Carbon in Tokyo, Japan. The 200 series Nicalon™ fibers were released in 1984. The Nicalon™ fibers are manufactured from a polycarbosilane (PCS) precursor, which is cured at 200°C to cross-link and

then subjected to a controlled temperature increase to 1200°C. The repeat element of the PCS precursor can be seen in Figure 5. The PCS is arraigned in a hexagonal, β-SiC pattern.

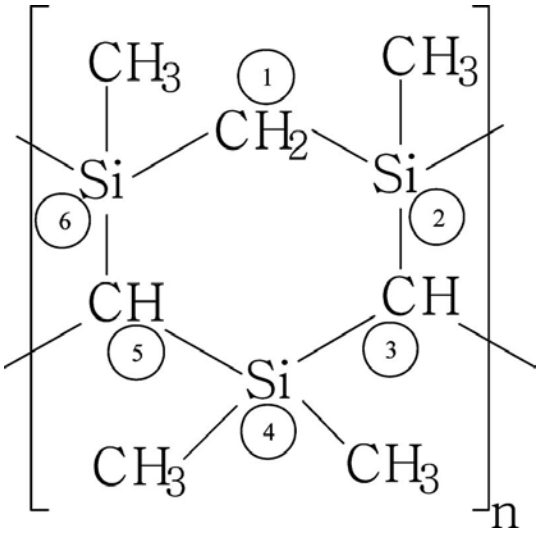


Figure 5 - PCS precursor arraigned in a hexagonal, β-SiC pattern. Reproduced with permission from Springer Science & Business Media B.V. [10] pg. 824, Figure 1. Copyright © 2005 by Springer-Verlag Berlin Heidelberg.

The composition of Nicalon™ fibers is 56.6% wt. Si, 31.7% wt. C and 11.7% wt. O. The Nicalon™ fibers had the strength of 2.0 GPa and Young's Modulus is 190 GPa. These first generation SiC fibers were of a small enough diameter (about 10-20 μm) and sufficiently flexible to be woven into plies to be incorporated into a CMC. Nicalon™ fibers retain their strength, resistance to corrosion and modulus of elasticity at temperatures below 1000°C. However, Nicalon™ fibers experience creep and strength degradation at temperatures in excess of 1000°C due to their non-stoichiometric composition. The Nicalon™ SiC fibers are non-stoichiometric because the PCS chains are cross-linked with oxygen. Thus, carbon is permitted to off-gas from

the fiber during pyrolysis and oxygen remains in the fibers in an amorphous intergranular Si-O-C phase [7].

Table 2 and Table 3 show the composition, cost, density, strength and stiffness parameters for the three generations of SiC fibers [12].

Table 2 - Details of manufacture, elemental composition and approximate cost of all three generations of SiC based fibers. Reproduced with permission from Springer Science & Business Media B.V. [10] pg. 826, Table 3. Copyright © 2005 by Springer-Verlag Berlin Heidelberg.

	Trade mark	Manufacturer	Cross linking method	Approximate maximum production temperature	Elemental composition (wt%)	Density (g/cm^3)	Average diameter (μm)	Cost (US $/kg)
First Gen.	Nicalon 200	Nippon Carbon	Oxygen	1200°C	56Si + 32C + 12O	2.55	14	2000
	Tyranno LOX-M	Ube Ind.	Oxygen	1200°C	54Si + 32C +12O + 2Ti	2.48	11	1250
Second Gen.	Hi-Nicalon	Nippon Carbon	Electron irradiation	1300°C	62.5Si + 37C +0.5O	2.74	12	8000
	Tyranno LOX-E	Ube Ind.	Electron irradiation	1300°C	55Si + 37.5 +5.5O + 2Ti	2.39	11	N/A
	Tyranno ZM	Ube Ind.	Oxygen	1300°C	57Si + 34.5C + 7.5O + 1Zr	2.48	11	1500
	Tyranno ZE	Ube Ind.	Electron irradiation	1300°C	58.5Si + 38.5C + 2O + 1Zr	2.55	11	N/A
Third Gen.	Tyranno SA 1	Ube Ind.	Oxygen	>1700°C	68Si + 32C +0.6Al	3.02	11	N/A
	Tyranno SA 3	Ube Ind.	Oxygen	>1700°C	68Si + 32C +0.6Al	3.1	7.5	5000
	Sylramic	COI ceramics	Oxygen	>1700°C	67Si + 29C +0.8O + 2.3B +0.4N +2.1Ti	3.05	10	10000
	Sylramic iBN	COI Ceramics	Oxygen	>1700°C	N/A	3.05	10	>10000
	Hi-Nicalon Type-S	Nippon Carbon	Electron irradiation	>1500°C	69Si + 31C + 0.2O	3.05	12	13000

Table 3 - Properties and compositions of silicon-based fibers. Reproduced from [14] pg. 2251, Table 1. Copyright © 2005 with permission from Elsevier.

Fibre type	Manufacturer	Trade mark	Composition (wt.%)	Diameter (μm)	Density (g/cm3)	Strength (GPa)	Strain to failure (%)	Young's modulus (GPa)
Si–C based	Nippon Carbide	Nicalon NLM 202	56.6 Si;31.7 C;11.7 O	14	2.55	2.0	1.05	190
	Nippon Carbide	Hi-Nicalon	62.4 Si;37.1 C;0.5 O	14	2.74	2.6	1.0	263
	Ube Industries	Tyranno Lox-M	54.0 Si;31.6 C;12.4 O;2.0 Ti	8.5	2.37	2.5	1.4	180
	Ube Industries	Tyranno Lox-E	54.8 Si;37.5 C;5.8 O;1.9 Ti	11	2.39	2.9	1.45	199
Near stoichiometric SiC	Nippon Carbon	Hi-Nicalon S	SiC + O + C	13	3.0	2.5	0.65	375
	Ube Industries	Tyranno SA	SiC + C + O + Al	10	3.0	2.5	0.75	330
	Dow Corning	Sylramic	SiC + TiB2 + C + O	10	3.1	3.0	0.75	390

1.4 Hi-Nicalon™ Fiber

It was determined that the limited performance of the first generation SiC fibers, Nicalon™, was due to their non-stoichiometric composition. Okamura pioneered a new method to fabricate SiC fibers by γ-rays or electron irradiation in vacuum to limit the amount of oxygen in the fibers [13]. Nippon Carbon then developed its second-generation SiC fibers utilizing this innovative approach to cure the PCS precursor with electron irradiation. In this process, oxygen is introduced after the curing process is completed. The resulting Hi-Nicalon™ fibers are nearly oxygen free. Furthermore, Hi-Nicalon™ fibers contain only trace amounts of the Si-O-C phase and therefore do not degrade at elevated temperatures [10]. The composition of Hi-Nicalon™ fibers is 62.4% wt. Si, 37.1% wt. C and 0.5% wt. O. Hi-Nicalon™ fibers have a strength of 2.5 GPa and a Young's Modulus of 375 GPa. Decreasing the amount of oxygen also allowed for an increase in grain size. The size of the β-SiC grains in Hi-Nicalon™ fibers is 5 to 10 nm. When the fibers are heat-treated at 1450°C, the average grain size increases to about 30 nm. As a result of heat treatment, the fibers gain creep resistance, chemical stability, as well as resistance to corrosive environments. Tensile strength and modulus of Hi-Nicalon™ fibers are nearly half that of bulk SiC.

1.5 Hi-Nicalon™ S Fiber

Hi-Nicalon™ S fibers are the third generation SiC fibers produced by Nippon Carbon. Hi-Nicalon™ S fibers have a near-stoichiometric composition. These fibers are manufactured from a PCS precursor and cured by electron irradiation. They are then pyrolyzed in a controlled

environment at temperatures greater than 1500°C. Sintering aids were removed from the PCS precursor. The diameter of the Hi-Nicalon™ S fiber is 12 μm and the β-SiC grain sizes are between 50 and 100 nm. The Young's Modulus of Hi-Nicalon™ S fibers is 375 GPa and the strength is 2.5 GPa. Figure 6 shows the manufacturing process for Hi-Nicalon™ S fiber.

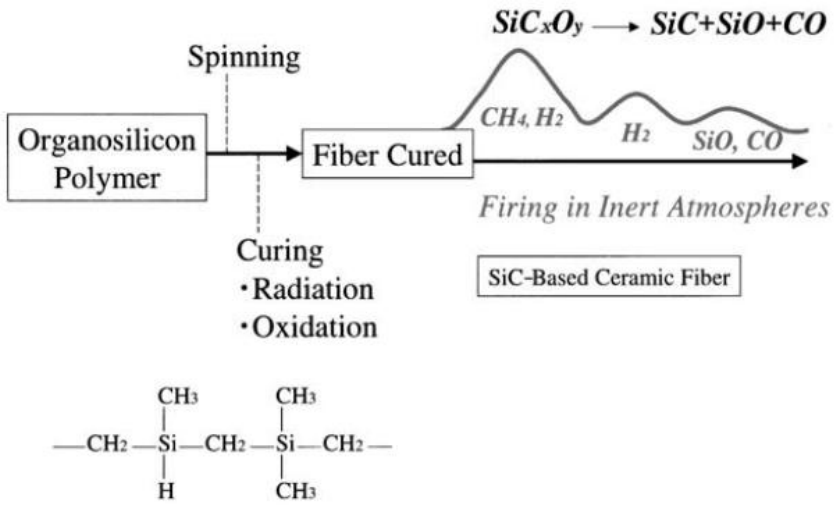


Figure 6 - Production process of SiC fibers from PCS Precursor. Reproduced with permission from Springer Science & Business Media B.V. [6] pg. 117, Figure 8. Copyright © 2005 by Springer-Verlag Berlin Heidelberg.

Figure 7 shows the three generations of SiC fiber manufactured by Nippon Carbon. Note the grain size of the β-SiC increases for each successive generation of SiC fibers. The larger grain size in the Hi-Nicalon™ S fibers improves their creep resistance and increases their Young's modulus to a level comparable to that of bulk SiC. However, Hi-Nicalon™ S fibers suffer from a reduction in strength when compared to the second-generation Hi-Nicalon™ fibers [10].

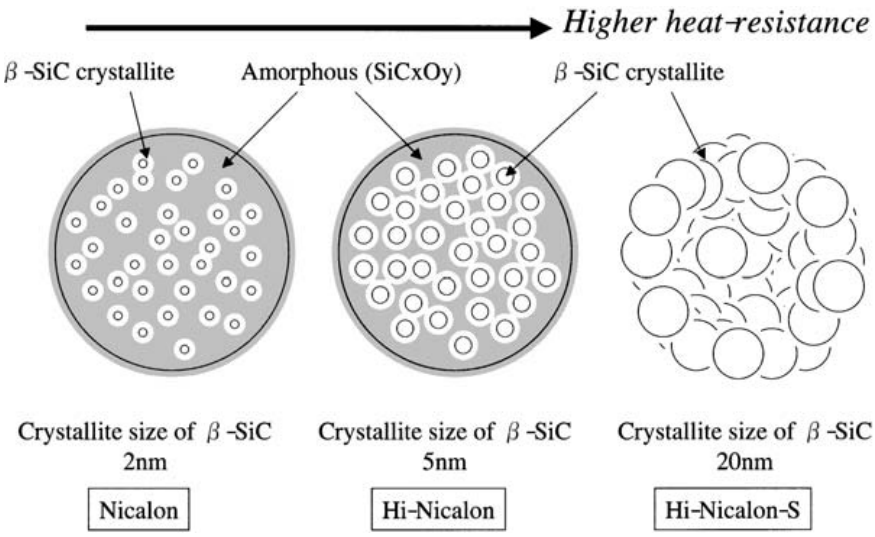


Figure 7 - Microstructure schematic of Nicalon™, Hi-Nicalon™, and Hi-Nicalon™ S fibers. Reproduced with permission from Springer Science & Business Media B.V. [6] pg. 118, Figure 9. Copyright © 2005 by Springer-Verlag Berlin Heidelberg.

1.6 Creep

It is widely recognized that SiC fibers are susceptible to creep at intermediate and elevated temperatures [14]. CMCs and PMCs are well-known to experience both time and temperature dependent behavior, as well as display a highly nonlinear response to applied loading [15]. Creep is a phenomenon is characterized by an increase in strain with time under constant load. Creep is often divided into three regions or stages: primary, secondary, and tertiary. Primary creep is categorized by a rapid increase in strain and a decreasing strain rate. Primary creep is associated with changes in the material structure (such as grain size, dislocation structure, etc.) or with the redistribution of stresses. The secondary stage is categorized by a nearly constant creep strain rate. The secondary or steady-state creep is viewed as the deformation of an invariant microstructure. Lastly, the tertiary stage of creep proceeds with an

increasing strain rate associated with the initiation of the failure processes. Figure 8 depicts a schematic of the three stages of creep.

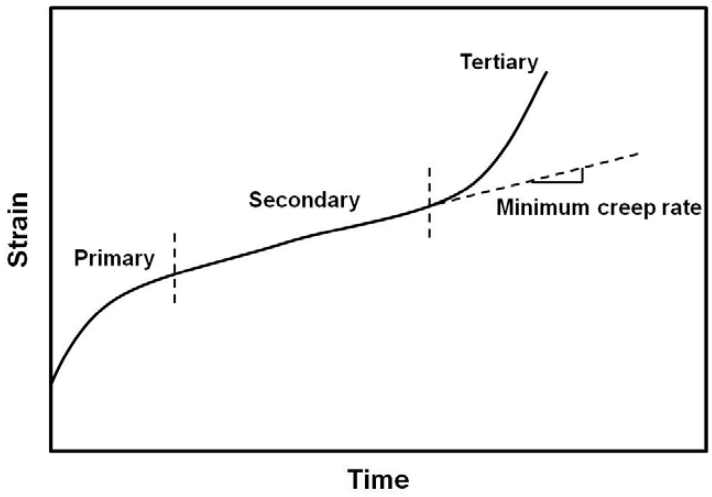


Figure 8 - Three regions of creep deformation: Primary, Secondary, and Tertiary. Reproduced from Armani [8].

The secondary or steady-state creep is the focus for most research into creep behavior of CMCs, ceramic fibers and ceramics in general [7]. Steady-state creep deformation in polycrystals can proceed by dislocation mechanisms and by diffusional mechanisms. While these two distinct mechanisms, they are frequently coupled and may be difficult to dissociate [8]. Dislocation-controlled creep proceeds by grain boundaries sliding or climbing next to each other due to shear [7]. In the case of the diffusion-controlled creep, the diffusion can occur through the grains (Nabarro-Herring creep) as well as along grain boundaries (Coble creep) by the Arrhenius rate equation below [16].

$$\dot{\varepsilon} = \frac{AD\mu b}{kT}\left(\frac{b}{d}\right)^{m}\left(\frac{\sigma}{\mu}\right)^{n} \quad (1)$$

In the Arrhenius rate equation, $\dot{\varepsilon}$ is the steady state creep rate, μ is the shear modulus, b is the Burgers vector, d is the grain size, k is the Boltzmann constant, T is the absolute temperature, σ is the applied stress, m is the grain size exponent, and n is the stress exponent. D is the diffusivity constant or coefficient which is calculated in Equation (2):

$$D = D_0 exp\left(\frac{-Q}{RT}\right) \quad (2)$$

Here D_0 is a frequency factor, Q is the creep activation energy, and R is the universal gas constant. Different creep mechanisms can be correlated to different values of exponents, m and n, which are from the experimental creep data. Hence, the controlling creep mechanism can be identified from the analysis of creep data. Table 4 gives a summary of predominant creep mechanisms observed in fine-grain ceramic polycrystals [8].

Table 4 - Creep mechanisms in fine grain ceramic polycrystals. Reproduced from Armani [8].

n stress exponent	*m* grain size exponent	Mechanism
1	2	Diffusional creep through lattice (Nabarro-Herring creep)
1	3	Diffusional creep along grain boundaries (Coble creep)
2	1	Grain boundary sliding and interface-reaction controlled creep
4	3	GBS and cavity growth
3-5	0	Dislocation creep: 3 –glide controlled, 5 –climb controlled
>5		Cavity growth controlled creep

1.7 Previous Work

DiCarlo et al [17] studied mechanical behavior of SiC/SiC composites and found that the fracture of SiC/SiC composites is primarily determined by creep-induced flaw growth in the SiC fibers. They noted the importance of improving the microstructure of the CMC by reducing impurity phases and increasing the grain size.

Yun et al [18] investigated strength properties and creep behavior of several stoichiometric SiC fibers at 1400°C. The findings revealed that the service life of stoichiometric SiC fibers was strongly dependent on manufacturing techniques, as well as on service environment. Furthermore, they noted a strength reduction of 20 to 40% in the Hi-Nicalon™ S fibers compared to the Hi-Nicalon™ fibers. Improved creep performance and an increase in

rupture strength of the Hi-Nicalon^{TM} S fibers was attributed to larger grain size, a reduction in oxygen impurity, and the restructuring of excess carbon. In a later work, Yun and DiCarlo [14] evaluated stoichiometric SiC through testing single fibers as well as fiber tows in both inert and oxidizing environments. The results revealed a significant difference in strength and creep response obtained for single fibers and for the fiber tows. The difference was even more pronounced for fibers with courser grains. Additionally, SiC fibers were coated with a BN interphase and tested. The BN-coated fibers tows were found to possess the strength obtained from single fiber tests.

Bodet and colleagues [19] studied the tensile creep behavior of Nicalon™ and Hi-Nicalon™ fibers at temperatures up to 1600°C. They concluded that the strength of Nicalon™ fibers and that of the Hi-Nicalon™ fibers were similar at temperatures above 1200°C. Necking of the fibers was also observed. Furthermore, reduction in fiber diameter by at least a factor of 2 was observed, indicating high levels of local deformation and stress. However, the Hi-Nicalon™ fibers exhibited much better creep resistance than the Nicalon™ fibers.

Bertrand et al [20] investigated SiC/SiC ceramic composites and the effect of fiber coating on composite performance. They tested Hi-Nicalon™ fibers at 700°C to determine tensile strength and static fatigue lifetimes. They found that properly designed fiber/matrix interphases improved the lifetime of the composite subject to static fatigue in air.

DiCarlo [21] investigated creep in polycrystalline SiC fibers and found that strength and creep resistance of fibers can degrade at temperatures as low as 800°C. Grain-boundary sliding

was identified as the reason for the changes. DiCarlo found that sintered SiC fibers with grain less than 100 nm in size exhibited the highest strength values and the best creep resistance. In later work, DiCarlo [22] noted that the high-temperature performance of the Hi-Nicalon™ fibers is limited by creep rather than strength.

Sauder and Lamon [23, 24] studied creep behavior of Hi-Nicalon™, Hi-Nicalon™ S, and Tyranno SA3 fibers at temperatures ranging from 1150°C to 1700°C. They observed all three stages of creep; primary, secondary and tertiary, in their tests. They attributed primary creep to viscoelastic deformation of carbon at the grain boundaries. It was noted that primary creep was more pronounced in fibers with higher carbon content such as Hi-Nicalon™. Secondary creep was quantified with the Arrhenius equation. The controlling creep mechanism was identified as grain-boundary sliding without grain elongation and glassy phases of the Rachinger type. Additionally, diffusion of either carbon or silicon was believed to occur in the Hi-Nicalon™ fibers. Lastly, tertiary creep was attributed to the reduction in the cross-sectional area of the Hi-Nicalon™ fiber due to degradation.

Dassios et al [25] evaluated the tensile strength of Nextel 720 single fibers and fiber tows. The authors found that in the process of pulling out a single fiber for testing weaker fibers would break. Only stronger fibers would survive the extraction process intact and be tested. As a result, these experiments would overestimate the strength of the tow. Therefore, fiber tow testing was determined to provide a more accurate and representative strength estimate.

Forio et al [26] conducted tests on Nicalon™ fibers at temperatures ranging from 600°C to 800°C. In tests performed with low stresses at intermediate temperatures, unexpected failure occurred in the fiber tows. Failure was attributed to a slow-crack-growth mechanism that was successfully characterized using the Paris law. A model was developed to predict the lifetime and failure in a fiber tow after a critical number of fibers have failed within the tow. Gauthier and Lamon [27] expanded upon this study and investigated delayed failure of Hi-Nicalon™ and Hi-Nicalon™ S fiber tows at intermediate temperatures. Stress vs. time to failure data obtained in these experiments were successfully modeled using a power law. Additionally, Gauthier and Lamon [27] found that Hi-Nicalon™ S fiber tows possessed greater resistance to crack-growth than Hi-Nicalon™ fiber tows. The greater fracture toughness was attributed to less free carbon in the near-stoichiometric fibers.

Calard and Lamon [28] aimed to determine how failure of fiber tows differs from failure of single fibers. A statistical model was employed to predict failure in Nicalon™ and Hi-Nicalon™ fiber tows using various probability and uncertainty principles. Strength was found to be dependent upon local load sharing between fibers within a tow. Additionally, tow strength was found to be highly variable as well as less than that predicted from single fiber tests.

Gauthier et al [29] studied static fatigue of Hi-Nicalon™ and of Hi-Nicalon™ S multifilament fiber tows and static fatigue of single filaments at 500°C-800°C in air. Delayed failure of the fibers was observed. Additionally, formation of a thin silica film on the surface of the fibers due to oxidation was noted. Free carbon and oxygen were also found on the fiber

surface in the form of defects. Gauthier et al concluded these defects allowed cracks to propagate through the fiber.

Opila et al [30] investigated the oxidation of SiC in water vapor at temperatures between 1200°C and 1400°C. It was found that silica scales volatized forming $Si(OH)_4(g)$ species. Opila and co-workers developed a paralinear relationship for the oxidation and volatilization reactions. The lifetime of a specimen, in an oxidizing environment, was determined by the rate of the volatization of the silica scales.

Shimoo et al [31] also investigated the active and passive oxidation of Nicalon, Hi-Nicalon™ and Hi-Nicalon™ S fibers at 1773 K. Active oxidation of both Nicalon™ and Hi-Nicalon™ caused an order of magnitude decrease in strength compared. However, Hi-Nicalon™ S fibers retained their strength under active oxidation. Shimoo et al found that the type of reaction was strongly dependent upon the partial pressure of oxygen in the environment.

Viricelle and colleagues [32] investigated the oxidation behavior of a SiC fiber, carbon and SiBC matrix CMC in air and in steam. The results indicated the boron nitride (BN) interphase degraded at intermediate temperatures (650°C to 900°C). Furthermore, at higher temperatures (900°C to 1200°C) the BN interphase was virtually non-existent. However, at the higher temperatures, both borosilicate and silica scale growth provided a self-healing property which strengthened the CMC in steam.

Costello and Tressler [33] researched the oxidation kinetics of single-crystal and polycrystalline SiC in dry air at temperatures ranging from 1200°C to 1500°C. Oxidation rates

and activation energies were determined for different faces. Impurities and regions of increased density were found to be prone to oxidation and scale growth. Song et al modified the Deal-Grove model [34] to account for the off-gassing of carbon monoxide (CO) from the CMC [35]. The modified model accounts for differences in oxidation rates on all three faces of the crystal. The diffusion of CO and SiO from fibers was noted by Jaskowiak and DiCarlo [36].

Hay and colleagues researched oxidation in Hi-Nicalon™ and Hi-Nicalon™ S fibers over the 700-1400°C temperature range. Crystalline scales were investigated and the growth kinetics of grains were modeled using the modified Deal-Grove relationship [34, 37]. Crystalline scales were observed to grow quickly parallel to the fiber surface. The amorphous scales were thicker than the crystalline scales, except where growth cracks allowed for quicker oxidation in the fiber. The modified Deal-Grove model [35, 38, 39, 40] predicts the growth rate of the SiO_2 scale (x) according to the Equations (3)-(5) below. Here A_0 and B_0 are constants, Q_a and Q_b are activation energies, B is the parabolic rate constant, B/A is the linear rate constant, R is the universal gas constant and T is the absolute temperature.

$$\frac{dx}{dt} = \frac{B}{(A + 2x)} \tag{3}$$

$$A = A_0 exp\left(\frac{-Q_a}{RT}\right) \tag{4}$$

$$B = B_0 exp\left(\frac{-Q_b}{RT}\right) \tag{5}$$

Given an initial SiO_2 scale thickness (x_i), the solution to Equation (3) is given by Equation (6) [41]. In Equation (7), the initial state of the oxide layer is taken into account through a time shift parameter,τ.

$$x = 1/2\, A\left\{[1 + (t + \tau)/(A^2/4B)]^{1/2} - 1\right\} \tag{6}$$

$$\tau = (\, x_i^2 + Ax_i)/B \tag{7}$$

Parthasarathy et al [42] continued the above work and modeled the grain growth and the oxidation kinetics of SiC fibers in argon, air and steam. A model was developed based on the classical normal grain growth and experimental data obtained for Hi-Nicalon™ and Hi-Nicalon™ S fibers.

Hay [37] aimed to determine how the growth of amorphous and crystallized SiO_2 scales created growth stresses on the fibers using the aforementioned flat-plate Deal-Grove parameters. Hay found that higher growth stresses occurred at intermediate temperatures (700-900 °C). At temperatures in excess of 1200°C the amorphous silica scale relaxed and served to relieve stress on the fibers. Hay [43] attributed the decrease in growth stress at the higher temperatures to a larger activation energy for silica viscosity. The findings revealed initial growth of an amorphous scale. However, as the temperature approached 1000°C, a crystallized scale began to develop. The difference in the coefficients of thermal expansion of the amorphous and crystalline scales created growth stresses, which led to cracking during cool-down [37].

Armani investigated the effects of air and steam on elevated-temperature creep behavior of Nextel 610 and Nextel 720 fiber tows [8]. Steffens [1] adapted the experimental procedure developed by Armani to testing of Hi-Nicalon™ S fiber tows at 800°C and 1100°C in air and in steam. Steffens found that at 800°C the presence of steam increased the steady-state creep rate by one order of magnitude and decreased the creep lifetime by three orders of magnitude. Creep performance in steam improved when the temperature was increased to 1100°C. The improvement was attributed to the growth of a protective silica scale in steam at higher temperatures.

Shillig [44] also studied creep of Hi-Nicalon™ S SiC fiber tows at 800, 900, 1000 and 1100 °C in laboratory air and in steam. Shillig noted the degradation in creep performance due to steam became less pronounced as temperature increased. Most importantly, testing in steam revealed that bottom sections of the fiber tow exhibited degradation due to active oxidation, whereas top sections of the fiber tow exhibited SiO_2 scale growth due to passive oxidation. Shillig concluded that steam was chemically altered as it traveled along the fiber tow, extracting silicon from the lower portion of the fiber tow specimen to become saturated with silicic acid ($Si(OH)_4$) as it reached the top portion. The steam saturation process caused a gradual change in oxidation mechanism of the Hi-Nicalon™-S fiber tow.

Robertson [7] in collaboration with Sprinkle [45] further modified the test setup used by Steffens [1] and Shillig [44]. The objective pursued by Robertson and Sprinkle was to achieve uniform oxidation along the length of the fiber tow specimen during high-temperature testing in

steam. This objective was achieved. The improved test facility ensured that steam was saturated with silicic acid and heated to test temperature prior to entering the test chamber. Robertson tested Hi-Nicalon™ S fiber tows at 800°C in air, steam and silicic acid-saturated steam. It was concluded that the unsaturated steam caused significantly greater degradation to the fibers than the silicic acid-saturated steam. Robertson found growth of a uniform oxide layer which sealed the surface of the fibers and helped increase the strength and creep performance of the fibers.

Piper [46] and Mitchell [47]continued investigating creep of Hi-Nicalon™ S fiber tows in air and in silicic acid-saturated steam at 700°C and 900°C, respectively. Piper found that creep performance of the fibers tows at 700°C differed little from that observed at 800°C. Piper noticed that a small percentage of fibers grew a thick, crystallized oxide layer. However, the excessive oxidation on those fibers had minimal impact on the overall performance of the fiber tow. Mitchell found unsaturated steam was significantly more damaging to the fibers than silicic acid-saturated steam at 900°C. Mitchell also observed silica scale growth and evidence of environmentally assisted crack growth on a small number of fibers.

II. Material and Test Specimen

2.1 Material

The material used in this research was Hi-Nicalon™ S fiber produced by Nippon Carbon Co., Ltd, in Tokyo, Japan. The focus of the research was to characterize creep behavior of Hi-Nicalon™ S fiber tows at 1000° C in air and silicic-acid saturated steam. The fiber tows consist of 500 individual fibers with an average diameter of 12 μm [48]. The calculated average cross-

sectional area for the fiber tows is 5.655 x 10^{-8} m^2. Specimens were prepared from the same spool as that used in prior work [1, 7, 44, 46, 47]. Characteristics of the Hi-Nicalon™ S fiber tow provided by the manufacturer are displayed in Table 4 [48].

Table 5 - Typical properties of Hi-Nicalon™ S fiber tow. Data reproduced from NGS Advanced Fibers Co., Ltd. [48]

Number of filaments	500
Filament diameter (μm)	12
Product Form	Tow
Sizing Agent	PVA
Linear density, tex (g/km)	198
Oxygen content (wt%)	0.8
Modulus of Elasticity (GPA)	380

2.2 Test Specimen

The SiC fiber tow test specimens were prepared by using the three tab method developed by Steffens [1]. Note that the three tab method was used in all research into behavior of SiC fiber tows carried out at AFIT to-date [45, 46, 47]. The dimensions of the three tabs used in this method are shown in Table 6. A solid model and a drawing of the he fiberglass tab layout are shown in Figures 9 and 10, respectively.

Table 6 - Fiberglass tab dimensions

Tab	Length	Width
Primary	1.5 in 0.0381 m	1.0 in 0.0254 m
Secondary	1.0 in 0.0254 m	1.0 in 0.0254 m
Tertiary	0.75 in 0.0191 m	0.75 in 0.0191 m

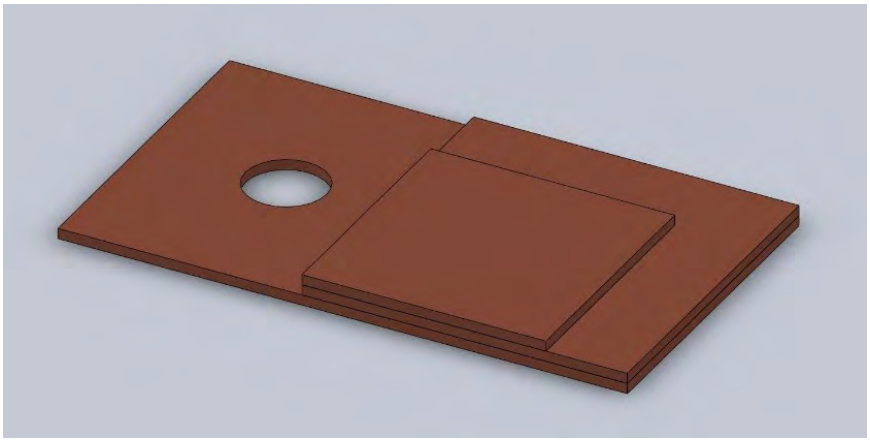


Figure 9 - A solid model of the three fiberglass tab configuration. Reproduced from Steffens [1].

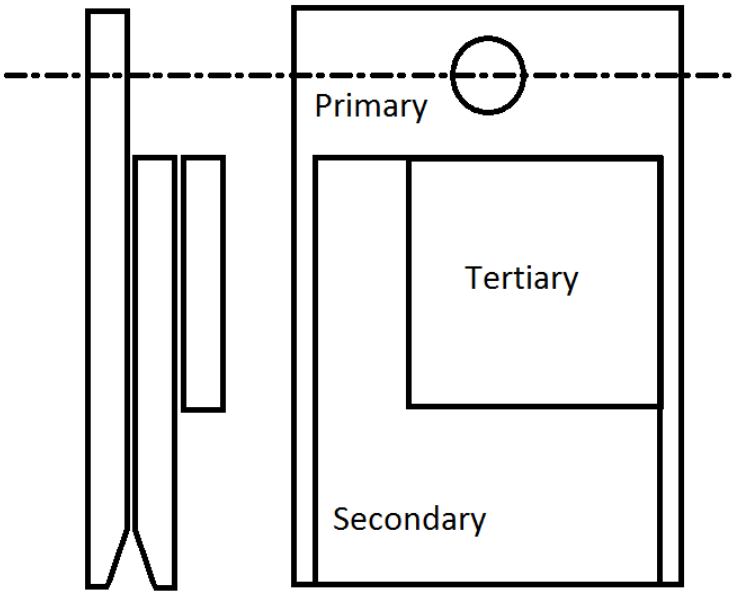


Figure 10 – Fiberglass tab layout with edges filed down for creep testing. Reproduced from Mitchell [47].

Detailed step-by-step specimen preparation procedure is given by Steffens in Appendix A1 of Ref. 1 [1]. A brief description is provided here. After the tabs are cut to size, a hole is punched in the primary tab along the centerline of the tab. The hole is used to secure the specimen on hook fixtures for the dead weight creep testing. The primary and secondary tabs are filed down to remove sharp edges to prevent the tabs from damaging the fiber tow. The primary tabs are then laid out and secured with tape on the grid of test specimen preparation board (see Figure 11) with a 0.178 m (7 in.) gap between the tab. Special case is taken to ensure that the grid lines on the preparation board bisect the hole in each primary tab as shown in Step 1 in Figure 12. Using the same grid line that was employed to ensure alignment, a length of fiber tow is then cut from the spool

and taped to the cutting board extending beyond the primary tab at each end (Step 2 in Figure 12**)**. It is important to align the fiber tow along the centerline of the hole in the primary tab in order to ensure that the fiber tow is subjected to axial loading only during the creep test. The secondary tab is then secured on top of the primary tab and fiber tow using a two-part epoxy (Step 3 in Figure 12**)**. The epoxy is allowed to set for 5 min before the excess fiber is folded over and secured using the tertiary tab and the same epoxy (Step 4 in Figure 12). The excess fiber that protrudes from the tertiary tab is cut with a razor blade (Step 5 in Figure 12**)**. The epoxy is allowed to cure for 24 h before further handling. Test specimens prepared for tensile testing under monotonic or sustained loading are shown in Figure 13.

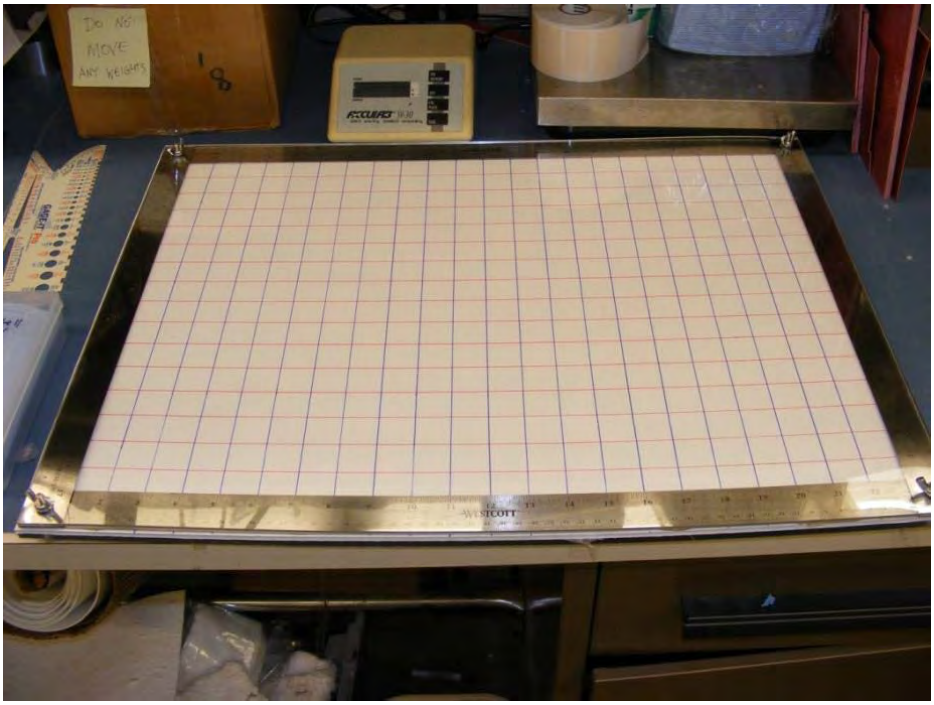


Figure 11 – Test specimen preparation board. Reproduced from Mitchell [47].

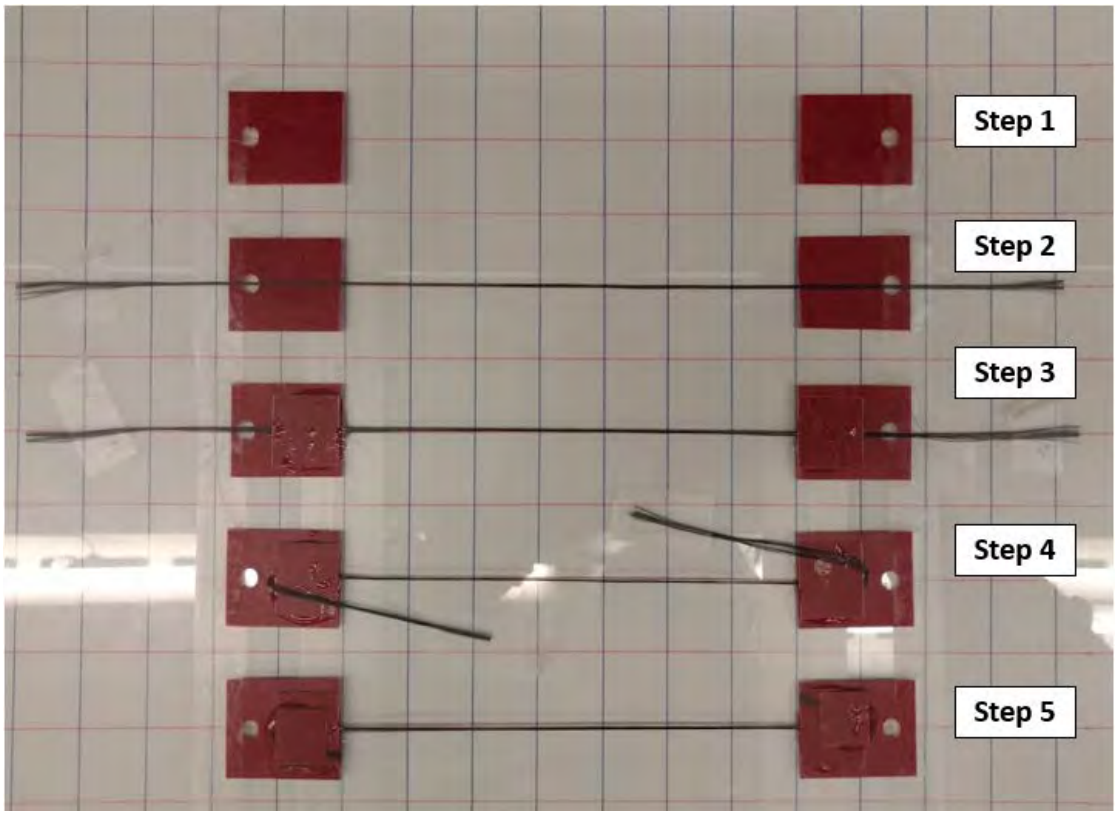


Figure 12 – Test specimen preparation process for creep testing.

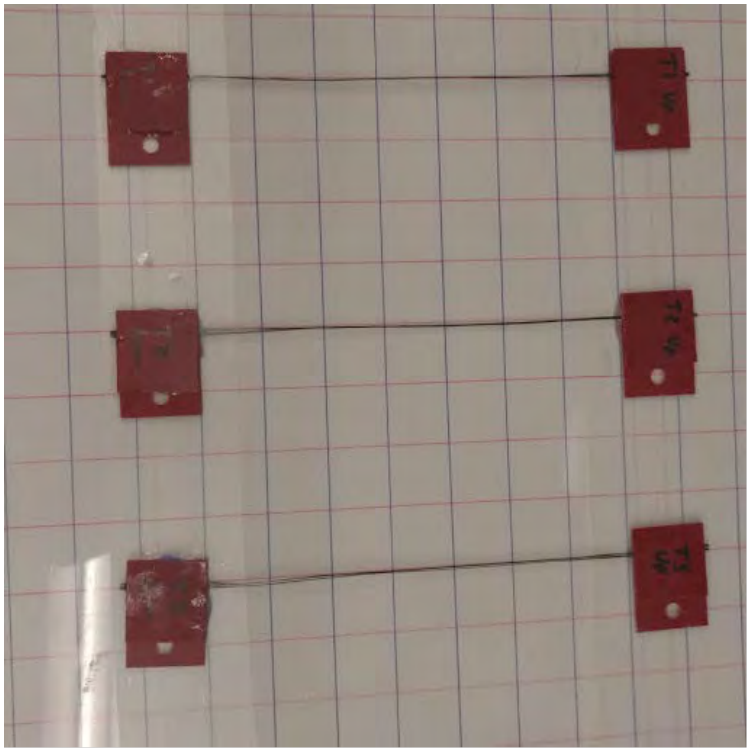


Figure 13 – Test specimens prepared for monotonic and creep tension testing.

2.3 Experimental Facility

All tests were conducted in the Mechanics of Advanced Aerospace Materials Laboratory (MAAML) of the Department of Aeronautics and Astronautics at AFIT. The experimental facility was first designed and set up by Armani [8] to test oxide fiber tows at elevated temperature in air and in steam. Subsequently Steffens [1] and then Shillig [44] modified the experimental facility to test Hi-Nicalon™ S SiC fiber tows at elevated temperature in air and in steam. Steffens [1] found that all fiber tow specimens failed near the location where steam entered the test chamber. Shillig [44] successfully corrected this problem by redesigning the

steam delivery system. Specimens tested by Shillig failed in different locations along the tow. However, Shillig also reported that fiber tow specimens tested in steam exhibited signs of active oxidation in the bottom portion and signs of passive oxidation process in the top portion of the specimen. This change in oxidation process from active to passive along the length of the fiber tow specimen was attributed to steam being chemically altered as it traveled upwards along the fiber tow. Robertson [7] postulated that steam was leaching Si from the bottom portion of the fiber tow and gradually becoming saturated with silicic acid ($Si(OH)_4$) as it reached the top portion of the fiber tow.

Robertson [7] in collaboration with Sprinkle [45] modified the test facility such that the steam was saturated with silicic acid and heated to test temperature prior to entering the test chamber. Robertson [7] argued that testing SiC fiber tows in steam with saturated silicic acid, while producing uniform oxidation along the fiber tow, also mimics environmental conditions experienced by SiC fibers in a SiC/SiC composite. When a SiC/SiC composite is subjected to mechanical loading at elevated temperature in steam, cracks first form on the composite exterior. Steam enters the composite through matrix cracks. As steam travels through the SiC matrix, it extracts Si from the SiC matrix and the crack-bridging SiC fibers to become saturated with silicic acid, $Si[OH]_4$. Hence, it is the silicic-acid-saturated steam that attacks the SiC fiber tows in the composite interior.

A detailed description of the modified fiber tow test facility is given by Roberson [7]. A brief summary is provided here. The overall view of the test facility is presented in Figures 14

and 15. A compact two-zone resistance-heated furnace (Model 653.03A, MTS Systems Corporation, Eden Prairie, MN) equipped with two temperature controllers (MTS 409.83) provides the high temperature environment. A ceramic susceptor (alumina tube with end caps) designed to fit inside the furnace is used to achieve a more uniform and repeatable temperature distribution along the fiber tow test specimen. The gauge section of the fiber tow specimen is located inside the susceptor with the specimen ends passing through slots in the susceptor end caps. The total length of the furnace is 124 mm and the length of the susceptor is 90 mm. Temperature profiles are measured throughout the length of the furnace in air and in steam with a K-type thermocouple. Because a cold gripping method is used in all tests, specimen elongation is measured outside the furnace with an LVDT (Schaevitz M12-30) attached to the bottom tab of the fiber tow specimen. For creep tests the dead weight is attached to the rod extending from the bottom of the LVDT. Displacement data is recorded using an MTS FlexTest 40 digital controller. In all tests performed in air, a specimen is heated to test temperature at 1°C/s then held at test temperature for at least 45-min prior to testing. A small weight (< 20 g) is used to keep the fiber tow specimen taut during heat-up to and heat-soak at test temperature. After the heat-soak, the dead-weight load is slowly applied to the fiber tow specimen using a hand-driven screw elevator.

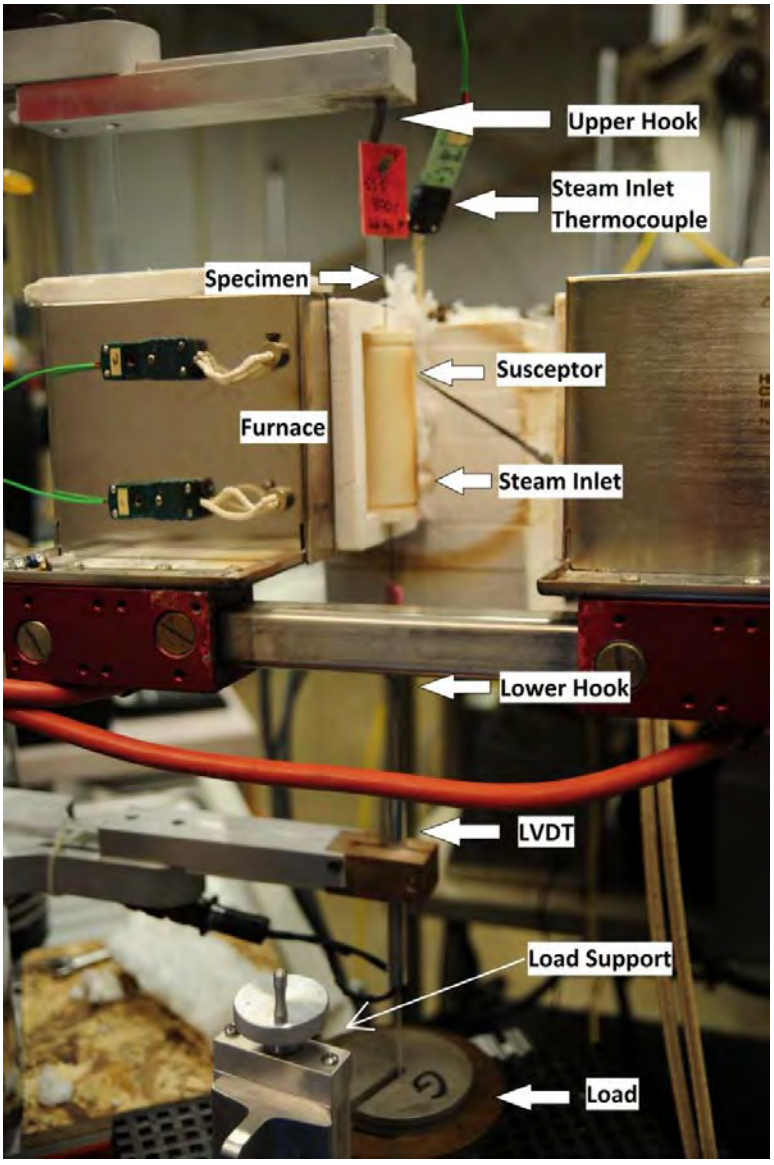


Figure 14 - Fiber tow specimen mounted in the creep testing rig. Reproduced from Robertson [7].

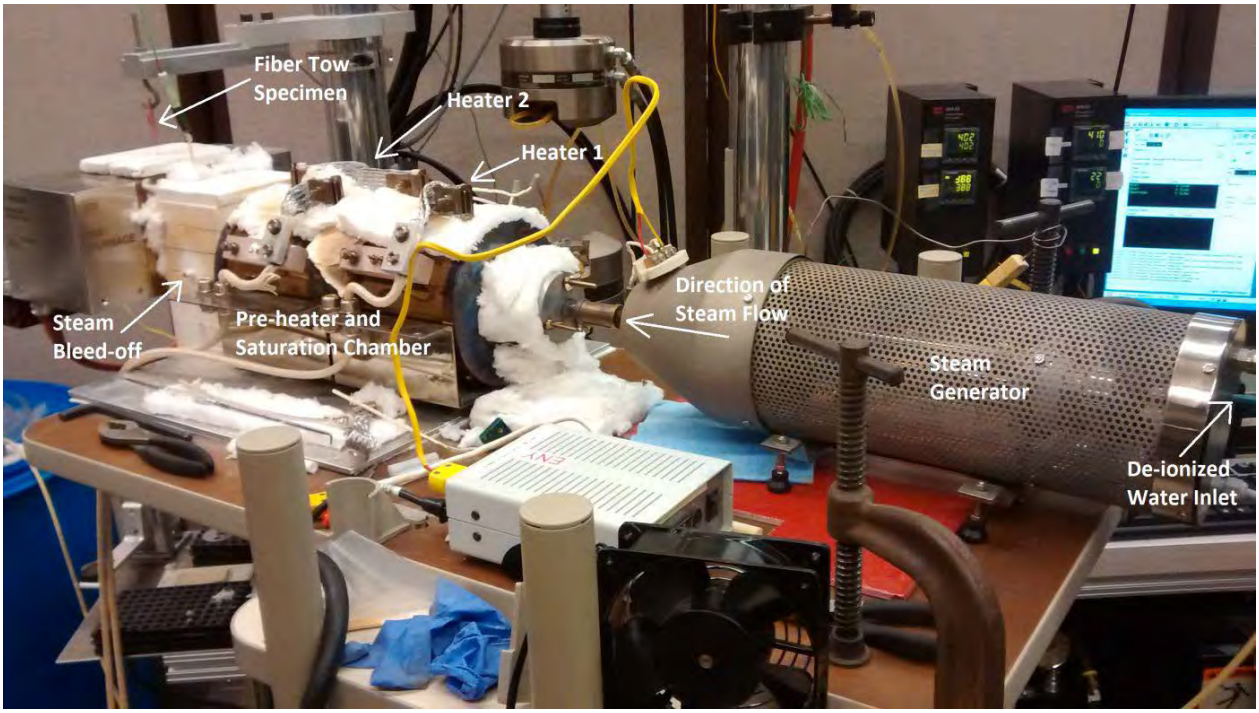


Figure 15 – Dead weight tensile creep test facility configured for saturated steam tests. Reproduced from Robertson [7].

For testing in silicic acid-saturated steam, steam was produced using a steam generator manufactured by Micropyretics Heaters International (MHI), model HGA-H. A Cole Parmer ® model 7518-10 peristaltic pump delivered 16-16.6 ml of deionized water to the steam generator from a 50 gallon reservoir. Power input to the steam generator was controlled using a Variac rheostat. Upon exiting the steam generator, steam passes through an alumina tube filled with sacrificial silica wool and becomes saturated with silicic acid (see Figure 16 and 17). The alumina tube fits inside two MHI CX1300 heaters equipped with heating coils fabricated by I Squared R Element Co. The two CX1300 heaters were controlled by an IBPAN variable rheostat.

The output of the IBPAN controller was sent to a transformer for the appropriate voltage adjustment before powering the CX1300 heaters. The heaters were covered with RATH KVS 174/400 insulation. Now the steam is saturated with silicic acid and heated to the target test temperature prior to entering the test chamber containing the fiber tow specimen. Note that the CX1300 preheaters were also used for testing in air in order to heat the air to test temperature before introducing it into the test chamber.

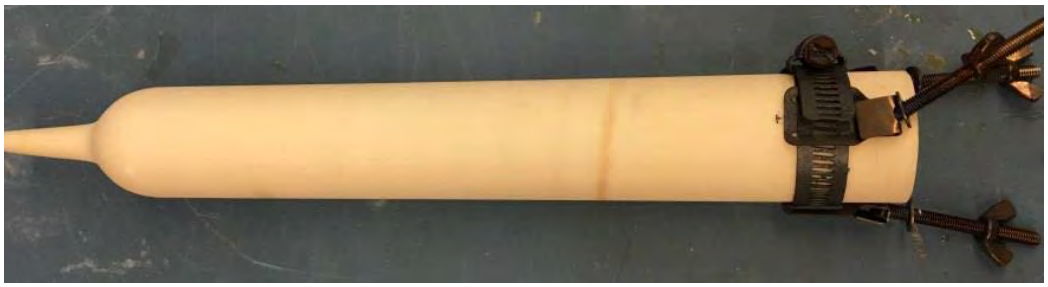


Figure 16 - Alumina tube used for steam saturation with silica wool. Reproduced from Piper [46].



Figure 17 – Sacrificial silica wool inserted into the alumina tube. Reproduced from Piper [46].

2.4 Temperature Profiles

Temperature profiles of the test chamber were determined for both the air and steam environments. The temperature profiles were used to calculate the effective length, L_{eff}, of the fiber tow test specimen. The effective length is needed to calculate the engineering strain from the displacement measured by the LVDT during tests. The method for calculating engineering strain is described in Section 4.3 below. Temperature along the centerline of the furnace was measured with a K-type thermocouple with an accuracy of ±3°C. Temperature readings were collected during a continuous vertical sweep along the centerline of the furnace and recorded in a data file using the MTS software. The temperature profiles obtained at 1000°C in air and in saturated steam environments are shown in Figure 18 and Figure 19, respectively. Note that the zero position corresponds to the middle of the furnace. Position of +60 mm corresponds to the top of the furnace and position of -60 mm, to the bottom of the furnace.

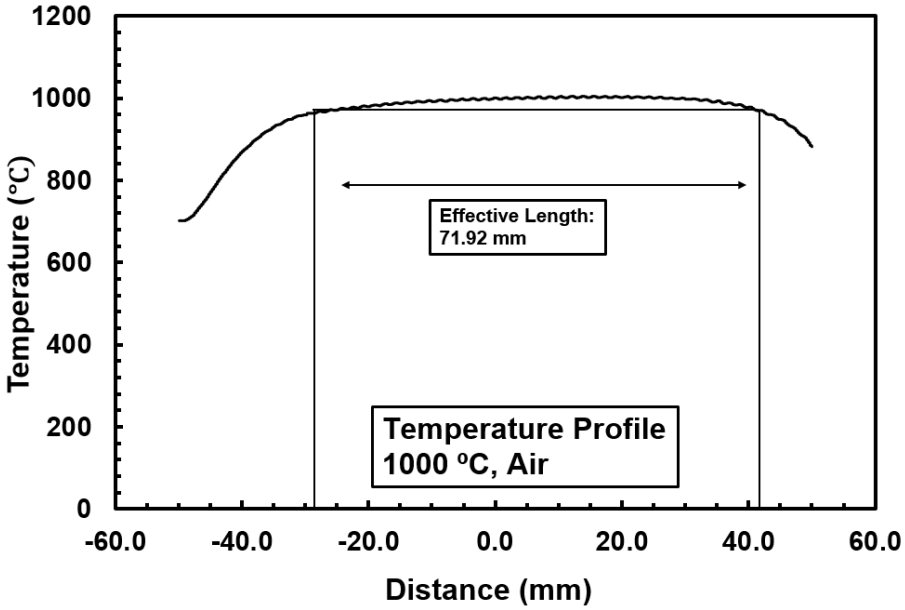


Figure 18 - Temperature profile obtained in laboratory air at 1000°C.

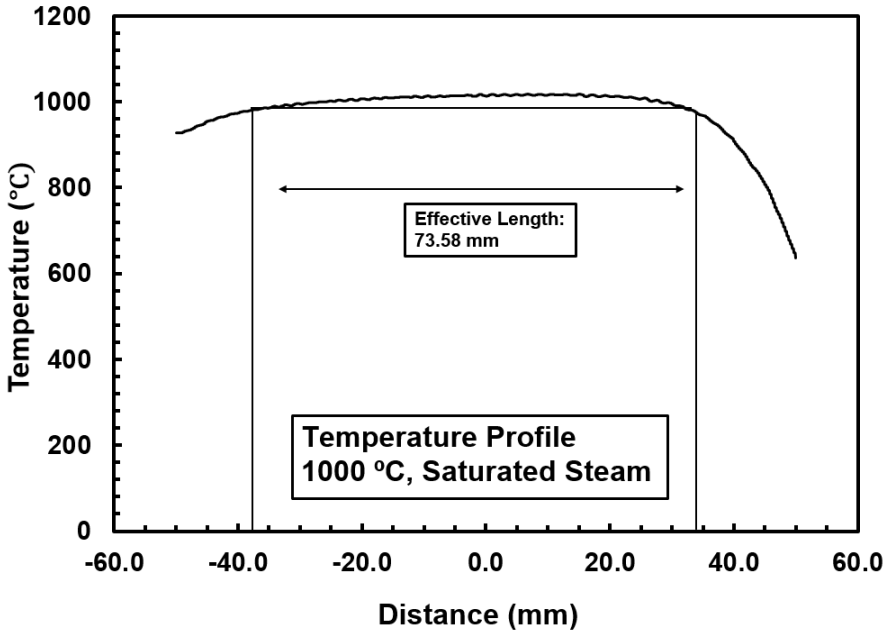


Figure 19 - Temperature profile obtained in saturated steam at 1000°C.

2.5 Engineering Strain Measurement

Fiber tow testing does not allow for direct measurement of strain using extensometry, only displacement data can be collected. Hence strain must be calculated from the displacement data. Because the cold gripping was employed to secure the fiber tow specimen during testing, the elongation of the specimen was measured in a cold zone outside the furnace. Therefore, methods employed to calculate strain from displacement data must account for temperature variation along the specimen.

The fiber tow specimen is exposed to room temperature above and below the furnace (the cold zone), the test temperature in the middle portion of the furnace (the hot zone), and transition temperatures inside the furnace but outside the hot zone (the temperature gradient zone). The three different temperature zones are determined by the temperature profile. The total elongation of the fiber tow specimen is the sum of the elongations produced in each of the aforementioned temperature zones. Strain and strain rate were calculated from displacement measurements using published methods [22], [49], [50]. A brief summary of the method is given below.

Consider a fiber tow test specimen with a constant cross-sectional area and a length of 2L. If the center of the specimen is defined as zero position, then creep occurs along the length of the fiber tow from –L to L. Creep is considered negligible outside of these bounds due to the low temperature. The total strain and strain rate can be found by Equations (8) and (9), respectively.

$$\varepsilon_m = \frac{\Delta l}{2L} = \int_0^t \dot{\varepsilon}_m dt \tag{8}$$

$$\dot{\varepsilon}_m = \frac{measured\ extension\ rate}{2L} = \frac{1}{2L}\int_{-L}^{L} \dot{\varepsilon} dl \tag{9}$$

Note that both the calculated strain and strain rate account for variations in strain along the fiber tow due to the temperature variations along the test specimen. The hottest region will produce a larger strain than the region with the lowest temperature. The desired test temperature is in the center of the furnace and is denoted with a subscript *0*. The strain at the center of the furnace is calculated as the time integral of the strain rate at the center of the furnace. The strain can also be described by the overall change in length, Δl, divided by a hypothetical length, $(2L)_{eff}$. The effective length can be described by the length obtained under a hypothetical step-function temperature profile where all the strain is accumulated under the peak temperature and zero strain is obtained under the lower temperature. At the desired maximum temperature, at the center of the furnace, the strain can be calculated as:

$$\varepsilon_o = \int_0^t \dot{\varepsilon}_o dt = \frac{\Delta l}{(2L)_{eff}} \tag{10}$$

Similarly, the strain rate at the maximum temperature can be expressed in terms of the effective gauge length as:

$$\dot{\varepsilon}_o = \frac{measured\ extension\ rate}{(2L)_{eff}} = \frac{1}{(2L)_{eff}}\int_{-L}^{L} \dot{\varepsilon} dl \tag{11}$$

The ratio of Equation (8) and (11) can then be written as:

$$\frac{\dot{\varepsilon}_m}{\dot{\varepsilon}_0} = \frac{\Delta l}{(2L)_{eff}} \tag{12}$$

Dead weight creep testing holds engineering stress constant. Temperature is a function of the location along the fiber tow. Steady-state creep can be described using the general power-law creep equation as:

$$\dot{\varepsilon} = A\sigma^n \exp\left(\frac{-Q}{RT(l)}\right) \tag{13}$$

Using Equations (9), (12), and (13), the ratio of the as measured strain rate to the actual strain rate can be written as solely a function of temperature:

$$\frac{\dot{\varepsilon}_m}{\dot{\varepsilon}_0} = \frac{1}{2L}\int_{-L}^{L} \exp\left\{\frac{-Q}{R}\left(\frac{1}{T(l)} - \frac{1}{T_0}\right)\right\} dl \tag{14}$$

Replacing the integral with a summation along the length of the fiber tow, $L = hk$, where h is an increment of length and k is an integer. The ratio of measured strain to actual strain can be written:

$$\frac{\dot{\varepsilon}_m}{\dot{\varepsilon}_0} = \frac{1}{2k}\sum_{i=-k}^{k} \exp\left\{\frac{-Q}{R}\left(\frac{1}{T(l)} - \frac{1}{T_0}\right)\right\} \tag{15}$$

The effective length can now be written as:

$$(2L)_{eff} = 2L\left(\frac{\dot{\varepsilon}_m}{\dot{\varepsilon}_0}\right) \tag{16}$$

With a creep activation energy of 177 kJ/mol from literature [27] and the temperature profiles found in the method described in Section 4.2, the effective length of the fiber tow specimen was found at 1000°C in air and in steam. These effective length values are reported in Table 7. Using the effective length of the fiber tow specimen, strain and strain rate can be calculated based on the elongation data collected from the LVDT.

Table 7 - Effective gauge lengths of Hi-Nicalon™ S fibers at 1000°C

	Air	Saturated Steam
Effective Length (mm)	71.92	73.58

III. Results and Discussion

3.1 Monotonic Tension Tests of Hi-Nicalon™ S Fiber Tows at 23°C

Hi-Nicalon™ S fiber tows were subjected to tension tests to failure at room temperature (23°C) in air. The objective of these tests was to verify the tensile strength and modulus of the fiber tow at 23°C. The fiber tow specimens used in tension tests were fabricated as described in Section 3.3 above but without the tertiary tab. An MTS Landmark™ 370 system with a test load capacity of up to 500N (110 lbs) was used to apply the load. Tension tests were performed in load control. An MTS FlexTest 40 digital controller was employed for the input signal generation and data acquisition. A detailed description of the MTS Landmark™ 370 system and the controller tuning procedures is given by Armani [8].

The results of the 3 monotonic tension tests are summarized in Table 8. The average tensile strength was 1.96 GPa and the average elastic modulus was 374 GPa. These values agree well with those reported in literature [48, 14].

Table 8 – Results of the monotonic tension tests of Hi-Nicalon™ S fiber tows in air at 23°C

Tensile Test Results		
Test ID	**Young's Modulus (GPa)**	**Tensile Strength (GPa)**
1	372	1.86
2	370	1.97
3	380	2.04
Average	374	1.96

Tensile stress-strain behavior of the fiber tow is typified in Figure 20. Note, the increase in slope of the curve near zero strain is caused by the fibers within the tow straightening out and aligning. Modulus of elasticity was calculated using the linear portion of the stress-strain curve.

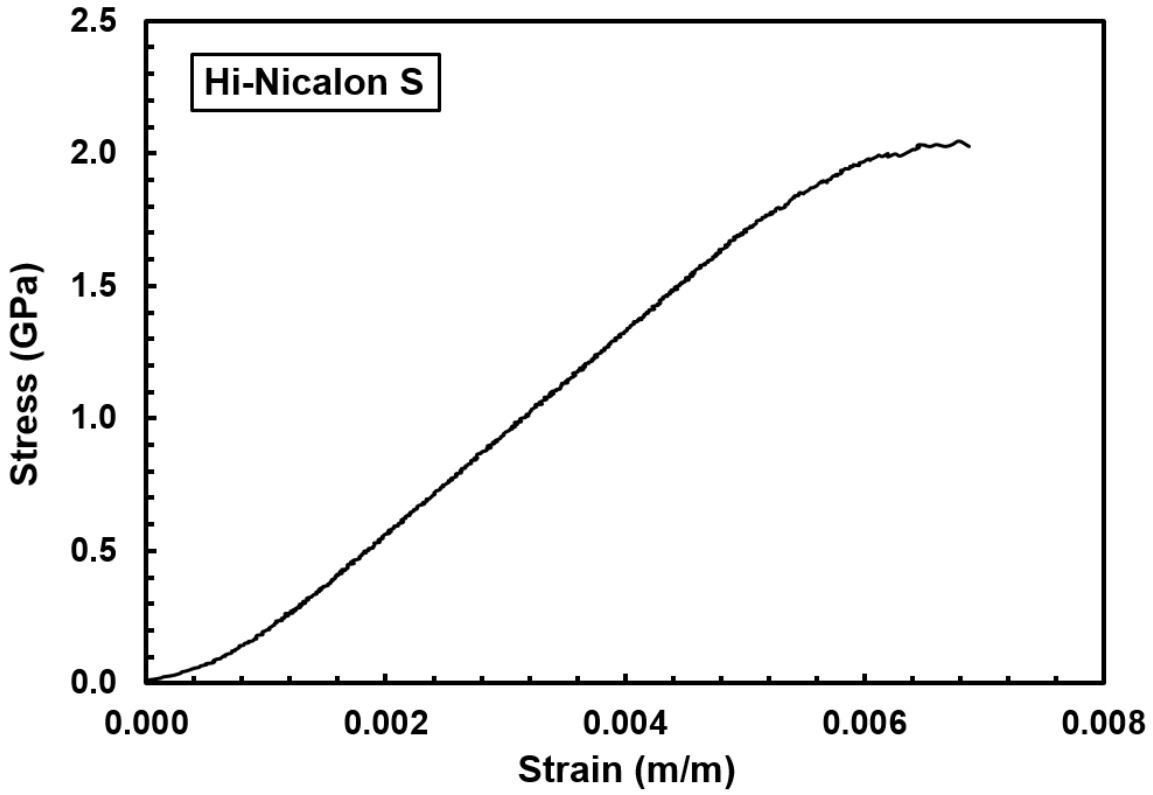


Figure 20 – Representative stress versus strain curve for Hi-Nicalon™ S fiber tows in laboratory air at 23°C

3.2 Creep of Hi-Nicalon™ S Fiber Tows at 1000°C

Tensile creep tests of Hi-Nicalon™ S fiber tows were performed at 1000°C in laboratory air and in silicic acid-saturated steam. Creep run-out was defined as 100 h at creep stress.

Results of the creep tests are summarized in Table 9, where creep strain, steady-state creep rate, and rupture time are shown for each creep stress level and test environment.

Table 9 - Summary of tensile creep test results for Hi-Nicalon™ S fiber tows at 1000°C in laboratory air and in silicic acid-saturated steam.

Specimen ID	Test Environment	Creep Stress (MPa)	Creep Lifetime (h)	Steady-State Creep Rate (s^{-1})	Creep Strain (%)
A1	Air	3.5	100†	7.98E-11	0.00669
A7	Air	300	100†	9.65E-10	0.08981
A11	Air	500	100†	4.96E-09	0.13432
A3	Air	700	62.5	5.16E-09	0.10324
A10	Air	800	31.0	4.35E-09	0.20633
S2	Saturated Steam	3.5	100†	4.50E-11	0.00815
S7	Saturated Steam	300	100†	3.00E-09	0.18095
S9	Saturated Steam	353	52.53	7.16E-09	0.20572
S5	Saturated Steam	400	30.83	6.84E-09	0.20206
S10	Saturated Steam	450	0.96	7.04E-08	0.13271
S6	Saturated Steam	500	0.02	‡	0.12402

† Creep run-out defined as 100 h at creep stress. Failure of specimen did not occur when the test was terminated.

‡ Insufficient data to determine creep and creep rate due to very short test duration.

Before drawing any conclusions from the above data, it is important to understand the assumptions made regarding the tests. First, the assumption was made that all 500 fibers in the fiber tow remained intact and we all loaded equally. With this assumption, the creep stress was

calculated using the same cross-sectional area for all fiber tow specimens. Additionally, the cross-sectional area of the fibers was assumed to remain unchanged despite the oxidation process occurring at elevated temperatures. It is recognized that the oxidation of the fibers, particularly in steam, reduces the effective cross-sectional area of the fiber tow, which would in turn increase the creep stress in a given test. Second, it was assumed steam was generated, saturated with silicic acid and delivered into the test chamber free of any contaminants. This assumption neglects the exposure of steam to the alumina tubing used to route steam from the steam generator through the preheaters and into the furnace. Lastly, it is difficult to clearly identify whether the fibers undergo a traditional creep deformation with time. It is also possible the deformation exhibited by the fiber tow is due to progressive failure of individual fibers or groups of fibers. It is possible that during the creep test single fibers (or small groups of fibers) fail and the applied load is transferred to the remaining fibers. As a result, the remaining fibers are subject to higher stress than the creep stress calculated for the entire tow. The continuing deformation is now a result of an increase in stress carried by the intact fibers and not due to creep.

The creep strain vs. time curves obtained at 1000°C in laboratory air are depicted in Figure 21. Creep run out was achieved at stress levels of 3.5 MPa, 300 MPa and 500 MPa. Primary and secondary creep regimes are observed in all tests performed in air. The transition from primary to secondary creep occurred early in each test. Tertiary creep was not observed.

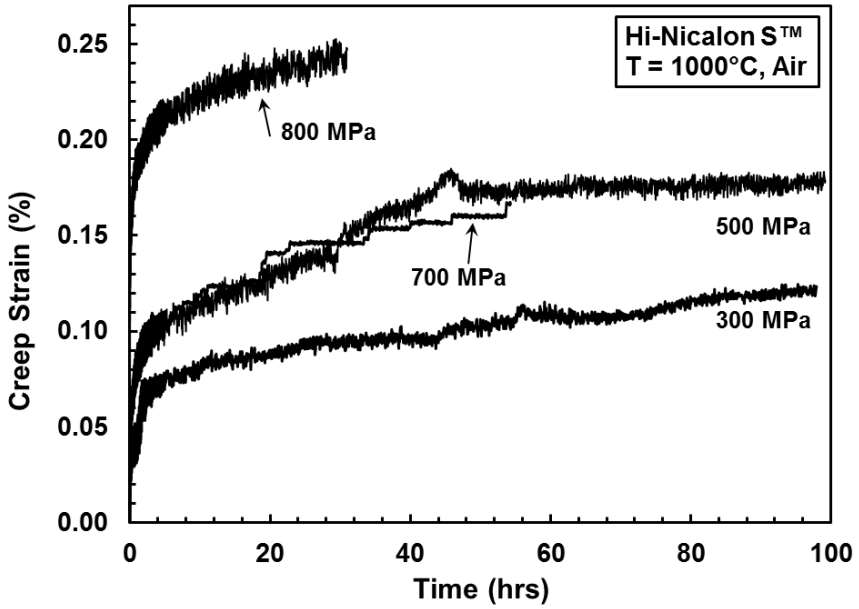


Figure 21 - Creep strain vs. time for Hi-Nicalon™ S fiber tows at 1000°C in laboratory air.

Representative creep strain vs. time curves obtained for Hi-Nicalon™ S fiber tows at 1000°C in silicic acid-saturated steam are shown in Figure 22 and in Figure 23. The presence of steam has a significant impact on the creep lifetime of the fibers. For this reason, much lower stress levels were used in the saturated-steam tests. Both primary and secondary creep regimes were observed in the saturated-steam tests, with the transition from primary to secondary creep occurring relatively early in the test. Secondary creep was not observed in the 500 MPa test performed in saturated steam due to the very short duration of the test. Creep run-out was achieved at 3.5 MPa and 300 MPa.

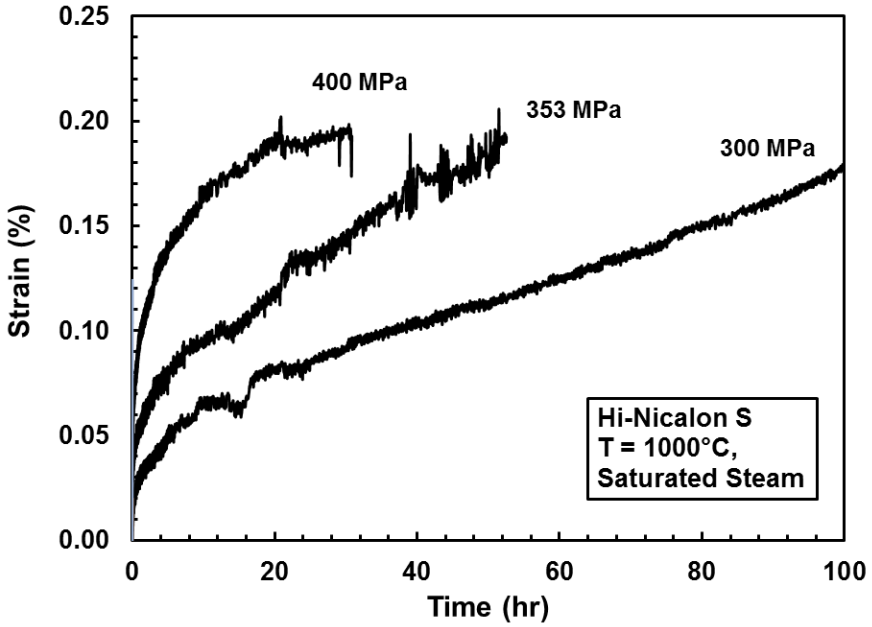


Figure 22 - Creep strain vs. time for Hi-Nicalon™ S fiber tows at 1000°C in saturated steam.

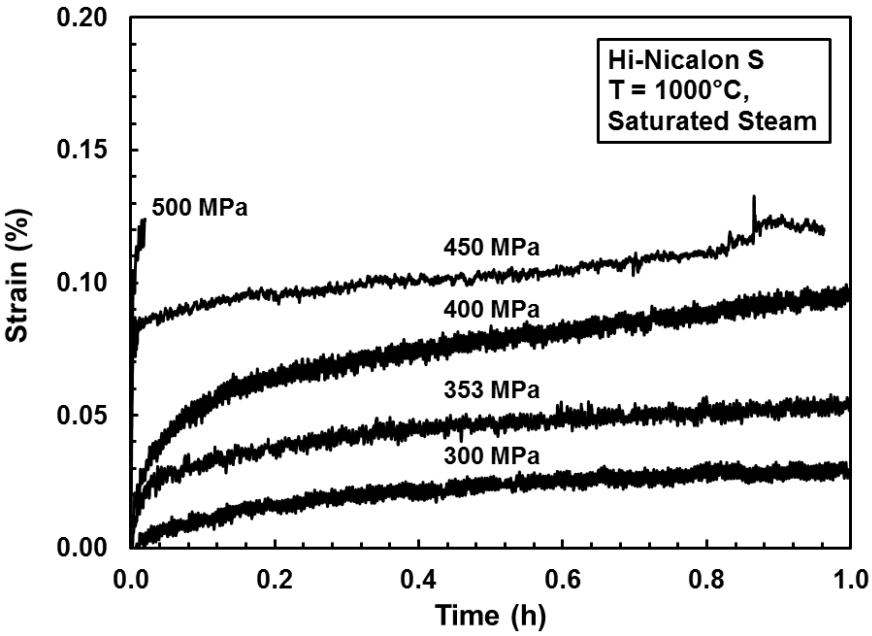


Figure 23 - Creep strain vs. time for Hi-Nicalon™ S fiber tows at 1000°C in saturated steam.

Secondary creep was observed in all tests in air and all but one test in saturated steam. The majority of each test consisted of steady-state creep. The steady state creep rates for each test that achieved secondary creep are displayed in Figure 24. The creep rates of Hi-Nicalon™ S fiber tows tests at 1000°C in air and in saturated steam were fitted with a Norton-Bailey power law equation of the form

$$\dot{\varepsilon} = A\sigma^n$$

Here $\dot{\varepsilon}$ is the minimum creep rate, A is a temperature-dependent coefficient which accounts for the activation energy, grain size and other variables in the full form of the power law, and σ is the applied stress. Utilizing a log-log plot of the creep rate as a function of applied stress, the stress exponent, n, was determined by linear regression as n = 2.0 in laboratory air, n = 1.8 in steam and n = 6.9 in saturated steam. With a creep exponent of $n \approx 6.9$, the results of the present work indicate that the dominant creep mechanism operating in silicic acid-saturated steam at 1000°C is cavity growth controlled creep. Piper [46] found a stress exponent as $n \approx 5.3$ at 700°C in saturated steam. Roberston [7] calculated a stress exponent of $n \approx 4.1$ at 800°C in saturated steam. Mitchell [47] found a stress exponent as $n \approx 5.7$ at 900°C in saturated steam. These results indicate that as temperature increases in saturated steam, the dominant creep mechanism transitions from being primarily dislocation climb controlled to cavity growth controlled creep. These creep mechanisms may not be valid if it is determined the fiber progressively failed within the fiber tow. However, a more accurate assessment can be obtained with additional testing to reduce the scatter in the data. Further creep testing is recommended at

higher temperatures. Sauder and Lamon [24] calculated a steady-state creep rate of $1.3x10^{-8}$ s^{-1} in tests of Hi-Nicalon™ S fiber tows at 1350°C under vacuum (~10^{-4} Pa), with a creep stress of 850 MPa.

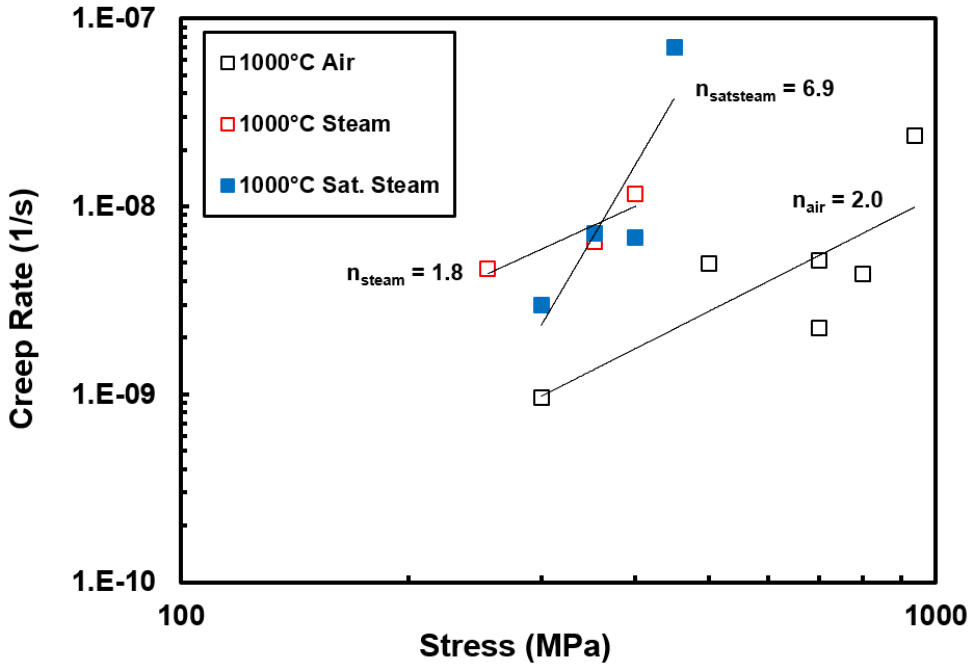


Figure 24 - Steady-state creep rate vs. applied stress for Hi-Nicalon™ S fiber tows at 1000°C in laboratory air, steam and silicic-acid saturated steam. Results from Shillig [44] in air and steam are included for comparison.

Rupture times as a function of creep stress is displayed in Figure 25, where results obtained at 1000°C in laboratory air and in steam by Shillig [44] are also included. Creep lifetime decreases as applied stress increases. The presence of saturated steam appears to reduce the creep lifetime of the fiber tow by one order of magnitude. A sharp transition from long creep lifetimes at lower creep stresses to short lifetimes at higher creep stresses is observed in all test

environments at 1000 °C. The same sharp transition was observed at 700°C by Piper [46], at 800°C by Robertson [7] and at 900°C by Mitchell [47].

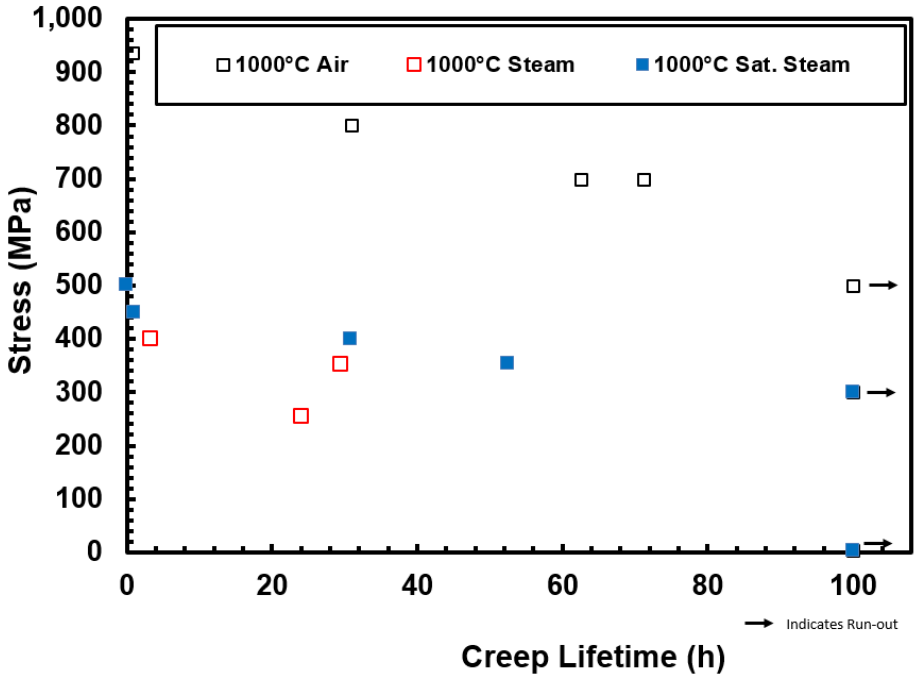


Figure 25 - Creep stress vs. time to rupture for Hi-Nicalon™ S fiber tows at 1000°C in air, steam and saturated steam. Data at 1000°C in air and steam from Shillig [44] is included. Arrow indicates specimen failure did not occur when test was terminated.

It is also informative to compare the results obtained in this effort to those of prior work (see Figures 26-29). At 800°C, data obtained in air and in steam by Shillig [44], as well as data obtained in air and in saturated steam by Robertson [7] were used for comparison. At 900°C, data in air and in steam obtained by Shillig [44] and data obtained in saturated steam by Mitchell [47] were used for comparison. Results of prior tests at 1000°C in air and in steam reported by Shillig [44] were also used for comparison. The results in Figures 25-28 demonstrate that

increasing temperatures had a detrimental impact on the level of stress the fibers could withstand in all three environments. Creep rates also increased as temperatures increased in all three environments. The presence of steam (Figure 26) and of saturated steam (Figure 28) had a detrimental impact on the level of creep stress that could be applied to a fiber tow when compared to air.

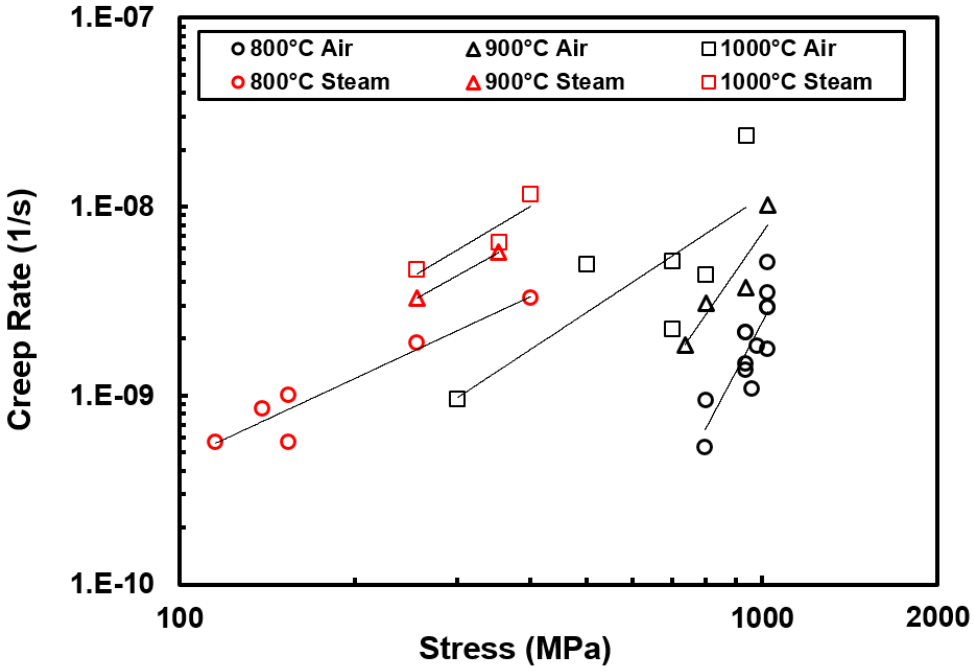


Figure 26 - Steady-state creep rate vs. applied stress for Hi-Nicalon™ S fiber tows at 800°C, 900°C and 1000°C in laboratory air and steam. Results from Shillig [44], Robertson [7], and Mitchell [47] are included for comparison.

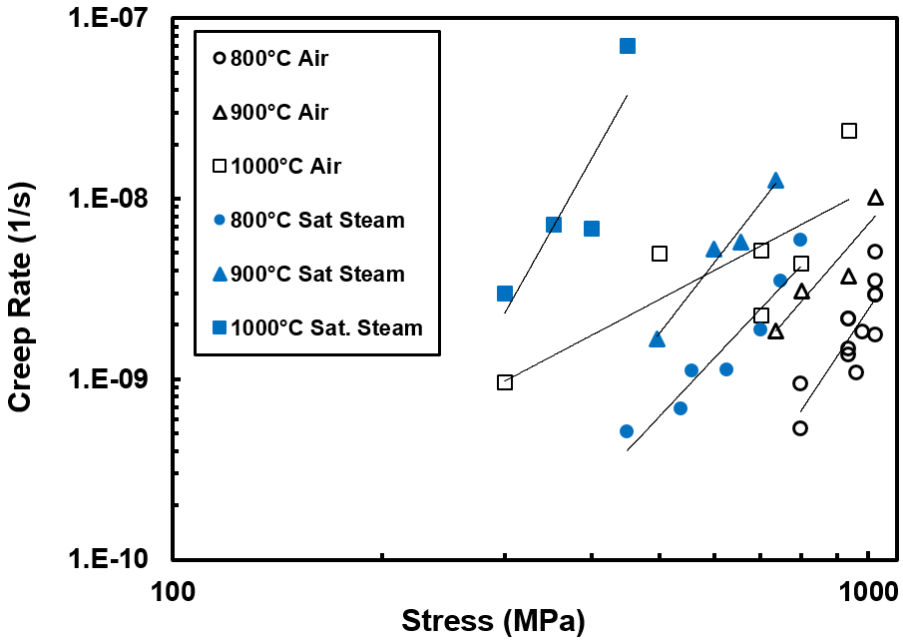


Figure 27 - Steady-state creep rate vs. applied stress for Hi-Nicalon™ S fiber tows at 800°C, 900°C and 1000°C in laboratory air and saturated steam. Results from Shillig [44], Robertson [7], and Mitchell [47] are included for comparison.

Notably, higher creep stresses can be applied in steam saturated with silicic acid than in unsaturated steam (see Figure 27). At all temperatures investigated, the highest steady-state creep rates were produced in unsaturated steam, followed by those produced in saturated steam (see Figures 27 and 28). The lowest steady-state creep rates were produced in air. In general, creep rates obtained in silicic acid-saturated steam are an order of magnitude higher than the creep rates obtained in dry air. However, creep rates produced in silicic acid-saturated steam are also an order of magnitude lower than the creep rates produced in unsaturated steam. A creep rate obtained at 450 MPa at 1000°C in saturated steam represents an exception. Additional tests

should be performed at 450 MPa at 1000°C in saturated steam to evaluate the corresponding steady-state creep rate with greater confidence.

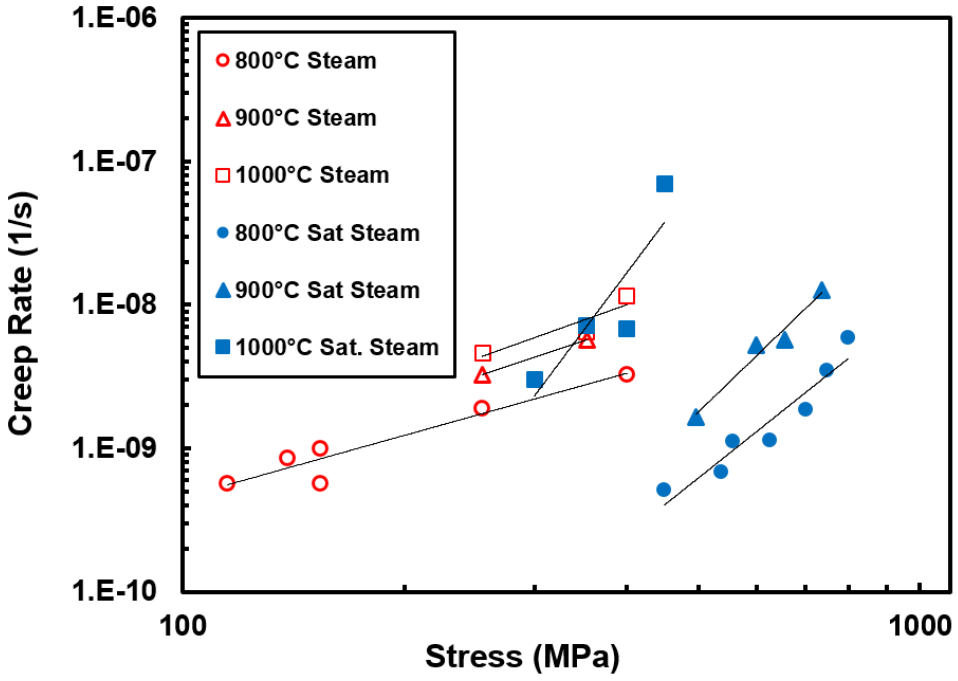


Figure 28 - Steady-state creep rate vs. applied stress for Hi-Nicalon™ S fiber tows at 800°C, 900°C and 1000°C in steam and saturated steam. Results from Shillig [44], Robertson [7], and Mitchell [47] are included for comparison.

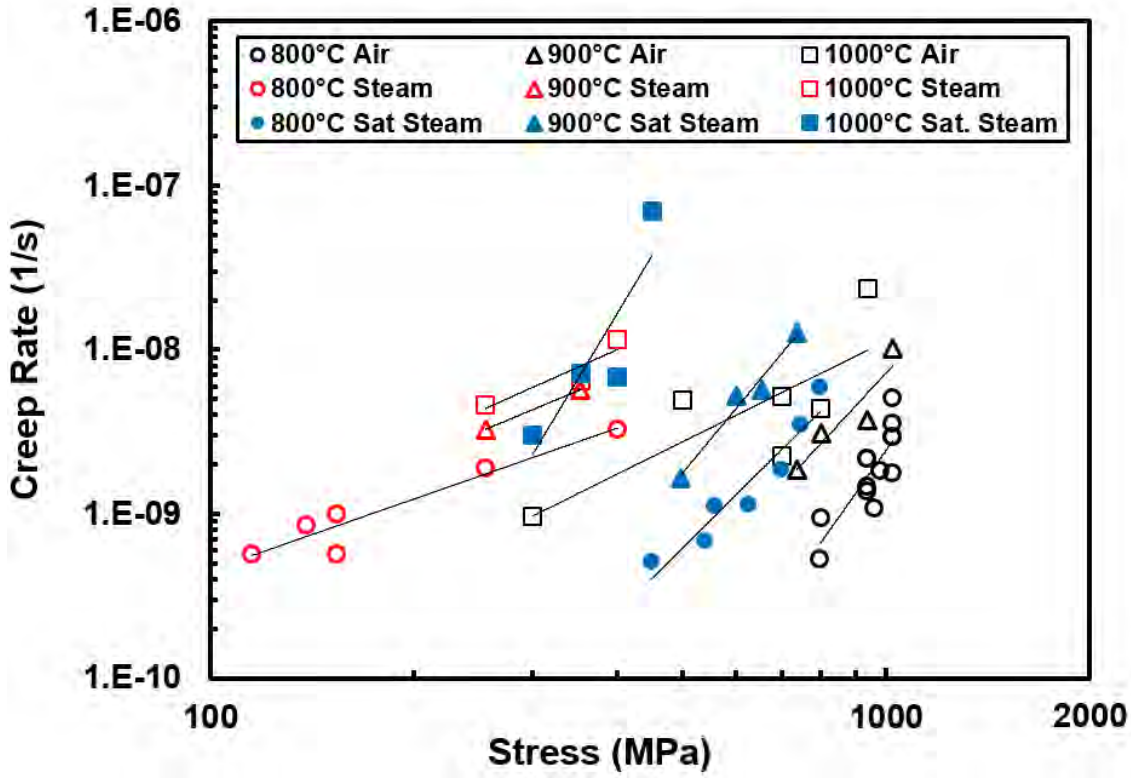


Figure 29 - Steady-state creep rate vs. applied stress for Hi-Nicalon™ S fiber tows at 800°C, 900°C and 1000°C in laboratory air, steam and saturated steam. Results from Shillig [44], Robertson [7], and Mitchell [47] are included for comparison.

The creep-rupture results obtained in laboratory air and in unsaturated steam are shown in Figure 30. The creep-rupture results obtained in laboratory air and in saturated steam are shown in Figure 31. Recall that creep run-out was defined as 100 h at creep stress. Results in Figures 30 and 31 reveal that for a given creep stress shorter creep lifetimes were produced at higher temperature. At all temperatures investigated, creep lifetimes were also reduced due to unsaturated steam and due to steam saturated with silicic acid.

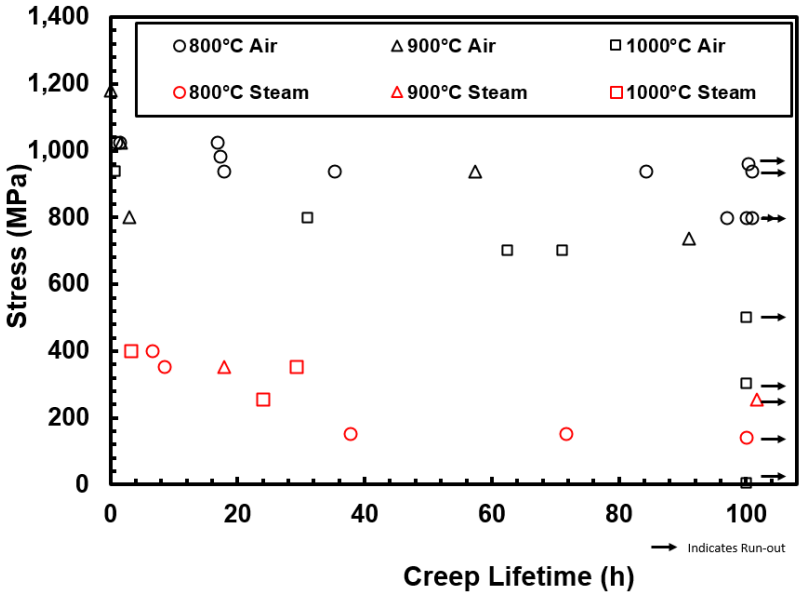


Figure 30 - Creep stress vs. time to rupture for Hi-Nicalon S fiber tows at 800°C, 900°C and 1000°C in laboratory air and steam. Results from Shillig [44], Robertson [7], and Mitchell [47] are included for comparison.

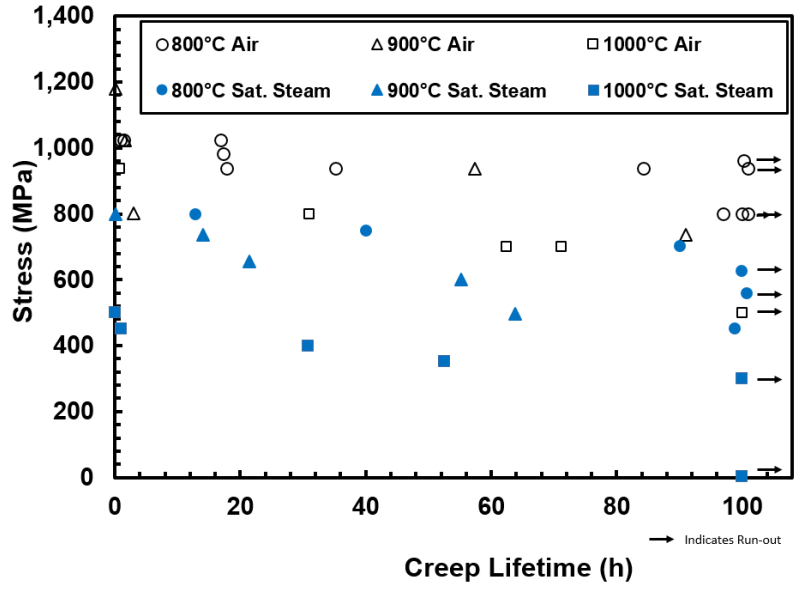


Figure 31 - Creep stress vs. time to rupture for Hi-Nicalon S fiber tows at 800°C, 900°C and 1000°C in laboratory air and saturated steam. Results from Shillig [44], Robertson [7], and Mitchell [47] are included for comparison.

The creep-rupture results obtained in laboratory air, unsaturated steam and in saturated steam are summarized in Figure 32, where the results reported previously by Shillig [44], Robertson [7], and Mitchell [47] are also included. The results in Figure 31 show an abrupt transition from a long lifetime a low stress to a short lifetime at a high stress for all temperatures and environments studied. At all temperatures investigated, the longest creep lifetimes were produced in air, followed by those produced in saturated steam. The shortest creep lifetimes were produced in unsaturated steam. Creep lifetimes obtained in silicic acid-saturated steam were an order of magnitude lower than creep lifetimes obtained in dry air. Yet creep lifetimes obtained in silicic acid-saturated steam were also at least an order of magnitude higher than those produced in unsaturated steam.

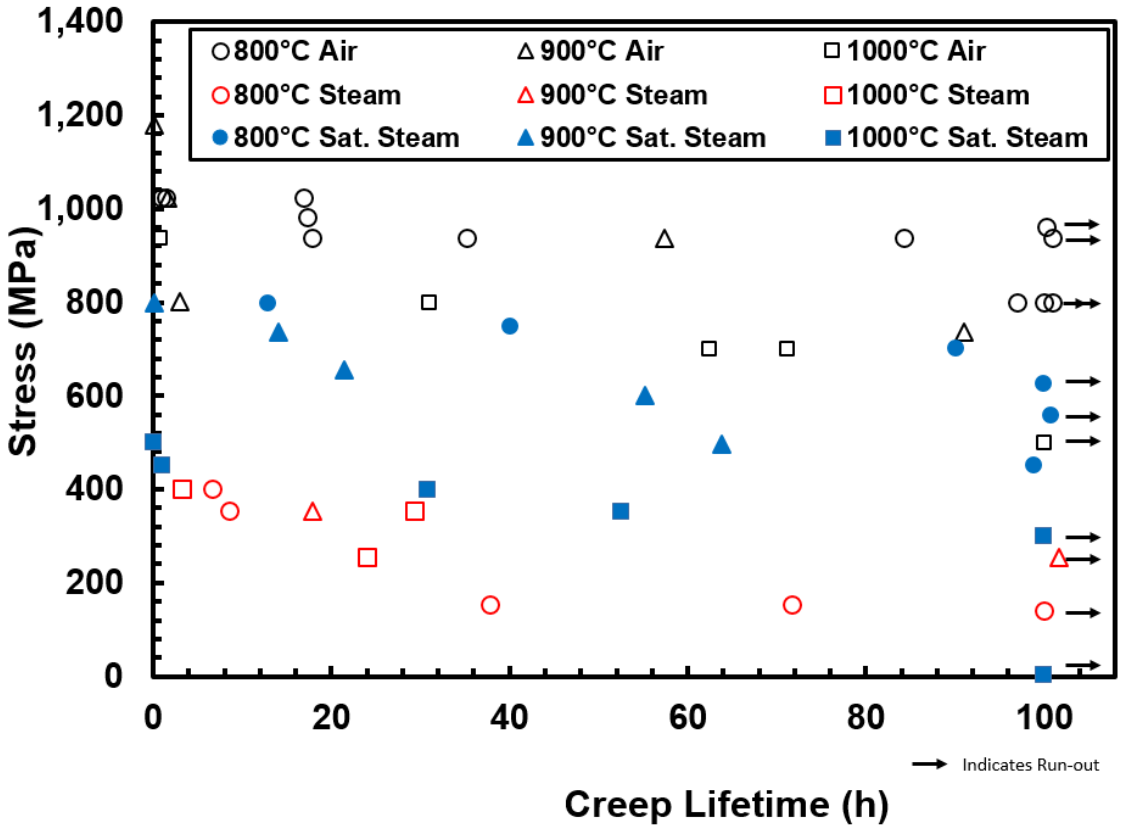


Figure 32- Creep stress vs. time to rupture for Hi-Nicalon S fiber tows at 800°C, 900°C and 1000°C in laboratory air, steam and saturated steam. Results from Shillig [44], Robertson [7], and Mitchell [47] are included for comparison.

A comparison of the results obtained in unsaturated steam with those produced in saturated indicates that unsaturated steam is a more damaging environment for the Hi-Nicalon™ S fibers. As mentioned in Section 2.3, silicic acid saturated steam is representative of the environment experienced by the SiC fiber tows inside a SiC/SiC composite. The experimental results revealing a less degrading effect of the silicic acid saturated steam provide a positive outlook for the future of advanced SiC/SiC CMCs.

3.3 Post-Test Microstructural Analysis of Hi-Nicalon™ S Fiber Tows

The post-test microstructure of the Hi-Nicalon™ S fiber tow specimens was examined using a Quanta 650 scanning electron microscope (SEM) in order to assess the damage and failure mechanisms. The SEM is shown in Figure 33. The fracture surfaces of four specimens tested in saturated steam and the fracture surfaces of the two specimens tested in laboratory air were examined. Additionally, 17 specimens were prepared for examination of the fiber tow cross-section with an SEM using standard methods (see Appendix A). A detailed description of the SEM specimen preparation is given elsewhere [7], [46], and [45]. The method for preparing fracture surfaces for the SEM examination is briefly outlined below.

Fiber tows were prepared for microstructural analysis of the fracture surface by mounting the fibers on an aluminum puck with a 45° surface. Double-sided carbon tape was first applied to the angled surface of the mounting puck. The fibers were then pressed onto the carbon tape such that the portion of the fibers to be analyzed protruded 1-5 mm above the angled surface. After placing the fibers on the puck, a second piece of double-sided carbon tape was applied on top to secure the fibers. After the fibers were securely fixed in place, the remainder of the fiber tow was cut at the bottom of the angled surface to separate it from the specimen to be analyzed. The fibers were then coated with 10 nm of Iridium using an EMS 150T ES coating machine shown in Figure 33. The coating provides electric conductivity between the fibers and the aluminum puck.



Figure 33 - Quanta 650 scanning electron microscope (SEM) in the Air Force Research Laboratory (AFRL) Materials and Manufacturing Directorate.



Figure 34 - EMS 150T ES coating machine in the Air Force Research Laboratory (AFRL) Materials and Manufacturing Directorate.

Three samples were examined for each fiber tow: a sample containing the fracture surface, a sample cut from the fiber tow above the fracture surface and a sample cut from the fiber tow below the fracture surface. Such selection of samples permits comparison of the oxidation modes along the length of the fiber tow. In the case of the fiber tows that achieved creep run-out of 100 h, a sample cut near the midpoint of the fiber tow was examined. A summary of the SEM specimens prepared in this work is given in Table 10. All SEM micrographs taken as part of this work are included in Appendix B and Appendix C as well as in this Chapter.

Table 10 - Hi-Nicalon™ S specimens prepared for analysis in the scanning electron microscope.

Test ID	Test Environment	Stress (MPa)	Creep Lifetime (h)	SEM Sample Location Within Fiber Tow
A1	Air	3.5	100†	Midpoint
A7	Air	300	100†	Midpoint
A11	Air	500	100†	Midpoint
A3	Air	700	62.5	Upper Section
				Fracture Surface
				Lower Section
A10	Air	800	31.0	Upper Section
				Fracture Surface
				Lower Section
S2	Steam	3.5	100†	Midpoint
S7	Steam	300	100†	Midpoint
S9	Steam	353	52.53	Upper Section
				Fracture Surface
				Lower Section
S5	Steam	400	30.83	Upper Section
				Fracture Surface
				Lower Section
S10	Steam	450	0.96	Upper Section
				Fracture Surface
				Lower Section
S6	Steam	500	0.02	Upper Section
				Fracture Surface
				Lower Section

† Creep run-out defined as 100 h at creep stress. Failure of specimen did not occur when the test was terminated.

The findings of Steffens [1] and Shillig [44] indicated a change in the oxidation process along the length of the fiber tow specimens. Both Steffens and Shillig noted the presence of

silica scale and pitting in the fiber tows. Robertson [7] reported that tests in saturated steam at 800°C yielded fiber tows with a more uniform appearance and chemical composition along the length of the fibers. Silica scale growth on the fiber surface was not discernible under an SEM in fiber tows tested in saturated steam at 700°C and 800°C. Silica scale growth was evident in fiber tows tested in saturated steam at 900°C. The scale is even more pronounced in fibers tested in saturated steam at 1000°C. An oxidation ring is readily seen in a representative fracture surface in Figure 35. Additionally, the smooth exterior surface of the fiber indicates that passive oxidation occurred in this test.

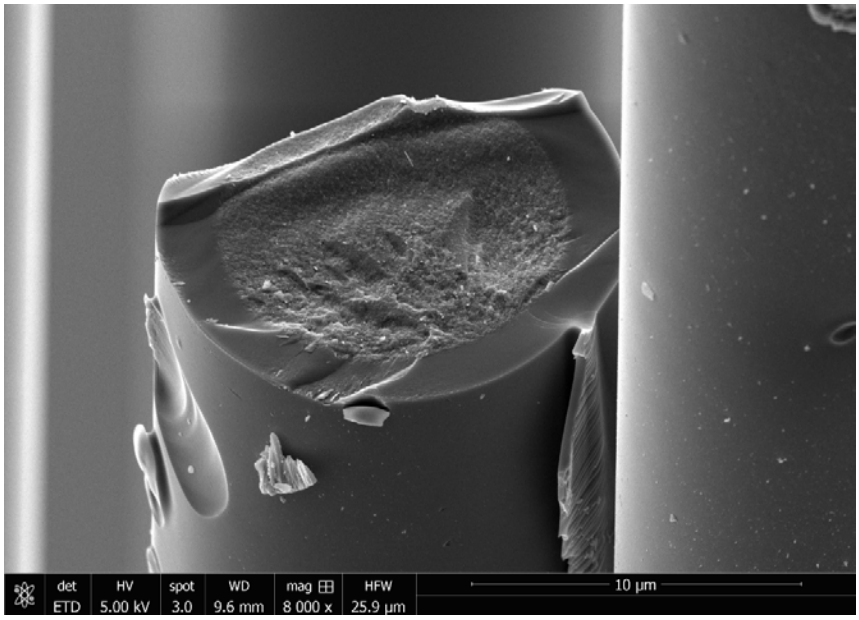


Figure 35 - Representative fiber from Hi-Nicalon™ S fiber tow specimen subjected to 353 MPa at 1000°C in silicic acid-saturated steam for 52.53 h. Oxide scale is visible.

It is noteworthy that silica scale was observed on the fracture surfaces of several fibers in this tow. The growth of silica scale on the fracture surface of a fiber indicates that this fiber failed

before the ultimate failure of the tow. It is likely that progressive failure of fibers in the tow took place during the test. Figure 36 shows growth of silica crystals on the fracture surface.

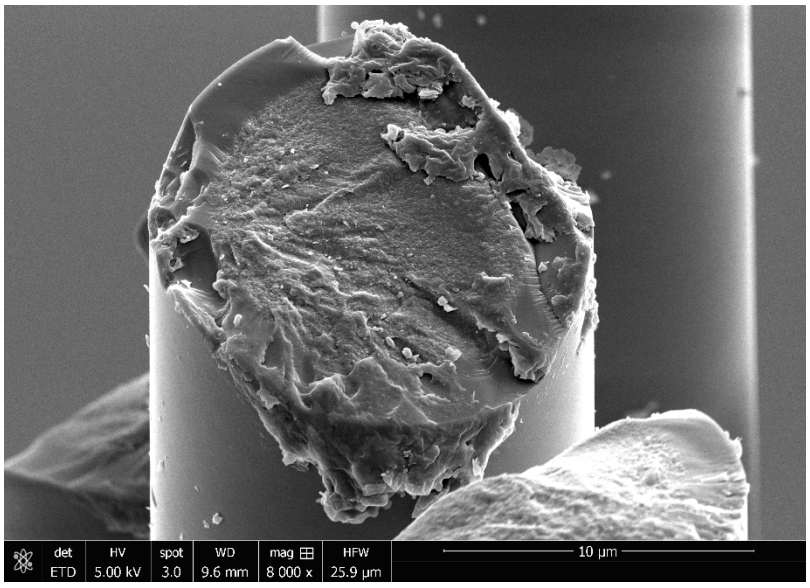


Figure 36 - SEM micrograph of the Hi-Nicalon™ S specimen "Steam 9" examining the fracture surface of a fiber subjected to creep in in silicic acid-saturated steam (σ_{cr} = 353 MPa, t_f = 52.53 h). Note oxide scale growth across the fracture surface.

All the fibers within a tow are not believed to be immaculate, it is recognized that the as-processed SiC fibers contain microstructural defects. Small defects or contaminants within a fiber are likely a result of deficiencies in the manufacturing process. These defects or contaminants provide an opportunity for a crack to initiate. Such defects leading to crack initiation and growth are seen in the fracture surfaces of some fibers. The fracture surface in Figure 37 show failure being initiated at a defect.

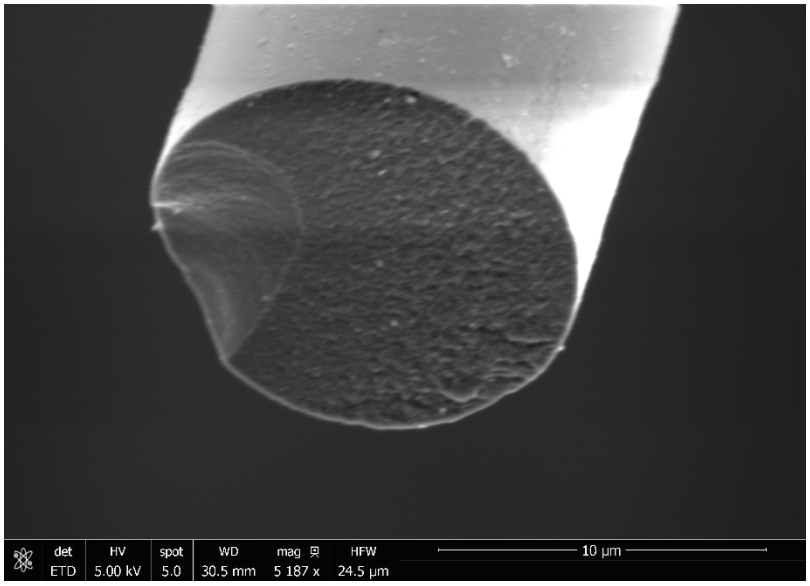


Figure 37 - SEM micrograph of the Hi-Nicalon™ S specimen "Air 10" examining the fracture surface of a fiber subjected to creep in air (σ_{cr} = 800 MPa, t_f = 31.0 h).

Figure 39 fracture propagating through the three fibers, likely because the three fibers were bonded together. Due to the short lifetime of this particular fiber tow the silica scale is not as readily visible. The fiber tows tested in steam that produced longer creep lifetimes exhibit a thicker scale, which appears to protect the fiber and prolong its lifetime.

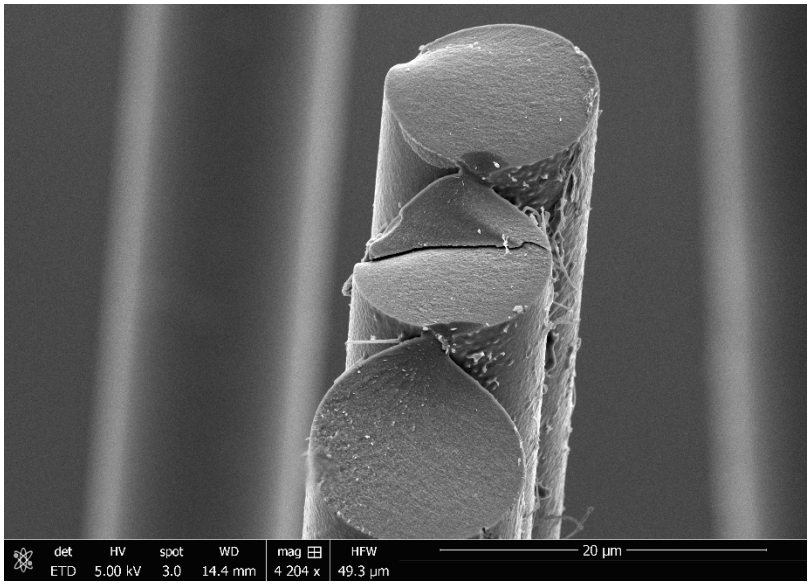


Figure 38 - SEM micrograph of the Hi-Nicalon™ S specimen "Steam 10" examining the fracture surface of a fiber subjected to creep in in silicic acid-saturated steam (σ_{cr} = 450 MPa, t_f = 0.96 h). Note signs of saturated steam exposure (silica deposition).

Some fiber tows examined in the SEM had dark regions on the surface of the fibers, see Figure 39. These dark regions appearing as straight lines directed along the length of the fibers are likely the result of contact between neighboring fibers. Piper [46] also observed this phenomenon and was able to collect Energy-dispersive X-ray spectroscopy (EDS) data from those regions. Piper found that the lighter areas in the SEM had a higher oxygen content, while the oxygen content was lower in the darker regions. He concluded that the contact between fibers limited the exposure of the fiber surfaces to oxidation, resulting in lower oxygen content along the lines of contact between the neighboring fibers.

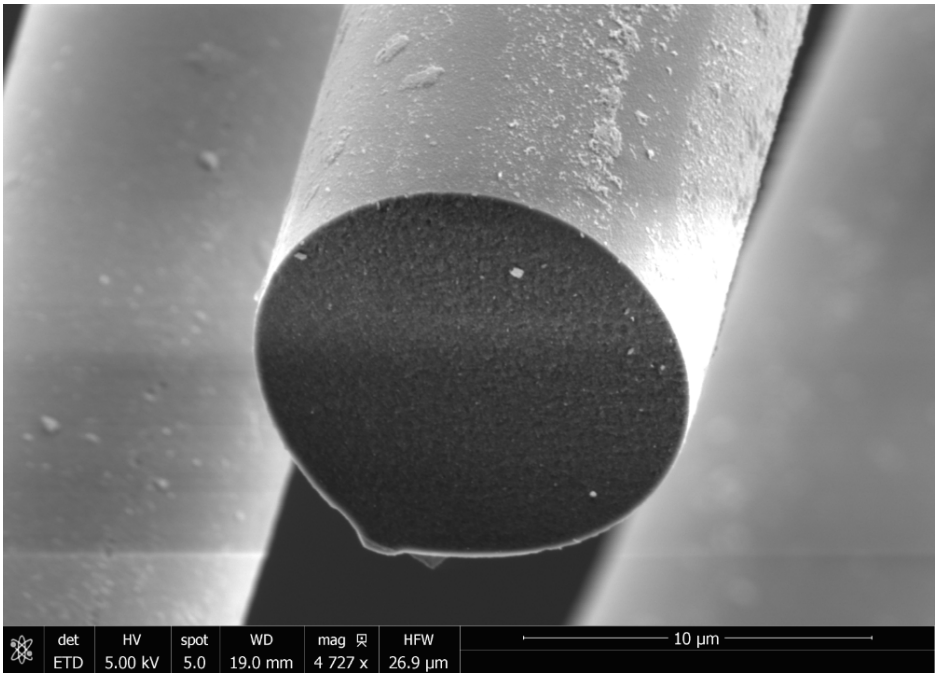


Figure 39 - Representative fiber from Hi-Nicalon™ S fiber tow specimen subjected to 800 MPa at 1000°C in laboratory air for 31.0 h. The dark line along the fiber tow is indicative of contact between fibers.

Several fiber tows tested in saturated steam, particularly those with longer creep lifetimes, developed both amorphous and crystalline scales on the fiber surfaces (see Figure 40). The amorphous scale is visible as a ring around the fiber while the growth of the crystallized scale is seen on the exterior surface of the fiber. In the case of SiC fibers, amorphous scale and crystallized scale have different coefficients of thermal expansion. The presence of both the amorphous scale and the crystallized scale on the fiber causes thermal stresses in the fiber. Of note is that several fibers that failed in saturated steam, typically failed underneath and/or around the crystallized scale.

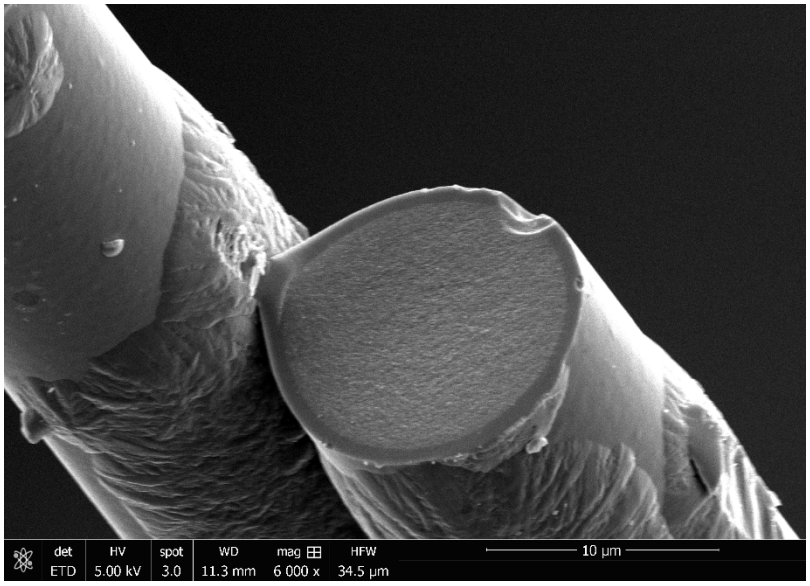


Figure 40 - SEM micrograph of the Hi-Nicalon™ S specimen "Steam 5" examining the fracture surface of a fiber subjected to creep in in silicic acid-saturated steam (σ_{cr} = 400 MPa, t_f = 30.83 h). Note defined silica amorphous and crystallized scale growth.

The thickness of the SiO_2 scale can be predicted using from the flat-plat Deal-Grove model, Equation (3). After long periods of time Equation (6) can be simplified yielding Equation (14).

$$x^2 = Bt \tag{14}$$

$$B = B_0 exp\left(\frac{-Q_b}{RT}\right) \tag{15}$$

Where B_0 is a constant and Q_b is the activation energy. In dry air, B_0 is 1.1x10^{-8} m^2/s and Q_b is 245 kJ/mol [51]. In a personal communication with Dr. Randall Hay, through experimentation of Hi-Nicalon™ S fiber tows in steam he has calculated the following: B_0 is

$6x10^{-14}$ m^2/s and Q_b is 80 kJ/mol, a publication is forthcoming. Predictions of the oxide scale thickness obtained using the aforementioned model for the duration of each test are summarized in Table 11.

Table 11 – Predictions of oxide scale thickness for test conditions obtained using Deal-Grove kinetics.

	Scale Thickness (μm)	
Time (h)	**Dry Air**	**Saturated Steam**
0.02	-	0.0
0.96	-	0.3
30.83	-	1.9
31.00	0.3	-
52.53	-	2.4
62.50	0.5	-
100.00	0.6	3.4

In addition to examining the fiber fracture surfaces, the mounted and polished cross-sections of the tested fibers were also examined with the SEM. The SEM micrographs of the representative polished cross section images can be found in Appendix C. A few of these SEM images are discussed here. In these images, a difference in composition is made visible by using the electron backscatter deflection detector on the SEM. Cross-sectional view of the fibers tested in an 800 MPa creep test in air (rupture time = 31 h) is shown in Figure 41.

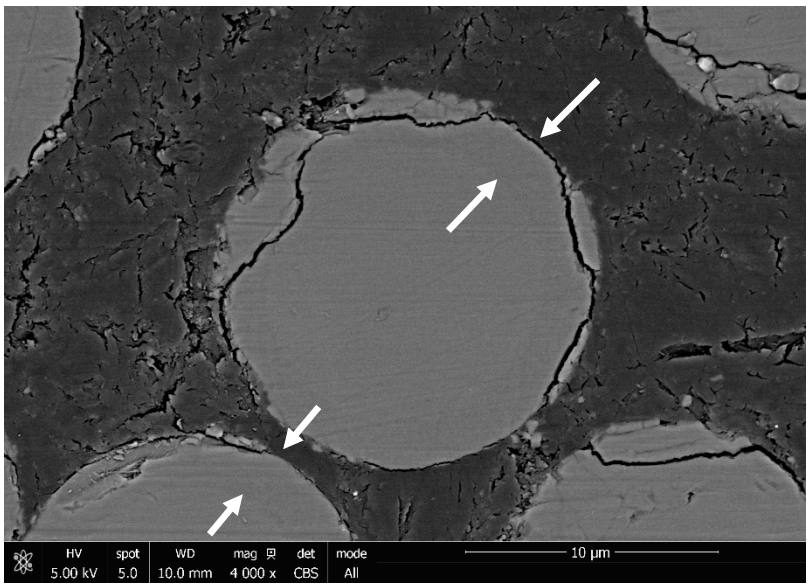


Figure 41 - SEM electron backscatter deflection micrograph of the Hi-Nicalon™ S specimen "Air 10" examining the cross section of the of a fiber tested in creep in air (σ_{cr} = 800 MPa, t_f = 31.0 h).

The white arrows in the SEM image point to the oxide scale. While the Deal-Grove model predicts an oxide scale thickness of 0.3 µm, the scale in the SEM micrographs appears to be 1-2 µm thick. The fracture surface in Figure 35 shows the scale thickness of approximately 2 µm, the model predicts a scale thickness of 2.4 µm. The model fits the observations made of the fiber tows subjected to saturated steam. There are several possible explanations for differences between the scale thickness values determined from the SEM micrographs and those predicted by the Deal-Grove model. Oxidation of SiC to SiO_2 is strongly influenced by the presence of contaminants. For example, aluminum particles that have contaminated the steam as it passed through the tubing in the preheater and/or through the alumina susceptor in the test chamber. If such contamination did indeed occur, it would cause a drastic decline in the oxidation rate.

Furthermore, the presence of a contaminant would also challenge one of the assumptions listed in Section 3.2. However, one should note that there are several oxidation kinetics models besides the Deal-Grove model. Based on the presence of amorphous and crystalline scale, activation energy and environment, some of these models overpredict scale growth, while the others underpredict the size of the scale [51].

We note that the oxide scale was not visible in the majority of the SEM images of the polished fiber cross-sections. There can be numerous explanation. The composition of the scale and that of the fiber are similar enough to push the limits of the detectors in the SEM, particularly when the scale is thin. Additionally, the oxide scale is softer than the SiC fiber. Therefore, the scale may have become damaged during the preparation of the polished sample. Notably, the fibers in many of the images in Appendix C did not maintain their edge. Lastly, the Iridium coating on the samples may have been too thick. In this case the SEM would simply image the topography of the sample surface.

IV. Conclusions and Recommendations

4.1 Conclusions

Creep tests of Hi-Nicalon™ S fiber tows were conducted at 1000°C in laboratory air and in silicic-acid saturated steam. Creep stresses ranged from 3.5 to 800 MPa in air and from 3.5 to 500 MPa in silicic-acid saturated steam. Creep run-out was defined as 100 hours at creep stress. Creep run-out was achieved at 500 MPa in air and at 300 MPa in silicic-acid saturated steam. The presence of silicic-acid saturated steam had a detrimental impact on the creep performance of the fibers. The creep lifetime decreased by one order of magnitude and the steady-state creep increased by one order of magnitude due to silicic-acid saturated steam.

Results of this effort were compared to those produced in prior work at AFIT at 800°C, 900°C and 1000°C in various environments. For all temperatures investigated, creep lifetimes obtained in silicic acid-saturated steam were an order of magnitude lower than creep lifetimes in dry air for a given creep stress. However, creep lifetimes in silicic acid-saturated steam were also at least an order of magnitude higher than creep lifetimes in unsaturated steam. Likewise, creep rates in silicic acid-saturated steam were an order of magnitude higher than creep rates in dry air. Yet, creep rates in silicic acid-saturated steam were also an order of magnitude lower than the creep rates in unsaturated steam. A comparison of the results obtained in unsaturated steam with those produced in silicic-acid saturated steam reveals that the unsaturated has a considerably stronger degrading effect on creep performance of the Hi-Nicalon™ S fibers at elevated temperatures than the silicic acid-saturated steam.

The analysis of the fiber tow microstructure revealed evidence of silica scale growth on fiber tows tested in tensile creep in silicic acid-saturated steam at 1000°C. A small number of fibers also showed evidence of scale formation on the fracture surface. Passive oxidation was found on the fibers tested in both air and saturated steam environments. No evidence was found of active oxidation.

The thickness of the SiO_2 scale was predicted using the Deal-Grove kinetics model. Both amorphous and crystallized scale were observed on the fracture surfaces of the fibers tested in saturated steam at 1000°C. Oxide scale was not visible on the fracture surfaces of the fibers tested in laboratory air. Polished cross-sections of the fibers were imaged with the SEM. The oxide scale was not immediately apparent in most of the polished cross-section samples.

4.2 Recommendations for Future Research

Creep behavior of Hi-Nicalon™ S fiber tows has been investigated at 700°C [46], 800°C [7], 900°C [47] and 1000°C in air and in silicic acid-saturated steam. Growth of silica scale became more pronounced at temperatures of 900°C and 1000°C. A study of the effects of silicic acid-saturated steam on creep of Hi-Nicalon™ S fibers at temperatures greater than 1000°C is recommended. Additional testing is needed to assess the growth of the silica scale and its impact on creep performance of Hi-Nicalon™ S fibers in the presence of silicic acid saturated steam.

Failure mechanisms operating in the fiber tows as well as the formation of an oxide scale on the surface of the fibers tested in creep at 1000°C in silicic acid-saturated steam were analyzed using SEM images. Further examination of the tested fibers using transmission

electron microscopy (TEM) is recommended. TEM permits higher magnification and a greater level of fidelity in determining the presence of an oxide layer as well as of other deposits on the surface of the fibers. Examination of the fiber cross-sections in a TEM is needed to discern the thickness of the oxide scale. Following TEM analysis of scale thickness, the results can be compared to predictions of oxidation kinetics model such as the flat-plate Deal-Grove model.

Future creep testing of Hi-Nicalon™ S fibers at elevated temperatures in air, unsaturated and saturated steam environments is also recommended to ascertain whether deformation and failure under constant load are the result of traditional creep of fibers or are due to progressive failures of individual filaments within the tow.

Appendix A. Polished Fiber Cross Section Preparation for SEM

1. TRIM FIBERS

Wearing latex gloves, cut fiber tow into two roughly 1 cm segments at point of interest. Prepare EPO-TEC® 353 ND two-part epoxy using a ratio of eight drops resin to one drop hardener. Mix the two together on a piece of foil with a toothpick. Mix slowly for about a minute. Place cut fibers in two-part epoxy.

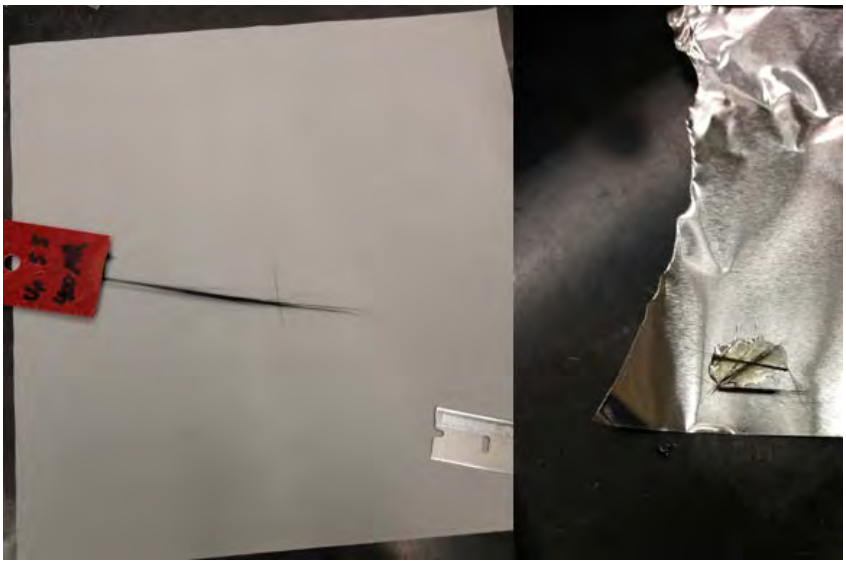


Figure 42 – Fibers cut and placed in two-part epoxy.

2. COAT FIBERS IN EPOXY

Massage epoxy into fibers by placing all the coated fibers on top of thumb. Using your index fingers transfer fibers between back and forth between your hands. The goal is to ensure all fibers are coated with epoxy.

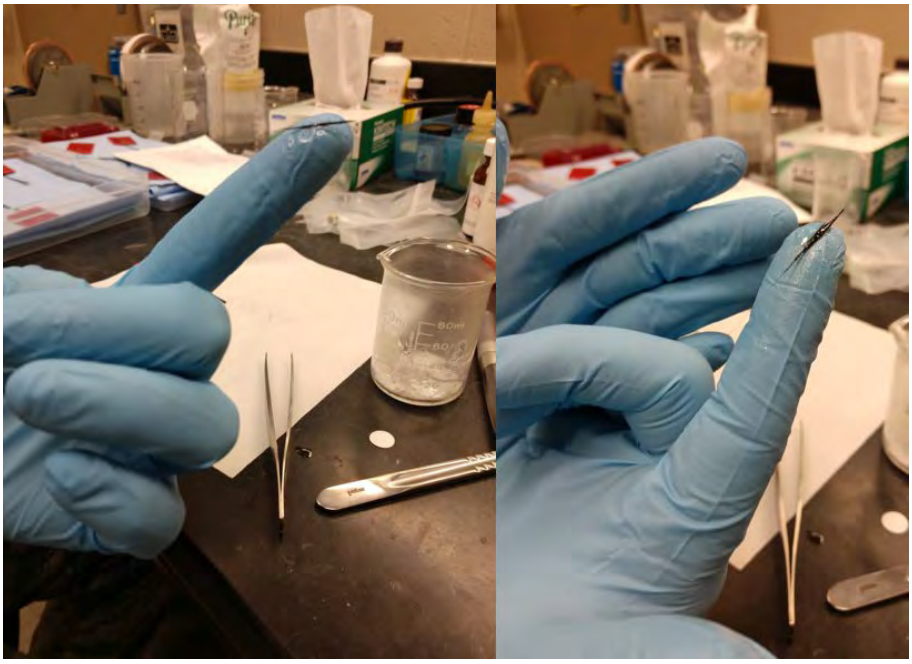


Figure 43 – Fiber segments were coated with two-part epoxy. Segments were transferred between finger tips to ensure full and even coating of epoxy.

3. PLACE FIBERS IN SHRINK TUBING

Using tweezers, push fibers through 105 PVC Insultab 1/16" tubing. Set the temperature of a hot plate between 180°C to 200°C. Place fibers and tubing on heated hot plate until tubing has shrunk around fibers. Keep the sample moving on the hot plate so it does not burn. You will see air bubbles in the epoxy being pushed out the sides of the tubing. Remove from hot plate when the epoxy turns amber in color and allow to cool.

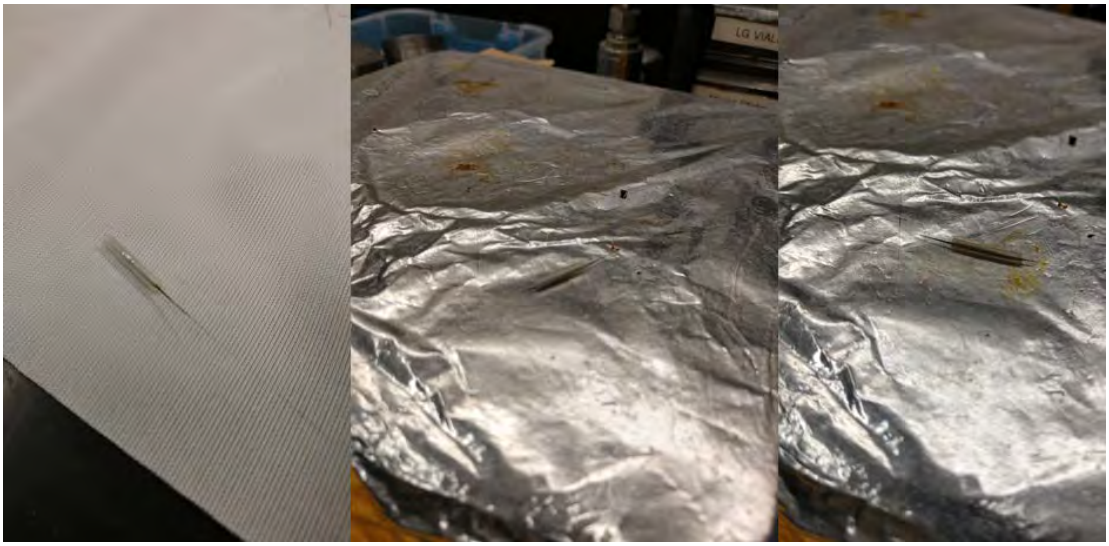


Figure 44 – Fiber segment placed in tubing and shrunk on a hotplate.

4. SLICE FIBERS

Once cool, slice fibers into approximately 1 mm segments.



Figure 45 – Fibers sliced into small pieces.

5. MOUNT FIBER SLICES TO TEFLON DISC

Place carbon tape on a Teflon disc. Write a label next to each sample using a marker. Stand fiber segments on end on carbon tape. Cover segments with epoxy. Note: Be sure epoxy gets in between and surrounds all segments of fibers.



Figure 46 – Mounting fibers on Teflon disc and coating with two-part epoxy.

6. CURE EPOXY

Cure in 80°C furnace for at least 90 minutes. Remove from furnace and allow to cool. Use a razor blade to pry samples off the Teflon disc.

7. SECURED FIBERS TO GLASS STUB

For this step you will need going to need a glass stub, a glass slide slightly bigger than the sample, crystal bond, and the cured sample. Set the temperature of a hot plate between 180°C to 200°C. Melt a small amount of crystal bond on the stub and put the slide on the stub. Melt more crystal bond

on the slide and put the sample on the slide. Remove from the hot plate and let cool. The type of crystal bond used was manufactured by Allied High Tech Products, part #71-10040.

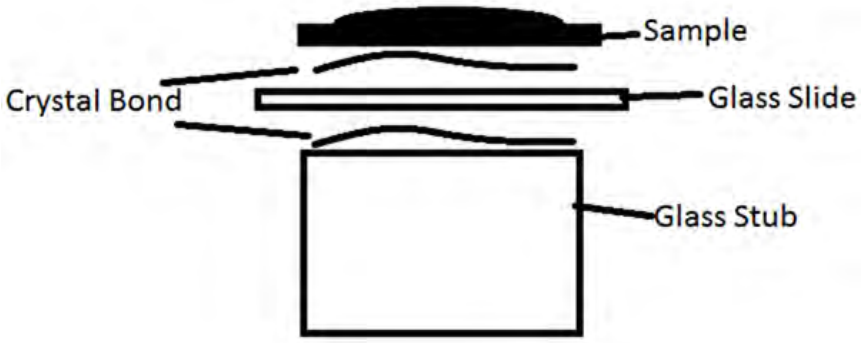


Figure 47 – Order for mounting sample to a glass stub using crystal bond.

8. GRIND SAMPLE TO LEVEL SURFACE

Secure sample in a tripod. Use feet to level the tripod. Using the 120 µm pad, begin grinding away material on the top of the sample. Grind the sample down until you have reached the desired surface for your sample. The goal is to grind away epoxy such that all the fibers are exposed and making sure the surface is as parallel as possible to the glass slide. Repeat with the 70 µm pad. Do not adjust the feet after this step.



Figure 48 – Tripod securing glass stub and sample for polishing.

9. POLISH SAMPLE

You are now ready to switch to the diamond embedded polishing pads. Use the films in the order of 30, 15, 6, 3 and then 1 μm. When polishing with each pad, ensure the surface is all the same plane. Do this by running the scratches in one direction and then shift the angle about 45 degrees. This will help get a better polish and protect your films from being damaged.

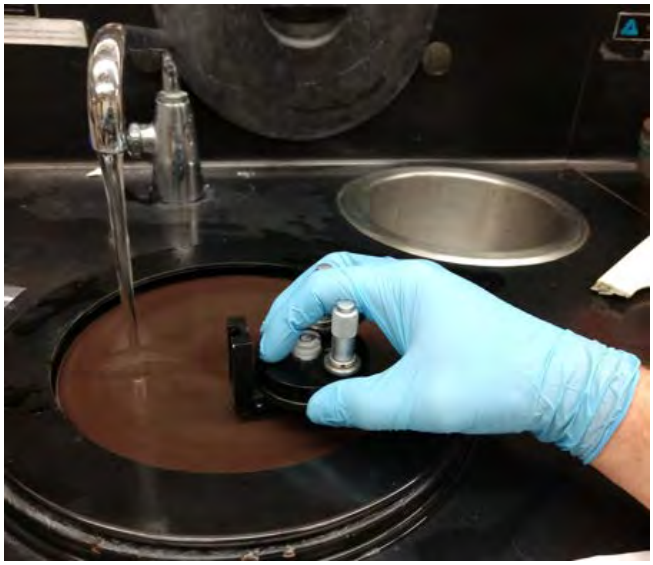


Figure 49 – Grinding sample to desired height using 120 µm pad.

10. MOUNT SAMPLE TO METAL STUB

Set the temperature of a hot plate between 180°C to 200°C. Place glass stub with polished sample on the hot plate. Once crystal bond has been softened remove the glass slide and sample from the glass stub by sliding it off. Once cool, place a piece of double-sided carbon tape on a flat metal stub. Place sample on metal stub.

11. COAT SAMPLE

The fibers were coated for the present research were coated with 10 nm of Iridium using an EMS 150T ES coating machine, see Figure 34.

Appendix B. Representative SEM Fracture Surface Images

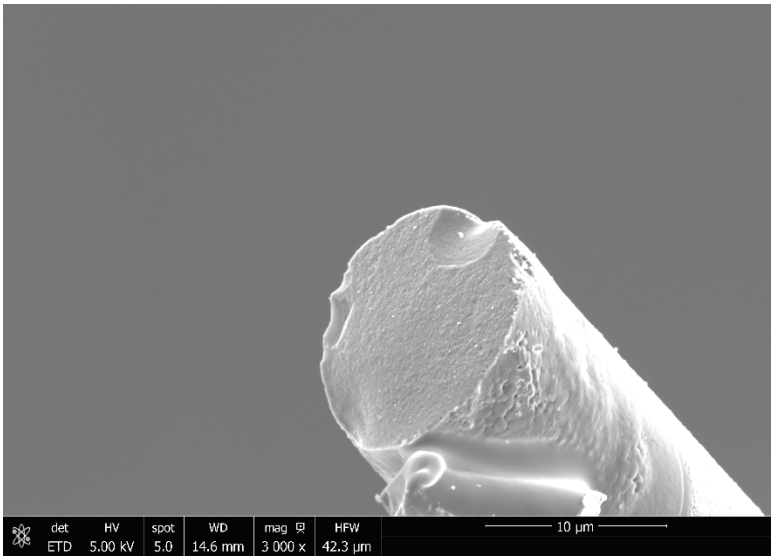


Figure 50- SEM micrograph of the Hi-Nicalon™ S specimen "Air 3" examining the fracture surface of a fiber (σ_{cr} = 700 MPa, t_f = 62.50 h).

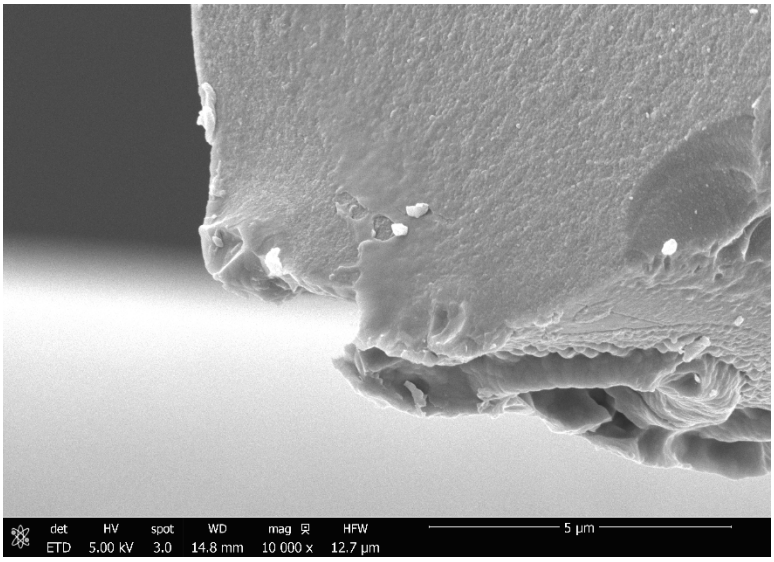


Figure 51 - SEM micrograph of the Hi-Nicalon™ S specimen "Air 3" examining features on the fracture surface of a fiber (σ_{cr} = 700 MPa, t_f = 62.50 h). Note pores in fiber were likely were crack initiated.

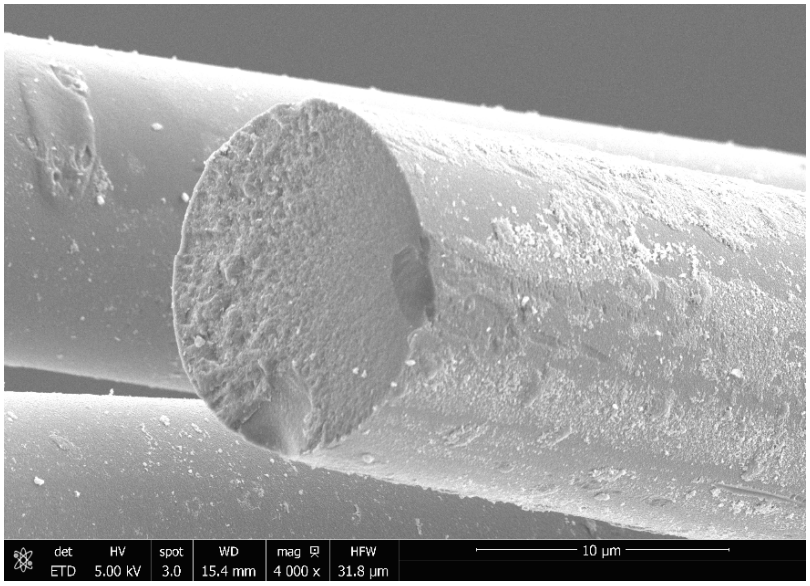


Figure 52 - SEM micrograph of the Hi-Nicalon™ S specimen "Air 3" examining the fracture surface of a fiber (σ_{cr} = 700 MPa, t_f = 62.50 h). Note longitudinal fiber-fiber contact.

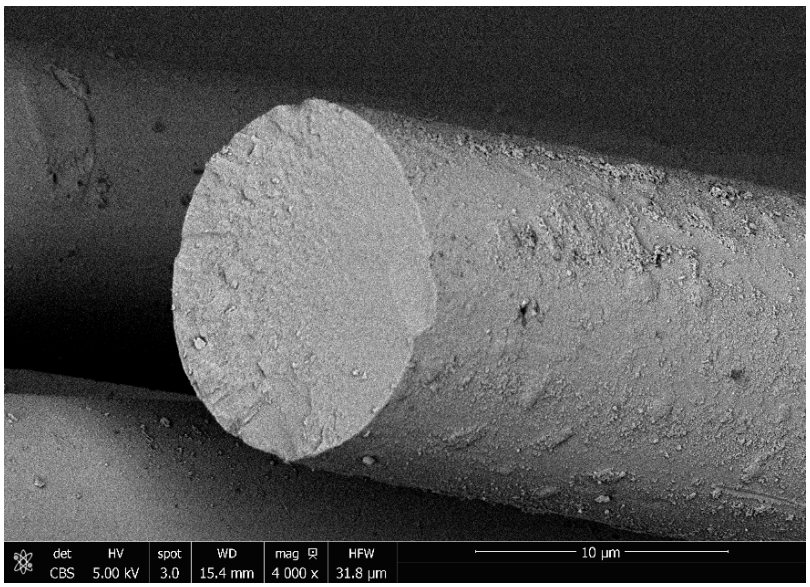


Figure 53 - SEM electron backscatter deflection micrograph of the Hi-Nicalon™ S specimen "Air 3" examining the fracture surface of a fiber (σ_{cr} = 700 MPa, t_f = 62.50 h).

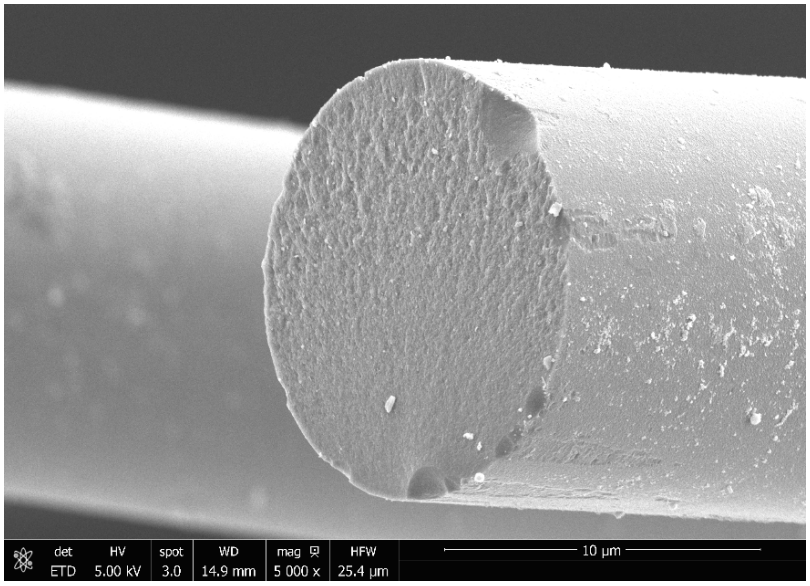


Figure 54 - SEM micrograph of the Hi-Nicalon™ S specimen "Air 3" examining the fracture surface of a fiber (σ_{cr} = 700 MPa, t_f = 62.50 h).

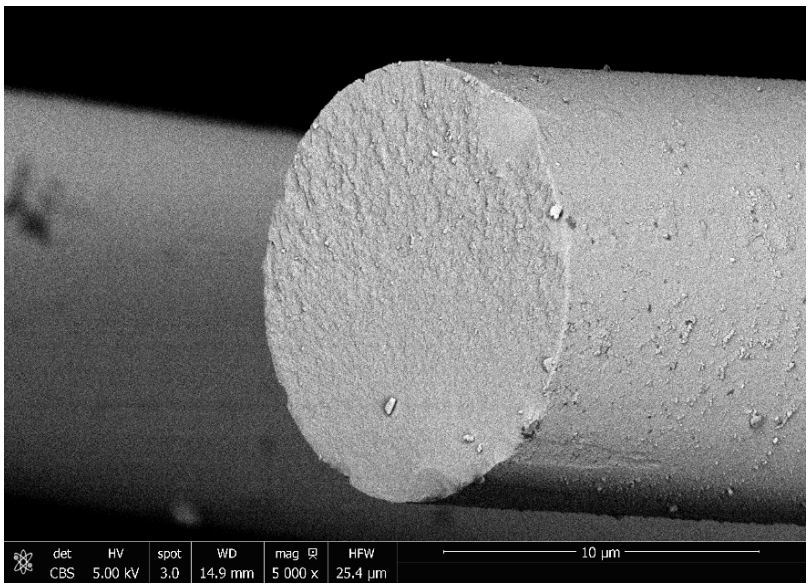


Figure 55 - SEM electron backscatter deflection micrograph of the Hi-Nicalon™ S specimen "Air 3" examining the fracture surface of a fiber (σ_{cr} = 700 MPa, t_f = 62.50 h).

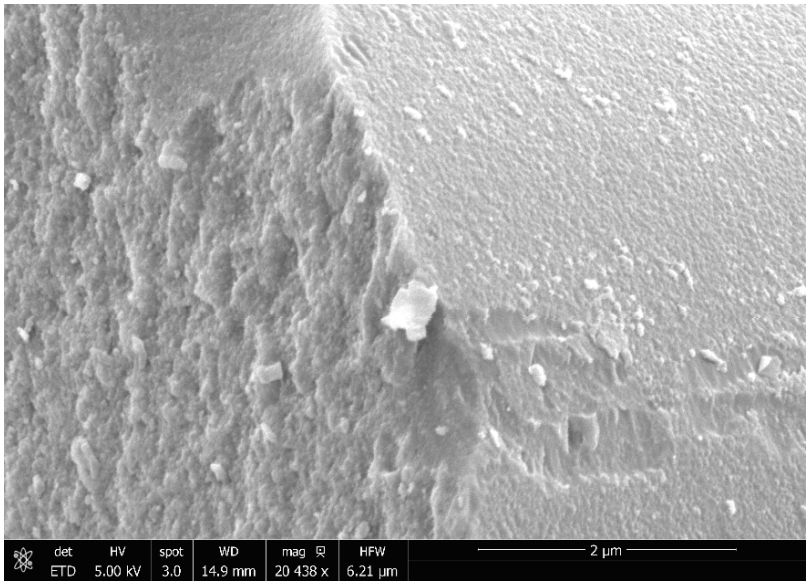


Figure 56 - SEM micrograph of the Hi-Nicalon™ S specimen "Air 3" examining features on the fracture surface of a fiber (σ_{cr} = 700 MPa, t_f = 62.50 h).

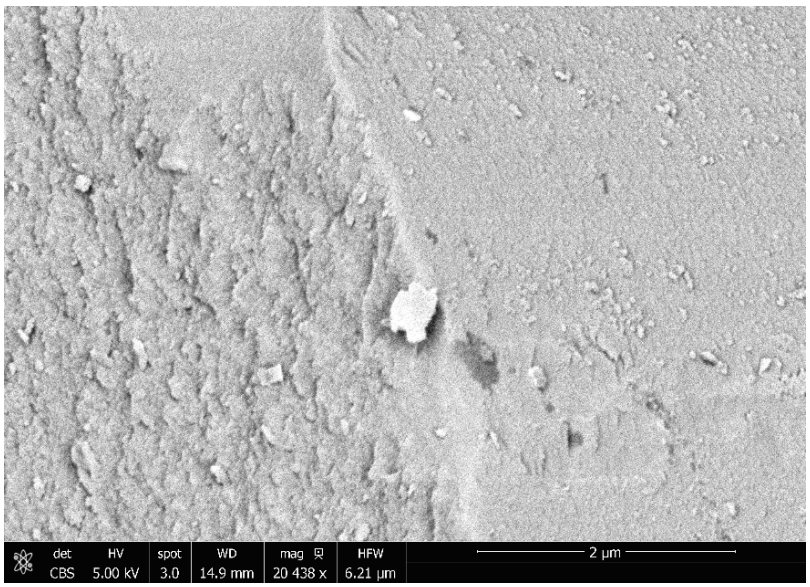


Figure 57 - SEM electron backscatter deflection micrograph of the Hi-Nicalon™ S specimen "Air 3" examining features on the fracture surface of a fiber (σ_{cr} = 700 MPa, t_f = 62.50 h).

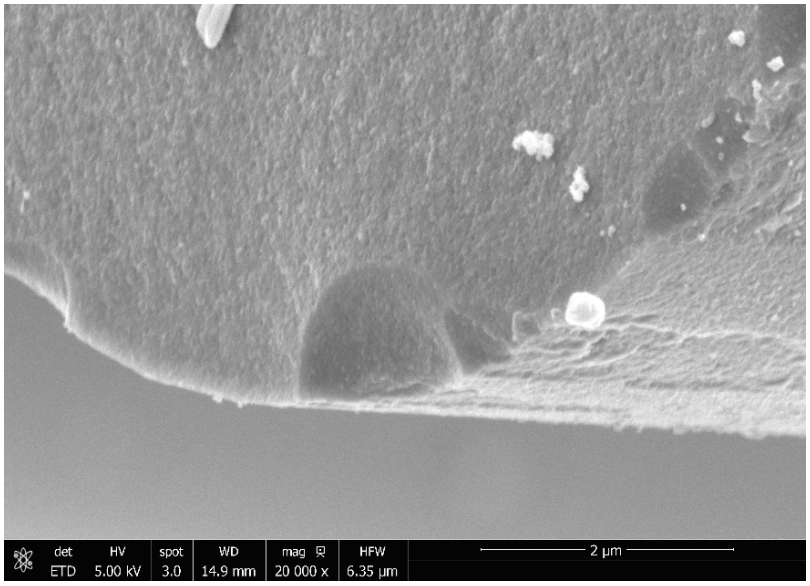


Figure 58 - SEM micrograph of the Hi-Nicalon™ S specimen "Air 3" examining features on the fracture surface of a fiber (σ_{cr} = 700 MPa, t_f = 62.50 h).

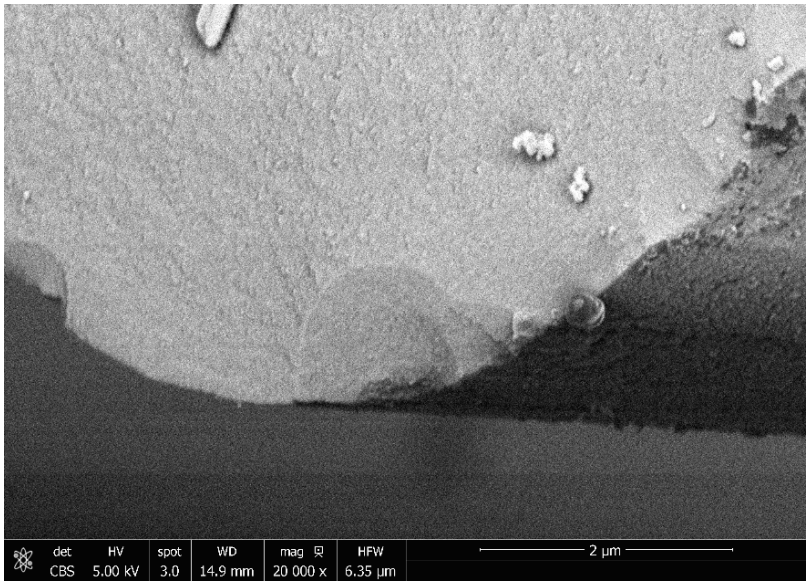


Figure 59 - SEM electron backscatter deflection micrograph of the Hi-Nicalon™ S specimen "Air 3" examining features on the fracture surface of a fiber (σ_{cr} = 700 MPa, t_f = 62.50 h).

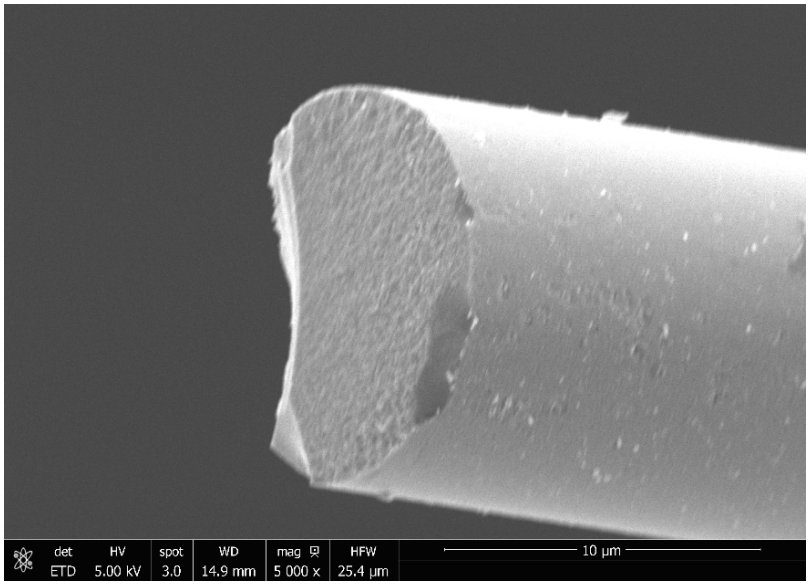


Figure 60 - SEM micrograph of the Hi-Nicalon™ S specimen "Air 3" examining the fracture surface of a fiber (σ_{cr} = 700 MPa, t_f = 62.50 h).

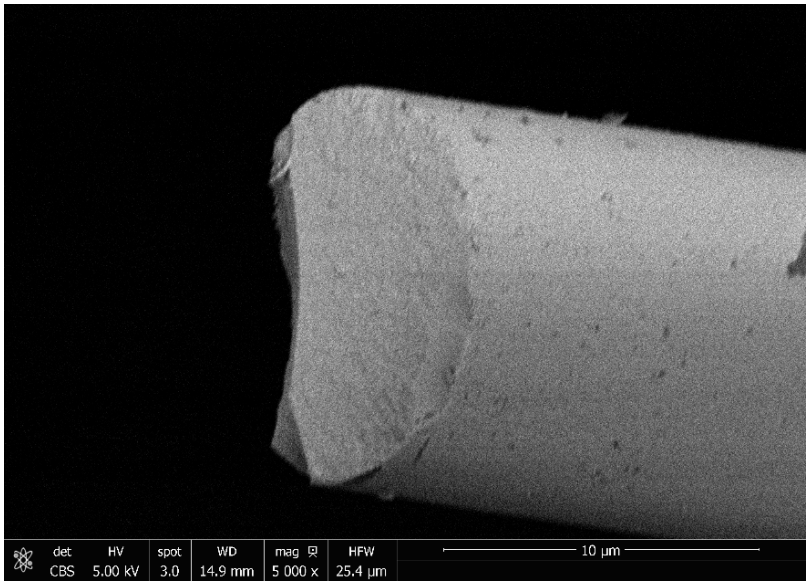


Figure 61 - SEM electron backscatter deflection micrograph of the Hi-Nicalon™ S specimen "Air 3" examining the fracture surface of a fiber (σ_{cr} = 700 MPa, t_f = 62.50 h).

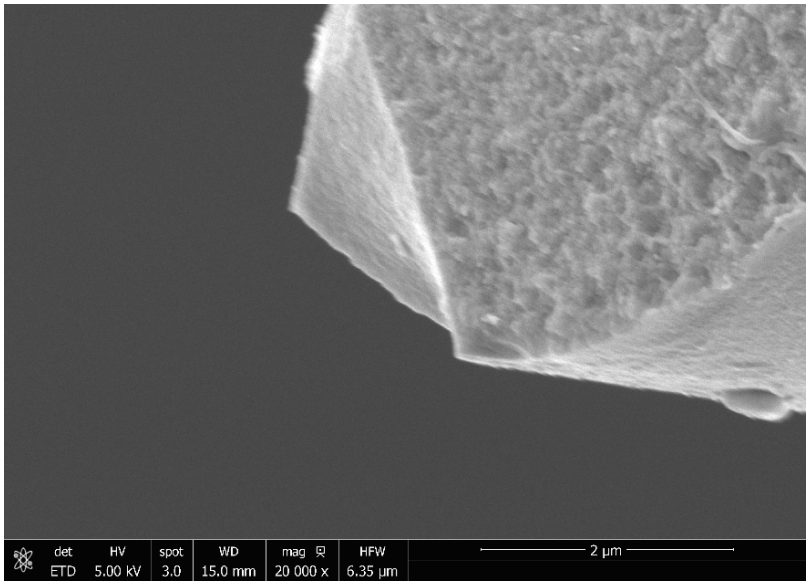


Figure 62 - SEM micrograph of the Hi-Nicalon™ S specimen "Air 3" examining features on the fracture surface of a fiber (σ_{cr} = 700 MPa, t_f = 62.50 h).

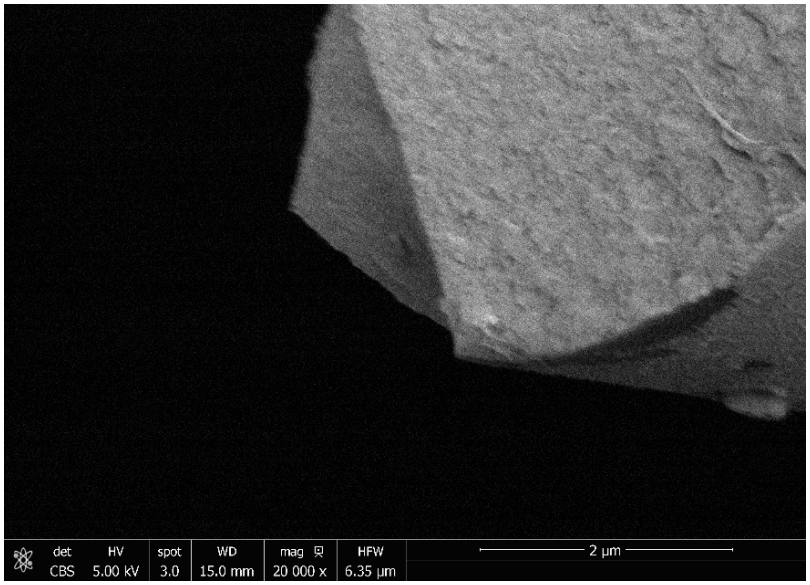


Figure 63 - SEM electron backscatter deflection micrograph of the Hi-Nicalon™ S specimen "Air 3" examining features on the fracture surface of a fiber (σ_{cr} = 700 MPa, t_f = 62.50 h).

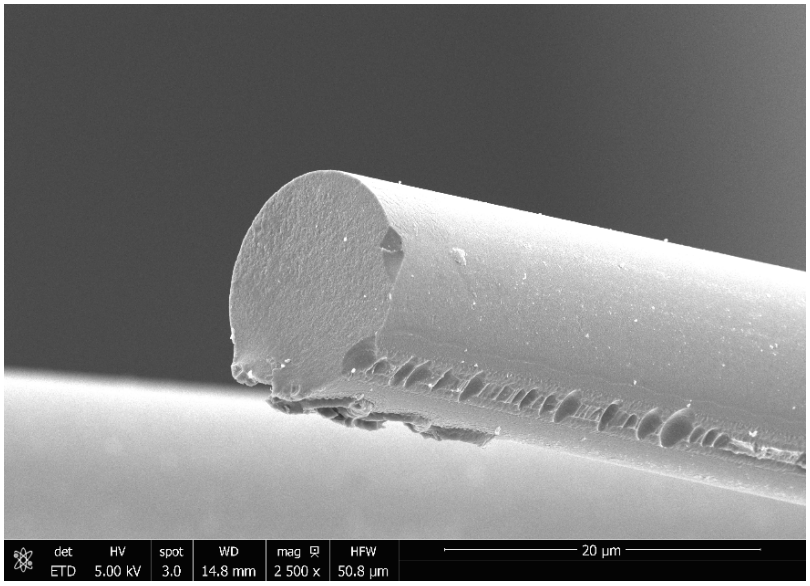


Figure 64 - SEM micrograph of the Hi-Nicalon™ S specimen "Air 3" examining the fracture surface of a fiber (σ_{cr} = 700 MPa, t_f = 62.50 h). Note signs of longitudinal fiber-fiber contact and pores in the fiber.

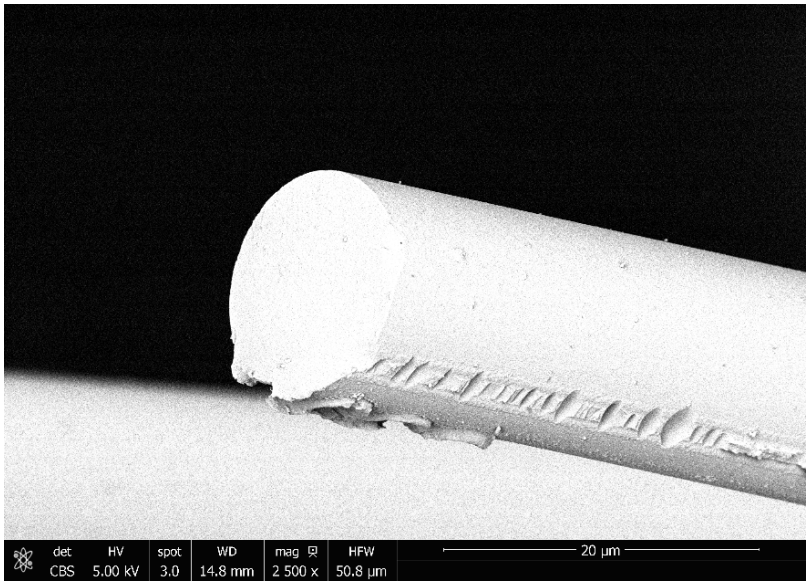


Figure 65 - SEM electron backscatter deflection micrograph of the Hi-Nicalon™ S specimen "Air 3" examining the fracture surface of a fiber (σ_{cr} = 700 MPa, t_f = 62.50 h). Note signs of longitudinal fiber-fiber contact.

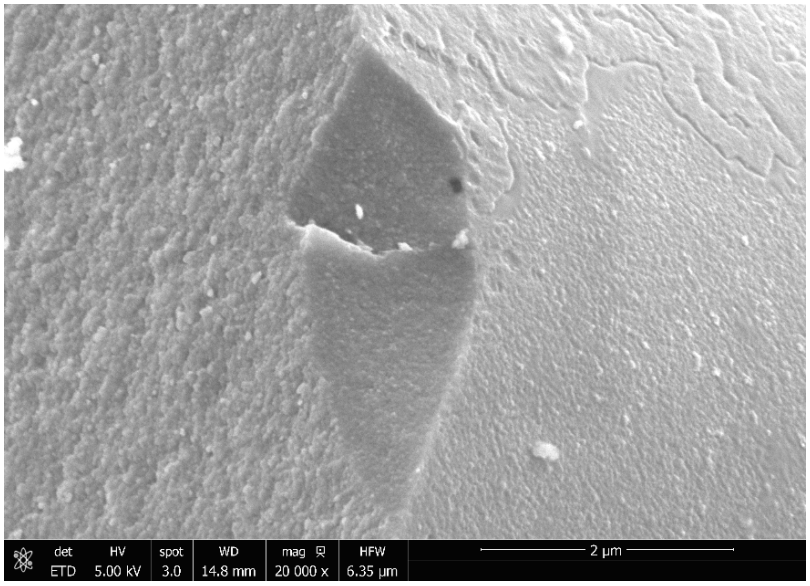


Figure 66 - SEM micrograph of the Hi-Nicalon™ S specimen "Air 3" examining features on the fracture surface of a fiber (σ_{cr} = 700 MPa, t_f = 62.50 h).

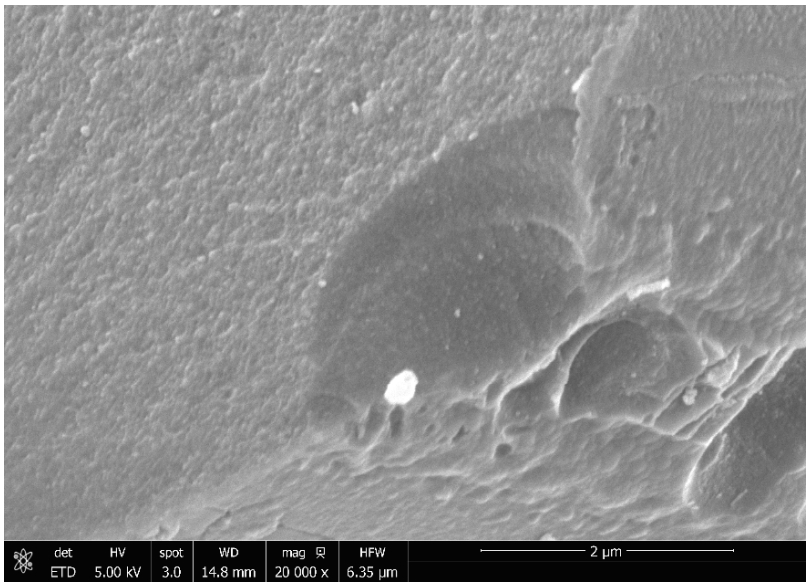


Figure 67 - SEM micrograph of the Hi-Nicalon™ S specimen "Air 3" examining features on the fracture surface of a fiber (σ_{cr} = 700 MPa, t_f = 62.50 h).

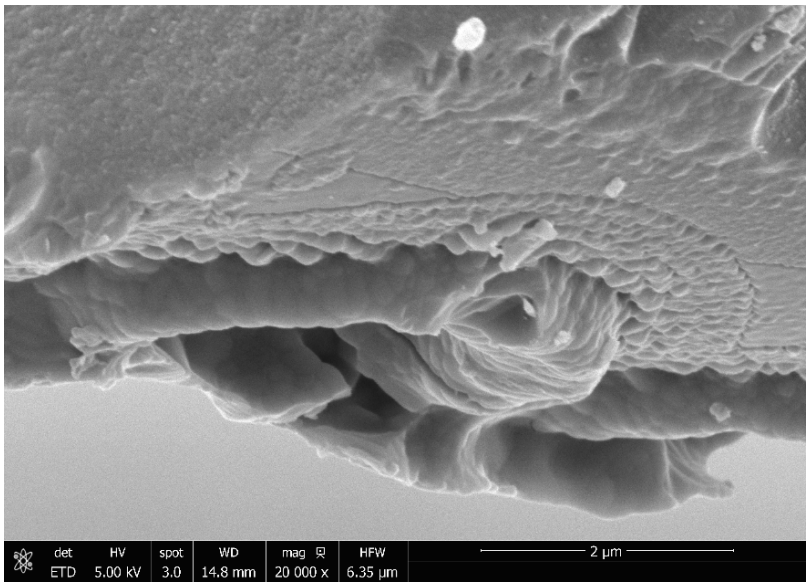


Figure 68 - SEM micrograph of the Hi-Nicalon™ S specimen "Air 3" examining defects near the fracture surface of a fiber (σ_{cr} = 700 MPa, t_f = 62.50 h). Note these defects are likely where crack initiated.

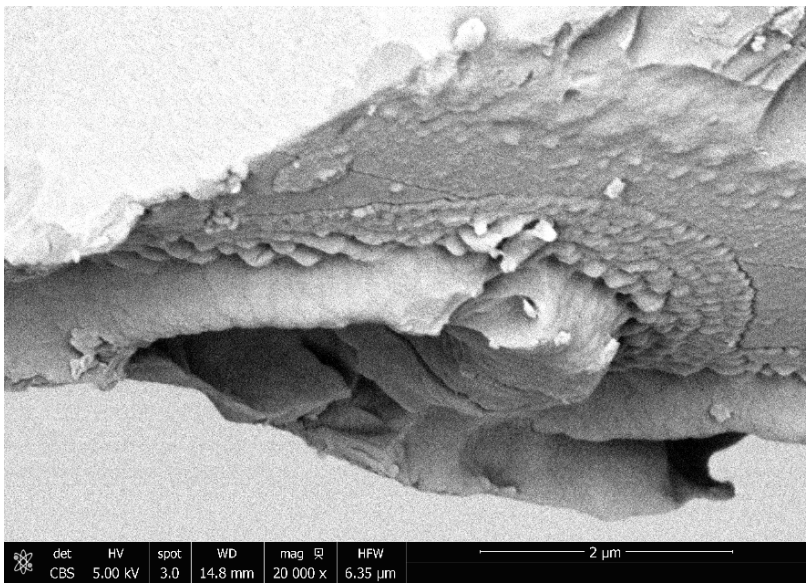


Figure 69 - SEM electron backscatter deflection micrograph of the Hi-Nicalon™ S specimen "Air 3" examining defects near the fracture surface of a fiber (σ_{cr} = 700 MPa, t_f = 62.50 h). Note these defects are likely where crack initiated.

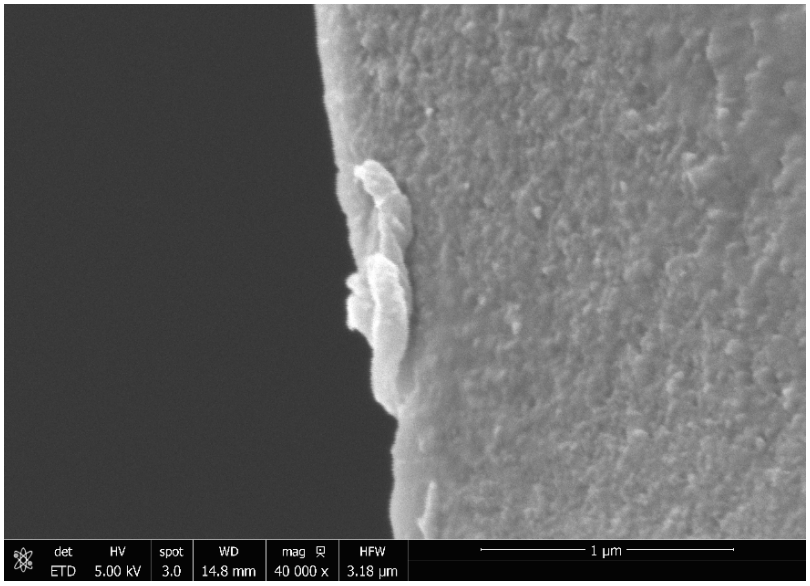


Figure 70 - SEM micrograph of the Hi-Nicalon™ S specimen "Air 3" examining the fracture surface of a fiber (σ_{cr} = 700 MPa, t_f = 62.50 h).

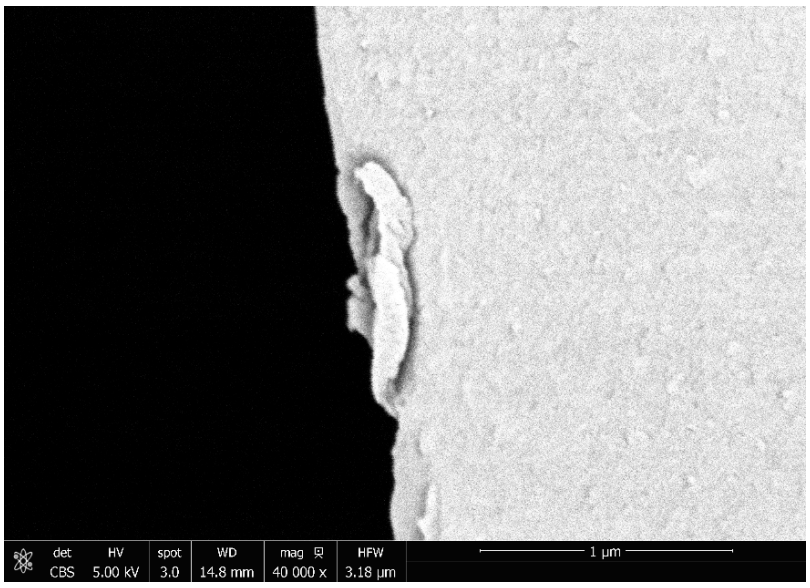


Figure 71 - SEM electron backscatter deflection micrograph of the Hi-Nicalon™ S specimen "Air 3" examining features on the fracture surface of a fiber (σ_{cr} = 700 MPa, t_f = 62.50 h).

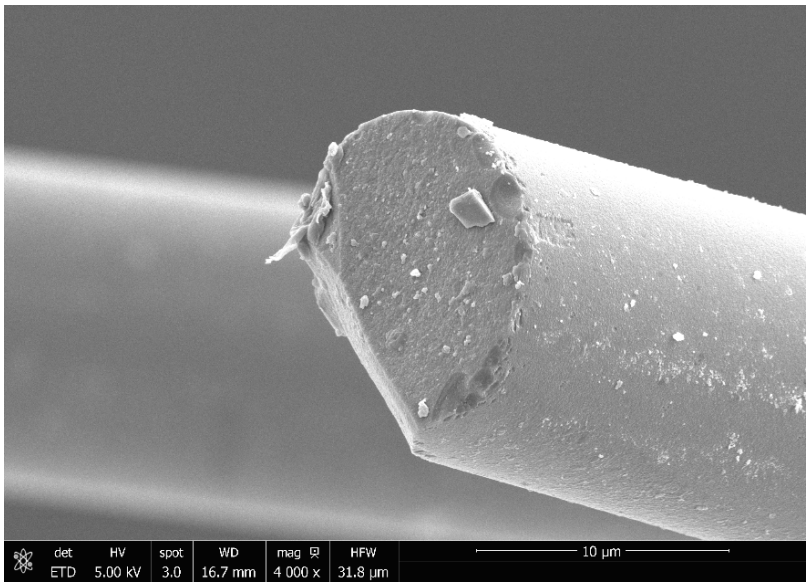


Figure 72 - SEM micrograph of the Hi-Nicalon™ S specimen "Air 3" examining the fracture surface of a fiber (σ_{cr} = 700 MPa, t_f = 62.50 h).

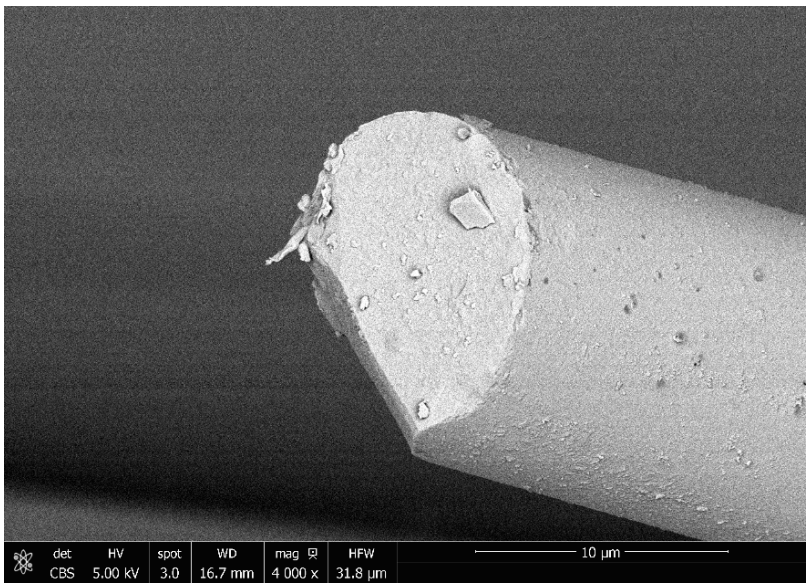


Figure 73 - SEM electron backscatter deflection micrograph of the Hi-Nicalon™ S specimen "Air 3" examining the fracture surface of a fiber (σ_{cr} = 700 MPa, t_f = 62.50 h).

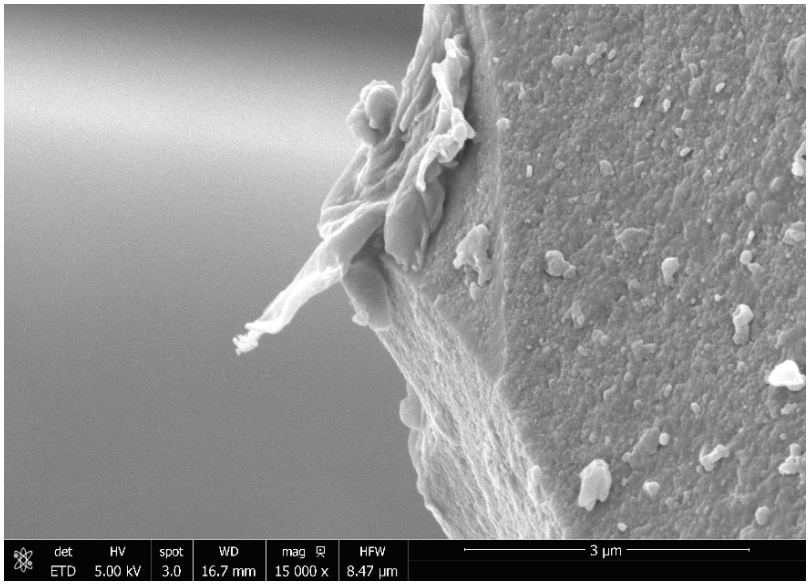


Figure 74 - SEM micrograph of the Hi-Nicalon™ S specimen "Air 3" examining features on the fracture surface of a fiber (σ_{cr} = 700 MPa, t_f = 62.50 h).

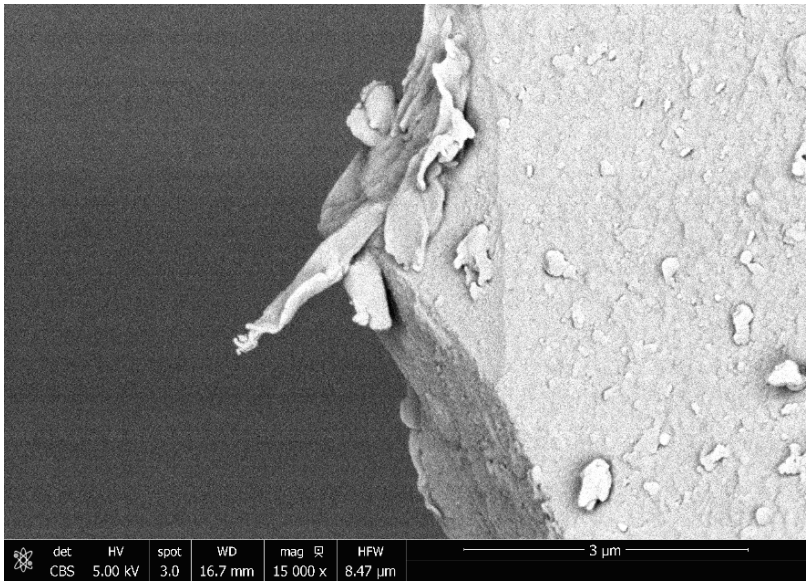


Figure 75 - SEM electron backscatter deflection micrograph of the Hi-Nicalon™ S specimen "Air 3" examining features on the fracture surface of a fiber (σ_{cr} = 700 MPa, t_f = 62.50 h).

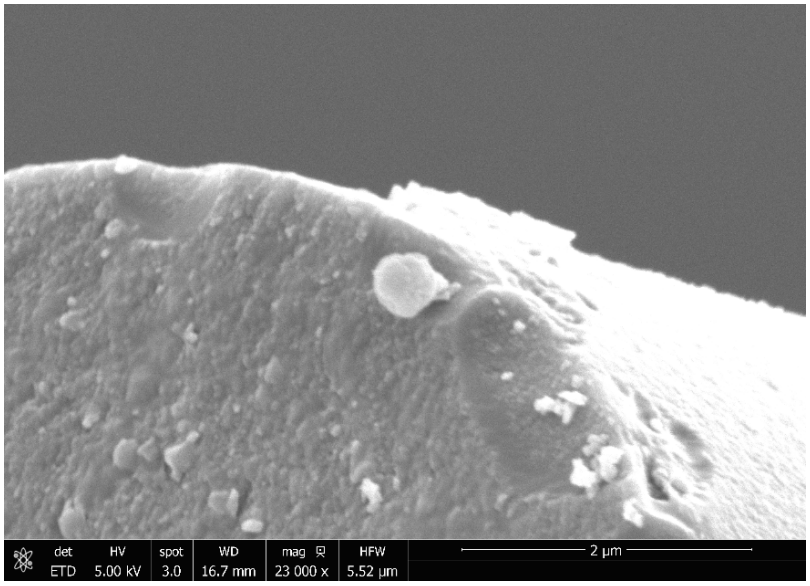


Figure 76 - SEM micrograph of the Hi-Nicalon™ S specimen "Air 3" examining features on the fracture surface of a fiber (σ_{cr} = 700 MPa, t_f = 62.50 h).

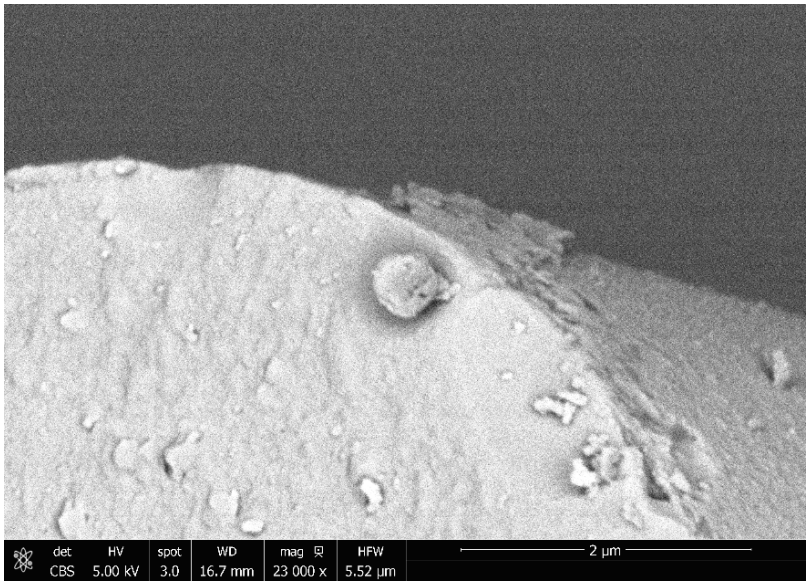


Figure 77 - SEM electron backscatter deflection micrograph of the Hi-Nicalon™ S specimen "Air 3" examining features on the fracture surface of a fiber (σ_{cr} = 700 MPa, t_f = 62.50 h).

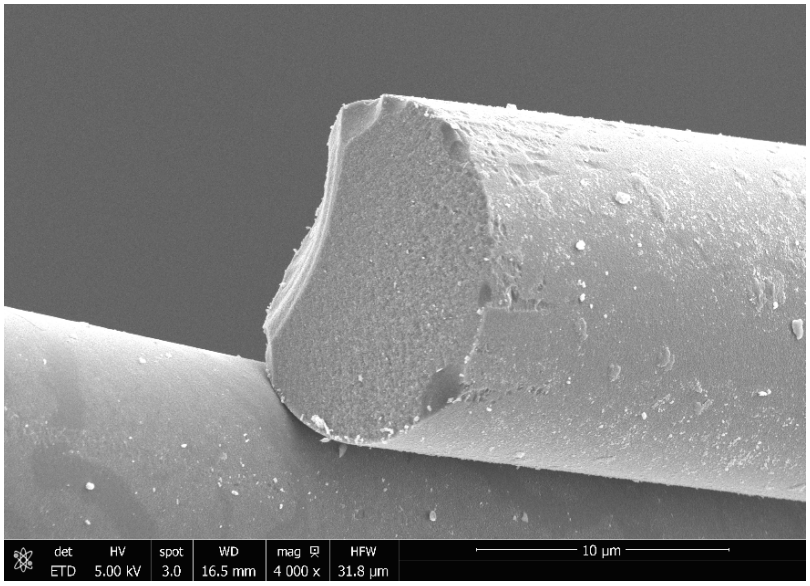


Figure 78 - SEM micrograph of the Hi-Nicalon™ S specimen "Air 3" examining the fracture surface of a fiber (σ_{cr} = 700 MPa, t_f = 62.50 h).

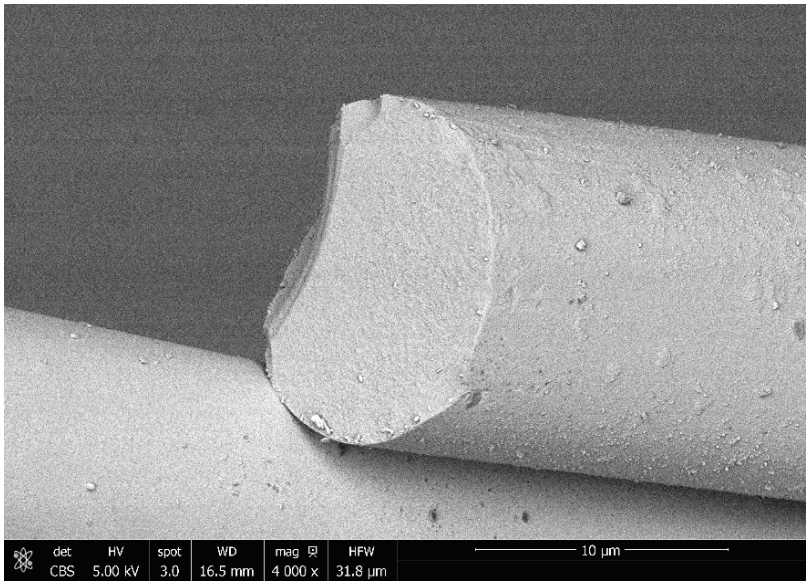


Figure 79 - SEM electron backscatter deflection micrograph of the Hi-Nicalon™ S specimen "Air 3" examining the fracture surface of a fiber (σ_{cr} = 700 MPa, t_f = 62.50 h).

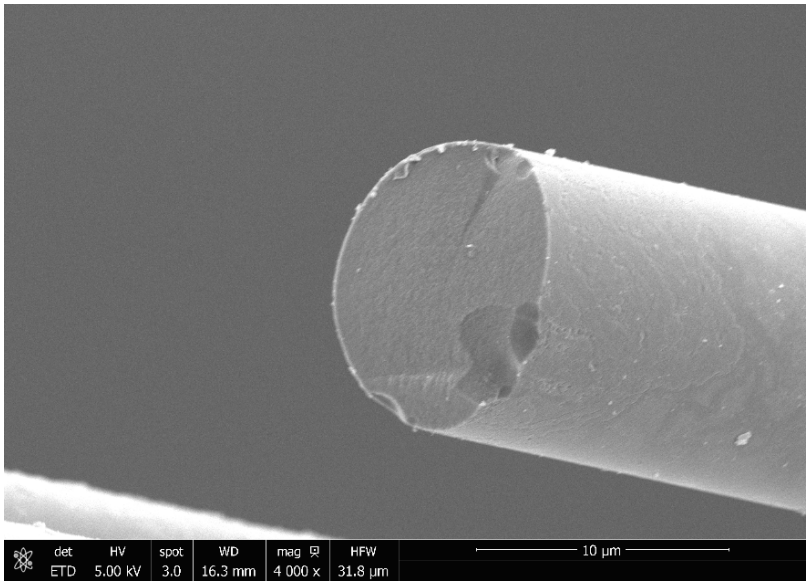


Figure 80 - SEM micrograph of the Hi-Nicalon™ S specimen "Air 3" examining the fracture surface of a fiber (σ_{cr} = 700 MPa, t_f = 62.50 h).

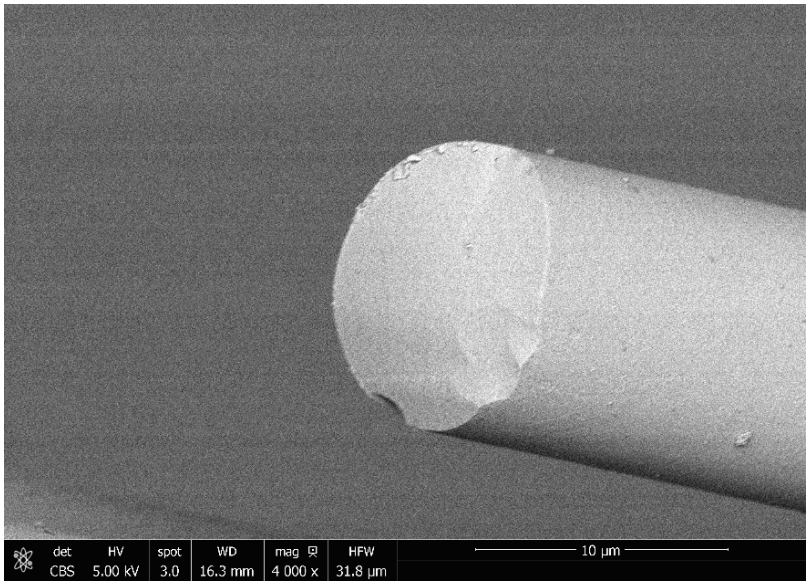


Figure 81 - SEM electron backscatter deflection micrograph of the Hi-Nicalon™ S specimen "Air 3" examining the fracture surface of a fiber (σ_{cr} = 700 MPa, t_f = 62.50 h).

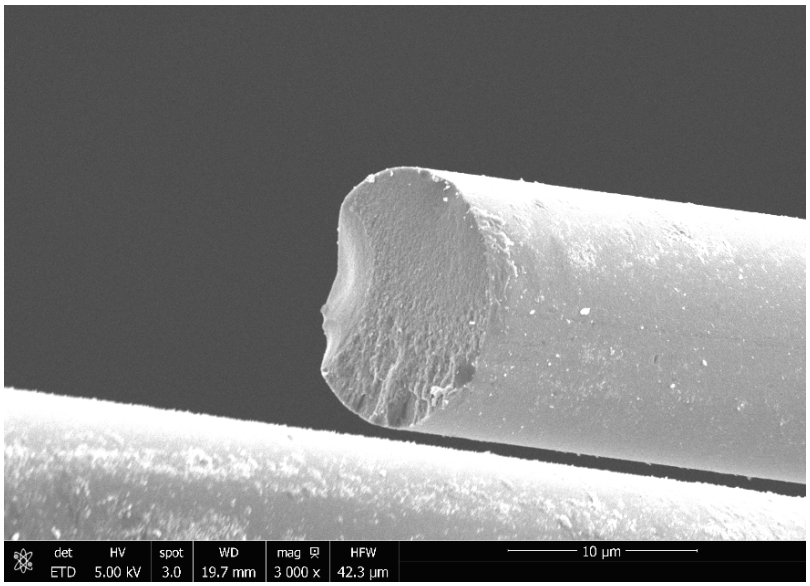


Figure 82 - SEM micrograph of the Hi-Nicalon™ S specimen "Air 3" examining the fracture surface of a fiber (σ_{cr} = 700 MPa, t_f = 62.50 h).

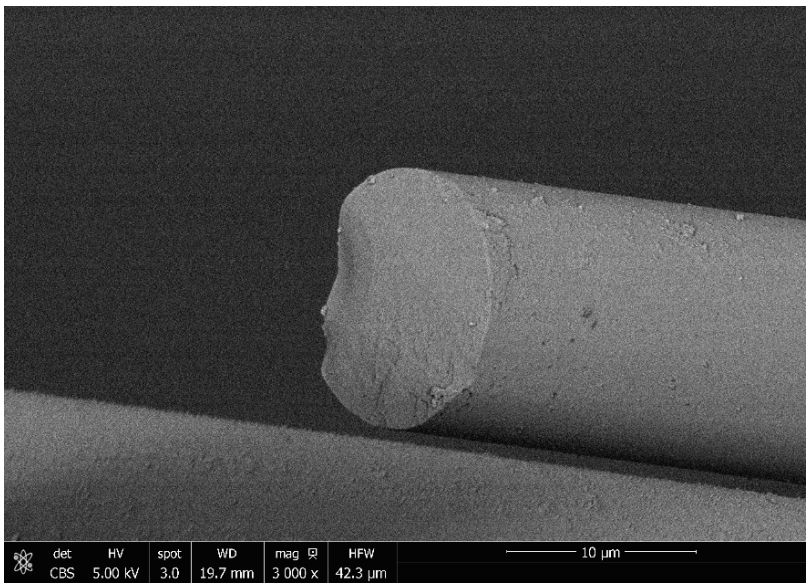


Figure 83 - SEM electron backscatter deflection micrograph of the Hi-Nicalon™ S specimen "Air 3" examining the fracture surface of a fiber (σ_{cr} = 700 MPa, t_f = 62.50 h).

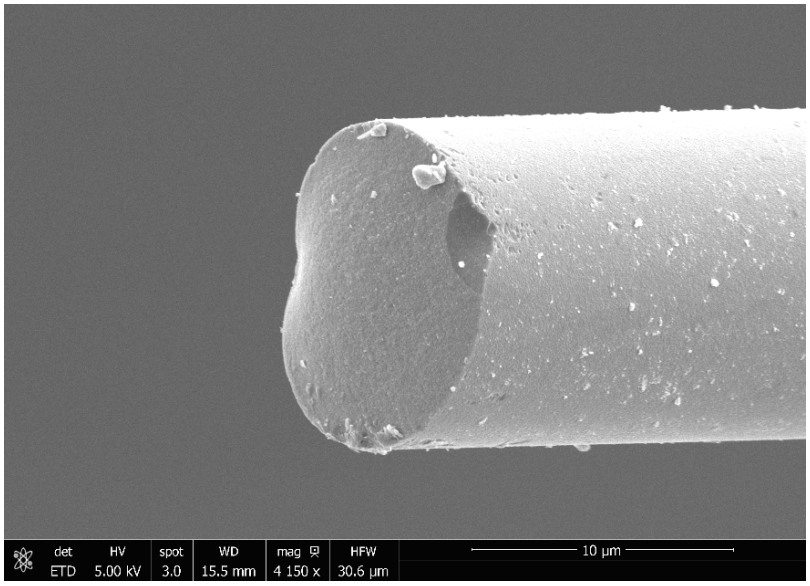


Figure 84 - SEM micrograph of the Hi-Nicalon™ S specimen "Air 3" examining the fracture surface of a fiber (σ_{cr} = 700 MPa, t_f = 62.50 h).

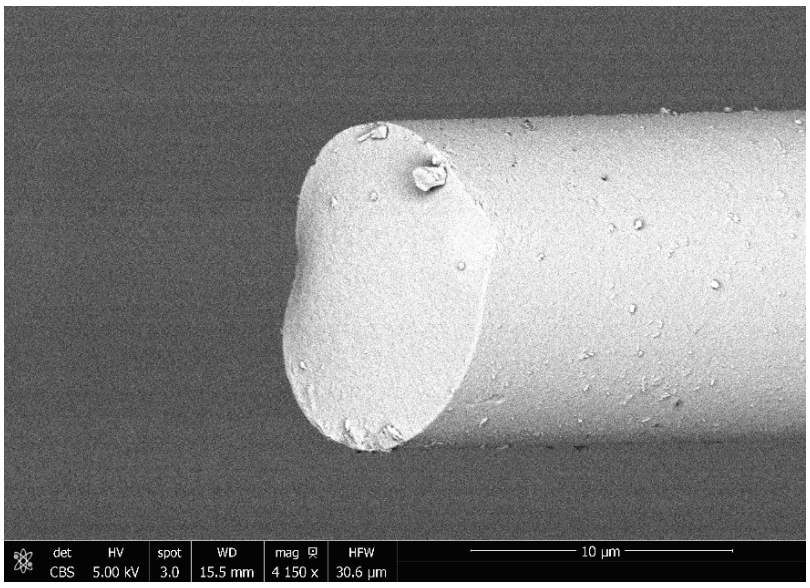


Figure 85 - SEM electron backscatter deflection micrograph of the Hi-Nicalon™ S specimen "Air 3" examining the fracture surface of a fiber (σ_{cr} = 700 MPa, t_f = 62.50 h).

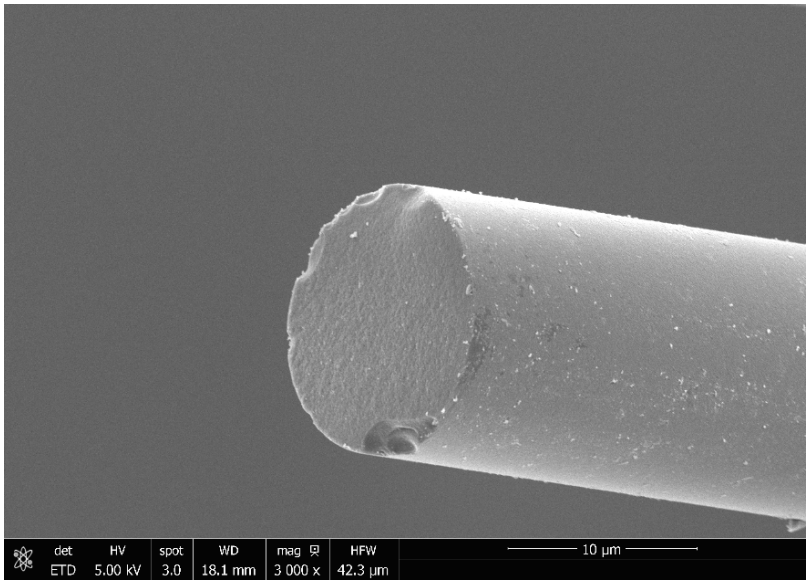


Figure 86 - SEM micrograph of the Hi-Nicalon™ S specimen "Air 3" examining the fracture surface of a fiber (σ_{cr} = 700 MPa, t_f = 62.50 h).

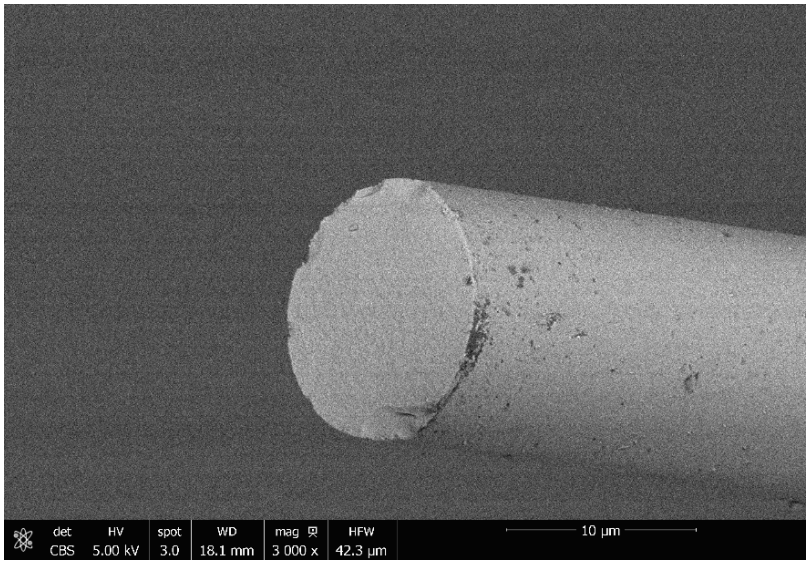


Figure 87 - SEM electron backscatter deflection micrograph of the Hi-Nicalon™ S specimen "Air 3" examining the fracture surface of a fiber (σ_{cr} = 700 MPa, t_f = 62.50 h).

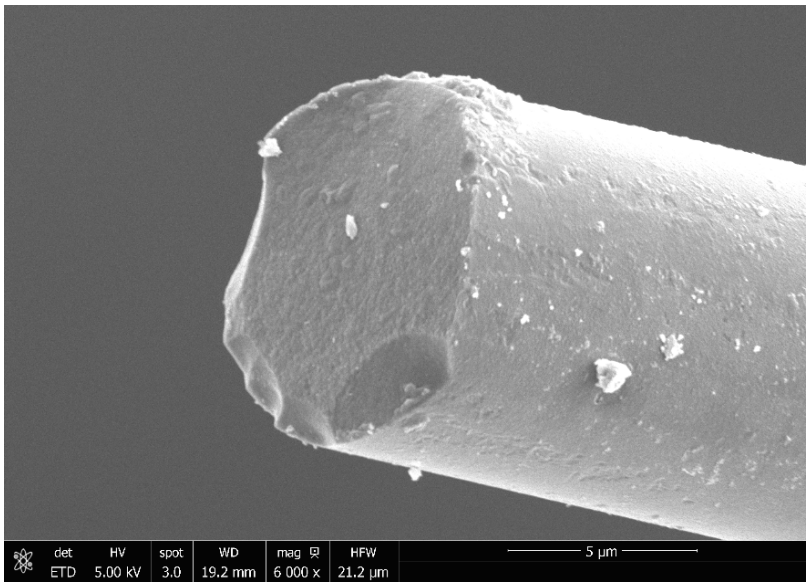


Figure 88 - SEM micrograph of the Hi-Nicalon™ S specimen "Air 3" examining the fracture surface of a fiber (σ_{cr} = 700 MPa, t_f = 62.50 h).

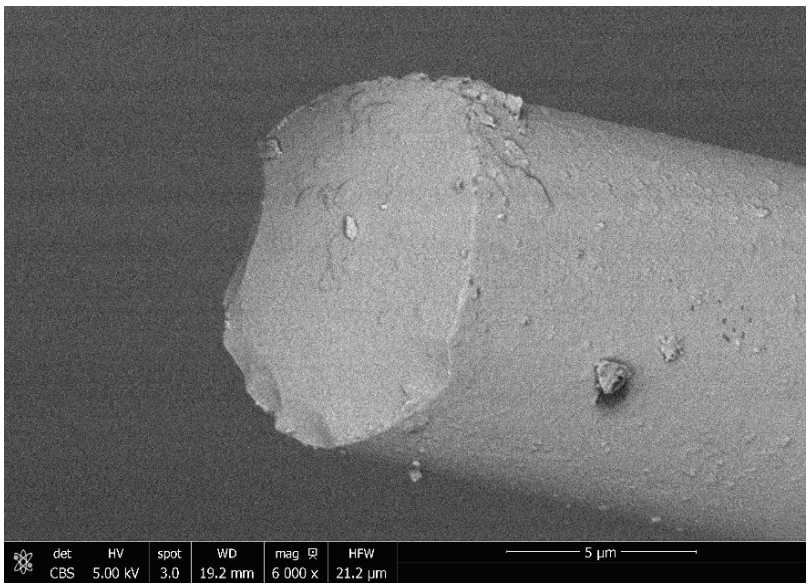


Figure 89 - SEM electron backscatter deflection micrograph of the Hi-Nicalon™ S specimen "Air 3" examining the fracture surface of a fiber (σ_{cr} = 700 MPa, t_f = 62.50 h).

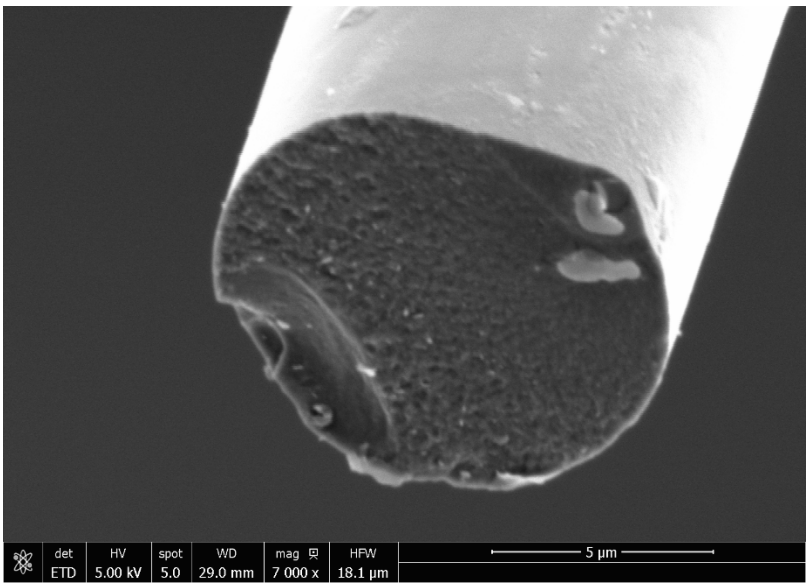


Figure 90 - SEM micrograph of the Hi-Nicalon™ S specimen "Air 10" examining the fracture surface of a fiber (σ_{cr} = 800 MPa, t_f = 31.0 h).

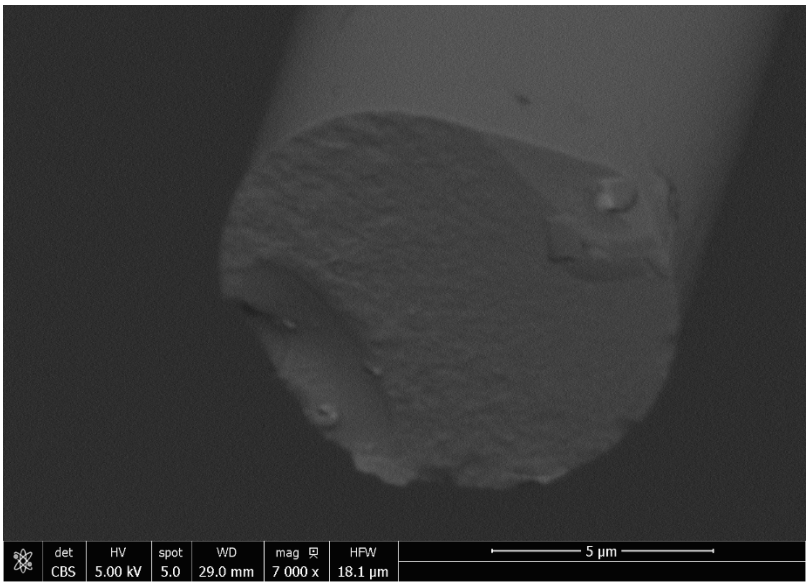


Figure 91 - SEM electron backscatter deflection micrograph of the Hi-Nicalon™ S specimen "Air 10" examining the fracture surface of a fiber (σ_{cr} = 800 MPa, t_f = 31.0 h).

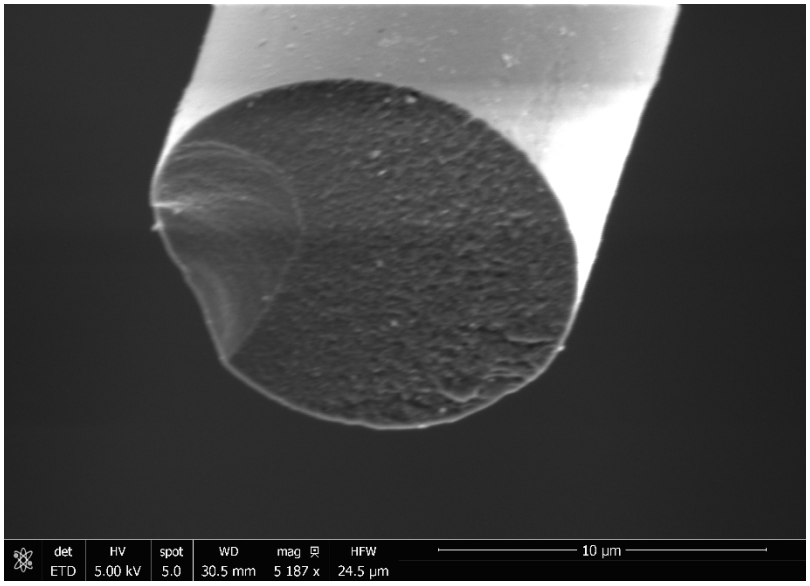


Figure 92 - SEM micrograph of the Hi-Nicalon™ S specimen "Air 10" examining the fracture surface of a fiber (σ_{cr} = 800 MPa, t_f = 31.0 h).

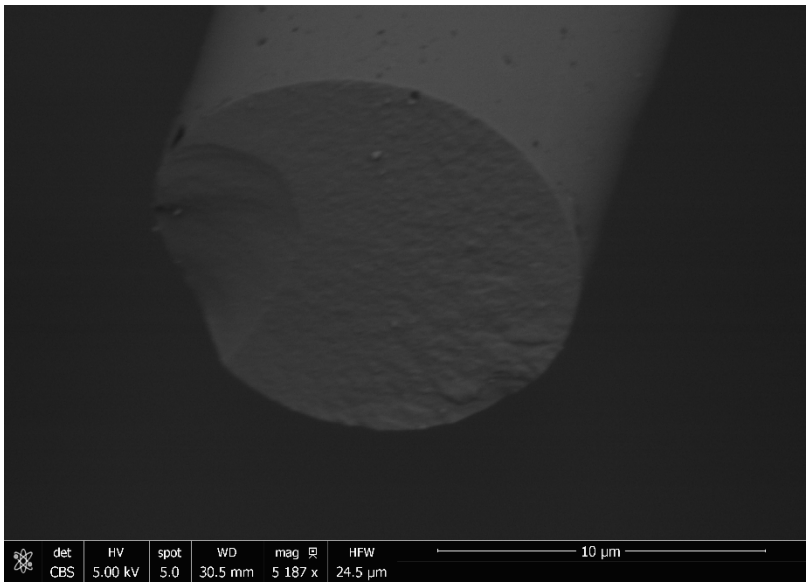


Figure 93 - SEM electron backscatter deflection micrograph of the Hi-Nicalon™ S specimen "Air 10" examining the fracture surface of a fiber (σ_{cr} = 800 MPa, t_f = 31.0 h).

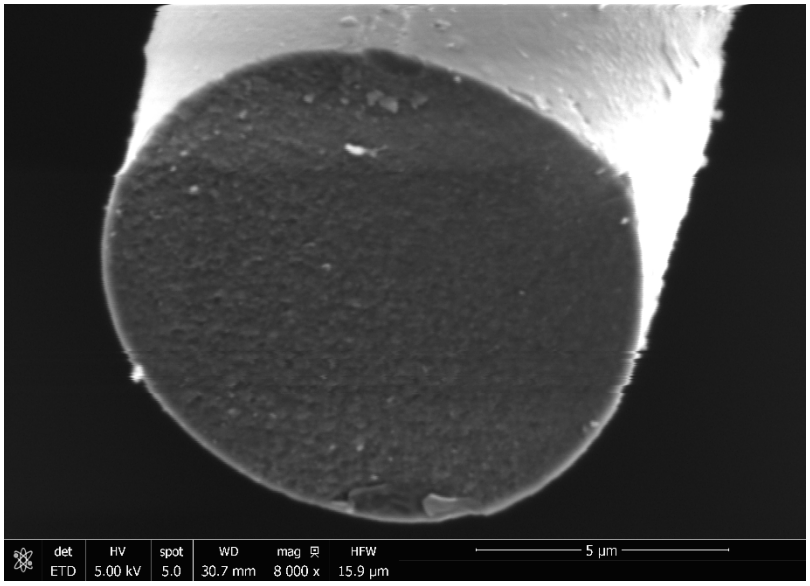


Figure 94 - SEM micrograph of the Hi-Nicalon™ S specimen "Air 10" examining the fracture surface of a fiber (σ_{cr} = 800 MPa, t_f = 31.0 h).

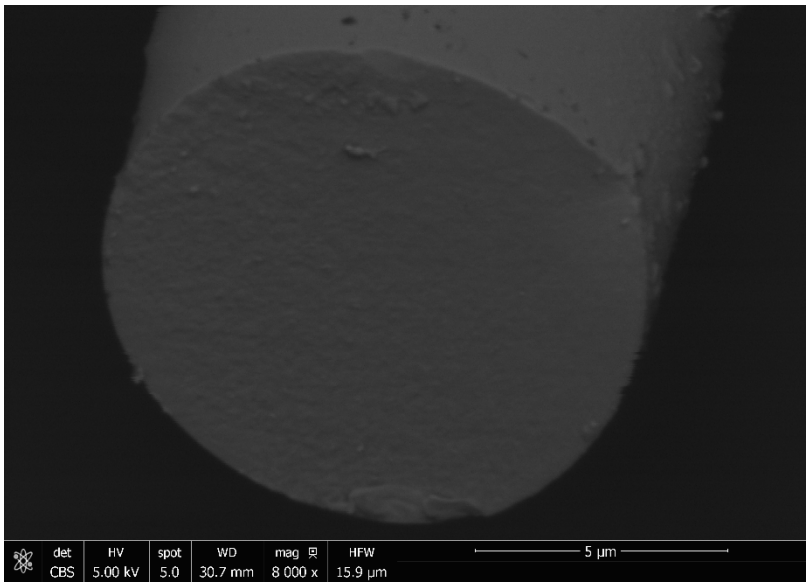


Figure 95 - SEM electron backscatter deflection micrograph of the Hi-Nicalon™ S specimen "Air 10" examining the fracture surface of a fiber (σ_{cr} = 800 MPa, t_f = 31.0 h).

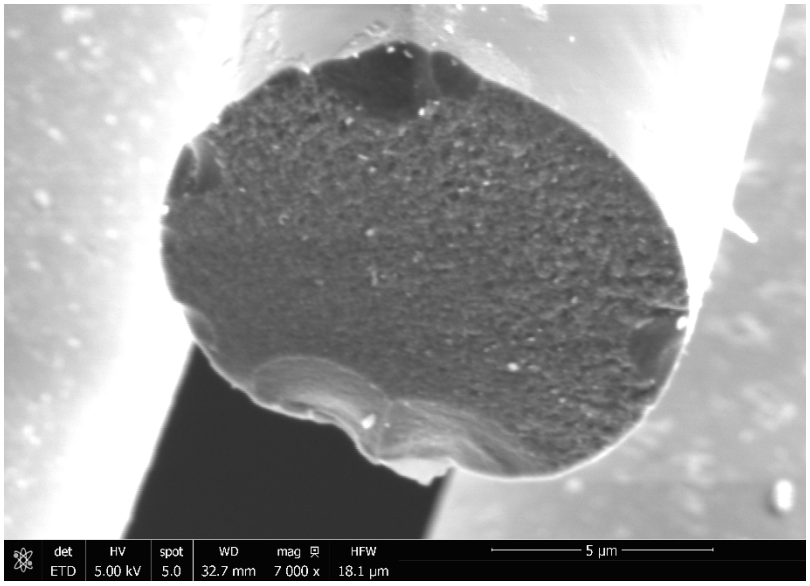


Figure 96 - SEM micrograph of the Hi-Nicalon™ S specimen "Air 10" examining the fracture surface of a fiber (σ_{cr} = 800 MPa, t_f = 31.0 h).

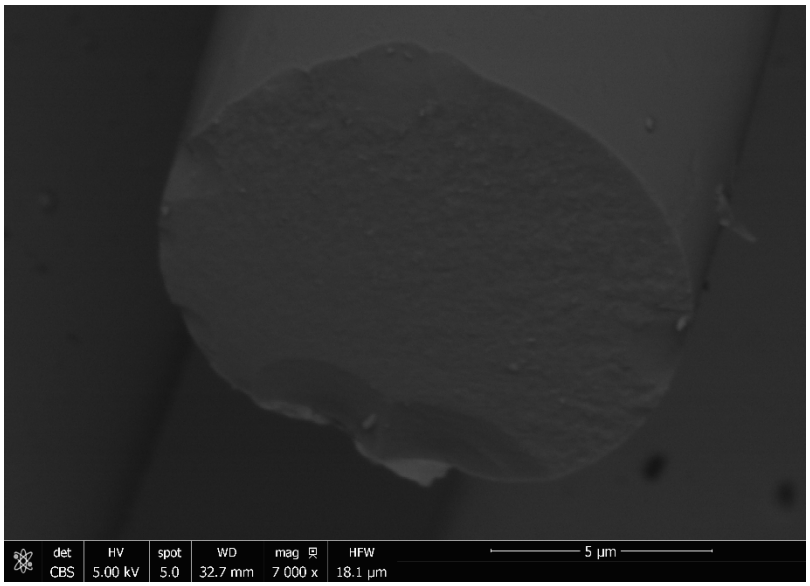


Figure 97 - SEM electron backscatter deflection micrograph of the Hi-Nicalon™ S specimen "Air 10" examining the fracture surface of a fiber (σ_{cr} = 800 MPa, t_f = 31.0 h).

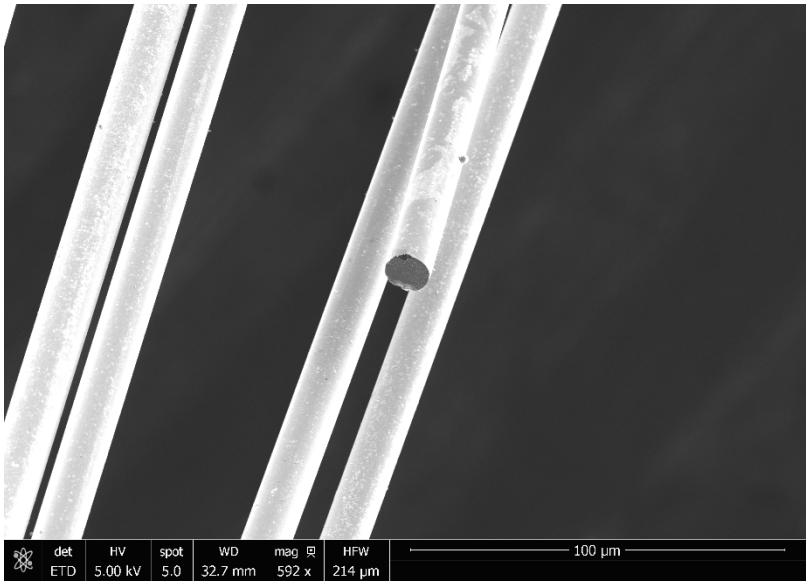


Figure 98 - SEM micrograph of the Hi-Nicalon™ S specimen "Air 10" examining the fracture surface of a fiber (σ_{cr} = 800 MPa, t_f = 31.0 h). Note signs of longitudinal fiber contact.

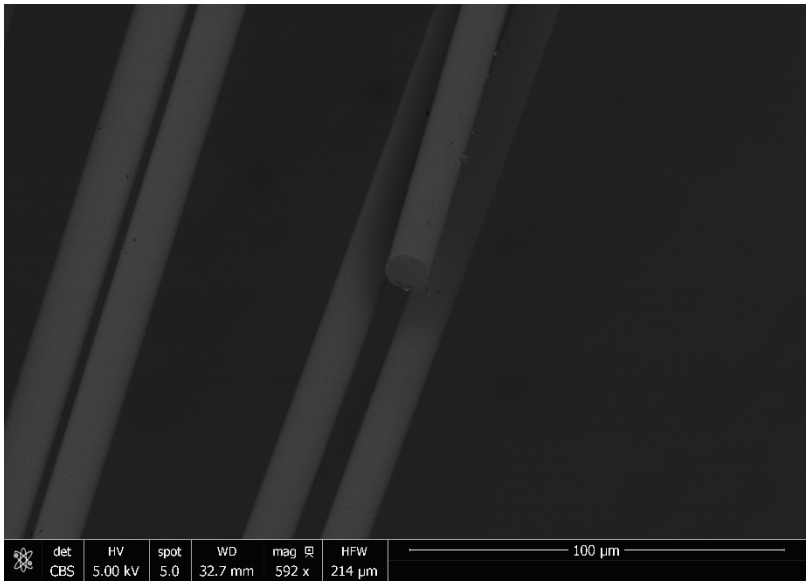


Figure 99 - SEM electron backscatter deflection micrograph of the Hi-Nicalon™ S specimen "Air 10" examining the fracture surface of a fiber (σ_{cr} = 800 MPa, t_f = 31.0 h).

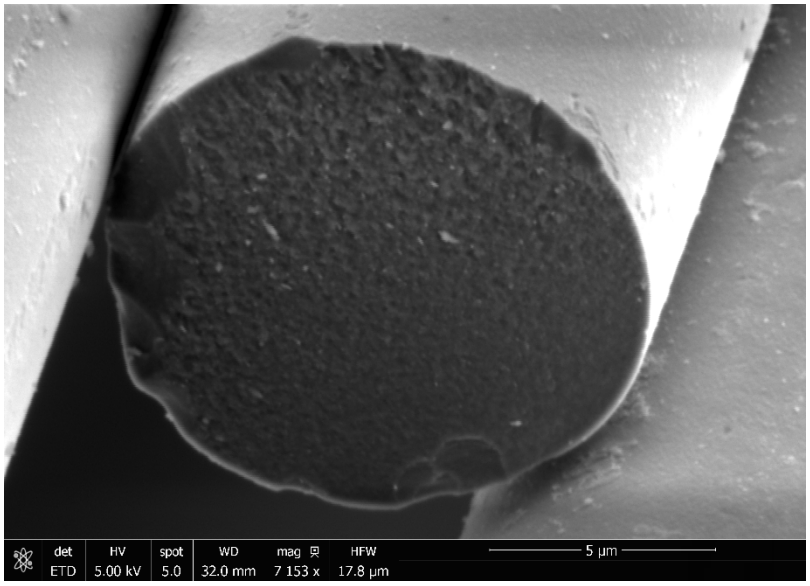


Figure 100 - SEM micrograph of the Hi-Nicalon™ S specimen "Air 10" examining the fracture surface of a fiber (σ_{cr} = 800 MPa, t_f = 31.0 h).

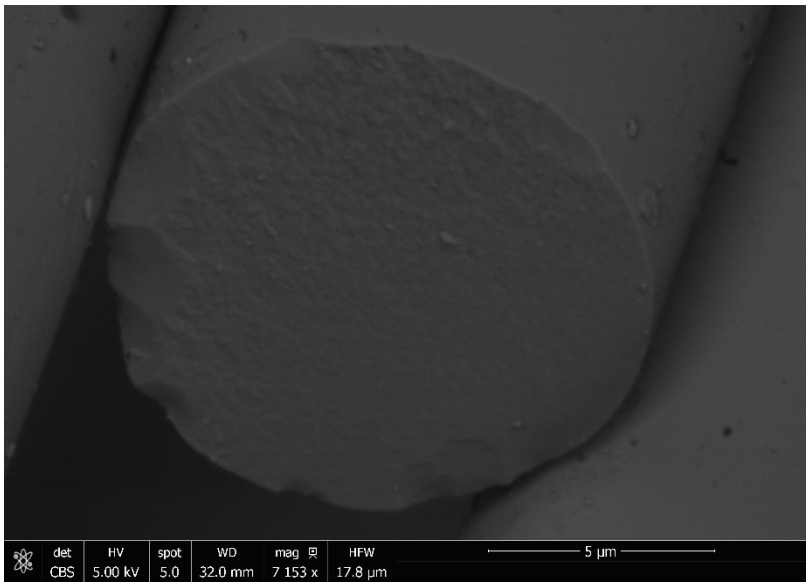


Figure 101 - SEM electron backscatter deflection micrograph of the Hi-Nicalon™ S specimen "Air 10" examining the fracture surface of a fiber (σ_{cr} = 800 MPa, t_f = 31.0 h).

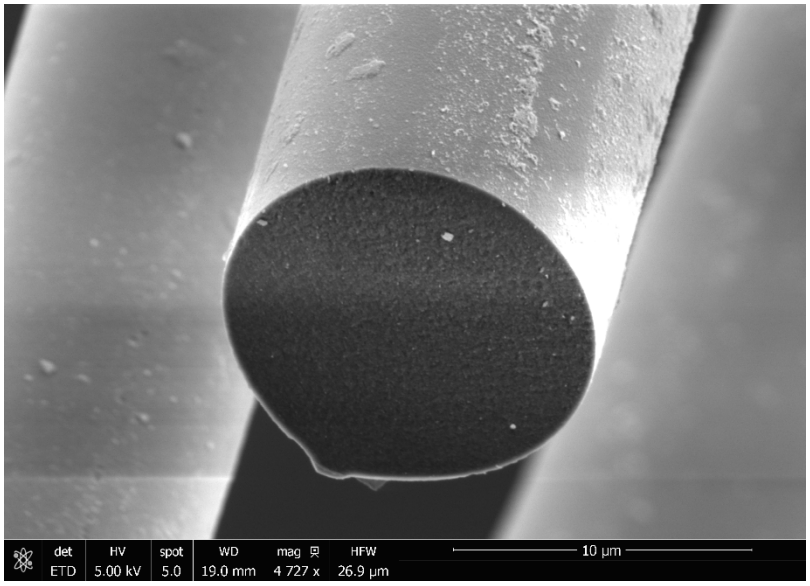


Figure 102 - SEM micrograph of the Hi-Nicalon™ S specimen "Air 10" examining the fracture surface of a fiber (σ_{cr} = 800 MPa, t_f = 31.0 h). Note signs longitudinal fiber contact.

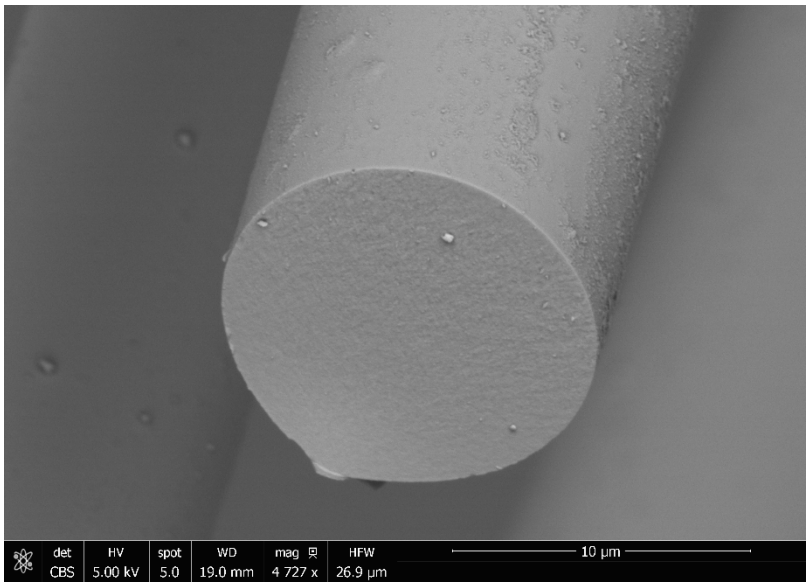


Figure 103 - SEM electron backscatter deflection micrograph of the Hi-Nicalon™ S specimen "Air 10" examining the fracture surface of a fiber (σ_{cr} = 800 MPa, t_f = 31.0 h).

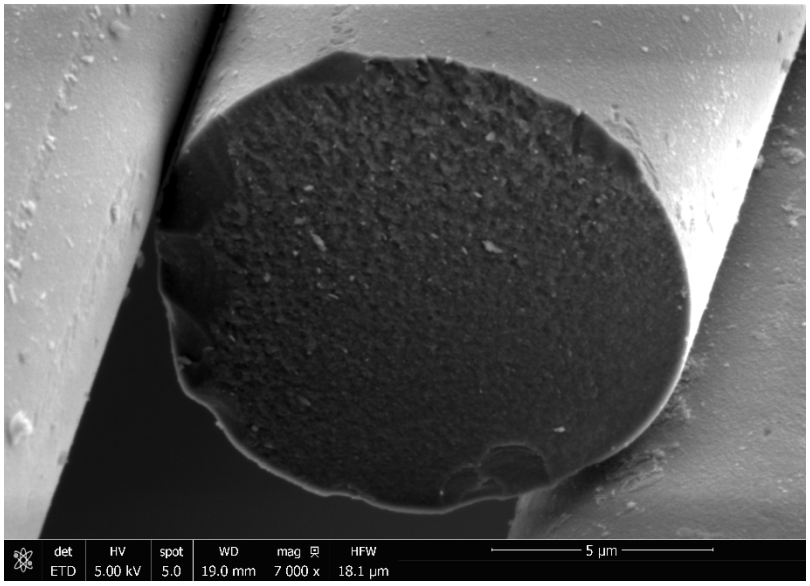


Figure 104 - SEM micrograph of the Hi-Nicalon™ S specimen "Air 10" examining the fracture surface of a fiber (σ_{cr} = 800 MPa, t_f = 31.0 h).

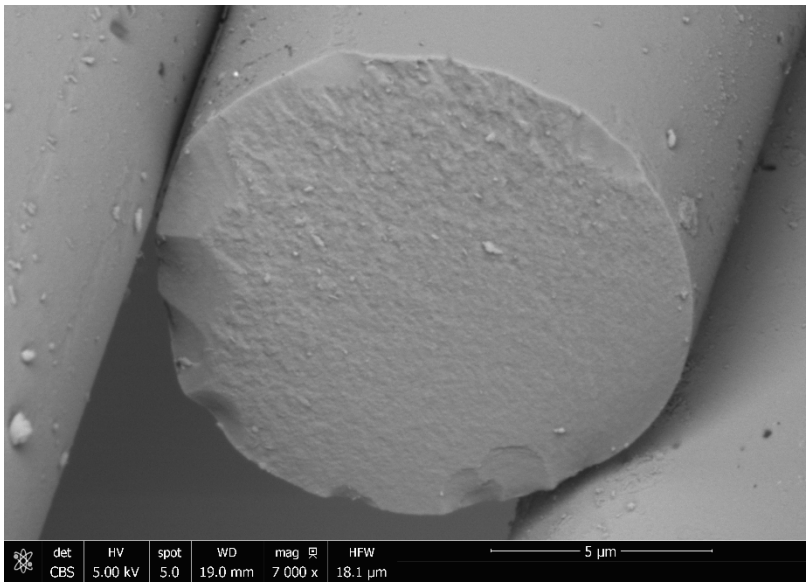


Figure 105 - SEM electron backscatter deflection micrograph of the Hi-Nicalon™ S specimen "Air 10" examining the fracture surface of a fiber (σ_{cr} = 800 MPa, t_f = 31.0 h).

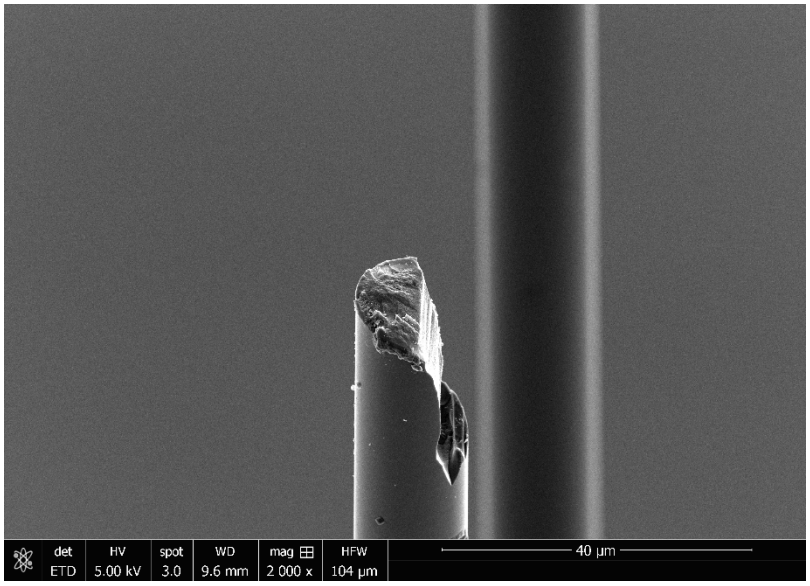


Figure 106 - SEM micrograph of the Hi-Nicalon™ S specimen "Steam 9" examining the fracture surface of a fiber (σ_{cr} = 353 MPa, t_f = 52.53 h). Note the silica scale ring and growth along facture surface.



Figure 107 - SEM electron backscatter deflection micrograph of the Hi-Nicalon™ S specimen "Steam 9" examining the fracture surface of a fiber (σ_{cr} = 353 MPa, t_f = 52.53 h).

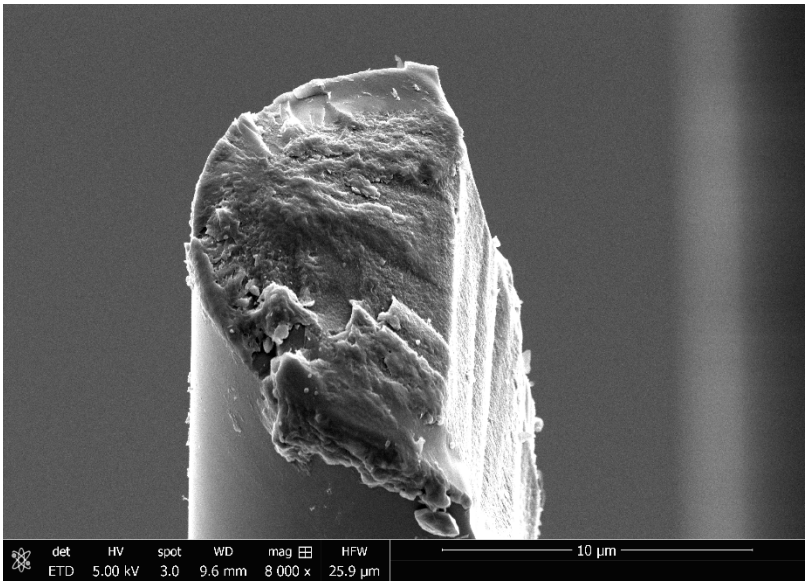


Figure 108 - SEM micrograph of the Hi-Nicalon™ S specimen "Steam 9" examining the fracture surface of a fiber (σ_{cr} = 353 MPa, t_f = 52.53 h). Note the silica scale ring and growth along facture surface.

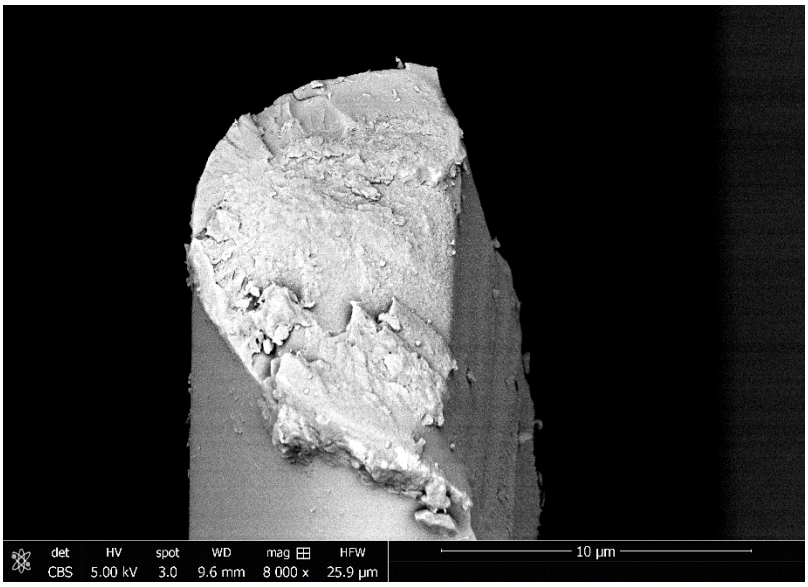


Figure 109 - SEM electron backscatter deflection micrograph of the Hi-Nicalon™ S specimen "Steam 9" examining the fracture surface of a fiber (σ_{cr} = 353 MPa, t_f = 52.53 h). Note the silica scale ring and growth along facture surface.

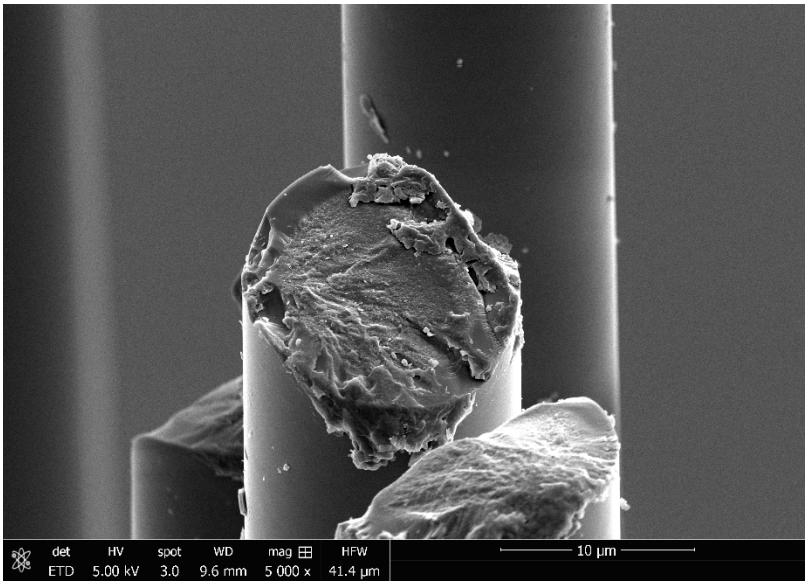


Figure 110 - SEM micrograph of the Hi-Nicalon™ S specimen "Steam 9" examining the fracture surface of a fiber (σ_{cr} = 353 MPa, t_f = 52.53 h). Note the defined silica scale ring and growth along facture surface.

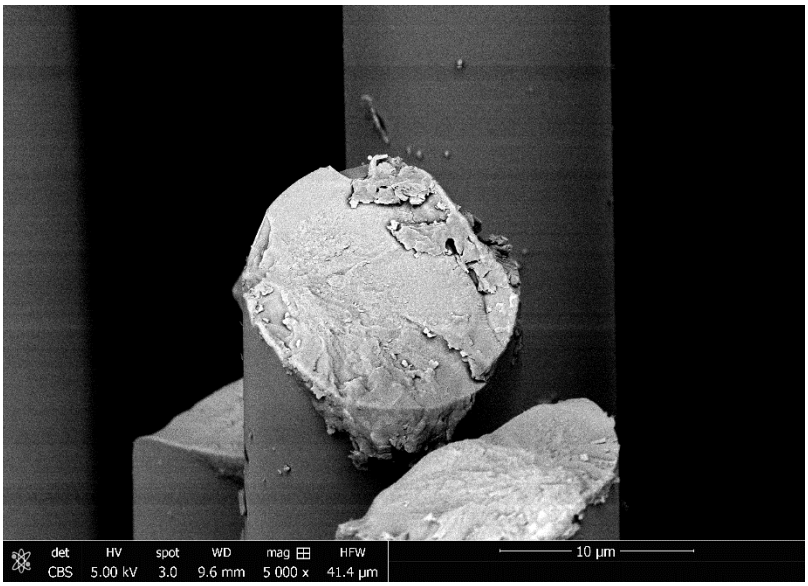


Figure 111 - SEM electron backscatter deflection micrograph of the Hi-Nicalon™ S specimen "Steam 9" examining the fracture surface of a fiber (σ_{cr} = 353 MPa, t_f = 52.53 h). Note the defined silica scale ring and growth along facture surface.

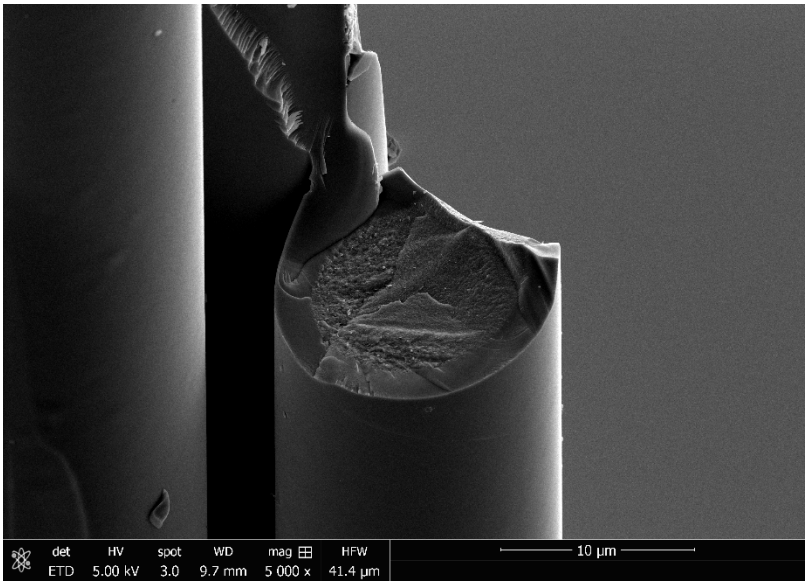


Figure 112 - SEM micrograph of the Hi-Nicalon™ S specimen "Steam 9" examining the fracture surface of a fiber (σ_{cr} = 353 MPa, t_f = 52.53 h). Note defined silica scale growth.

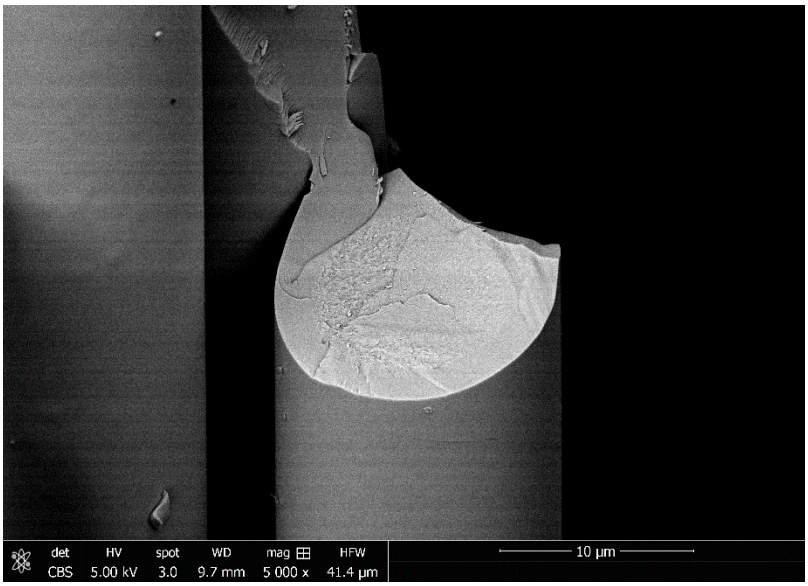


Figure 113 - SEM electron backscatter deflection micrograph of the Hi-Nicalon™ S specimen "Steam 9" examining the fracture surface of a fiber (σ_{cr} = 353 MPa, t_f = 52.53 h). Note defined silica scale growth.

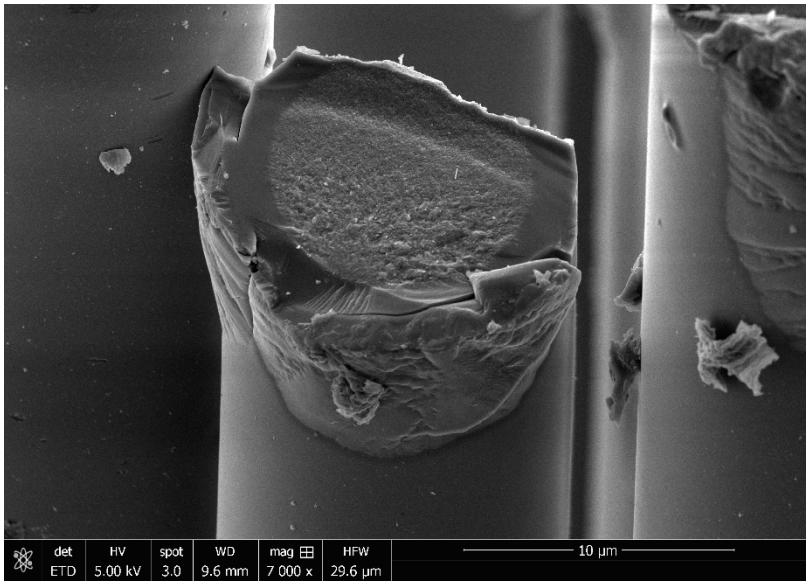


Figure 114 - SEM micrograph of the Hi-Nicalon™ S specimen "Steam 9" examining the fracture surface of a fiber (σ_{cr} = 353 MPa, t_f = 52.53 h). Note defined silica scale growth.

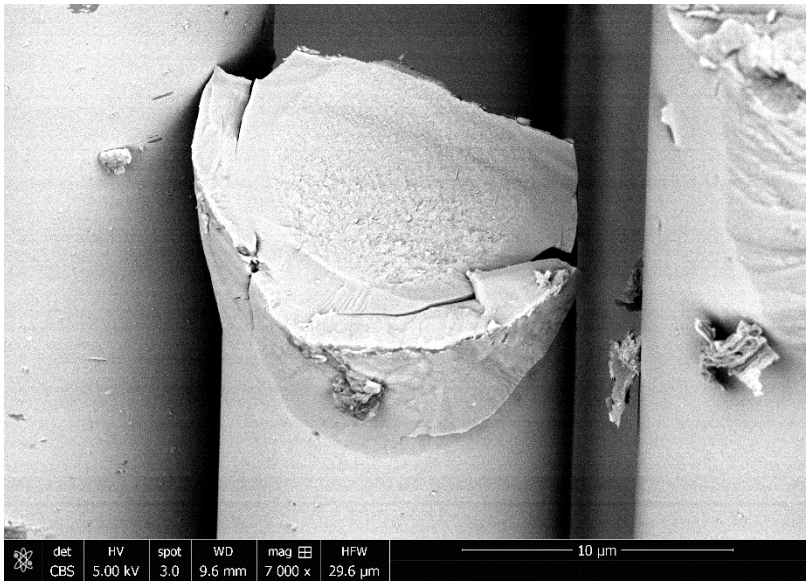


Figure 115 - SEM electron backscatter deflection micrograph of the Hi-Nicalon™ S specimen "Steam 9" examining the fracture surface of a fiber (σ_{cr} = 353 MPa, t_f = 52.53 h). Note defined silica scale growth.

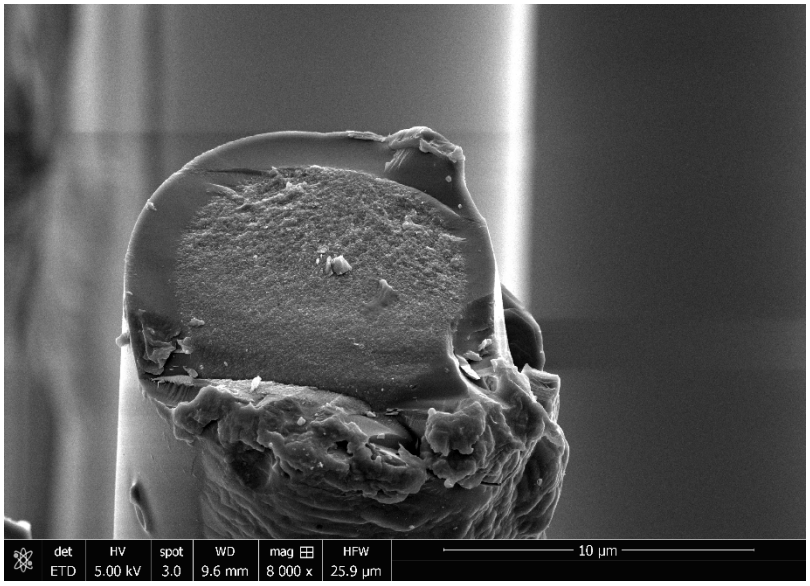


Figure 116 - SEM micrograph of the Hi-Nicalon™ S specimen "Steam 9" examining the fracture surface of a fiber (σ_{cr} = 353 MPa, t_f = 52.53 h). Note defined silica scale growth.

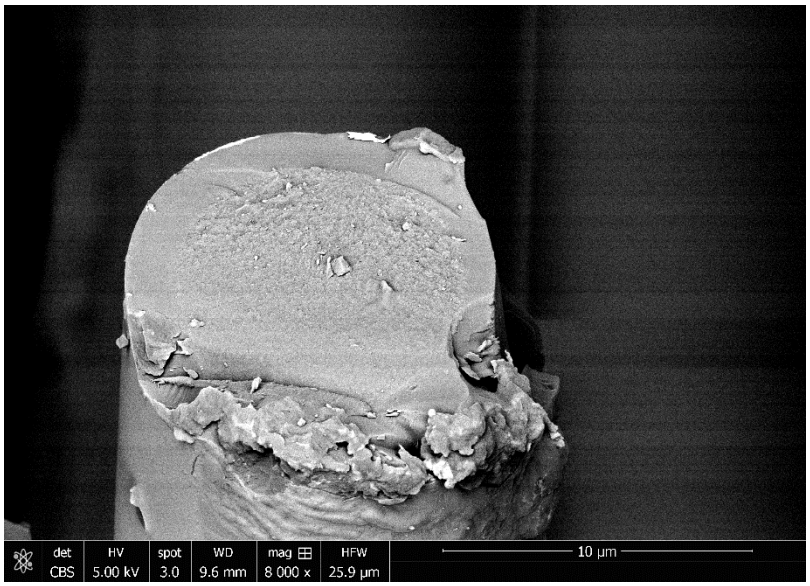


Figure 117 - SEM electron backscatter deflection micrograph of the Hi-Nicalon™ S specimen "Steam 9" examining the fracture surface of a fiber (σ_{cr} = 353 MPa, t_f = 52.53 h). Note defined silica scale growth.

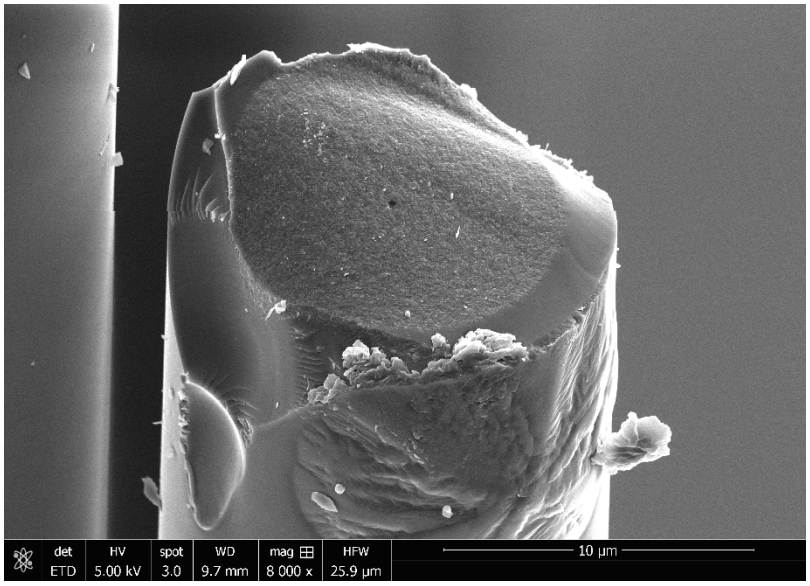


Figure 118 - SEM micrograph of the Hi-Nicalon™ S specimen "Steam 9" examining the fracture surface of a fiber (σ_{cr} = 353 MPa, t_f = 52.53 h). Note defined silica amorphous and crystallized scale growth.

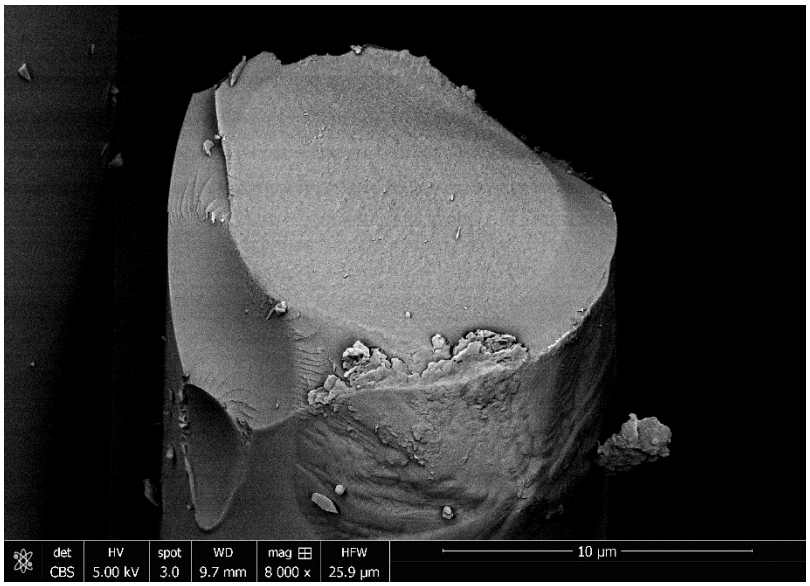


Figure 119 - SEM electron backscatter deflection micrograph of the Hi-Nicalon™ S specimen "Steam 9" examining the fracture surface of a fiber (σ_{cr} = 353 MPa, t_f = 52.53 h). Note defined silica amorphous and crystallized scale growth.

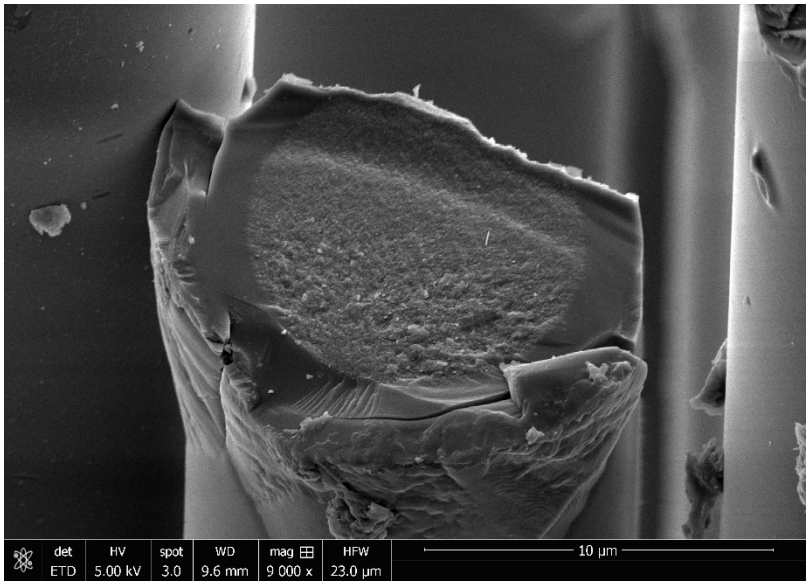


Figure 120 - SEM micrograph of the Hi-Nicalon™ S specimen "Steam 9" examining the fracture surface of a fiber (σ_{cr} = 353 MPa, t_f = 52.53 h). Note defined silica scale growth.

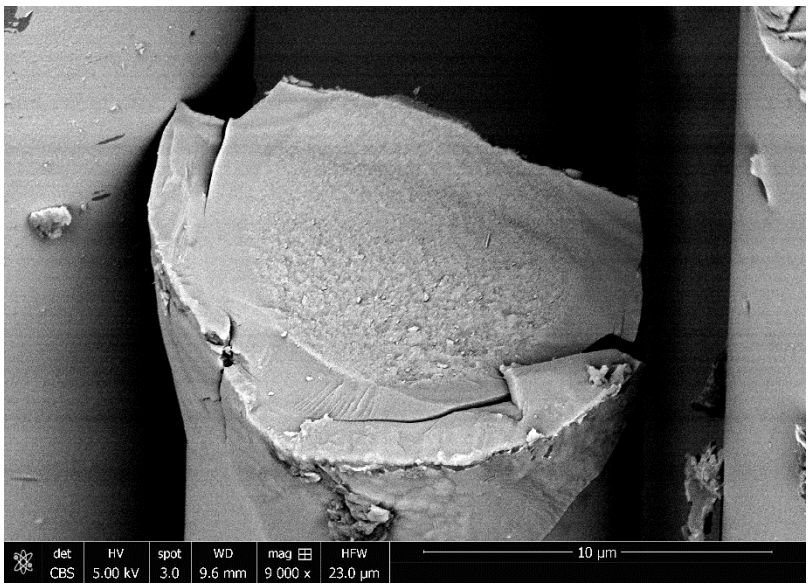


Figure 121 - SEM electron backscatter deflection micrograph of the Hi-Nicalon™ S specimen "Steam 9" examining the fracture surface of a fiber (σ_{cr} = 353 MPa, t_f = 52.53 h). Note defined silica scale growth.

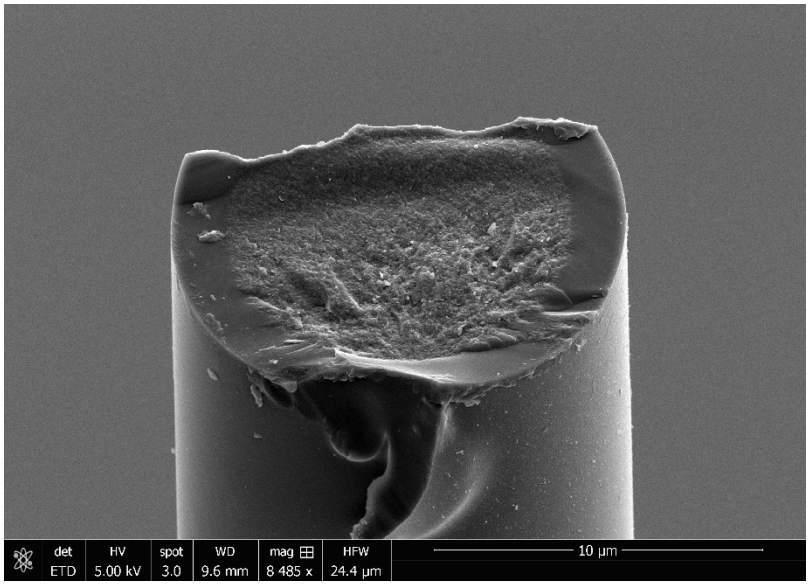


Figure 122 - SEM micrograph of the Hi-Nicalon™ S specimen "Steam 9" examining the fracture surface of a fiber (σ_{cr} = 353 MPa, t_f = 52.53 h). Note defined silica scale growth.

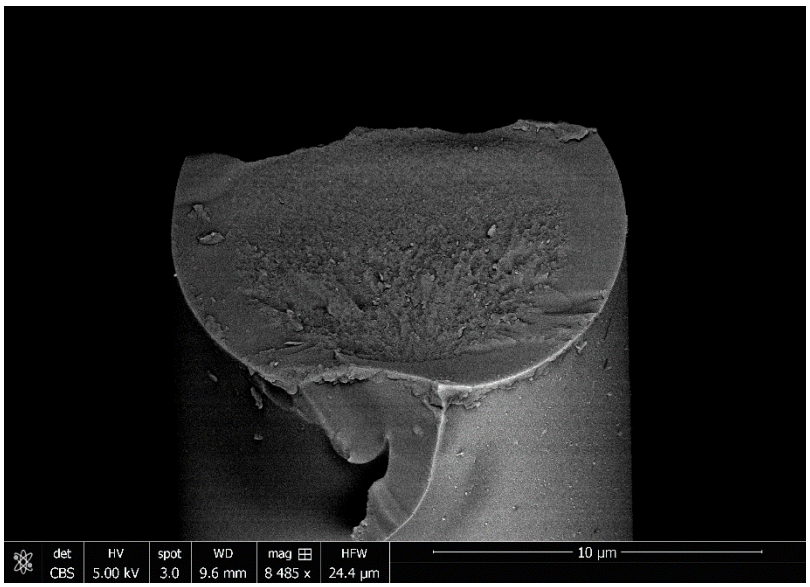


Figure 123 - SEM electron backscatter deflection micrograph of the Hi-Nicalon™ S specimen "Steam 9" examining the fracture surface of a fiber (σ_{cr} = 353 MPa, t_f = 52.53 h). Note defined silica scale growth.

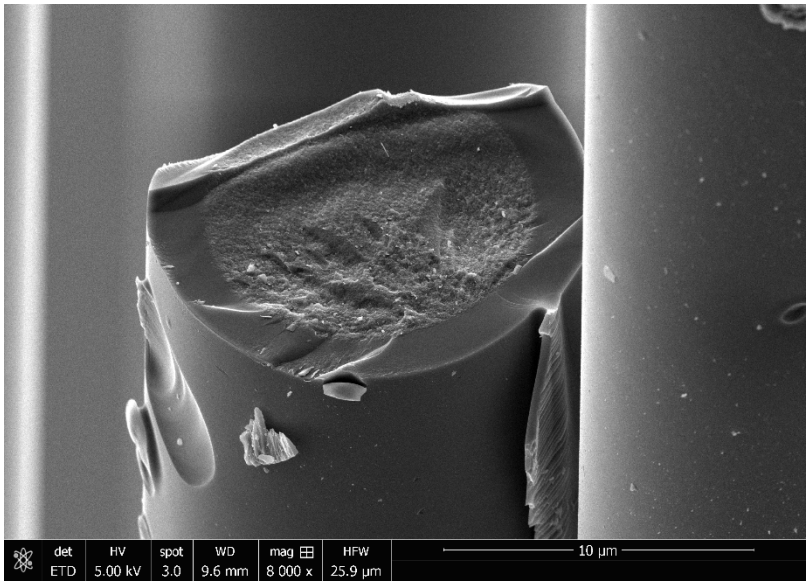


Figure 124 - SEM micrograph of the Hi-Nicalon™ S specimen "Steam 9" examining the fracture surface of a fiber (σ_{cr} = 353 MPa, t_f = 52.53 h). Note defined silica scale growth.

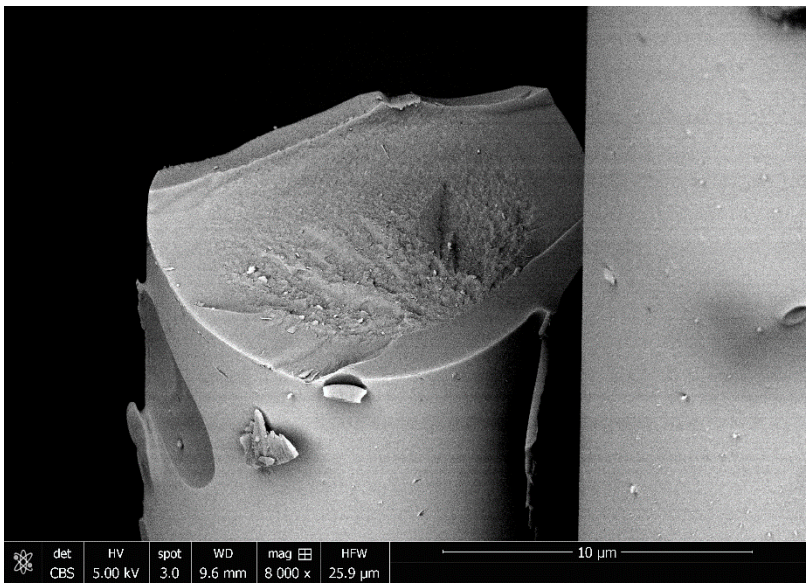


Figure 125 - SEM electron backscatter deflection micrograph of the Hi-Nicalon™ S specimen "Steam 9" examining the fracture surface of a fiber (σ_{cr} = 353 MPa, t_f = 52.53 h). Note defined silica scale growth.

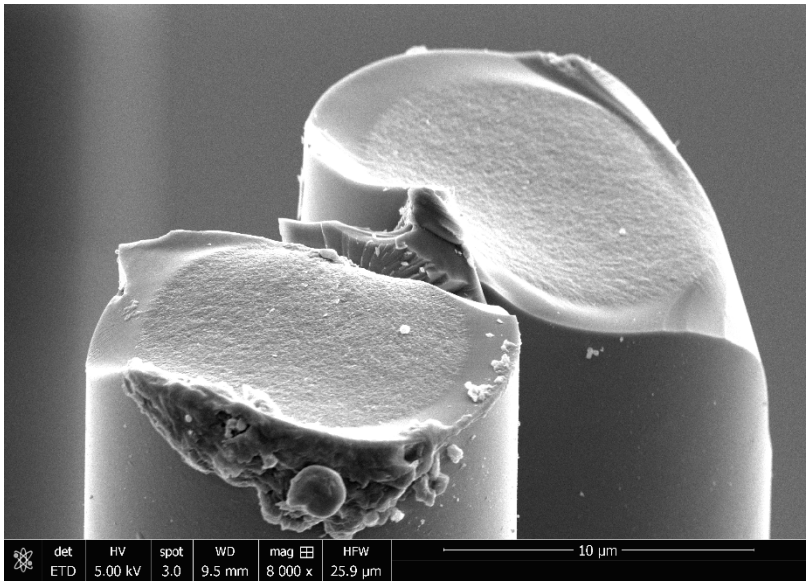


Figure 126 - SEM micrograph of the Hi-Nicalon™ S specimen "Steam 9" examining the fracture surface of a fiber (σ_{cr} = 353 MPa, t_f = 52.53 h). Note defined silica amorphous and crystallized scale growth.

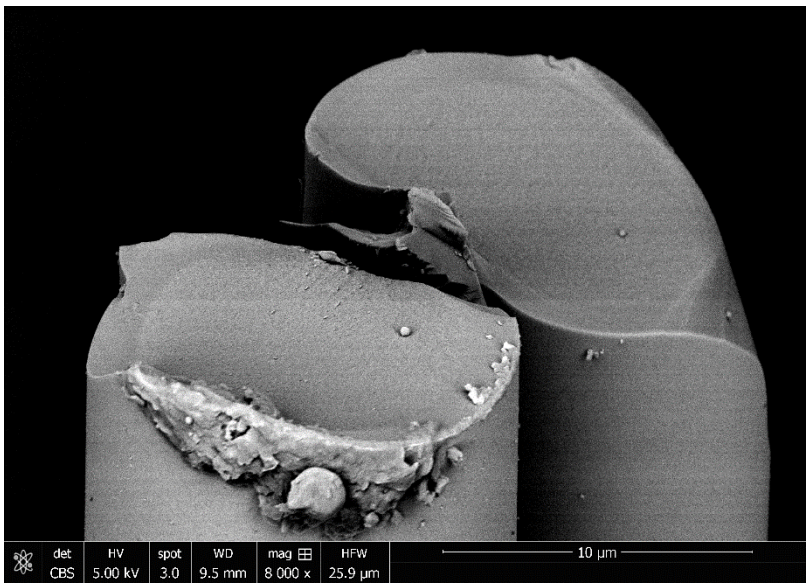


Figure 127 - SEM electron backscatter deflection micrograph of the Hi-Nicalon™ S specimen "Steam 9" examining the fracture surface of a fiber (σ_{cr} = 353 MPa, t_f = 52.53 h). Note defined silica amorphous and crystallized scale growth.

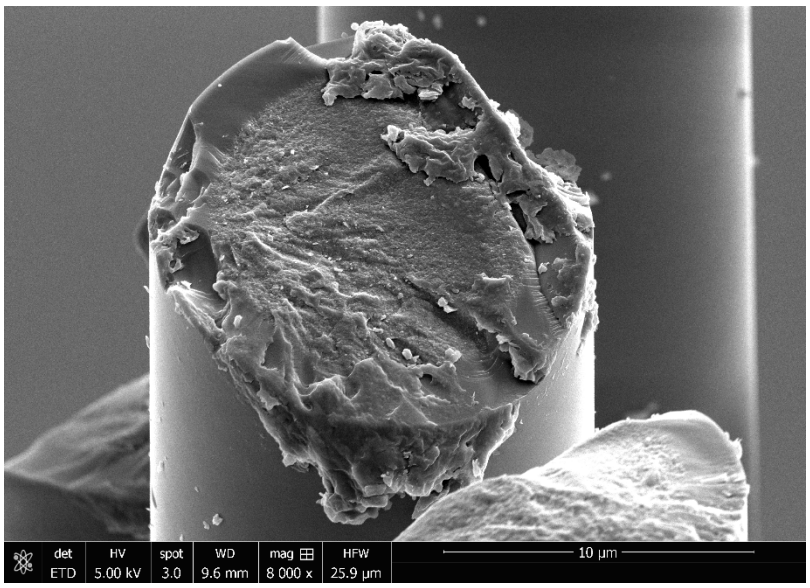


Figure 128 - SEM micrograph of the Hi-Nicalon™ S specimen "Steam 9" examining the fracture surface of a fiber (σ_{cr} = 353 MPa, t_f = 52.53 h). Note oxide scale growth across the fracture surface.

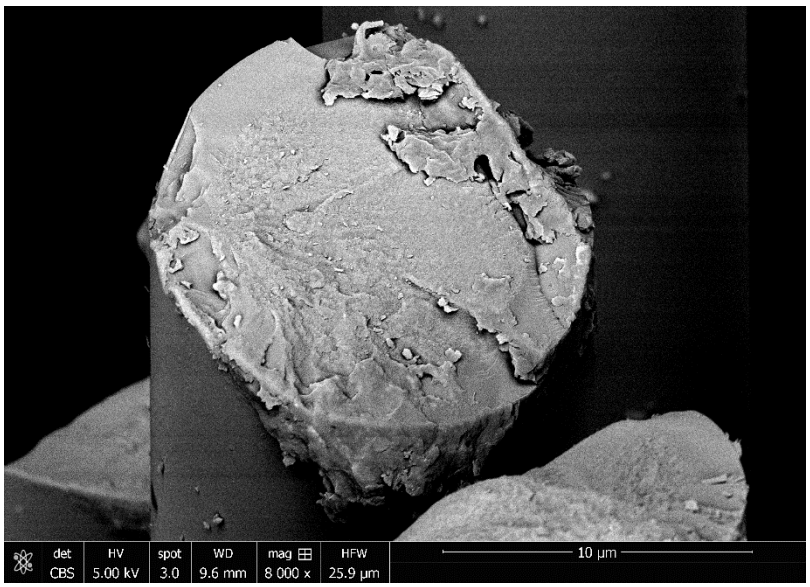


Figure 129 - SEM electron backscatter deflection micrograph of the Hi-Nicalon™ S specimen "Steam 9" examining the fracture surface of a fiber (σ_{cr} = 353 MPa, t_f = 52.53 h). Note oxide scale growth across the fracture surface.

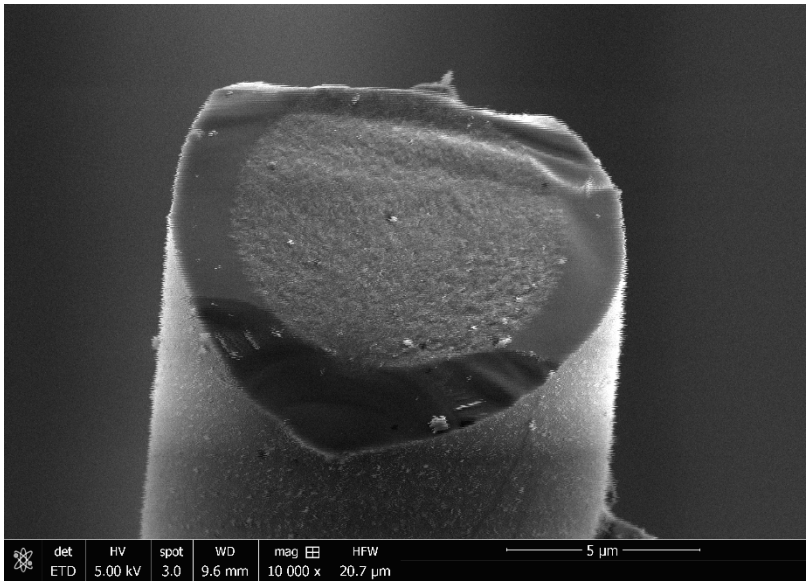


Figure 130 - SEM micrograph of the Hi-Nicalon™ S specimen "Steam 9" examining the fracture surface of a fiber (σ_{cr} = 353 MPa, t_f = 52.53 h). Note defined silica scale growth.

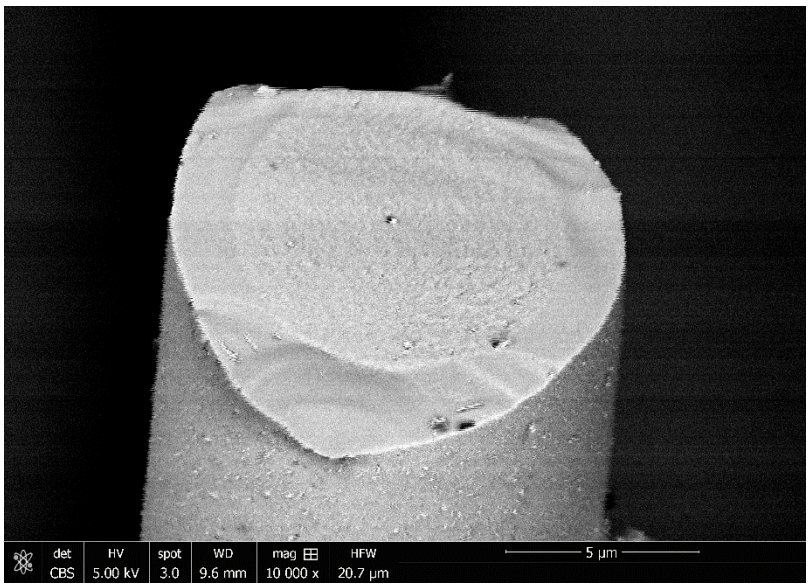


Figure 131 - SEM electron backscatter deflection micrograph of the Hi-Nicalon™ S specimen "Steam 9" examining the fracture surface of a fiber (σ_{cr} = 353 MPa, t_f = 52.53 h). Note defined silica scale growth.

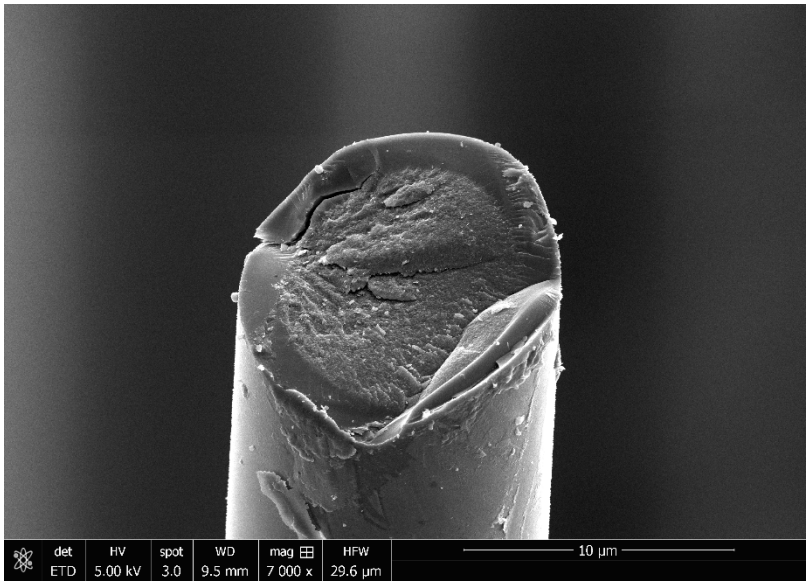


Figure 132 - SEM micrograph of the Hi-Nicalon™ S specimen "Steam 9" examining the fracture surface of a fiber (σ_{cr} = 353 MPa, t_f = 52.53 h). Note defined silica scale growth.

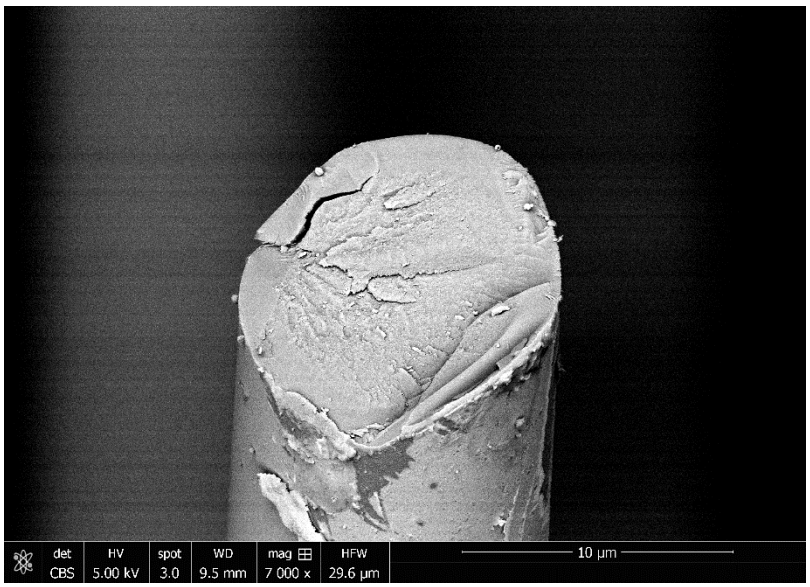


Figure 133 - SEM electron backscatter deflection micrograph of the Hi-Nicalon™ S specimen "Steam 9" examining the fracture surface of a fiber (σ_{cr} = 353 MPa, t_f = 52.53 h). Note defined silica scale growth.

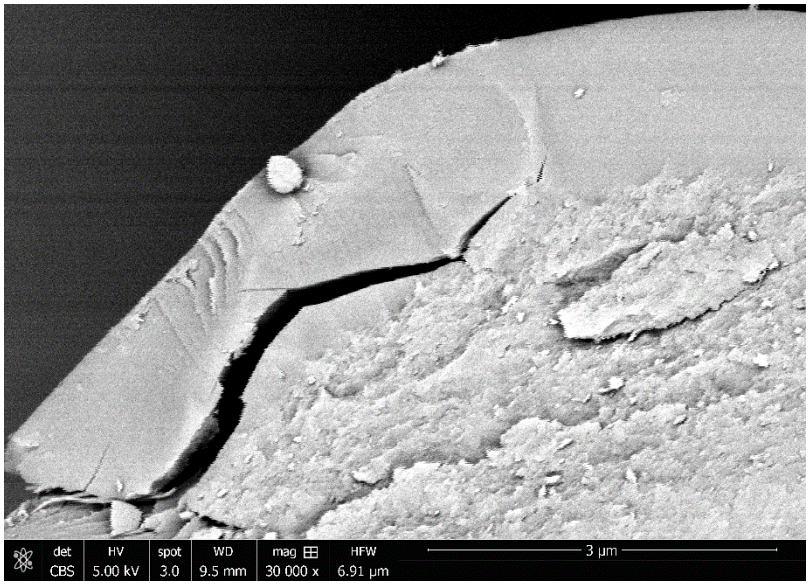


Figure 134 - SEM micrograph of the Hi-Nicalon™ S specimen "Steam 9" examining features on the fracture surface of a fiber (σ_{cr} = 353 MPa, t_f = 52.53 h). Note silica scale is chipping off the fiber.

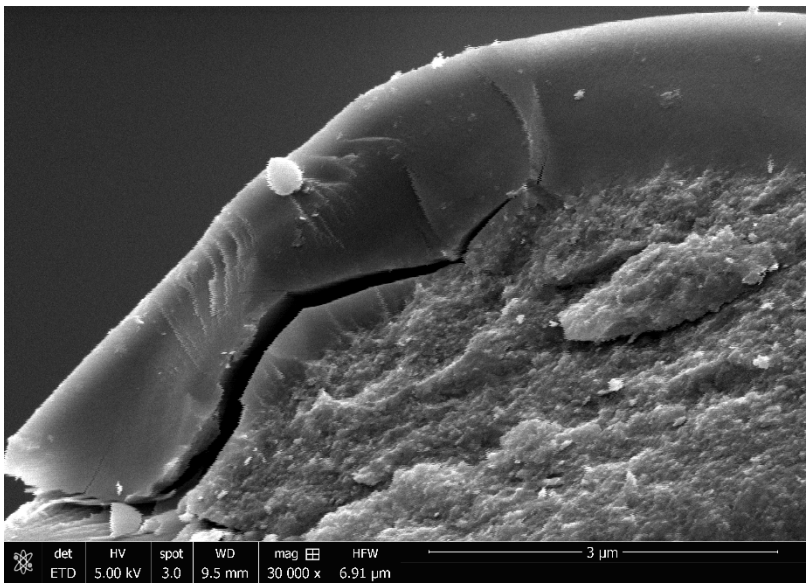


Figure 135 - SEM electron backscatter deflection micrograph of the Hi-Nicalon™ S specimen "Steam 9" examining features on the fracture surface of a fiber (σ_{cr} = 353 MPa, t_f = 52.53 h). Note silica scale is chipping off the fiber.

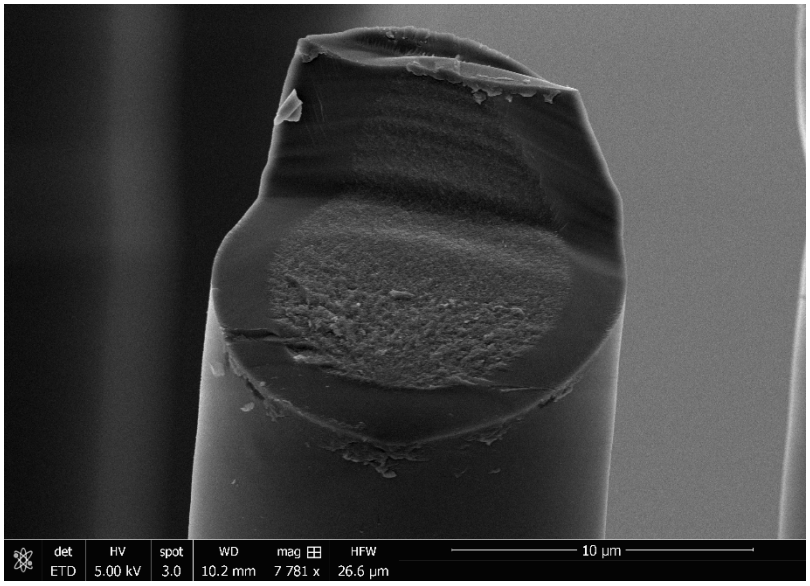


Figure 136 - SEM micrograph of the Hi-Nicalon™ S specimen "Steam 9" examining the fracture surface of a fiber (σ_{cr} = 353 MPa, t_f = 52.53 h). Note defined silica scale growth.

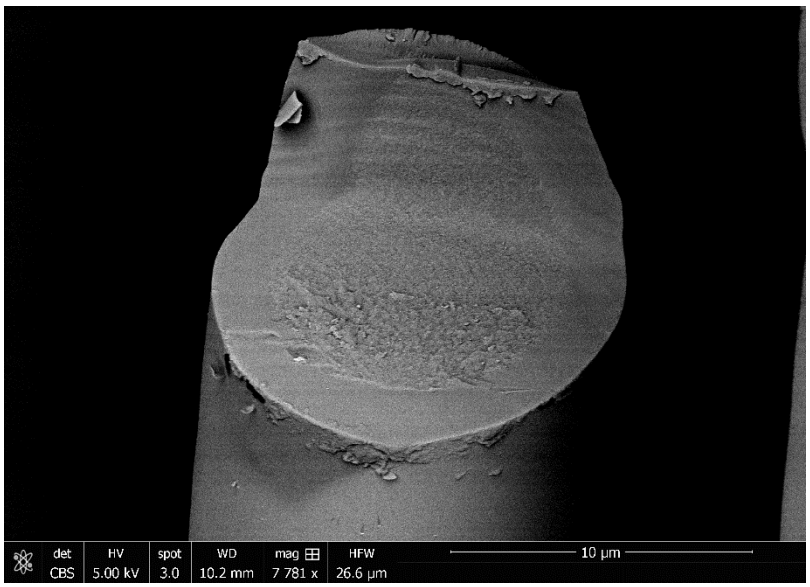


Figure 137 - SEM electron backscatter deflection micrograph of the Hi-Nicalon™ S specimen "Steam 9" examining the fracture surface of a fiber (σ_{cr} = 353 MPa, t_f = 52.53 h). Note defined silica scale growth.

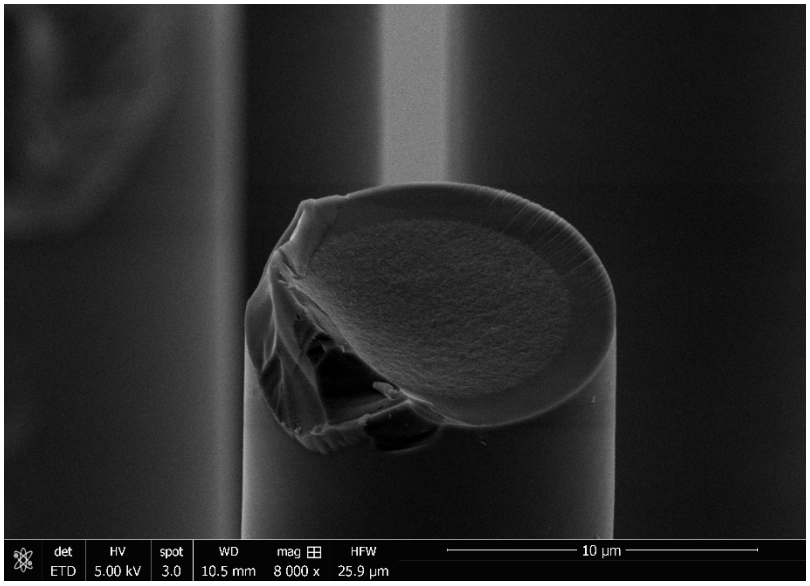


Figure 138 - SEM micrograph of the Hi-Nicalon™ S specimen "Steam 9" examining the fracture surface of a fiber (σ_{cr} = 353 MPa, t_f = 52.53 h). Note defined silica scale growth.

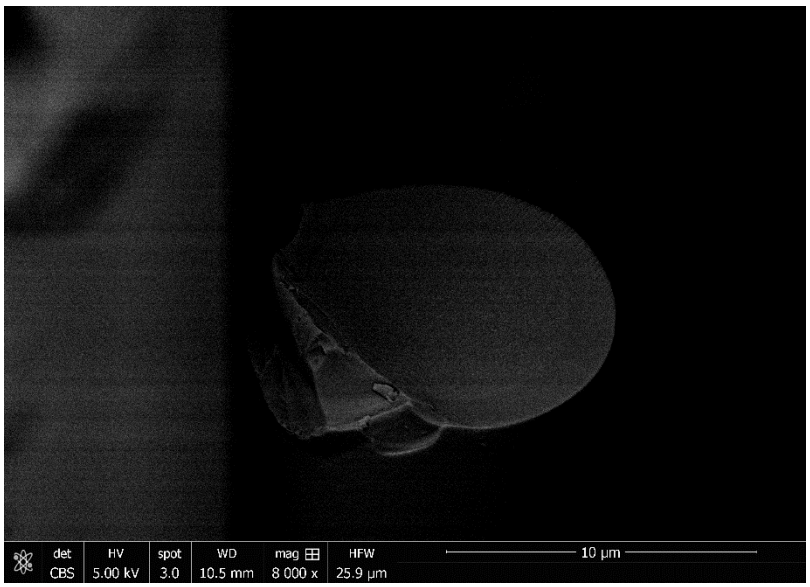


Figure 139 - SEM electron backscatter deflection micrograph of the Hi-Nicalon™ S specimen "Steam 9" examining the fracture surface of a fiber (σ_{cr} = 353 MPa, t_f = 52.53 h). Note defined silica scale growth.

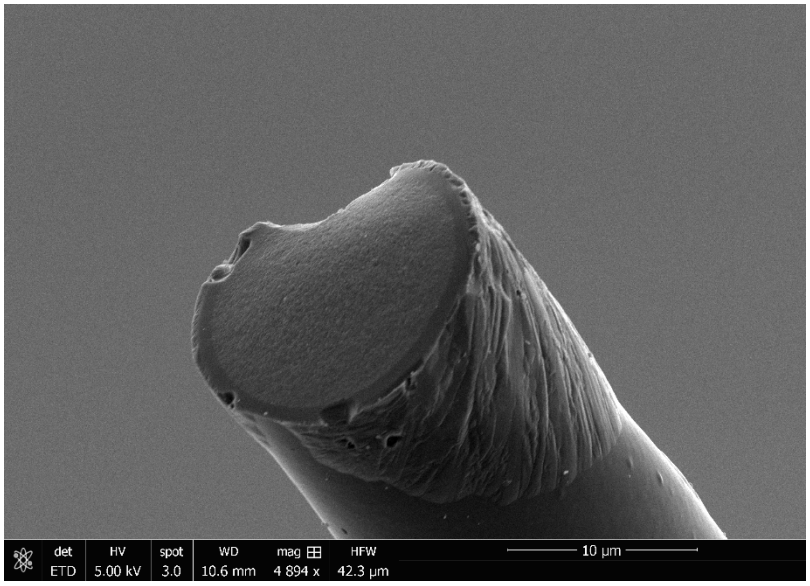


Figure 140 - SEM micrograph of the Hi-Nicalon™ S specimen "Steam 5" examining the fracture surface of a fiber (σ_{cr} = 400MPa, t_f = 30.83 h). Note defined silica amorphous and crystallized scale growth.

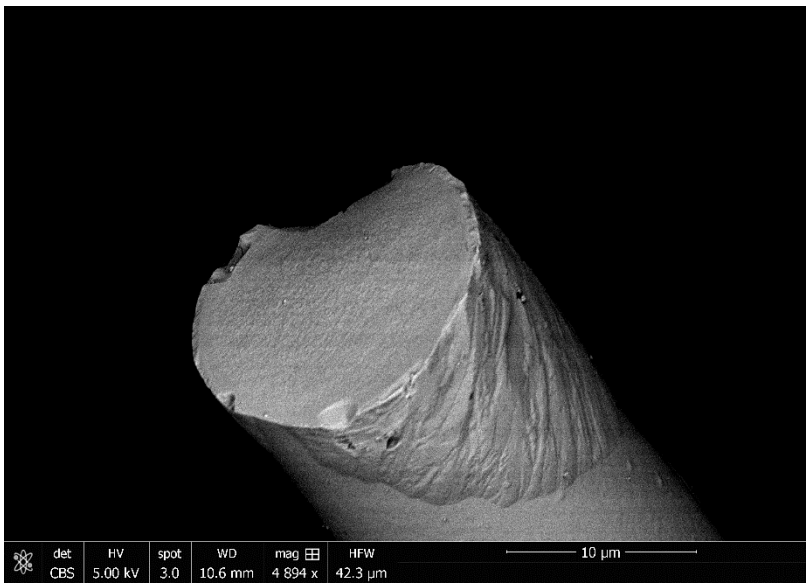


Figure 141 - SEM electron backscatter deflection micrograph of the Hi-Nicalon™ S specimen "Steam 5" examining the fracture surface of a fiber (σ_{cr} = 400 MPa, t_f = 30.83 h). Note defined silica amorphous and crystallized scale growth.

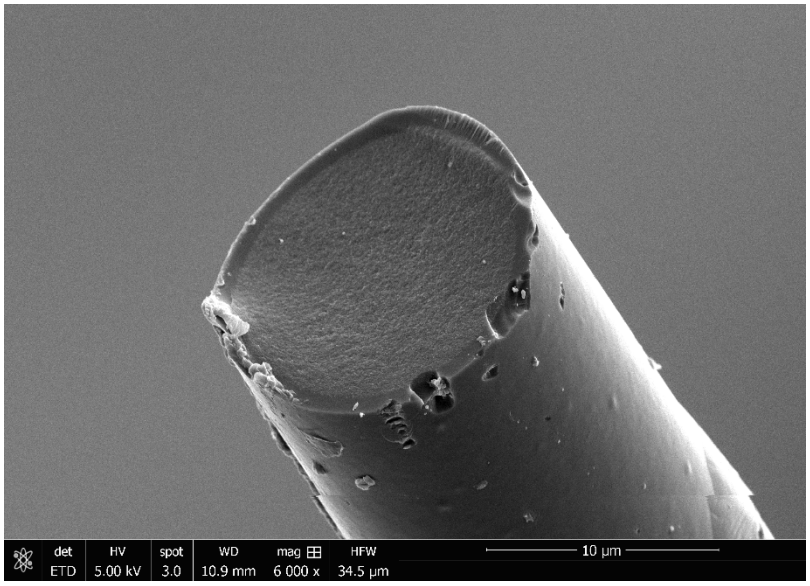


Figure 142 - SEM micrograph of the Hi-Nicalon™ S specimen "Steam 5" examining the fracture surface of a fiber (σ_{cr} = 400 MPa, t_f = 30.83 h). Note defined silica scale growth.

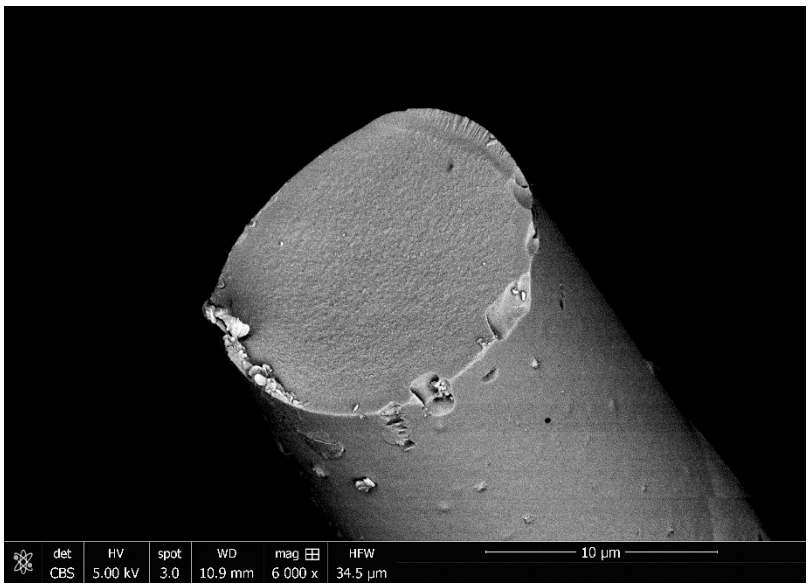


Figure 143 - SEM electron backscatter deflection micrograph of the Hi-Nicalon™ S specimen "Steam 5" examining the fracture surface of a fiber (σ_{cr} = 400 MPa, t_f = 30.83 h). Note defined silica scale growth.

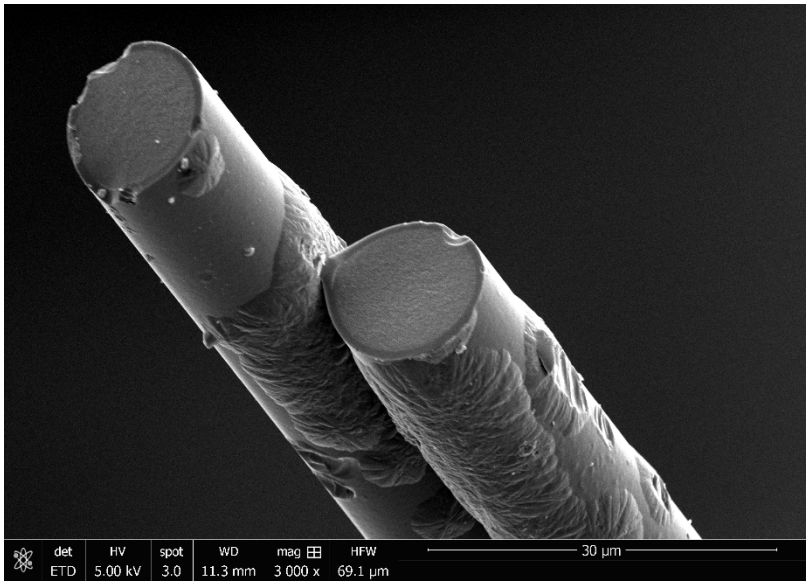


Figure 144 - SEM micrograph of the Hi-Nicalon™ S specimen "Steam 5" examining the fracture surface of a fiber (σ_{cr} = 400 MPa, t_f = 30.83 h). Note defined silica amorphous and crystallized scale growth.

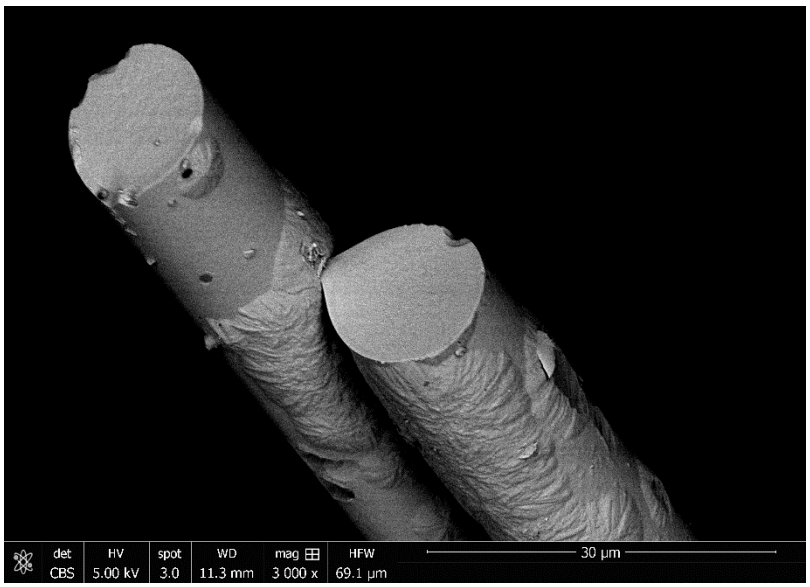


Figure 145 - SEM electron backscatter deflection micrograph of the Hi-Nicalon™ S specimen "Steam 5" examining the fracture surface of a fiber (σ_{cr} = 400 MPa, t_f = 30.83 h). Note defined silica amorphous and crystallized scale growth.

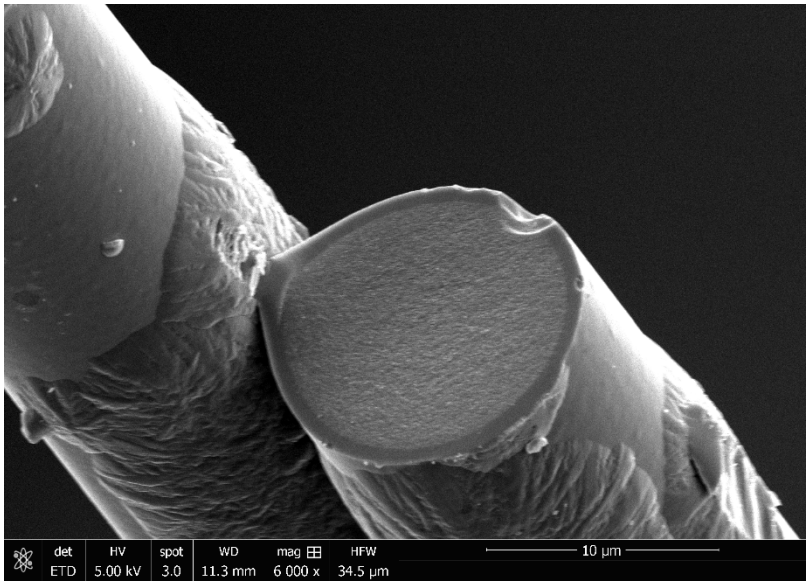


Figure 146 - SEM micrograph of the Hi-Nicalon™ S specimen "Steam 5" examining the fracture surface of a fiber (σ_{cr} = 400 MPa, t_f = 30.83 h). Note defined silica amorphous and crystallized scale growth.

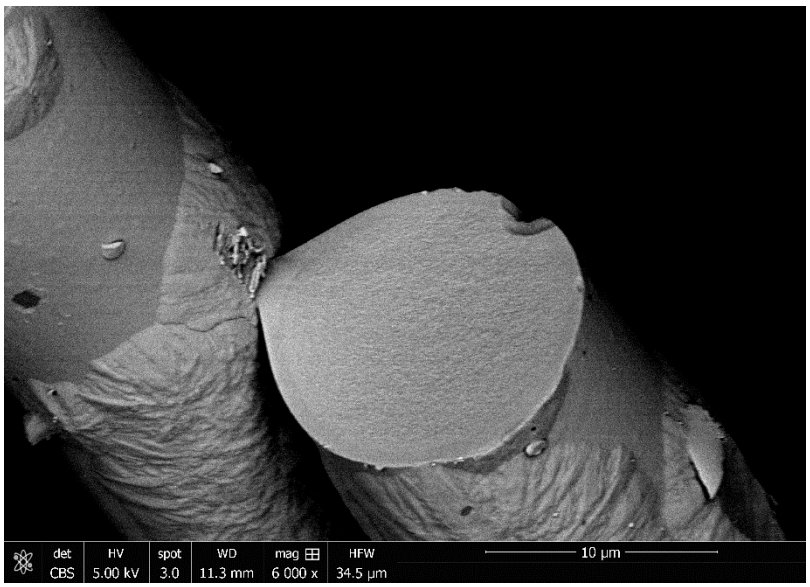


Figure 147 - SEM electron backscatter deflection micrograph of the Hi-Nicalon™ S specimen "Steam 5" examining the fracture surface of a fiber (σ_{cr} = 400 MPa, t_f = 30.83 h). Note defined silica amorphous and crystallized scale growth.

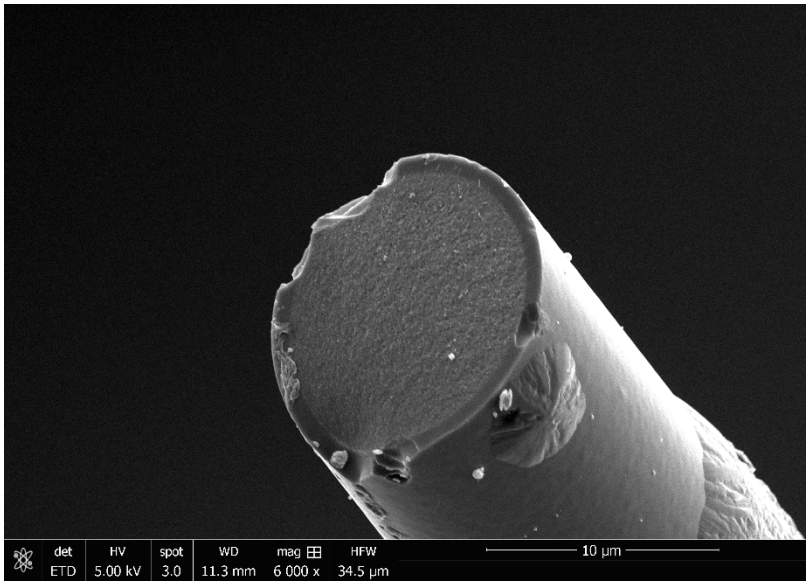


Figure 148 - SEM micrograph of the Hi-Nicalon™ S specimen "Steam 5" examining the fracture surface of a fiber (σ_{cr} = 400 MPa, t_f = 30.83 h). Note defined silica amorphous and crystallized scale growth.

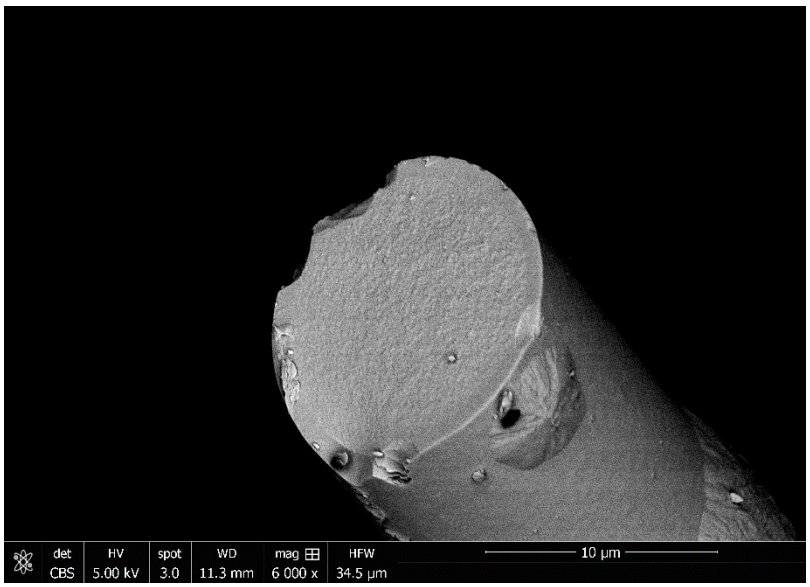


Figure 149 - SEM electron backscatter deflection micrograph of the Hi-Nicalon™ S specimen "Steam 5" examining the fracture surface of a fiber (σ_{cr} = 400 MPa, t_f = 30.83 h). Note defined silica amorphous and crystallized scale growth.

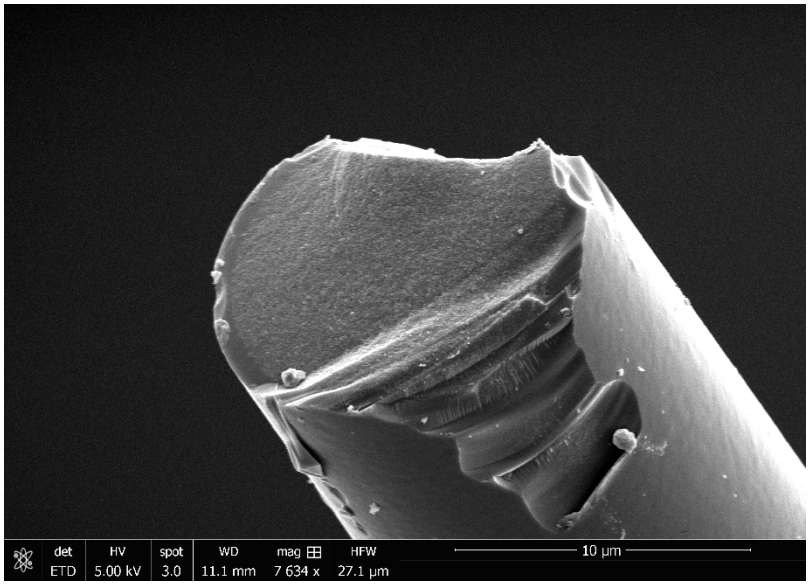


Figure 150 - SEM micrograph of the Hi-Nicalon™ S specimen "Steam 5" examining the fracture surface of a fiber (σ_{cr} = 400 MPa, t_f = 30.83 h). Note defined silica scale growth.

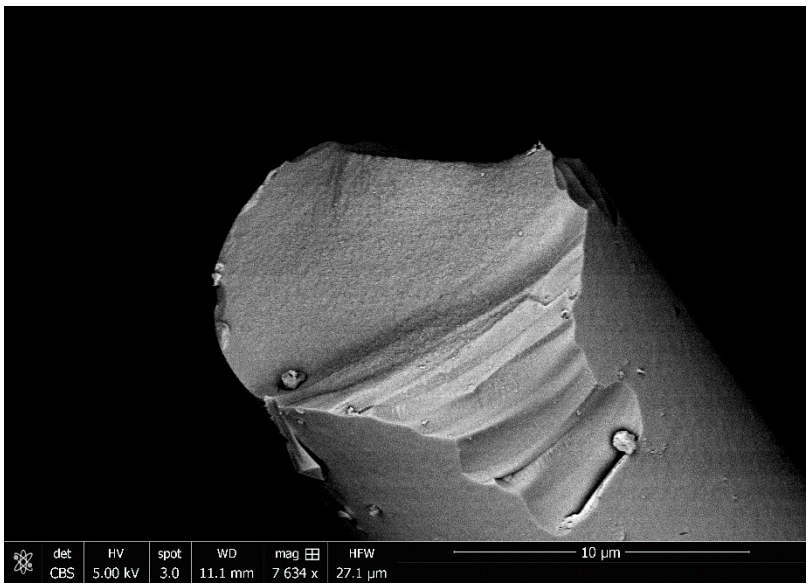


Figure 151 - SEM electron backscatter deflection micrograph of the Hi-Nicalon™ S specimen "Steam 5" examining the fracture surface of a fiber (σ_{cr} = 400 MPa, t_f = 30.83 h). Note defined silica scale growth.

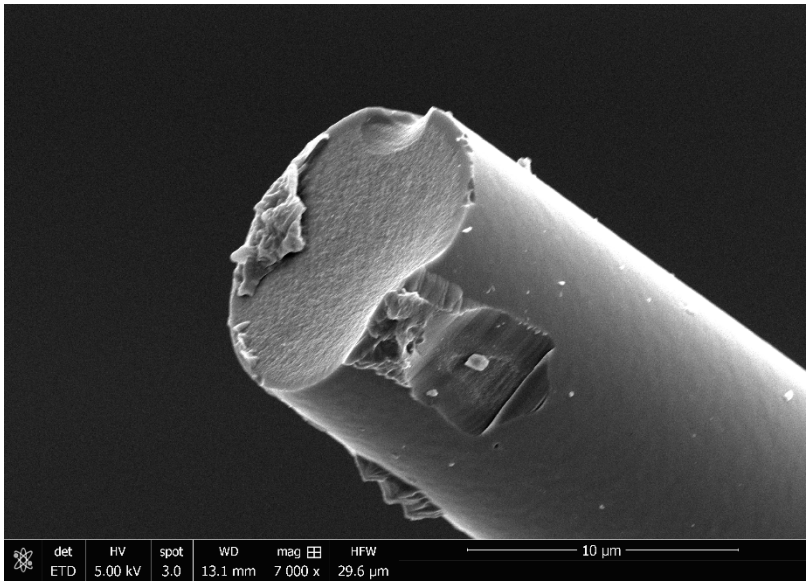


Figure 152 - SEM micrograph of the Hi-Nicalon™ S specimen "Steam 5" examining the fracture surface of a fiber (σ_{cr} = 400 MPa, t_f = 30.83 h). Note defined silica scale growth.

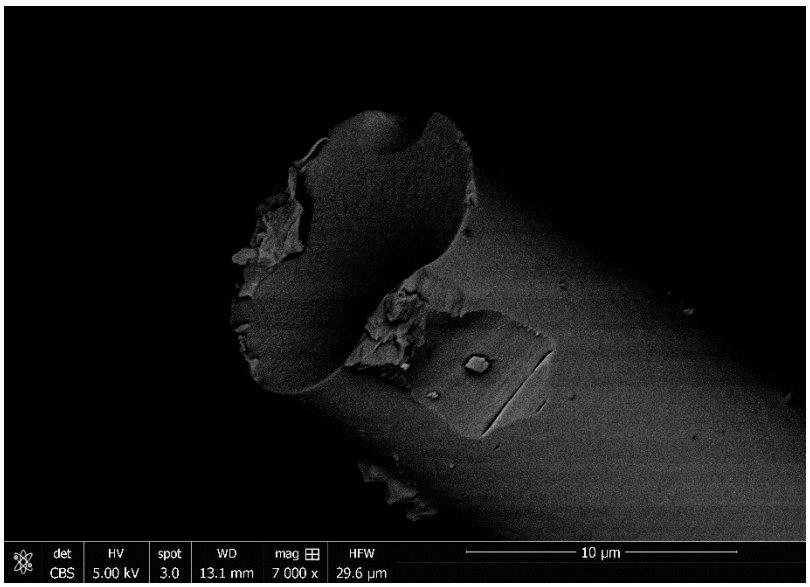


Figure 153 - SEM electron backscatter deflection micrograph of the Hi-Nicalon™ S specimen "Steam 5" examining the fracture surface of a fiber (σ_{cr} = 400 MPa, t_f = 30.83 h). Note defined silica scale growth.

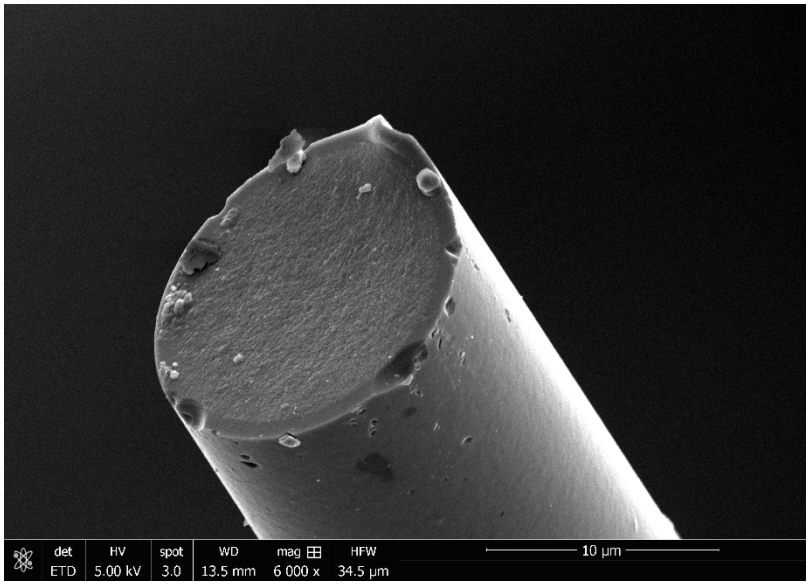


Figure 154 - SEM micrograph of the Hi-Nicalon™ S specimen "Steam 5" examining the fracture surface of a fiber (σ_{cr} = 400 MPa, t_f = 30.83 h). Note defined silica scale growth.

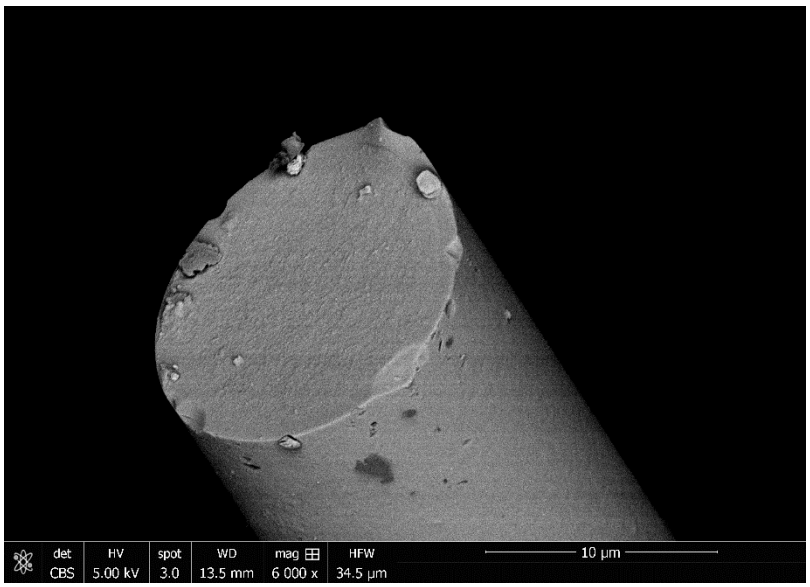


Figure 155 - SEM electron backscatter deflection micrograph of the Hi-Nicalon™ S specimen "Steam 5" examining the fracture surface of a fiber (σ_{cr} = 400 MPa, t_f = 30.83 h). Note defined silica scale growth.

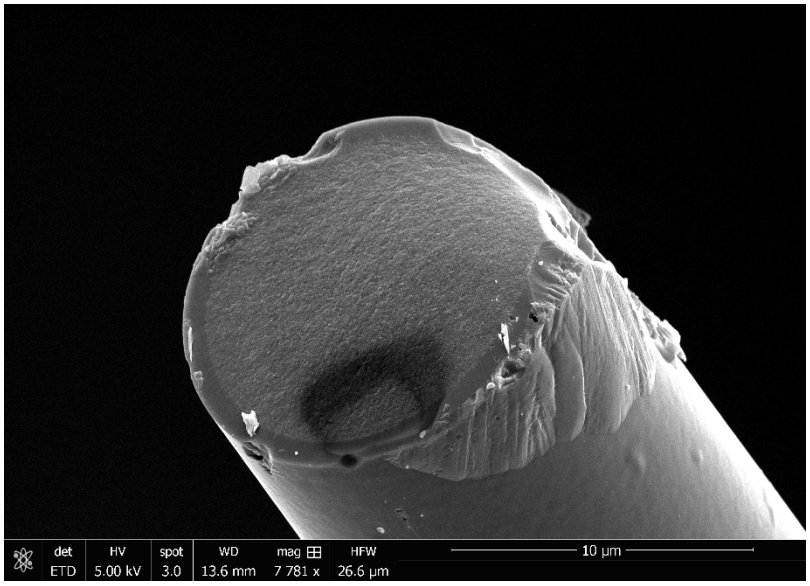


Figure 156 - SEM micrograph of the Hi-Nicalon™ S specimen "Steam 5" examining the fracture surface of a fiber (σ_{cr} = 400 MPa, t_f = 30.83 h). Note defined silica amorphous and crystallized scale growth.

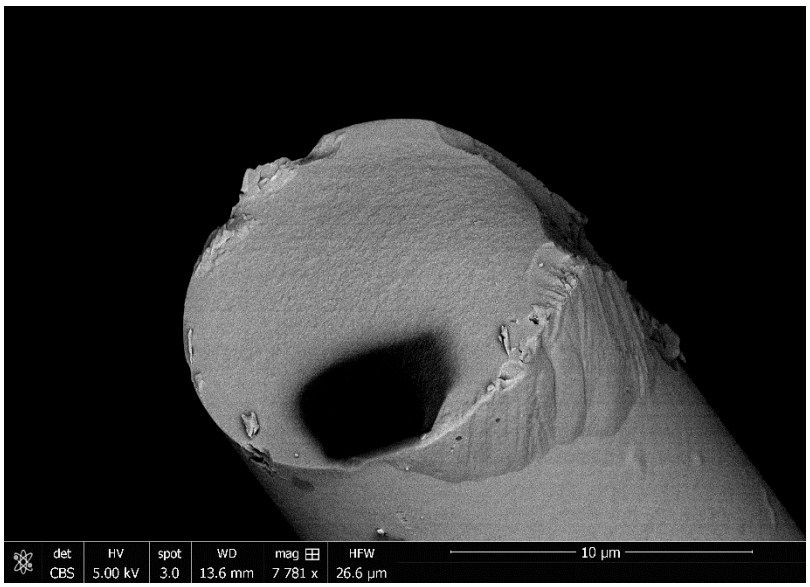


Figure 157 - SEM electron backscatter deflection micrograph of the Hi-Nicalon™ S specimen "Steam 5" examining the fracture surface of a fiber (σ_{cr} = 400 MPa, t_f = 30.83 h). Note defined silica amorphous and crystallized scale growth.

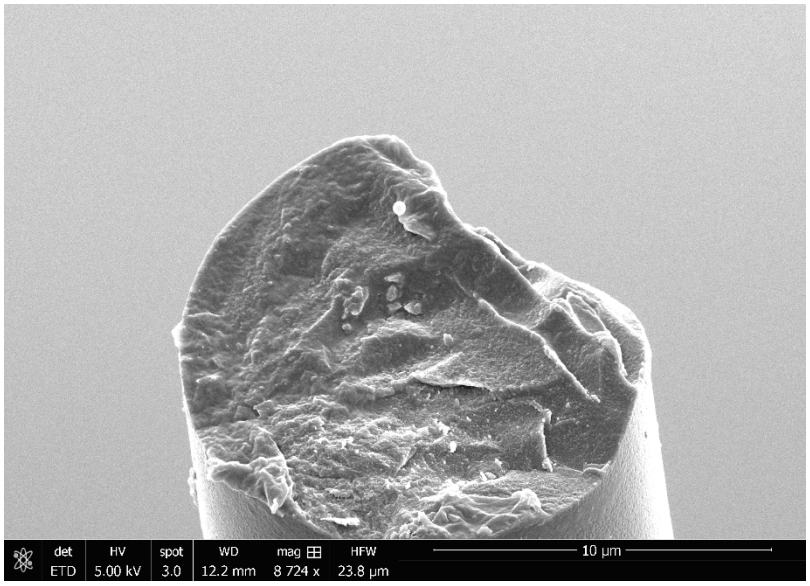


Figure 158 - SEM micrograph of the Hi-Nicalon™ S specimen "Steam 10" examining features on the fracture surface of a fiber (σ_{cr} = 450 MPa, t_f = 0.96 h).



Figure 159 - SEM electron backscatter deflection micrograph of the Hi-Nicalon™ S specimen "Steam 10" examining features on the fracture surface of a fiber (σ_{cr} = 450 MPa, t_f = 0.96 h).

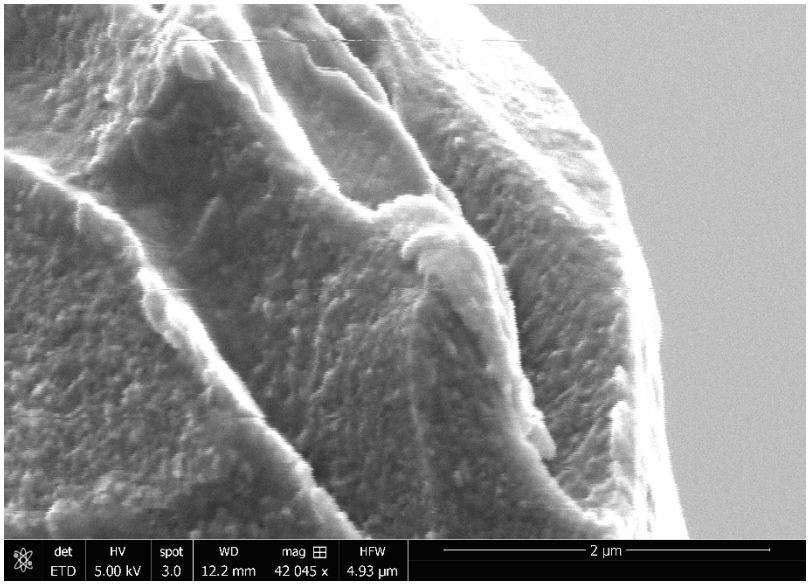


Figure 160 - SEM micrograph of the Hi-Nicalon™ S specimen "Steam 10" examining features on the fracture surface of a fiber (σ_{cr} = 450 MPa, t_f = 0.96 h).

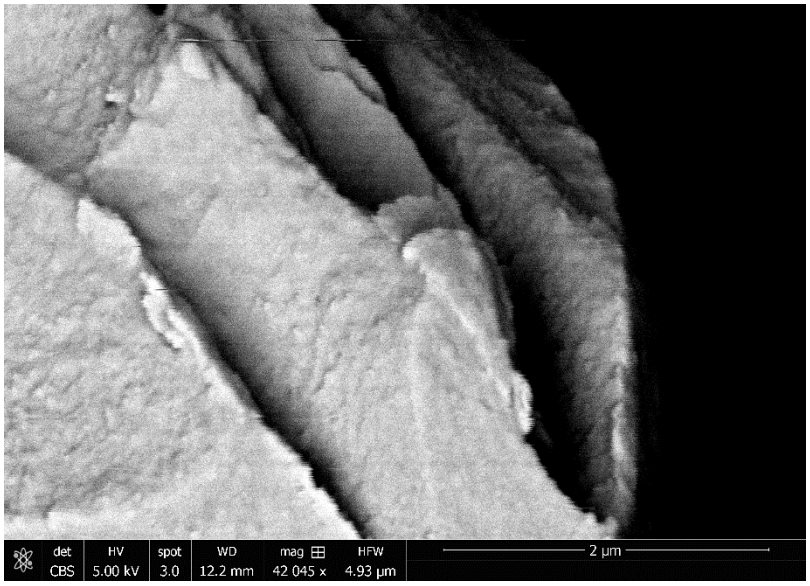


Figure 161 - SEM electron backscatter deflection micrograph of the Hi-Nicalon™ S specimen "Steam 10" examining features on the fracture surface of a fiber (σ_{cr} = 450 MPa, t_f = 0.96 h).

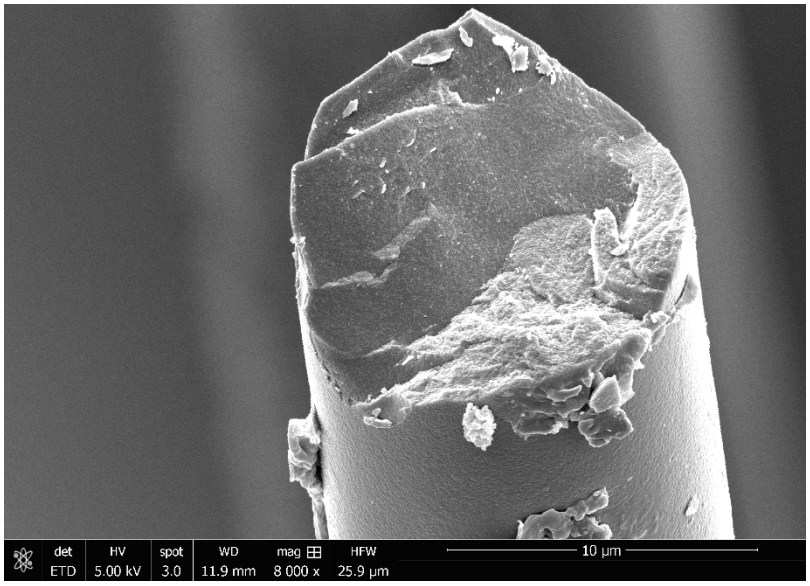


Figure 162 - SEM micrograph of the Hi-Nicalon™ S specimen "Steam 10" examining the fracture surface of a fiber (σ_{cr} = 450 MPa, t_f = 0.96 h).

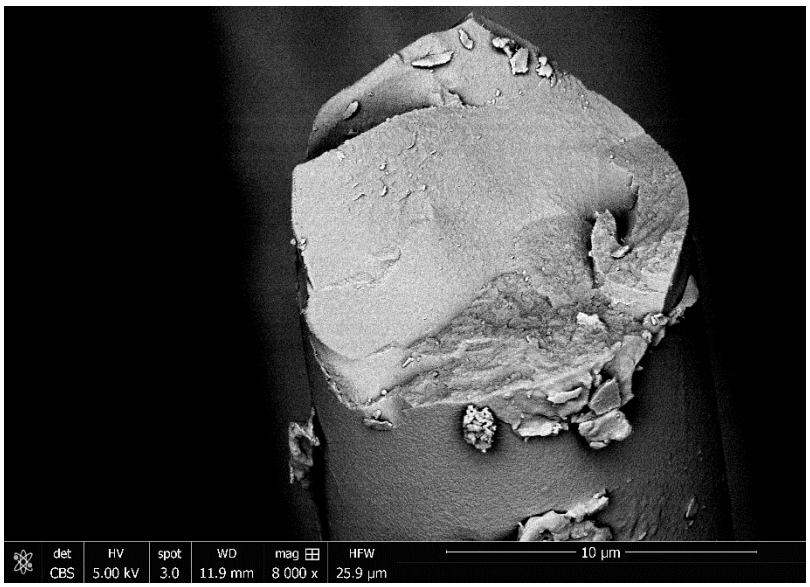


Figure 163 - SEM electron backscatter deflection micrograph of the Hi-Nicalon™ S specimen "Steam 10" examining the fracture surface of a fiber (σ_{cr} = 450 MPa, t_f = 0.96 h).

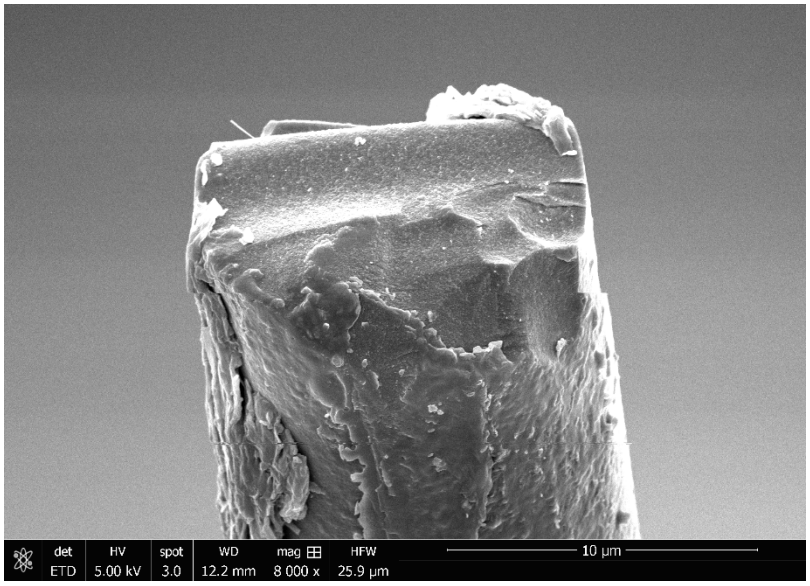


Figure 164 - SEM micrograph of the Hi-Nicalon™ S specimen "Steam 10" examining the fracture surface of a fiber (σ_{cr} = 450 MPa, t_f = 0.96 h).

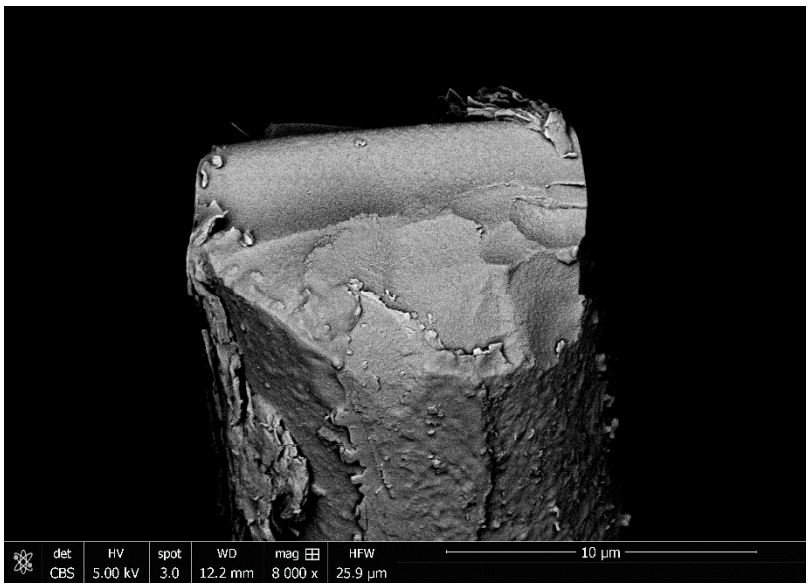


Figure 165 - SEM electron backscatter deflection micrograph of the Hi-Nicalon™ S specimen "Steam 10" examining the fracture surface of a fiber (σ_{cr} = 450 MPa, t_f = 0.96 h).

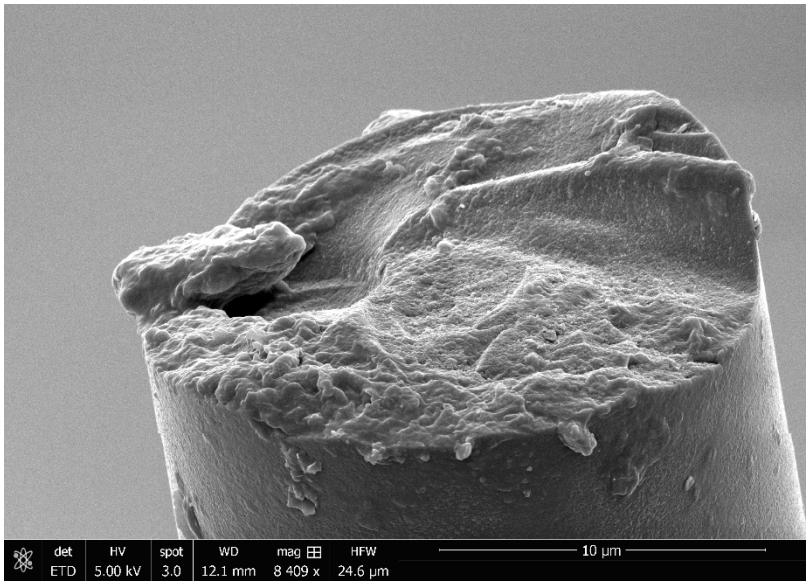


Figure 166 - SEM micrograph of the Hi-Nicalon™ S specimen "Steam 10" examining the fracture surface of a fiber (σ_{cr} = 450 MPa, t_f = 0.96 h).

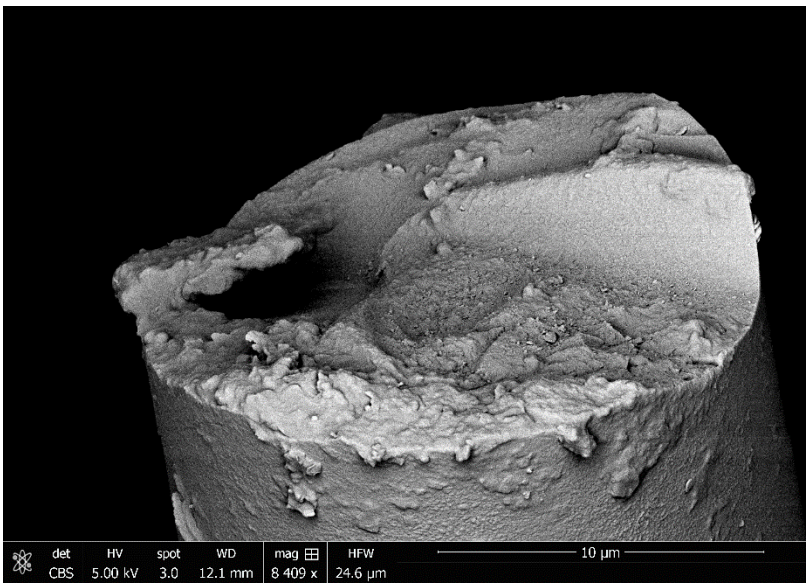


Figure 167 - SEM electron backscatter deflection micrograph of the Hi-Nicalon™ S specimen "Steam 10" examining the fracture surface of a fiber (σ_{cr} = 450 MPa, t_f = 0.96 h).

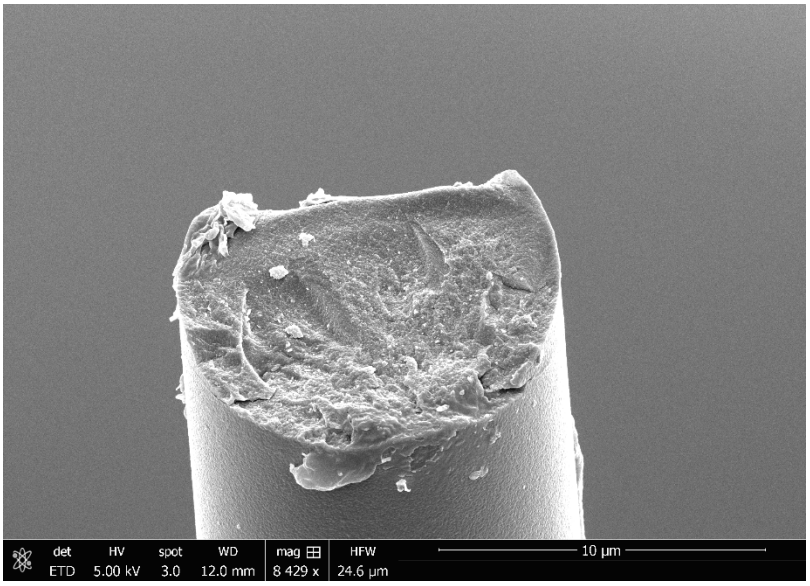


Figure 168 - SEM micrograph of the Hi-Nicalon™ S specimen "Steam 10" examining the fracture surface of a fiber (σ_{cr} = 450 MPa, t_f = 0.96 h).

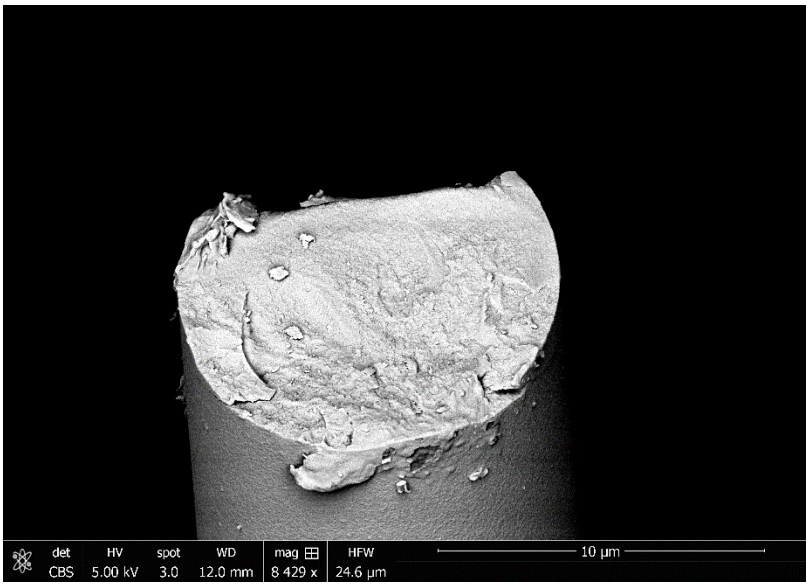


Figure 169 - SEM electron backscatter deflection micrograph of the Hi-Nicalon™ S specimen "Steam 10" examining the fracture surface of a fiber (σ_{cr} = 450 MPa, t_f = 0.96 h).

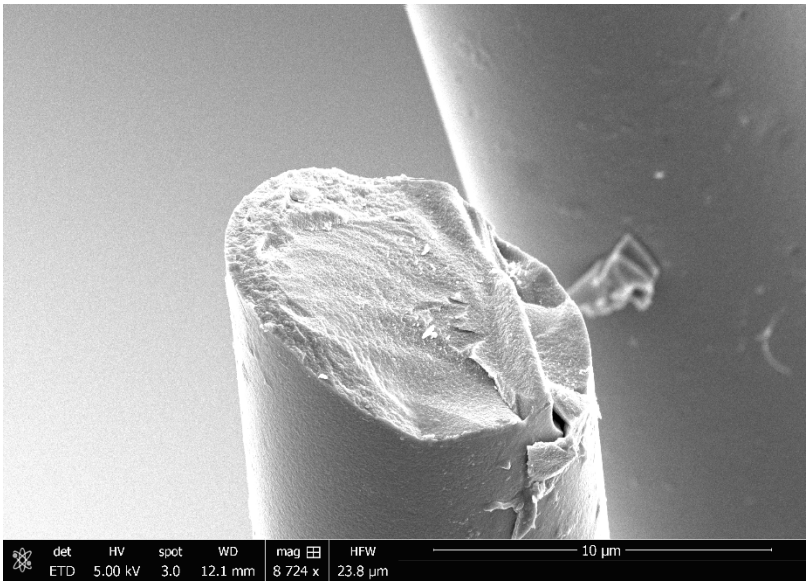


Figure 170 - SEM micrograph of the Hi-Nicalon™ S specimen "Steam 10" examining the fracture surface of a fiber (σ_{cr} = 450 MPa, t_f = 0.96 h).

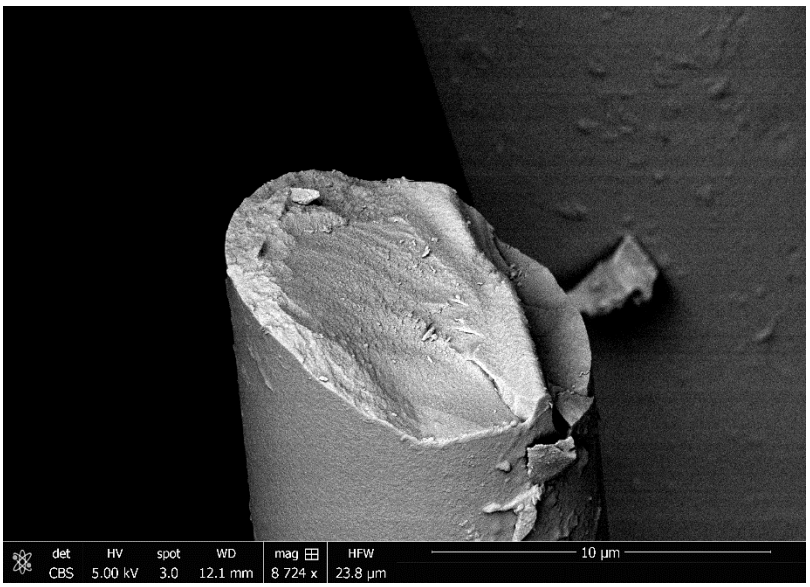


Figure 171 - SEM electron backscatter deflection micrograph of the Hi-Nicalon™ S specimen "Steam 10" examining the fracture surface of a fiber (σ_{cr} = 450 MPa, t_f = 0.96 h).

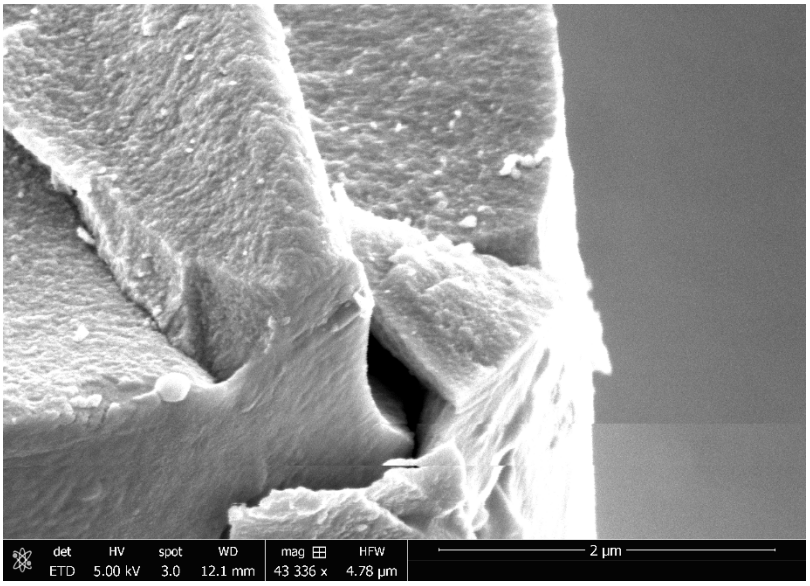


Figure 172 - SEM micrograph of the Hi-Nicalon™ S specimen "Steam 10" examining features on the fracture surface of a fiber (σ_{cr} = 450 MPa, t_f = 0.96 h).

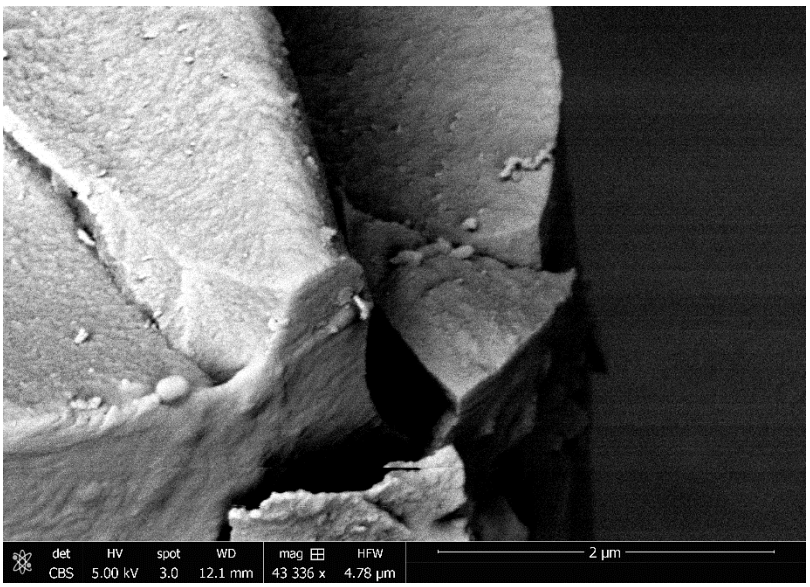


Figure 173 - SEM electron backscatter deflection micrograph of the Hi-Nicalon™ S specimen "Steam 10" examining features on the fracture surface of a fiber (σ_{cr} = 450 MPa, t_f = 0.96 h).

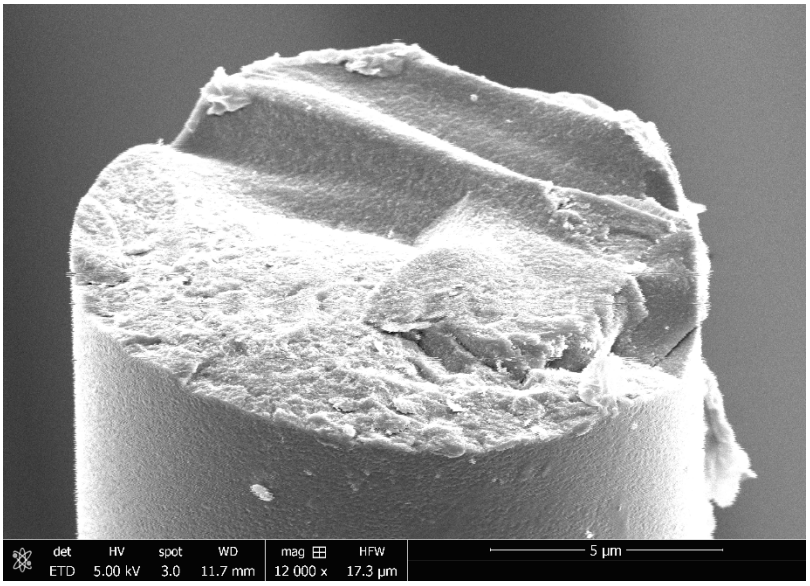


Figure 174 - SEM micrograph of the Hi-Nicalon™ S specimen "Steam 10" examining the fracture surface of a fiber (σ_{cr} = 450 MPa, t_f = 0.96 h).

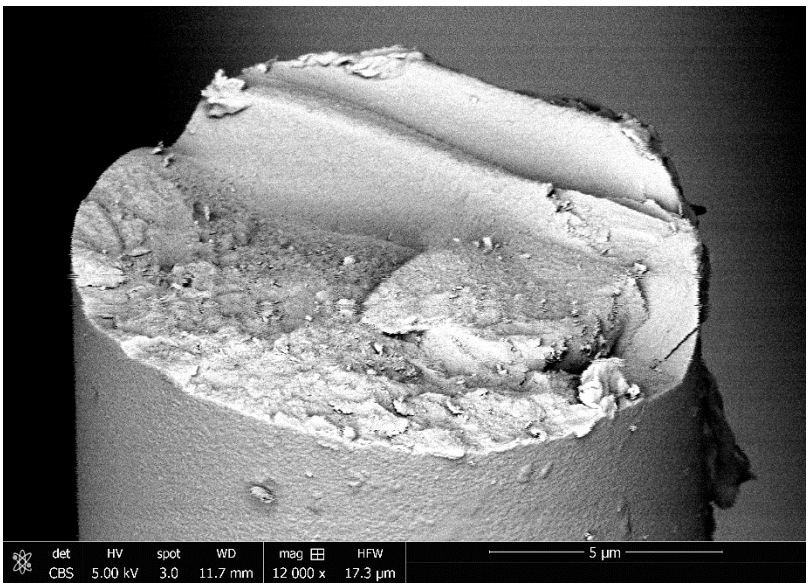


Figure 175 - SEM electron backscatter deflection micrograph of the Hi-Nicalon™ S specimen "Steam 10" examining the fracture surface of a fiber (σ_{cr} = 450 MPa, t_f = 0.96 h).

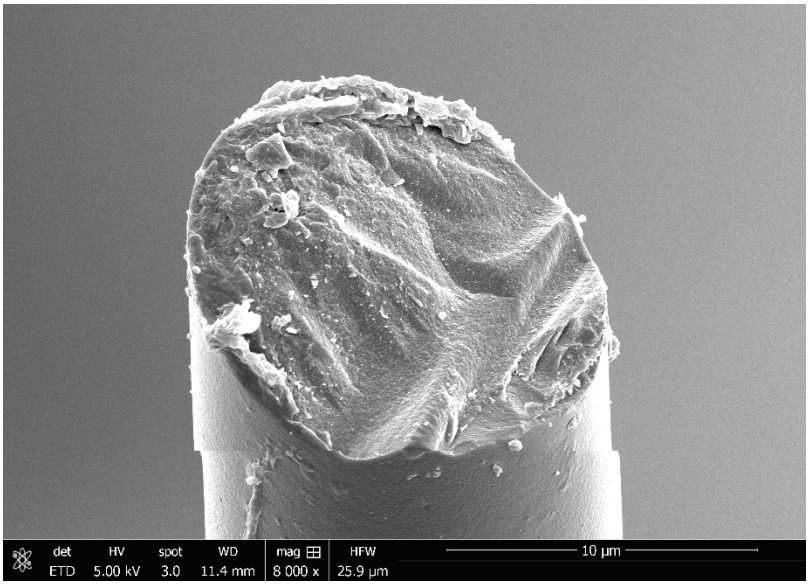


Figure 176 - SEM micrograph of the Hi-Nicalon™ S specimen "Steam 10" examining the fracture surface of a fiber (σ_{cr} = 450 MPa, t_f = 0.96 h).

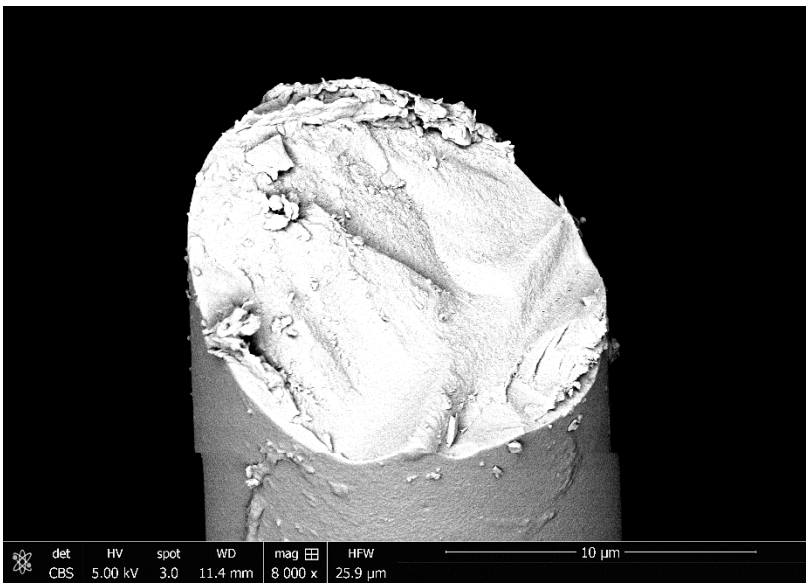


Figure 177 - SEM electron backscatter deflection micrograph of the Hi-Nicalon™ S specimen "Steam 10" examining the fracture surface of a fiber (σ_{cr} = 450 MPa, t_f = 0.96 h).

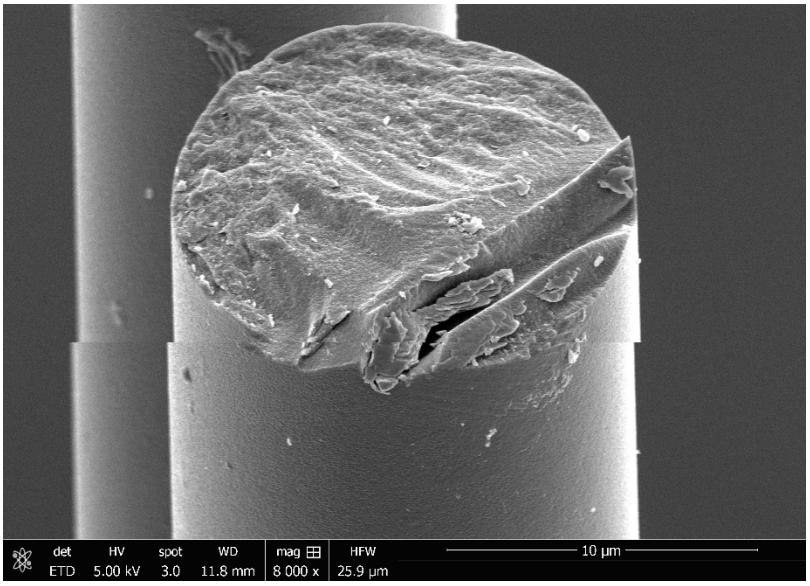


Figure 178 - SEM micrograph of the Hi-Nicalon™ S specimen "Steam 10" examining the fracture surface of a fiber (σ_{cr} = 450 MPa, t_f = 0.96 h).

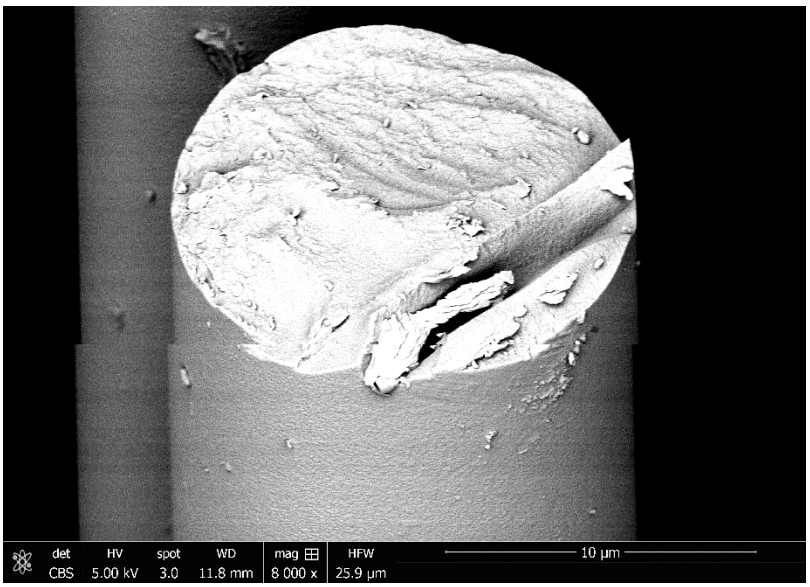


Figure 179 - SEM electron backscatter deflection micrograph of the Hi-Nicalon™ S specimen "Steam 10" examining the fracture surface of a fiber (σ_{cr} = 450 MPa, t_f = 0.96 h).

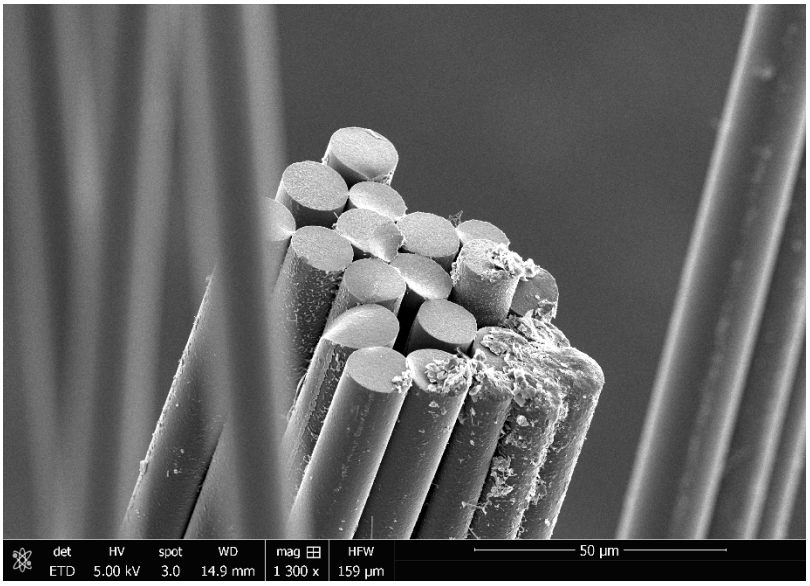


Figure 180 - SEM micrograph of the Hi-Nicalon™ S specimen "Steam 10" examining the fracture surface of a fiber (σ_{cr} = 450 MPa, t_f = 0.96 h). Note signs of saturated steam exposure (silica deposition).

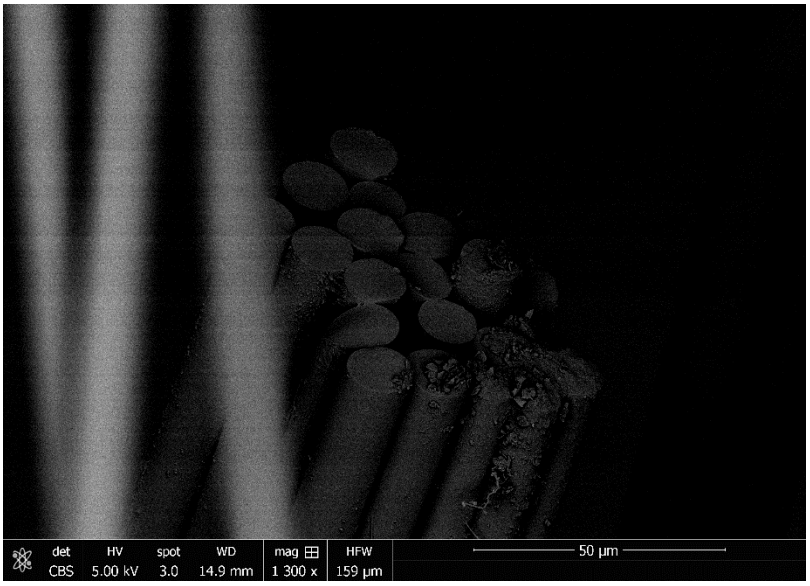


Figure 181 - SEM electron backscatter deflection micrograph of the Hi-Nicalon™ S specimen "Steam 10" examining the fracture surface of a fiber (σ_{cr} = 450 MPa, t_f = 0.96 h).

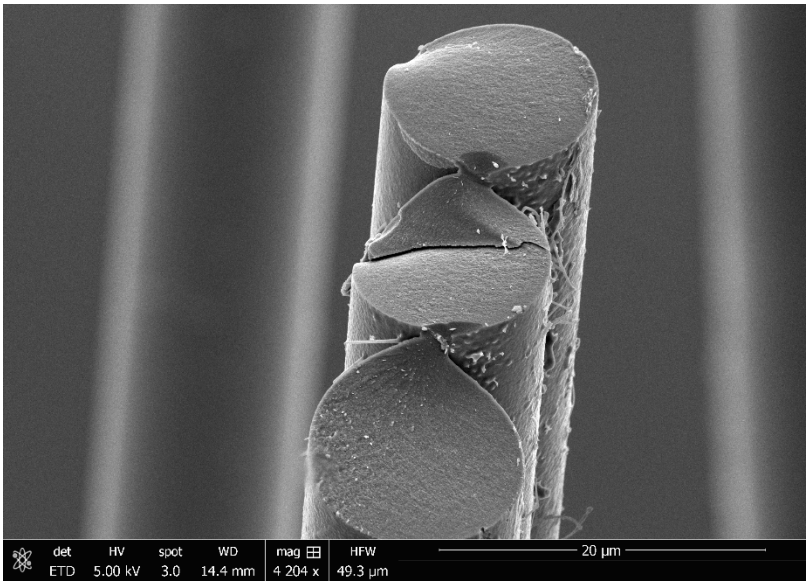


Figure 182 - SEM micrograph of the Hi-Nicalon™ S specimen "Steam 10" examining the fracture surface of a fiber (σ_{cr} = 450 MPa, t_f = 0.96 h). Note signs of saturated steam exposure (silica deposition).

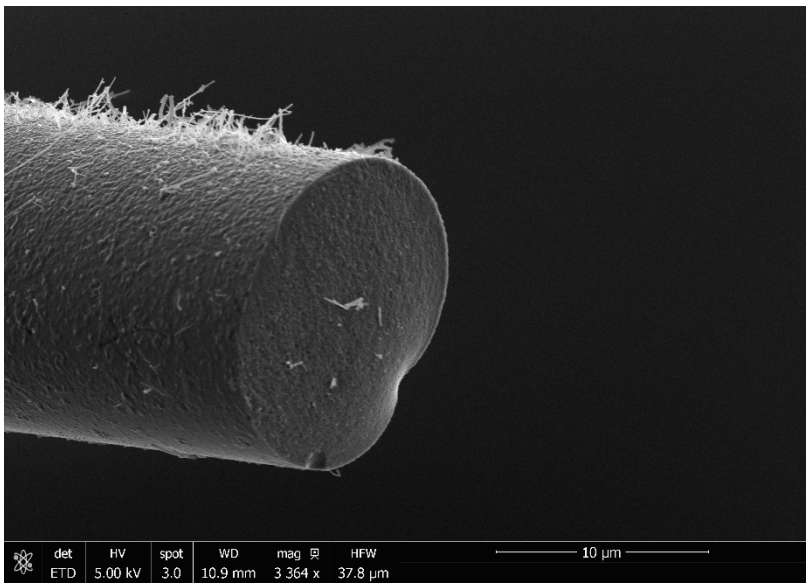


Figure 183 - SEM micrograph of the Hi-Nicalon™ S specimen "Steam 6" examining the fracture surface of a fiber (σ_{cr} = 500 MPa, t_f = 0.02 h). Note signs of saturated steam exposure (silica deposition).

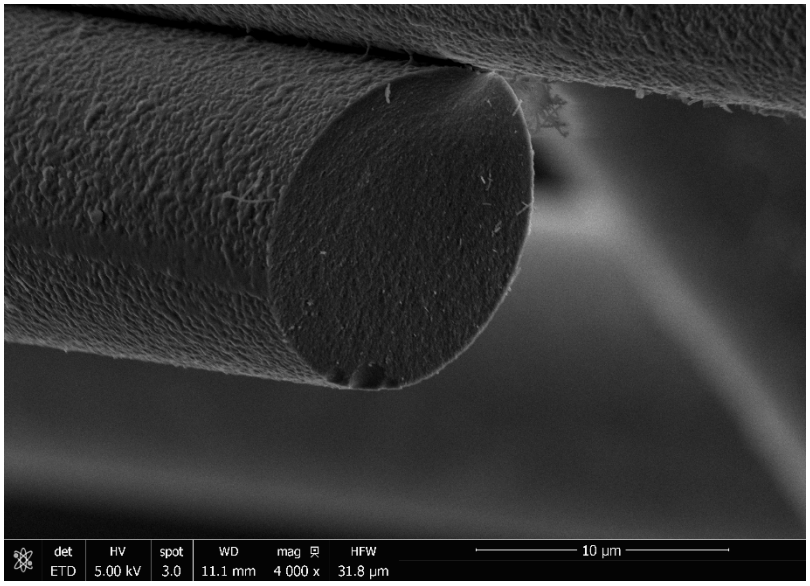


Figure 184 - SEM micrograph of the Hi-Nicalon™ S specimen "Steam 6" examining the fracture surface of a fiber (σ_{cr} = 500 MPa, t_f = 0.02 h). Note signs of saturated steam exposure (silica deposition) and signs of fiber-fiber contact.

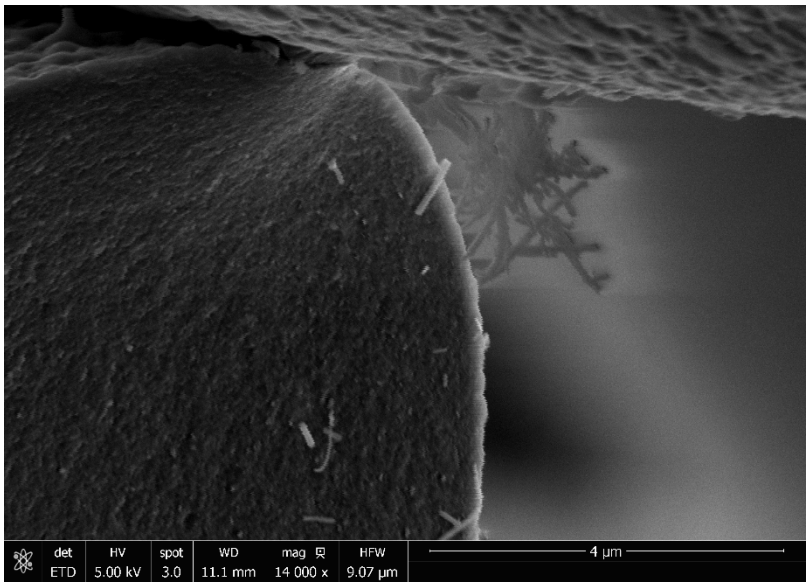


Figure 185 - SEM micrograph of the Hi-Nicalon™ S specimen "Steam 6" examining features on the fracture surface of a fiber (σ_{cr} = 500 MPa, t_f = 0.02 h). Note signs of saturated steam exposure (silica deposition).

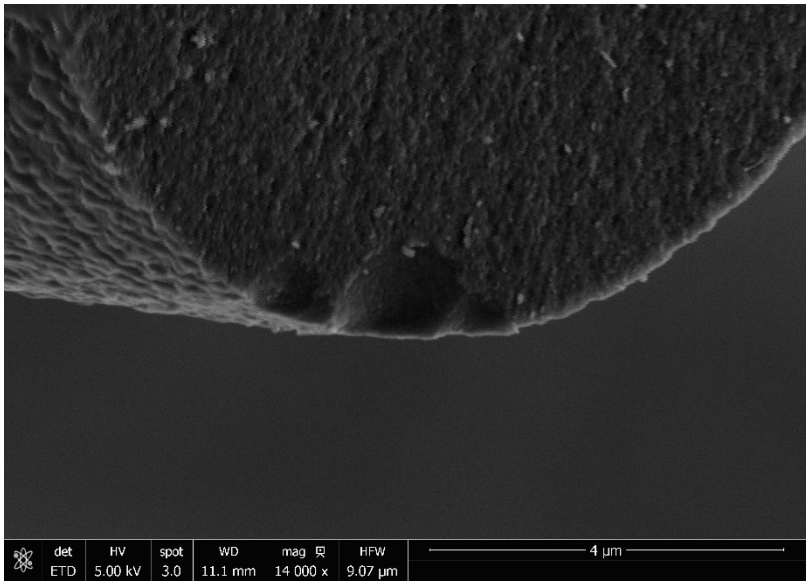


Figure 186 - SEM micrograph of the Hi-Nicalon™ S specimen "Steam 6" examining features on the fracture surface of a fiber (σ_{cr} = 500 MPa, t_f = 0.02 h).

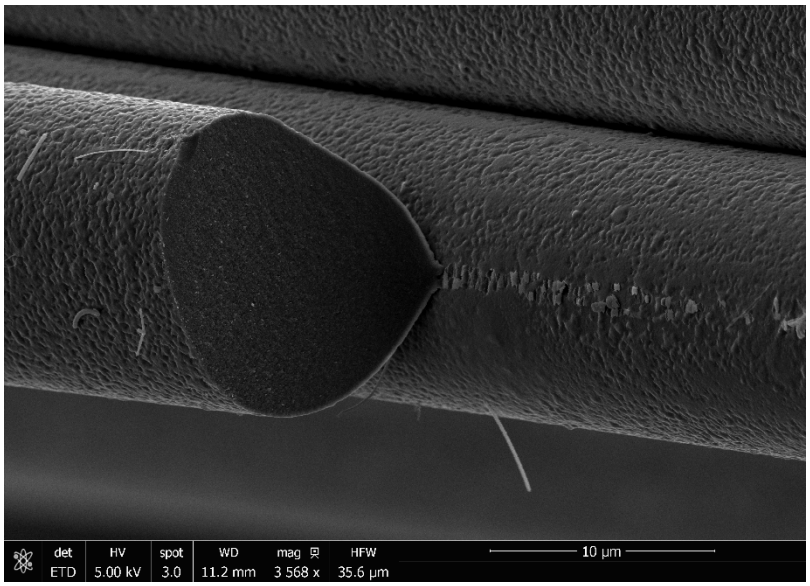


Figure 187 - SEM micrograph of the Hi-Nicalon™ S specimen "Steam 6" examining the fracture surface of a fiber (σ_{cr} = 500 MPa, t_f = 0.02 h). Note signs of fiber-fiber contact.

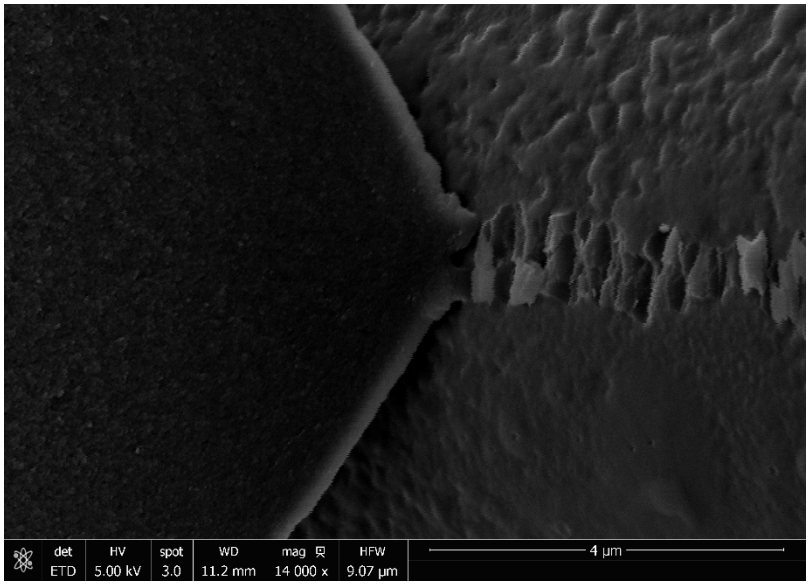


Figure 188 - SEM micrograph of the Hi-Nicalon™ S specimen "Steam 6" examining features on the fracture surface of a fiber (σ_{cr} = 500 MPa, t_f = 0.02 h). Note signs of fiber-fiber contact.

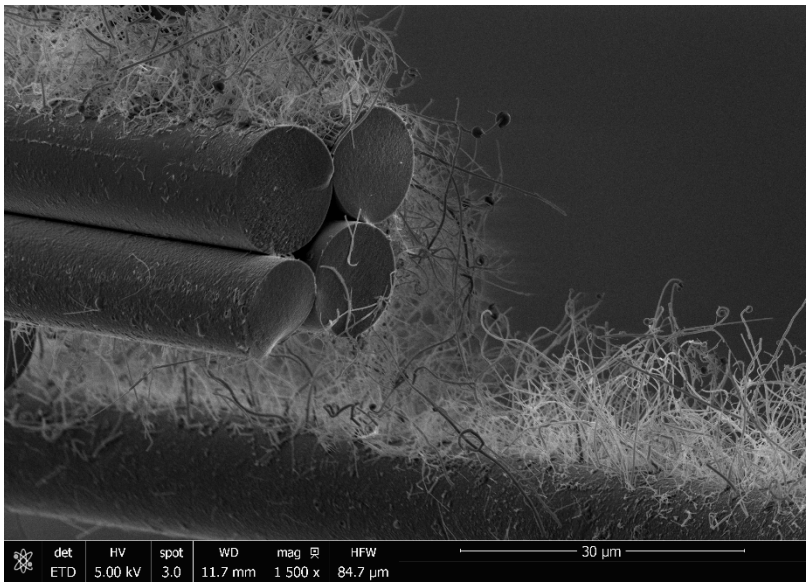


Figure 189 - SEM micrograph of the Hi-Nicalon™ S specimen "Steam 6" examining the fracture surfaces four fibers (σ_{cr} = 500 MPa, t_f = 0.02 h). Note signs of saturated steam exposure (silica deposition) signs of fiber-fiber contact.

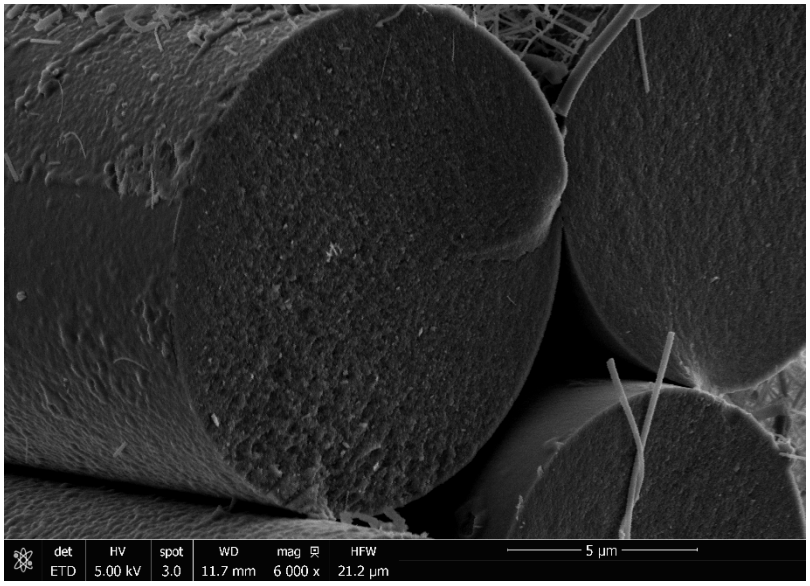


Figure 190 - SEM micrograph of the Hi-Nicalon™ S specimen "Steam 6" examining the fracture surface of a fiber (σ_{cr} = 500 MPa, t_f = 0.02 h). Note signs of saturated steam exposure (silica deposition).

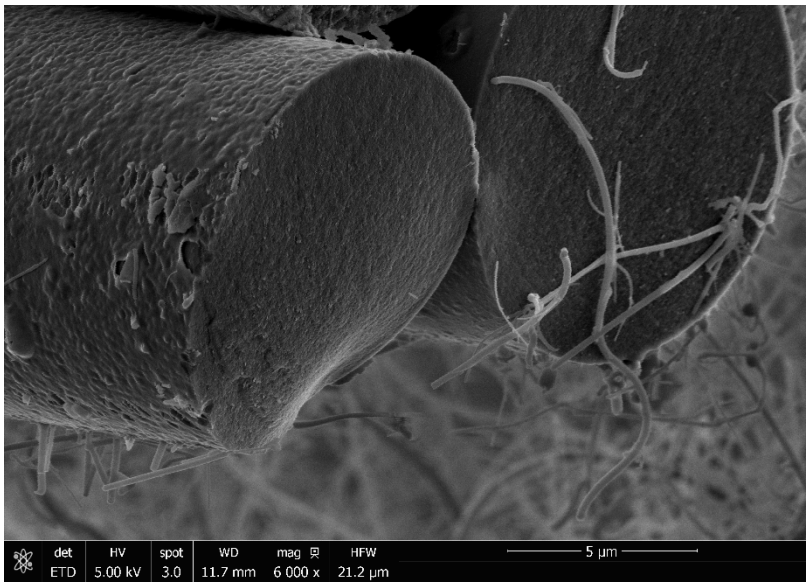


Figure 191 - SEM micrograph of the Hi-Nicalon™ S specimen "Steam 6" examining the fracture surface of a fiber (σ_{cr} = 500 MPa, t_f = 0.02 h). Note signs of saturated steam exposure (silica deposition).

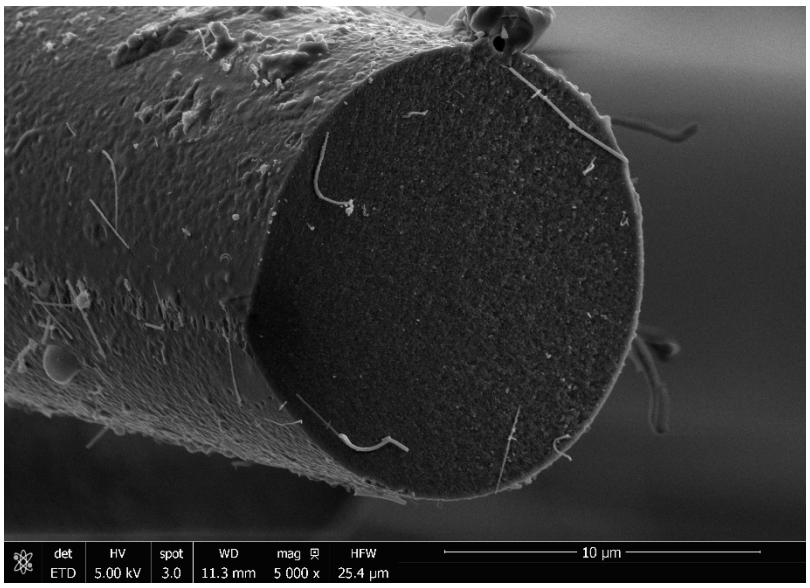


Figure 192 - SEM micrograph of the Hi-Nicalon™ S specimen "Steam 6" examining the fracture surface of a fiber (σ_{cr} = 500 MPa, t_f = 0.02 h). Note signs of saturated steam exposure (silica deposition).

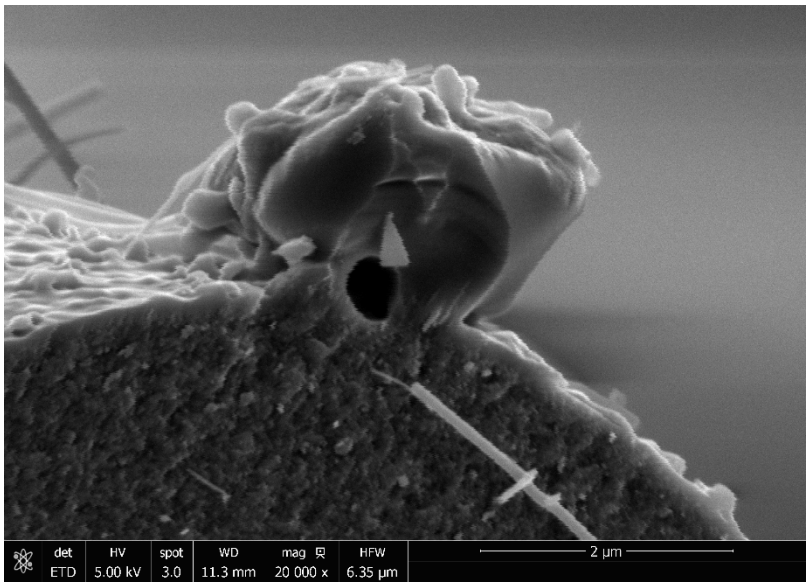


Figure 193 - SEM micrograph of the Hi-Nicalon™ S specimen "Steam 6" examining features on the fracture surface of a fiber (σ_{cr} = 500 MPa, t_f = 0.02 h). Note signs of saturated steam exposure (silica deposition/dewetting).

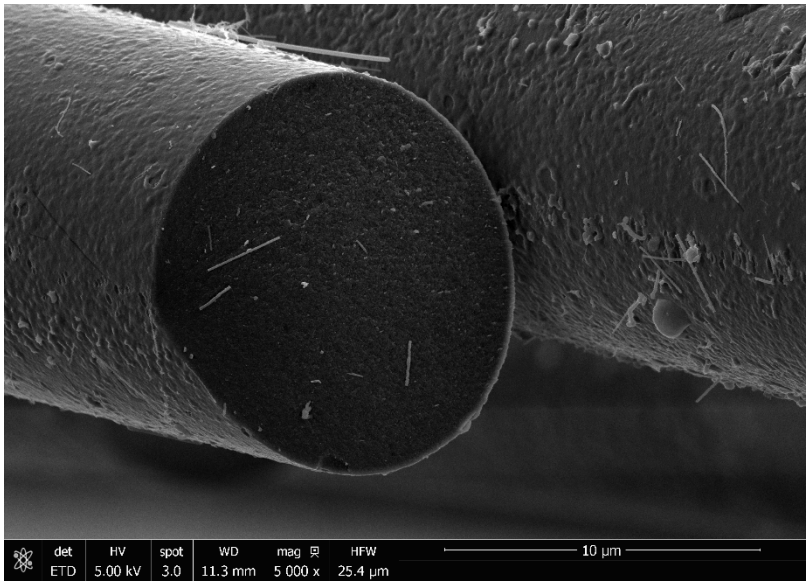


Figure 194 - SEM micrograph of the Hi-Nicalon™ S specimen "Steam 6" examining the fracture surface of a fiber (σ_{cr} = 500 MPa, t_f = 0.02 h). Note signs of saturated steam exposure (silica deposition).

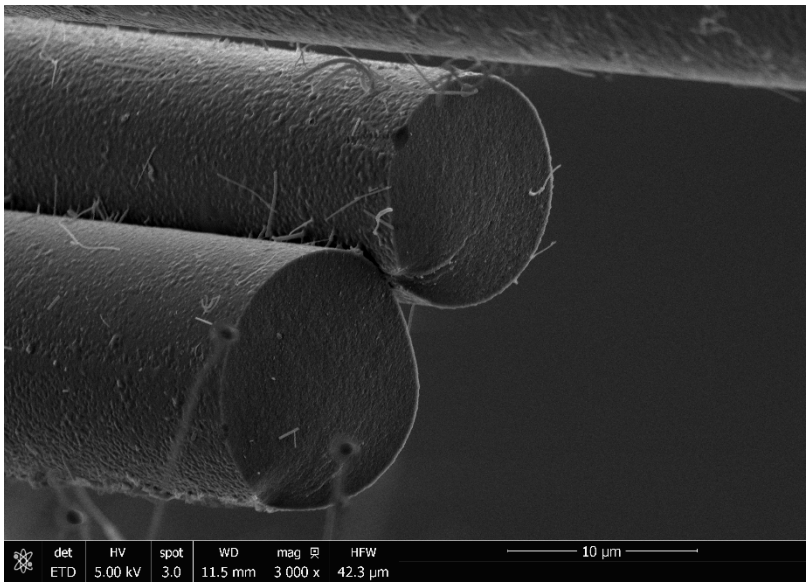


Figure 195 - SEM micrograph of the Hi-Nicalon™ S specimen "Steam 6" examining the fracture surface of a fiber (σ_{cr} = 500 MPa, t_f = 0.02 h). Note signs of saturated steam exposure (silica deposition).

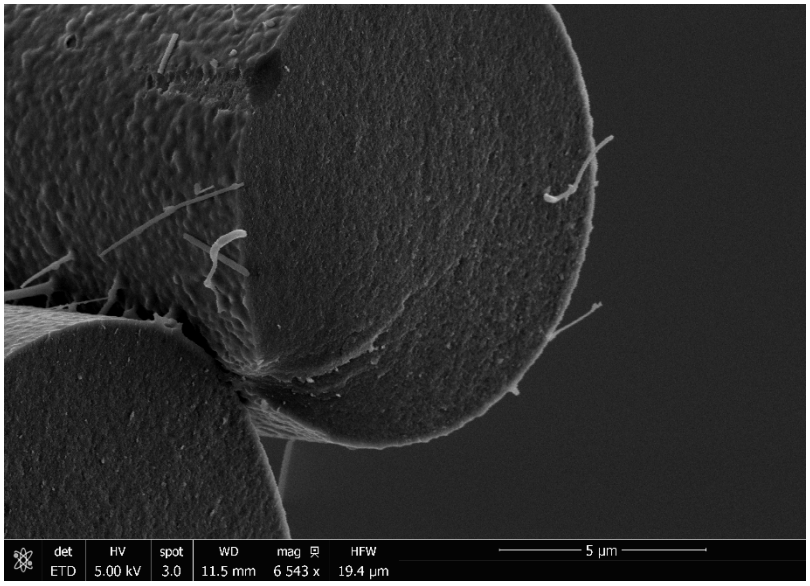


Figure 196 - SEM micrograph of the Hi-Nicalon™ S specimen "Steam 6" examining the fracture surface of a fiber (σ_{cr} = 500 MPa, t_f = 0.02 h). Note signs of saturated steam exposure (silica deposition).

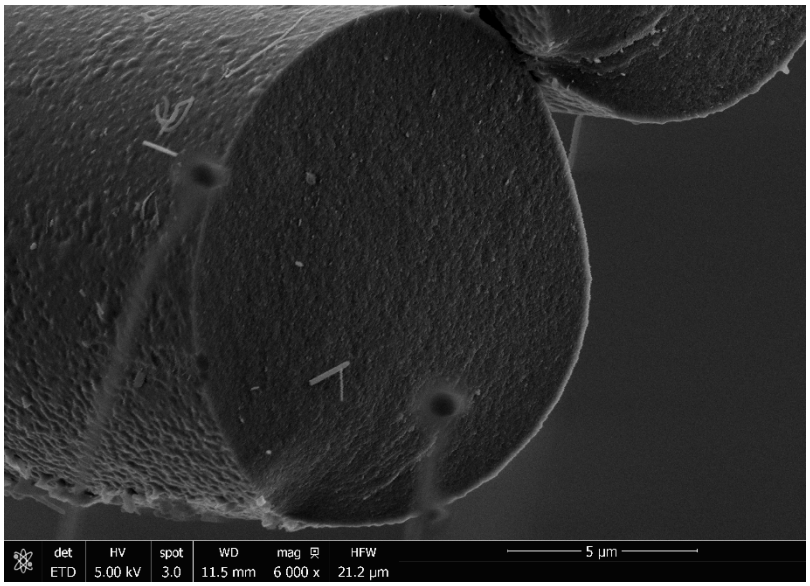


Figure 197 - SEM micrograph of the Hi-Nicalon™ S specimen "Steam 6" examining the fracture surface of a fiber (σ_{cr} = 500 MPa, t_f = 0.02 h). Note signs of saturated steam exposure (silica deposition).

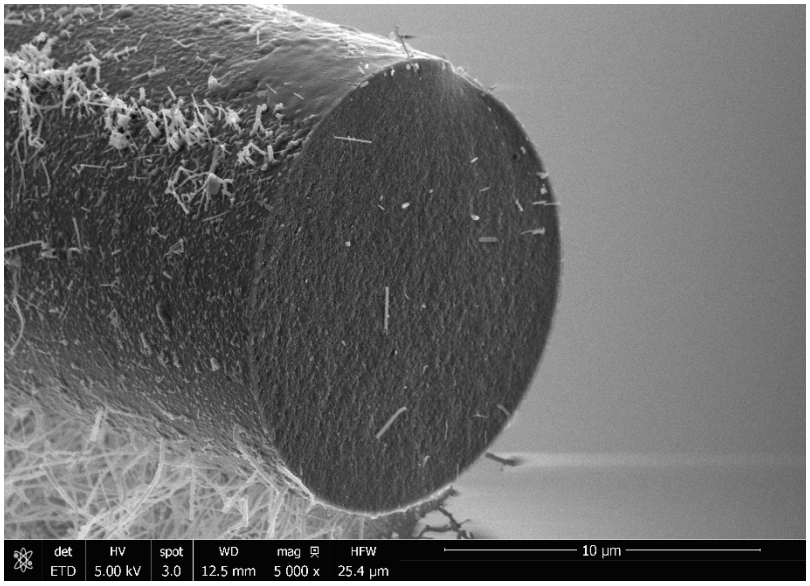


Figure 198 - SEM micrograph of the Hi-Nicalon™ S specimen "Steam 6" examining the fracture surface of a fiber (σ_{cr} = 500 MPa, t_f = 0.02 h). Note signs of saturated steam exposure (silica deposition).

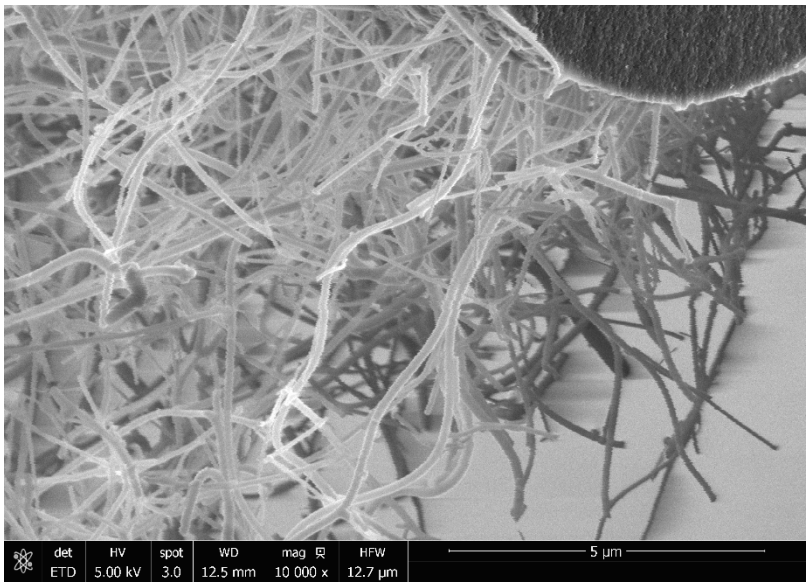


Figure 199 - SEM micrograph of the Hi-Nicalon™ S specimen "Steam 6" examining silica deposition near a fiber (σ_{cr} = 500 MPa, t_f = 0.02 h).

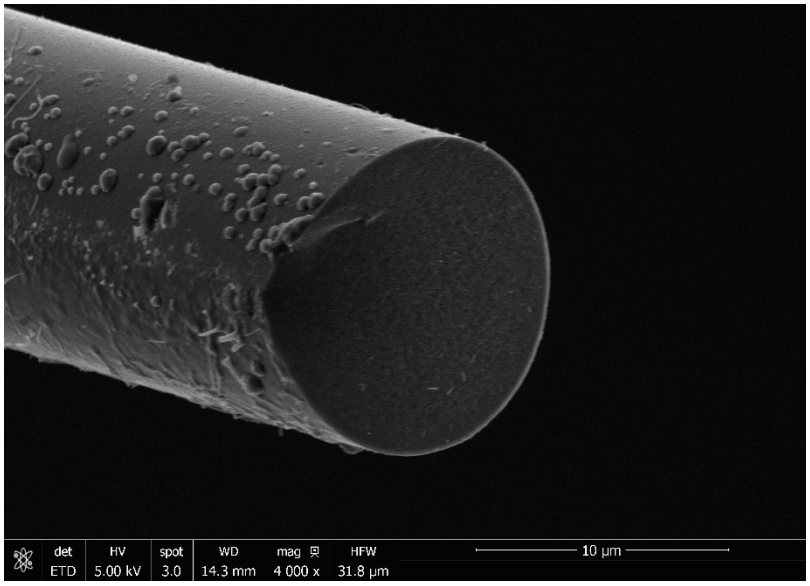


Figure 200 - SEM micrograph of the Hi-Nicalon™ S specimen "Steam 6" examining the fracture surface of a fiber (σ_{cr} = 500 MPa, t_f = 0.02 h). Note signs of saturated steam exposure (dewetting).

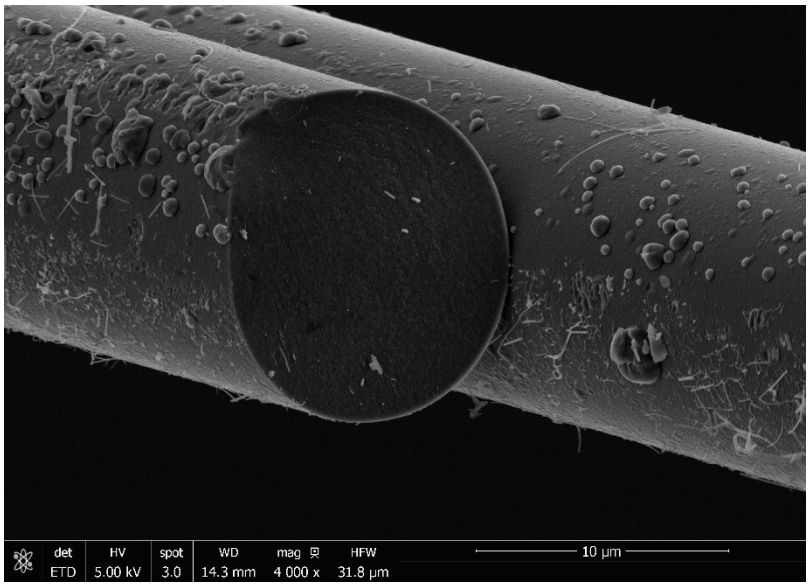


Figure 201 - SEM micrograph of the Hi-Nicalon™ S specimen "Steam 6" examining the fracture surface of a fiber (σ_{cr} = 500 MPa, t_f = 0.02 h). Note signs of saturated steam exposure (silica deposition/dewetting).

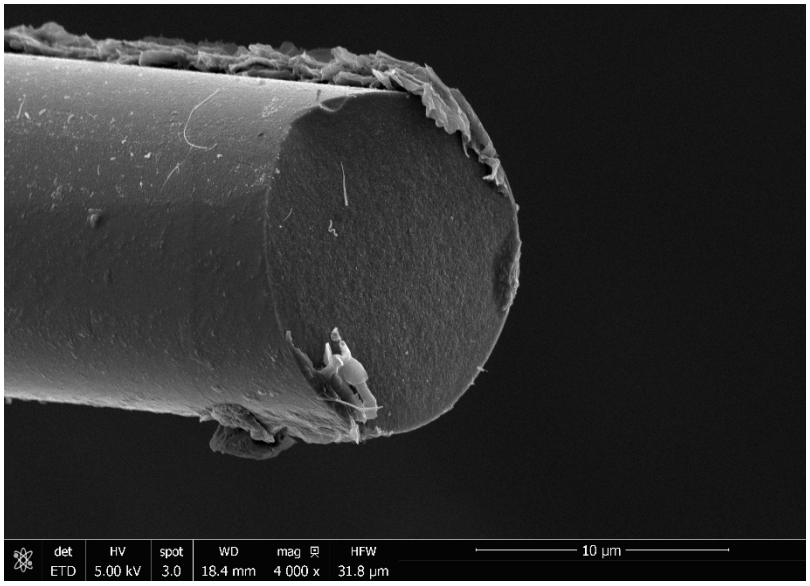


Figure 202 - SEM micrograph of the Hi-Nicalon™ S specimen "Steam 6" examining the fracture surface of a fiber (σ_{cr} = 500 MPa, t_f = 0.02 h). Note possible oxide scale growth.

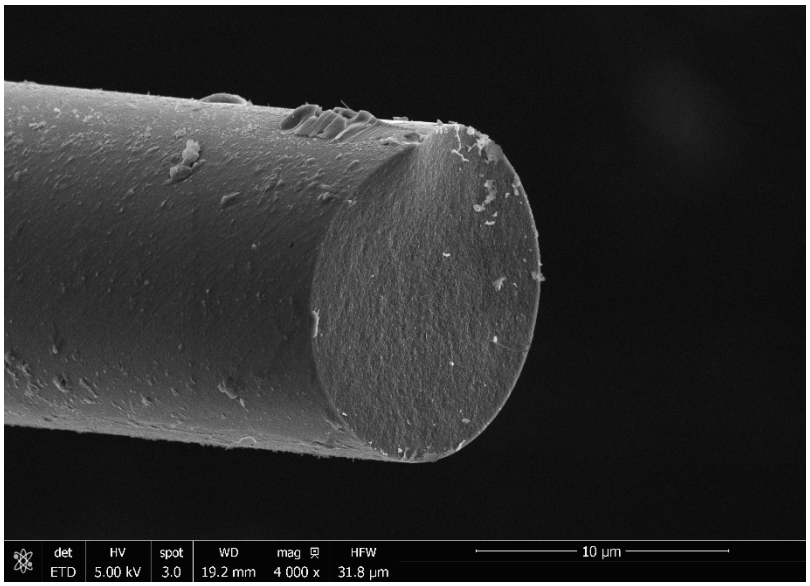


Figure 203 - SEM micrograph of the Hi-Nicalon™ S specimen "Steam 6" examining the fracture surface of a fiber (σ_{cr} = 500 MPa, t_f = 0.02 h).

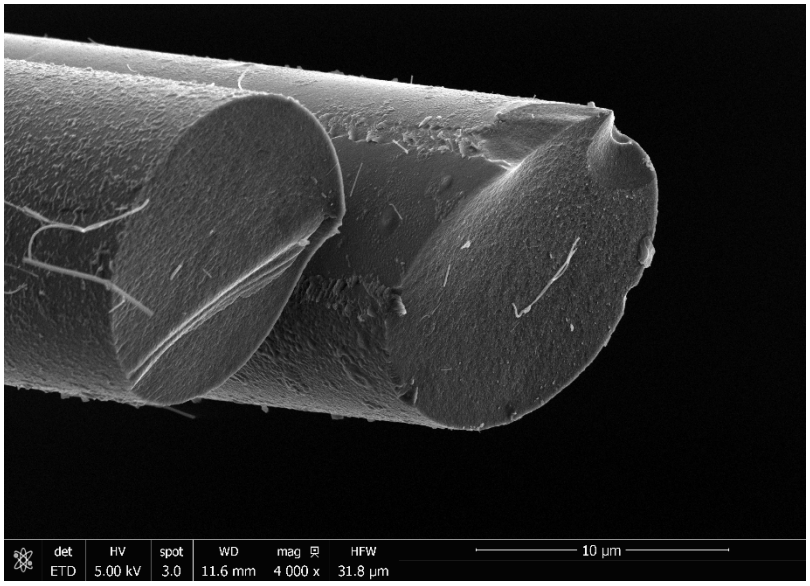


Figure 204 - SEM micrograph of the Hi-Nicalon™ S specimen "Steam 6" examining the fracture surface of a fiber (σ_{cr} = 500 MPa, t_f = 0.02 h). Note signs of saturated steam exposure (silica deposition).

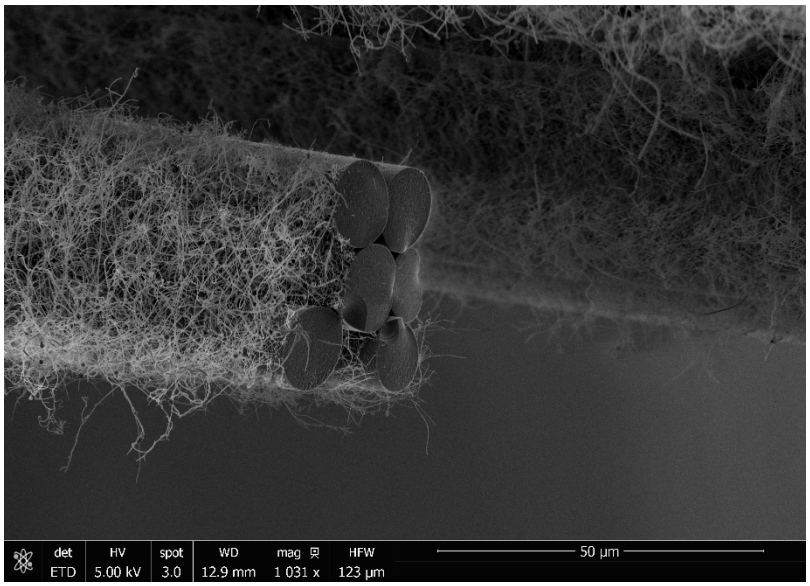


Figure 205 - SEM micrograph of the Hi-Nicalon™ S specimen "Steam 6" examining the fracture surfaces of six fibers (σ_{cr} = 500 MPa, t_f = 0.02 h). Note signs of saturated steam exposure (silica deposition).

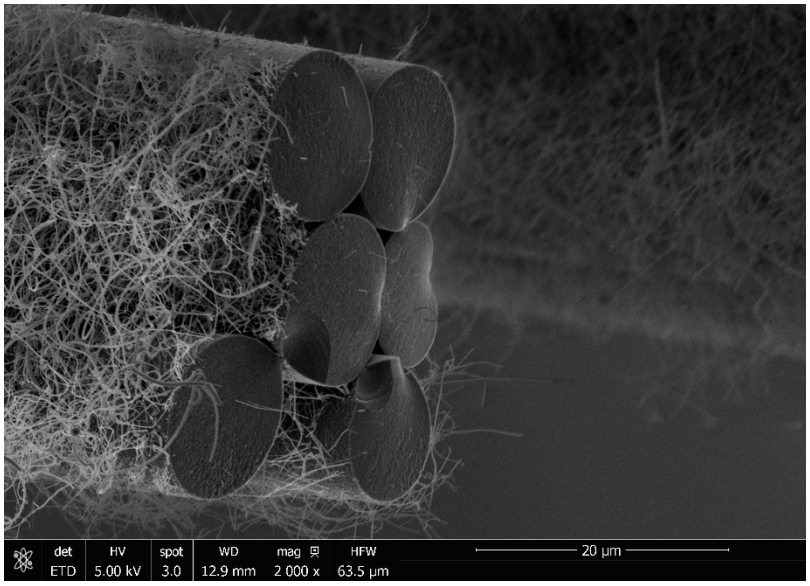


Figure 206 - SEM micrograph of the Hi-Nicalon™ S specimen "Steam 6" examining the fracture surfaces of six fibers (σ_{cr} = 500 MPa, t_f = 0.02 h). Note signs of saturated steam exposure (silica deposition).

Appendix C. Representative SEM Polished Cross Section Images

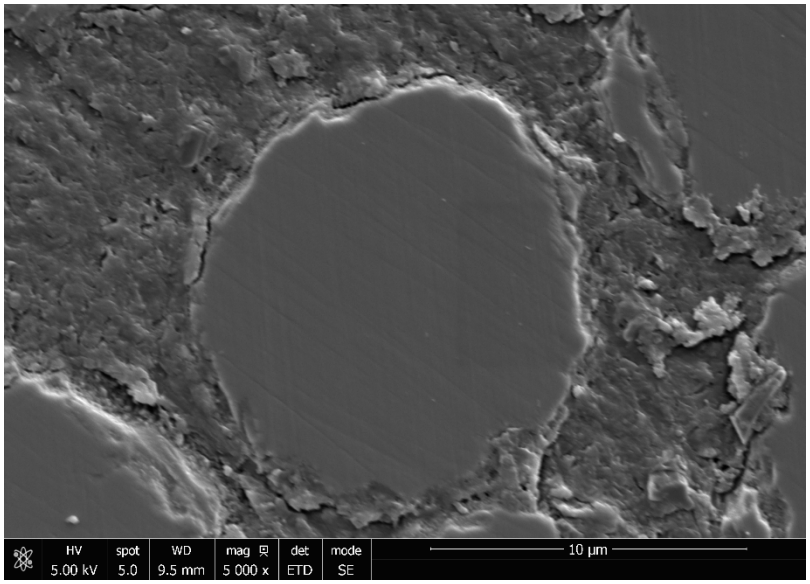


Figure 207 - SEM micrograph of the Hi-Nicalon™ S specimen "Air 7" examining the cross section at the midpoint of a fiber (σ_{cr} = 300 MPa, t_f = 100 h).

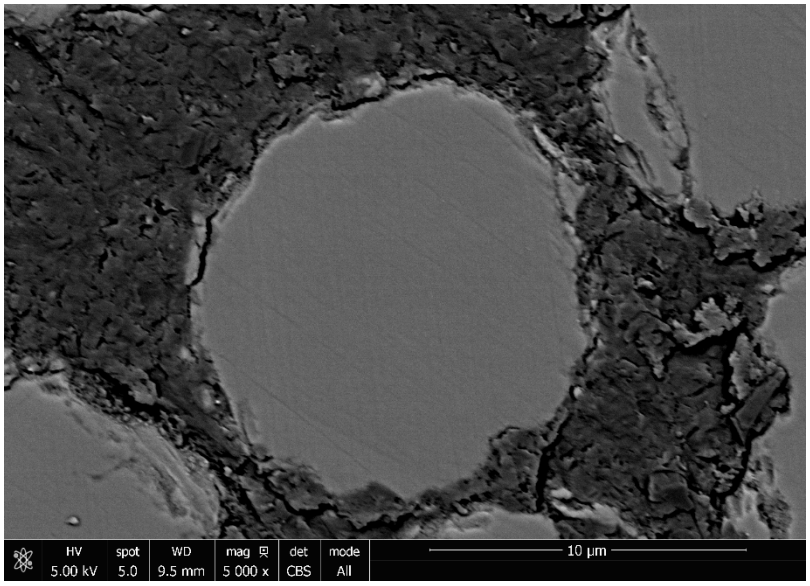


Figure 208 - SEM electron backscatter deflection micrograph of the Hi-Nicalon™ S specimen "Air 7" examining the cross section at the midpoint of a fiber (σ_{cr} = 300 MPa, t_f = 100 h).

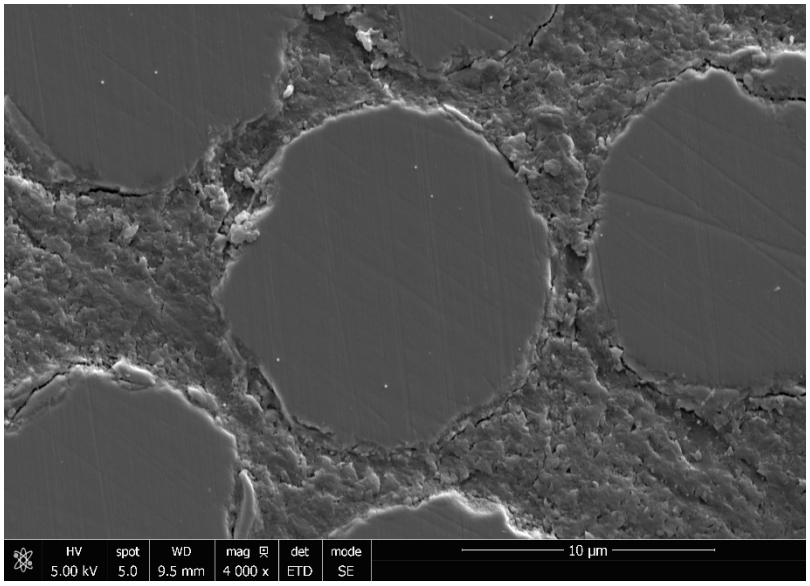


Figure 209 - SEM micrograph of the Hi-Nicalon™ S specimen "Air 7" examining the cross section at the midpoint of a fiber (σ_{cr} = 300 MPa, t_f = 100 h).

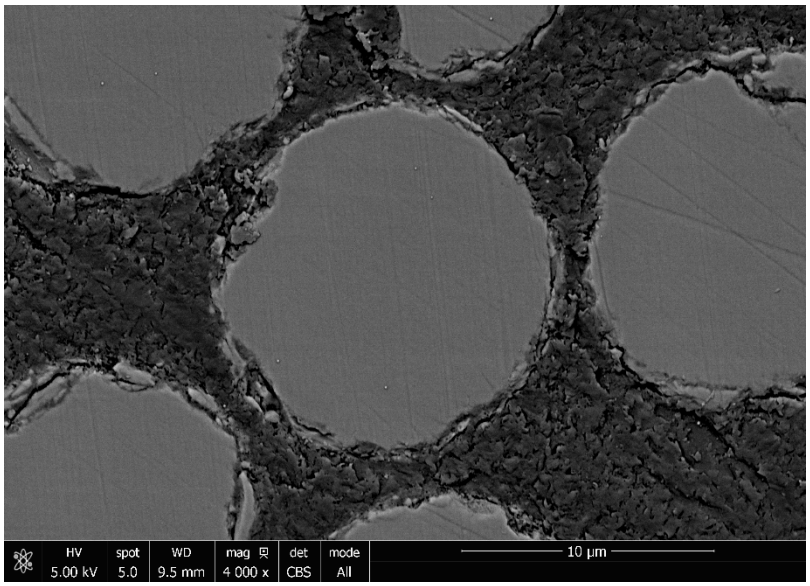


Figure 210 - SEM electron backscatter deflection micrograph of the Hi-Nicalon™ S specimen "Air 7" examining the cross section at the midpoint of a fiber (σ_{cr} = 300 MPa, t_f = 100 h).

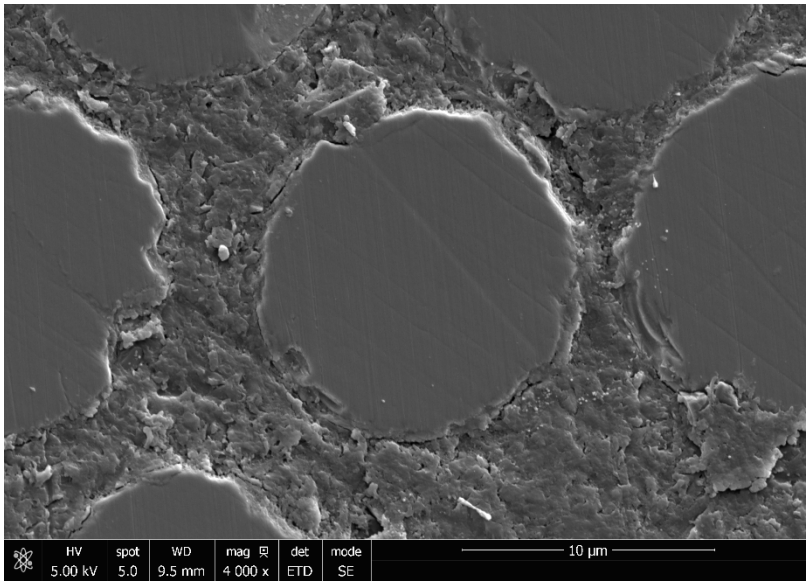


Figure 211 - SEM micrograph of the Hi-Nicalon™ S specimen "Air 7" examining the cross section at the midpoint of a fiber (σ_{cr} = 300 MPa, t_f = 100 h).

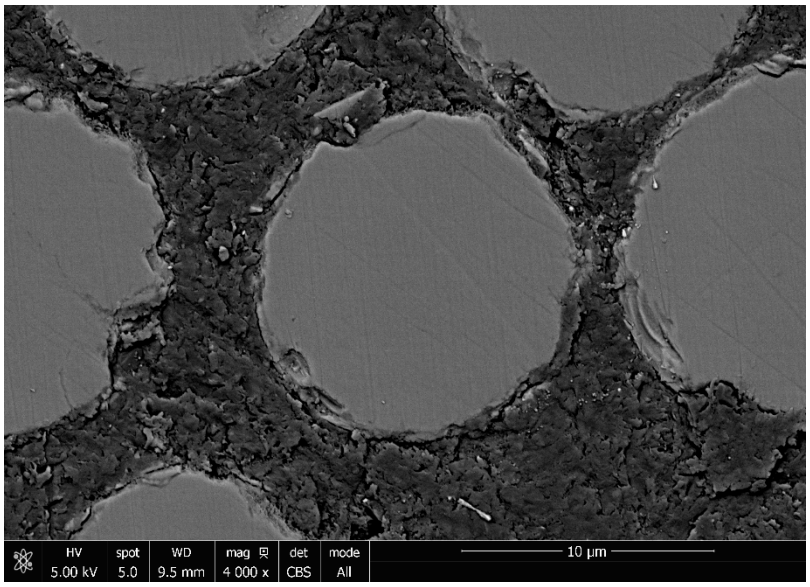


Figure 212 - SEM electron backscatter deflection micrograph of the Hi-Nicalon™ S specimen "Air 7" examining the cross section at the midpoint of a fiber (σ_{cr} = 300 MPa, t_f = 100 h).

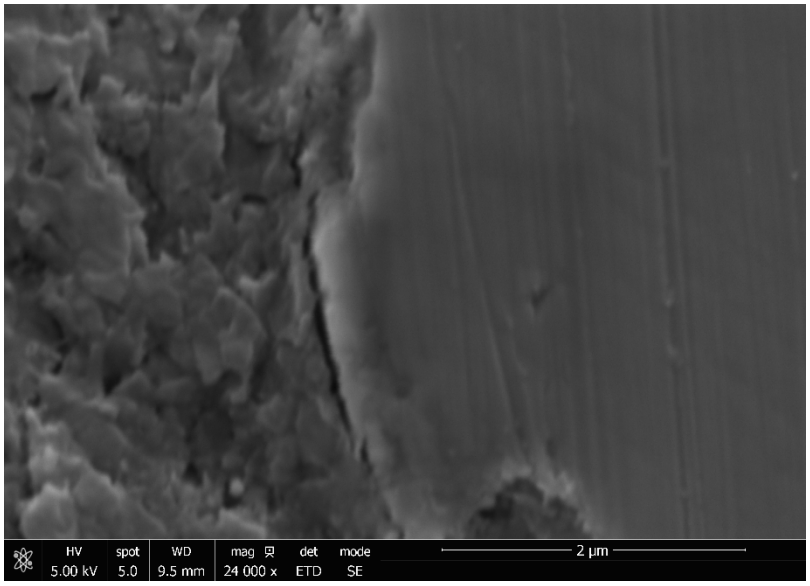


Figure 213 - SEM micrograph of the Hi-Nicalon™ S specimen "Air 7" examining a portion of the cross section at the midpoint of a fiber (σ_{cr} = 300 MPa, t_f = 100 h).

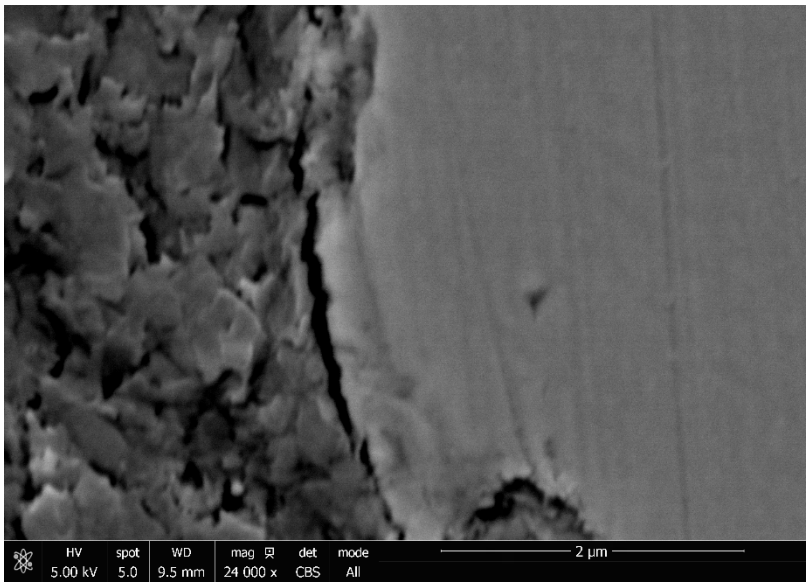


Figure 214 - SEM electron backscatter deflection micrograph of the Hi-Nicalon™ S specimen "Air 7" examining a portion of the cross section at the midpoint of a fiber (σ_{cr} = 300 MPa, t_f = 100 h).

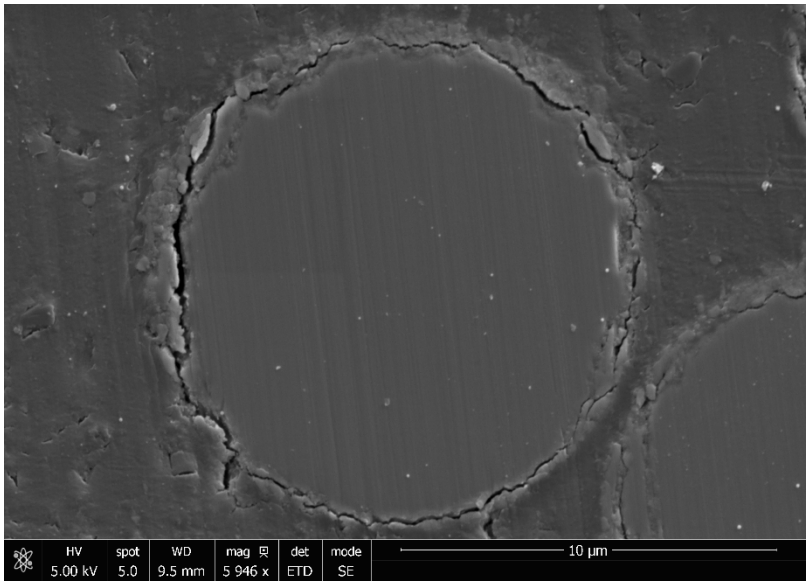


Figure 215 - SEM micrograph of the Hi-Nicalon™ S specimen "Air 7" examining the cross section at the midpoint of a fiber (σ_{cr} = 300 MPa, t_f = 100 h).

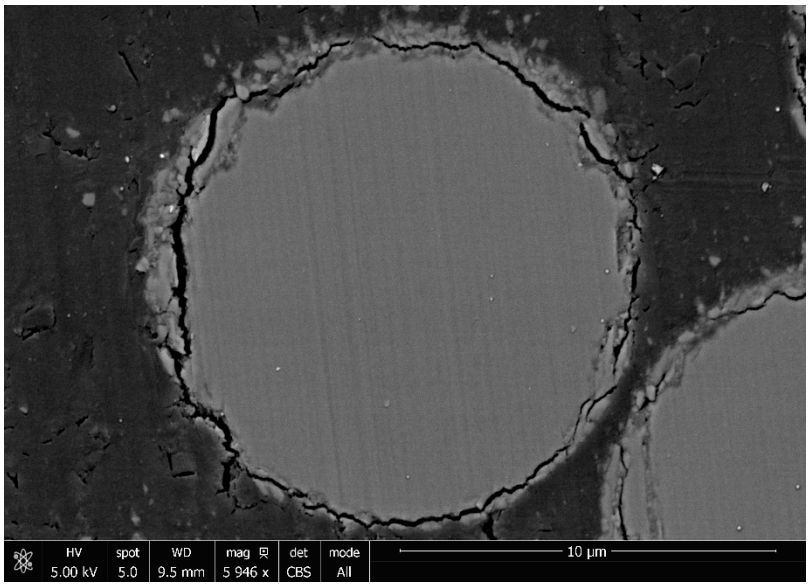


Figure 216 - SEM electron backscatter deflection micrograph of the Hi-Nicalon™ S specimen "Air 7" examining the cross section at the midpoint of a fiber (σ_{cr} = 300 MPa, t_f = 100 h).

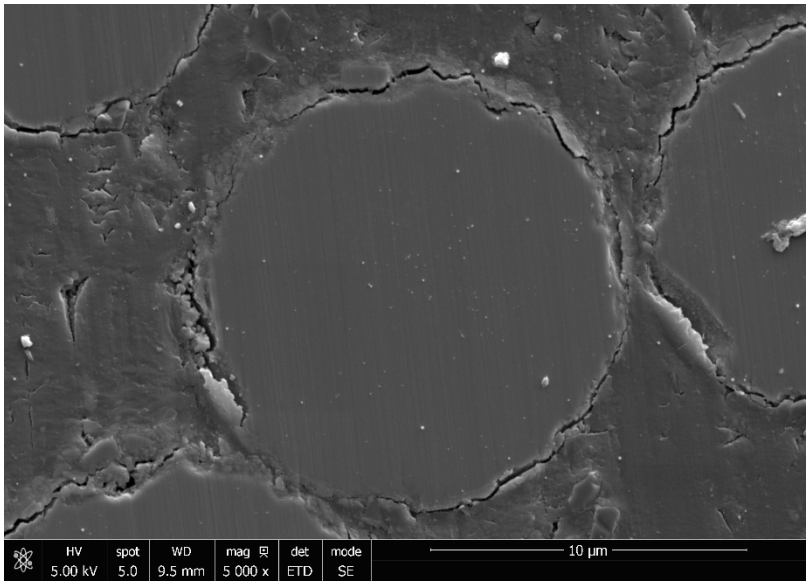


Figure 217 - SEM micrograph of the Hi-Nicalon™ S specimen "Air 7" examining the cross section at the midpoint of a fiber (σ_{cr} = 300 MPa, t_f = 100 h).

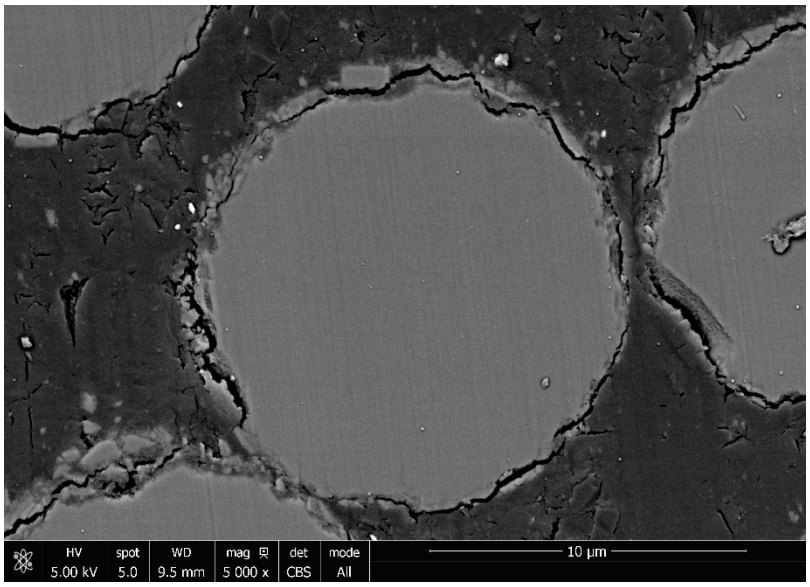


Figure 218 - SEM electron backscatter deflection micrograph of the Hi-Nicalon™ S specimen "Air 7" examining the cross section at the midpoint of a fiber (σ_{cr} = 300 MPa, t_f = 100 h).

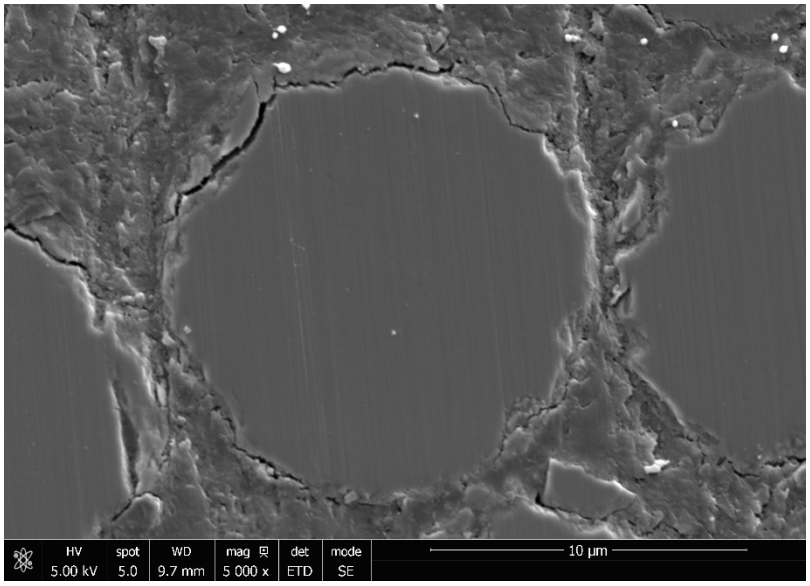


Figure 219 - SEM micrograph of the Hi-Nicalon™ S specimen "Air 7" examining the cross section at the midpoint of a fiber (σ_{cr} = 300 MPa, t_f = 100 h).

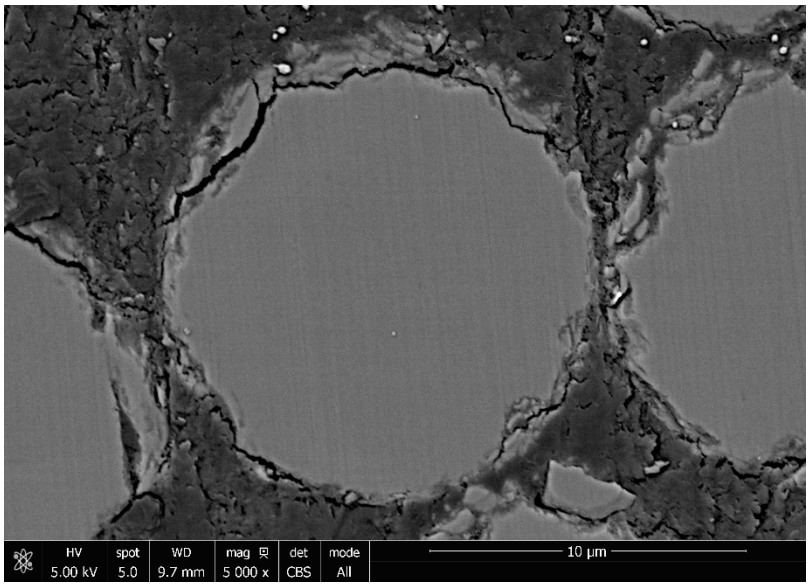


Figure 220 - SEM electron backscatter deflection micrograph of the Hi-Nicalon™ S specimen "Air 7" examining the cross section at the midpoint of a fiber (σ_{cr} = 300 MPa, t_f = 100 h).

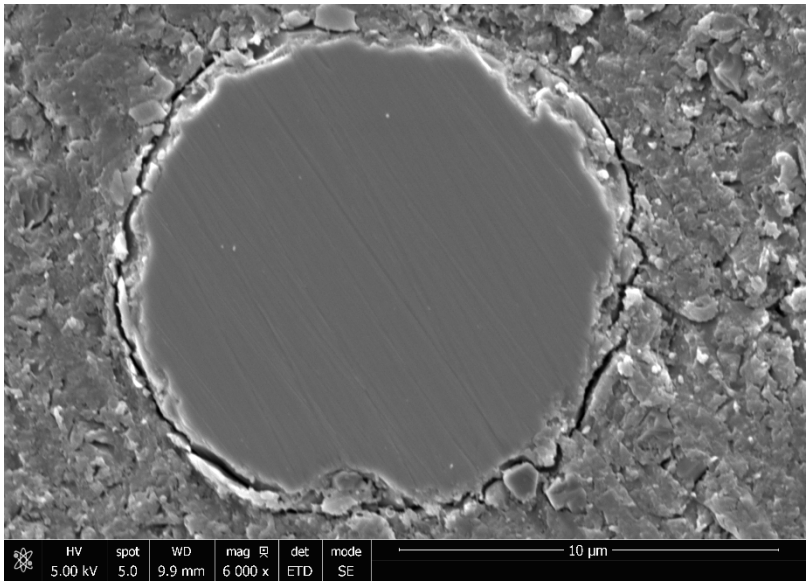


Figure 221 - SEM micrograph of the Hi-Nicalon™ S specimen "Air 11" examining the cross section at the midpoint of a fiber (σ_{cr} = 500 MPa, t_f = 100 h).

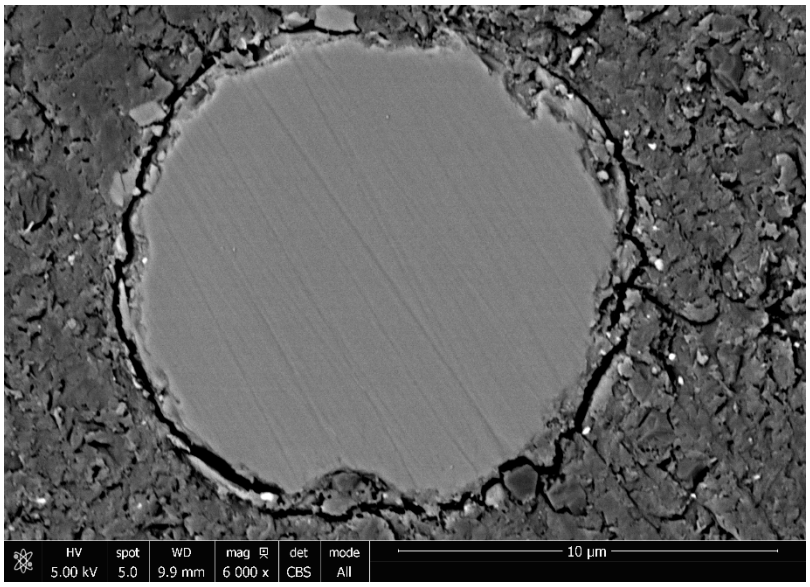


Figure 222 - SEM electron backscatter deflection micrograph of the Hi-Nicalon™ S specimen "Air 11" examining the cross section at the midpoint of a fiber (σ_{cr} = 500 MPa, t_f = 100 h).

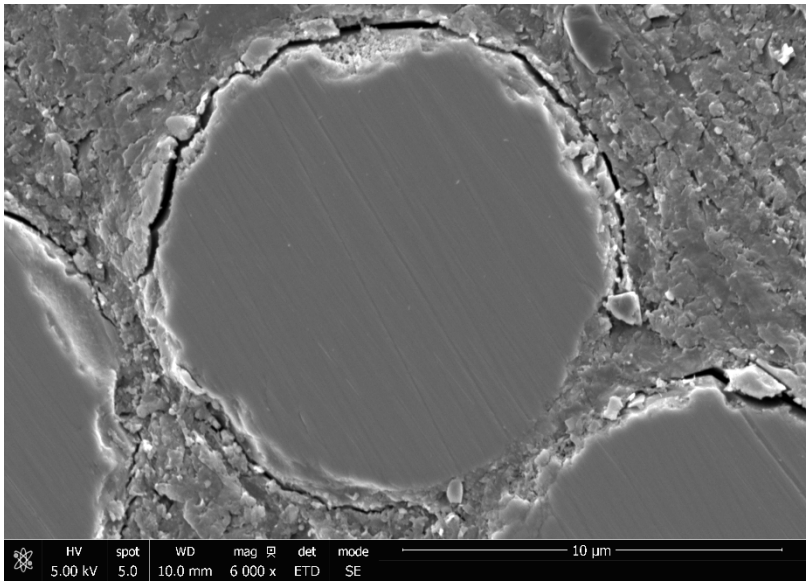


Figure 223 - SEM micrograph of the Hi-Nicalon™ S specimen "Air 11" examining the cross section at the midpoint of a fiber (σ_{cr} = 500 MPa, t_f = 100 h).

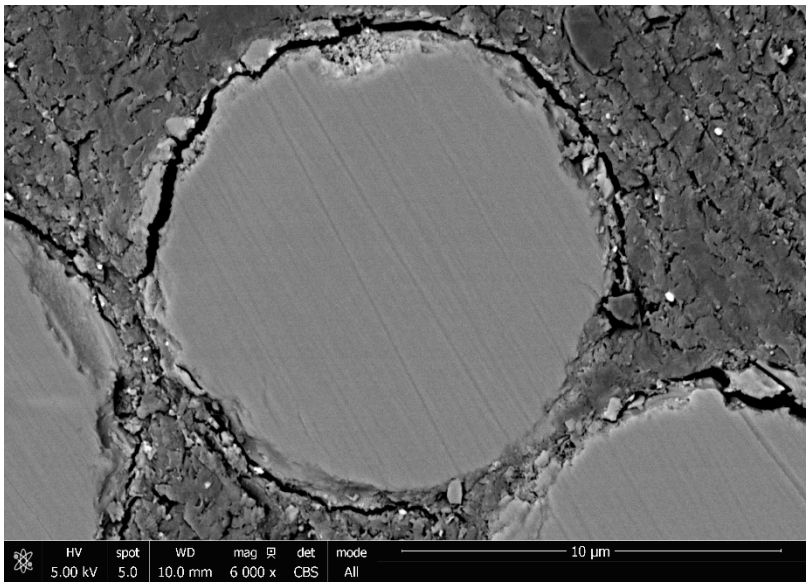


Figure 224 - SEM electron backscatter deflection micrograph of the Hi-Nicalon™ S specimen "Air 11" examining the cross section at the midpoint of a fiber (σ_{cr} = 500 MPa, t_f = 100 h).

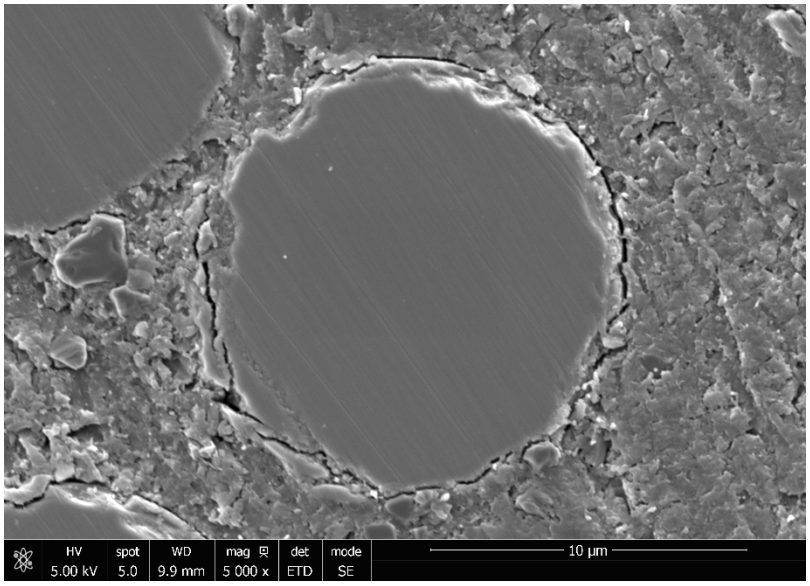


Figure 225 - SEM micrograph of the Hi-Nicalon™ S specimen "Air 11" examining the cross section at the midpoint of a fiber (σ_{cr} = 500 MPa, t_f = 100 h).

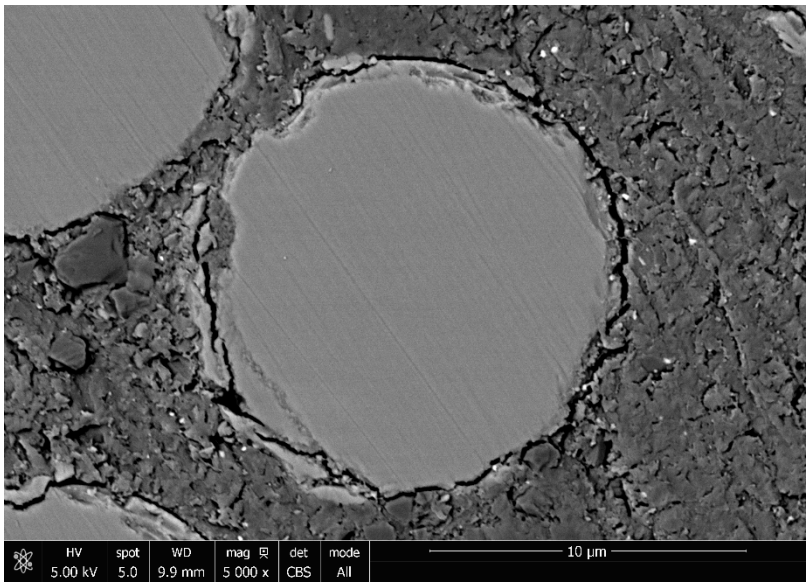


Figure 226 - SEM electron backscatter deflection micrograph of the Hi-Nicalon™ S specimen "Air 11" examining the cross section at the midpoint of a fiber (σ_{cr} = 500 MPa, t_f = 100 h).

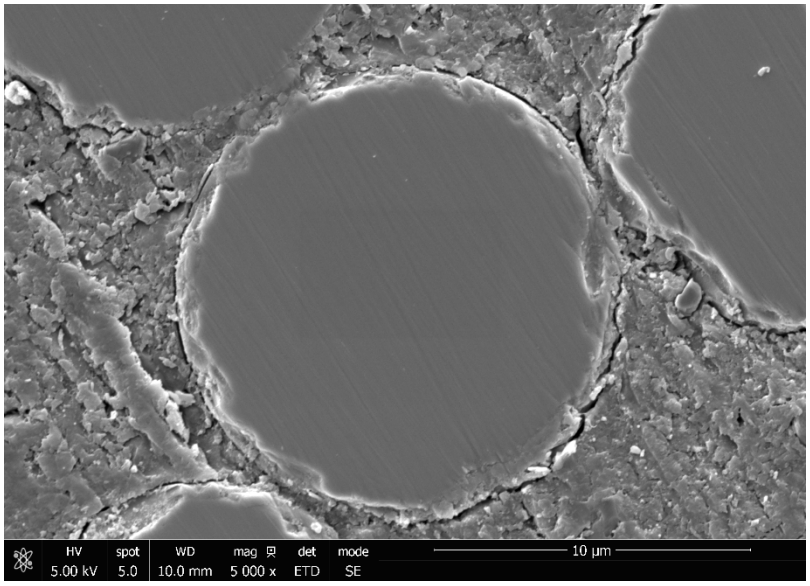


Figure 227 - SEM micrograph of the Hi-Nicalon™ S specimen "Air 11" examining the cross section at the midpoint of a fiber (σ_{cr} = 500 MPa, t_f = 100 h).

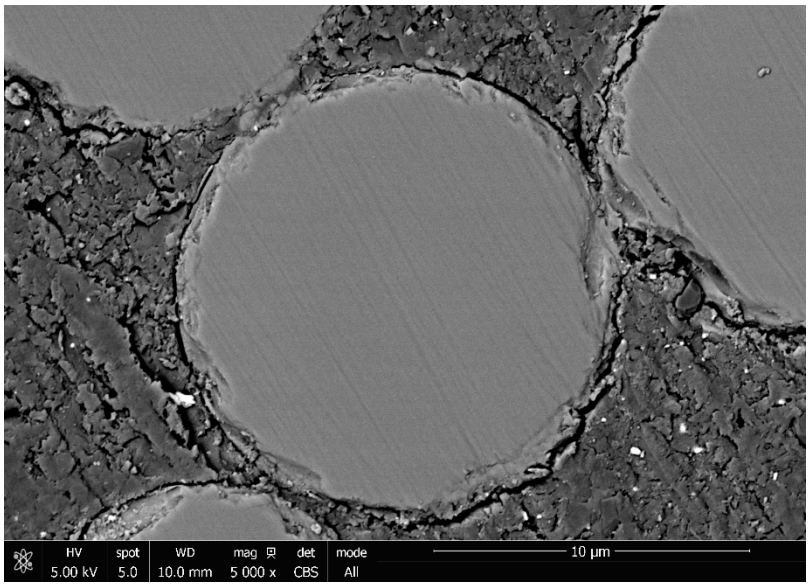


Figure 228 - SEM electron backscatter deflection micrograph of the Hi-Nicalon™ S specimen "Air 11" examining the cross section at the midpoint of a fiber (σ_{cr} = 500 MPa, t_f = 100 h).

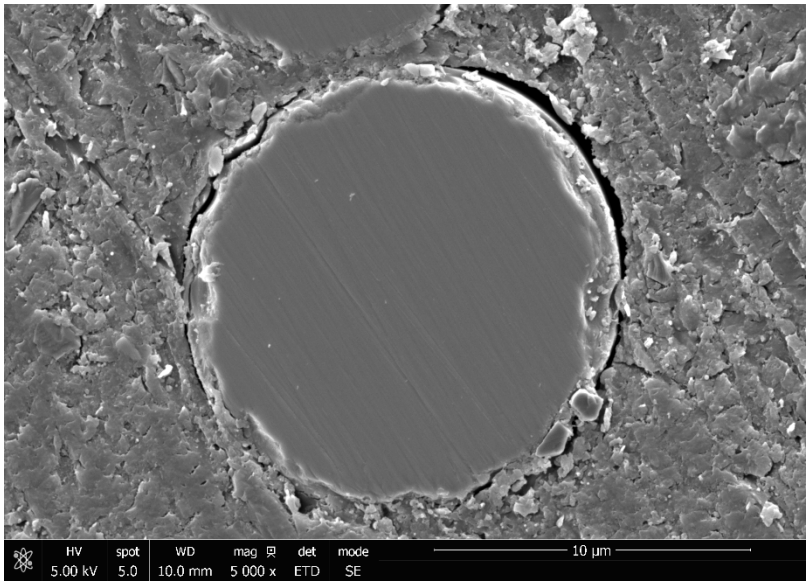


Figure 229 - SEM micrograph of the Hi-Nicalon™ S specimen "Air 11" examining the cross section at the midpoint of a fiber (σ_{cr} = 500 MPa, t_f = 100 h).

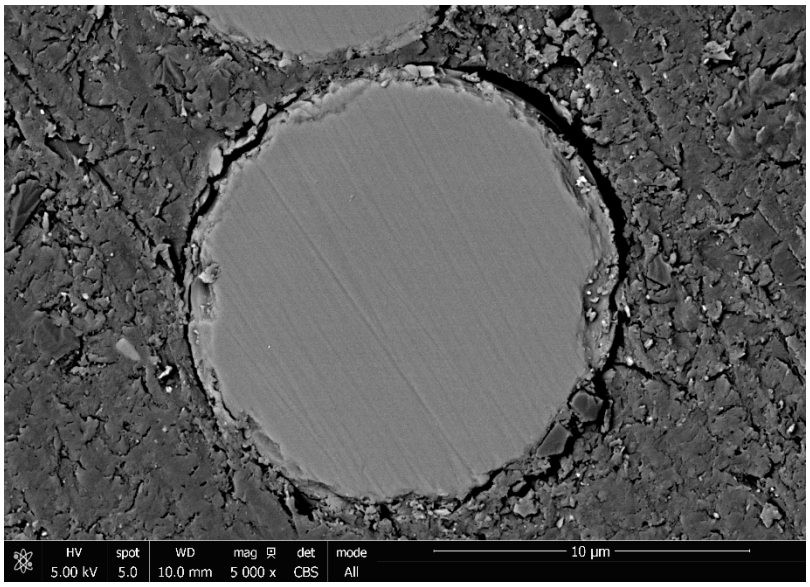


Figure 230 - SEM electron backscatter deflection micrograph of the Hi-Nicalon™ S specimen "Air 11" examining the cross section at the midpoint of a fiber (σ_{cr} = 500 MPa, t_f = 100 h).

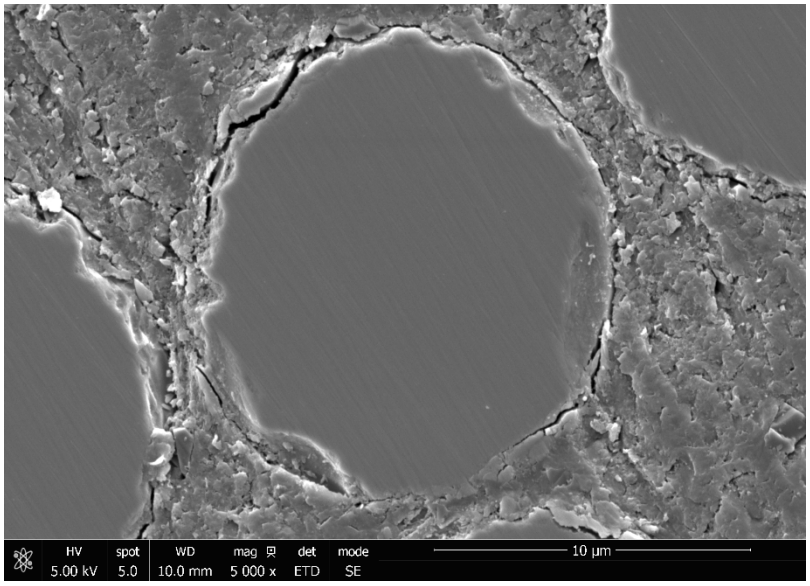


Figure 231 - SEM micrograph of the Hi-Nicalon™ S specimen "Air 11" examining the cross section at the midpoint of a fiber (σ_{cr} = 500 MPa, t_f = 100 h).

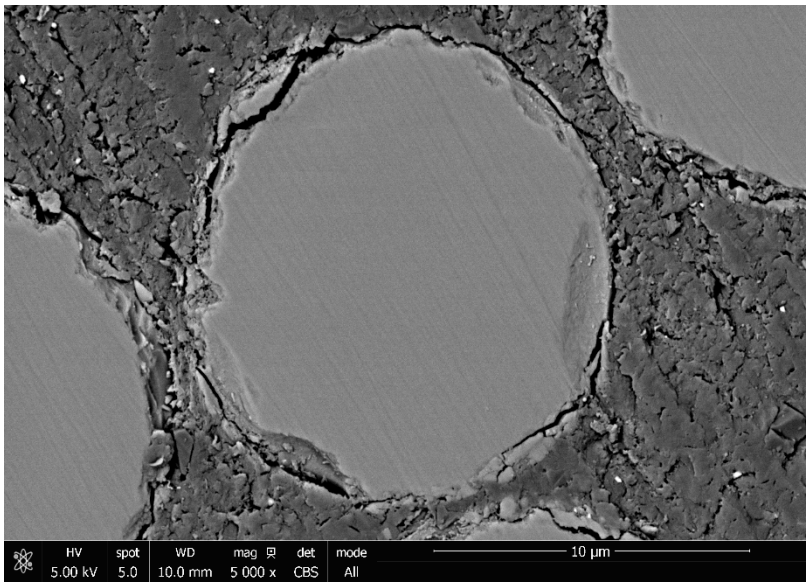


Figure 232 - SEM electron backscatter deflection micrograph of the Hi-Nicalon™ S specimen "Air 11" examining the cross section at the midpoint of a fiber (σ_{cr} = 500 MPa, t_f = 100 h).

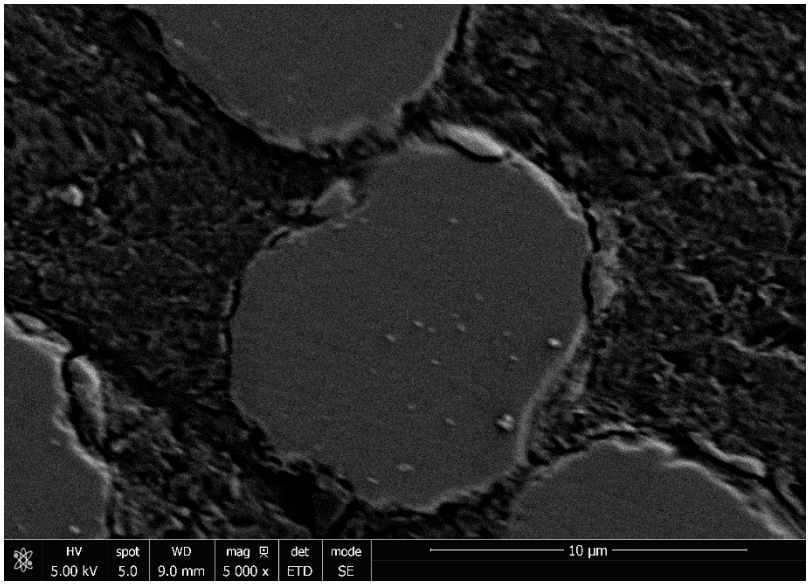


Figure 233 - SEM micrograph of the Hi-Nicalon™ S specimen "Air 3" examining the cross section at the lower portion of a fiber (σ_{cr} = 700 MPa, t_f = 62.5 h).

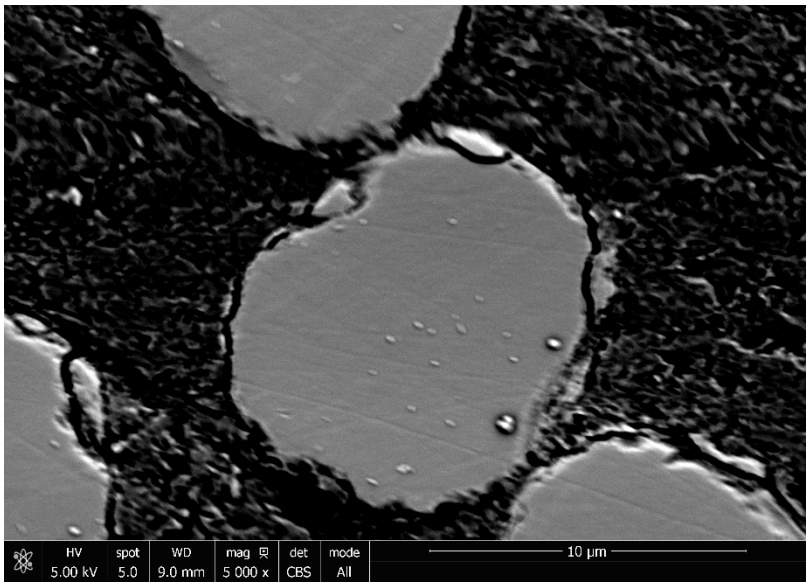


Figure 234 - SEM electron backscatter deflection micrograph of the Hi-Nicalon™ S specimen "Air 3" examining the cross section of the lower portion of a fiber (σ_{cr} = 700 MPa, t_f = 62.5 h).

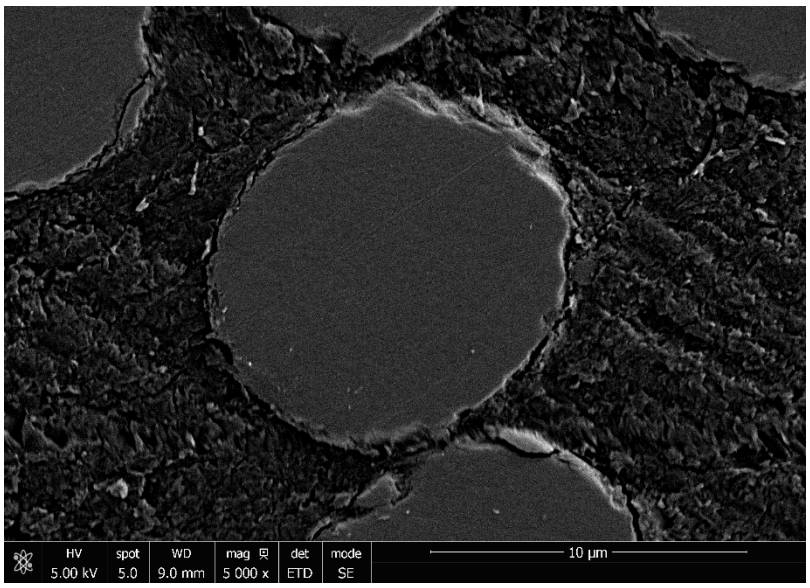


Figure 235 - SEM micrograph of the Hi-Nicalon™ S specimen "Air 3" examining the cross section of the lower portion of a fiber (σ_{cr} = 700 MPa, t_f = 62.5 h).

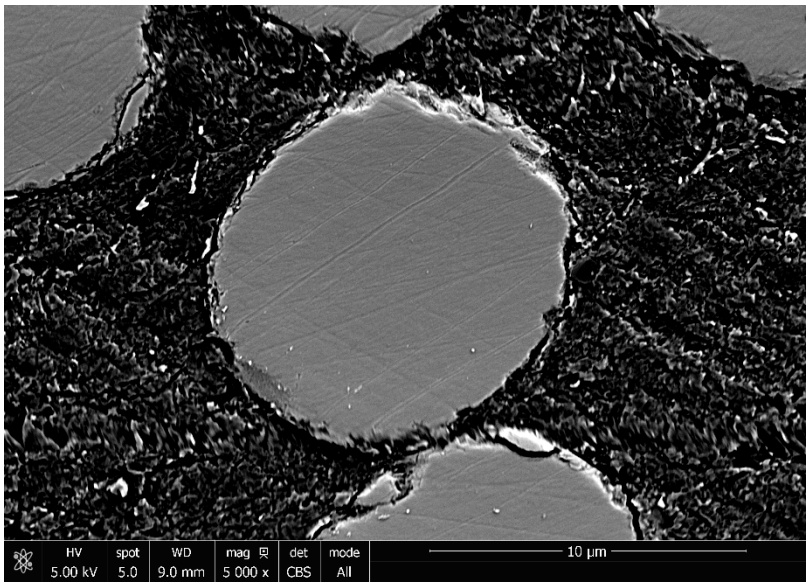


Figure 236 - SEM electron backscatter deflection micrograph of the Hi-Nicalon™ S specimen "Air 3" examining the cross section of the lower portion of a fiber (σ_{cr} = 700 MPa, t_f = 62.5 h).

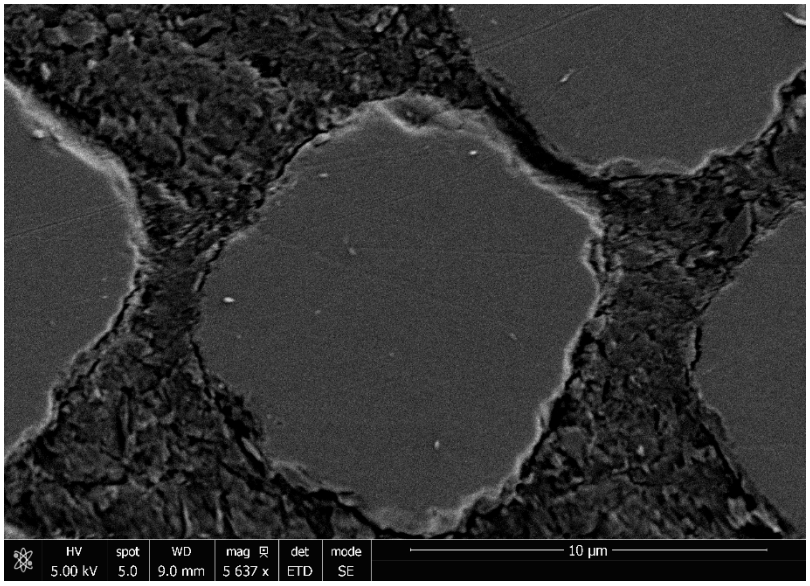


Figure 237 - SEM micrograph of the Hi-Nicalon™ S specimen "Air 3" examining the cross section of the lower portion of a fiber (σ_{cr} = 700 MPa, t_f = 62.5 h).

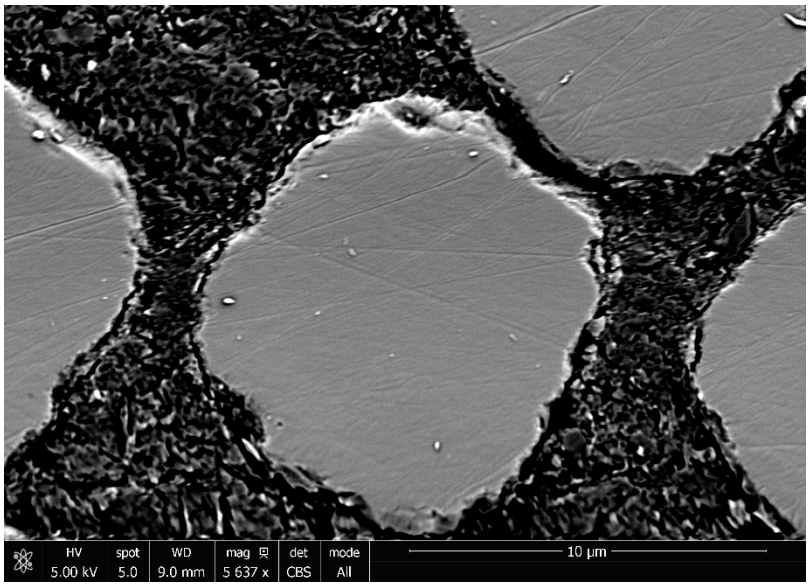


Figure 238 - SEM electron backscatter deflection micrograph of the Hi-Nicalon™ S specimen "Air 3" examining the cross section of the lower portion of a fiber (σ_{cr} = 700 MPa, t_f = 62.5 h).

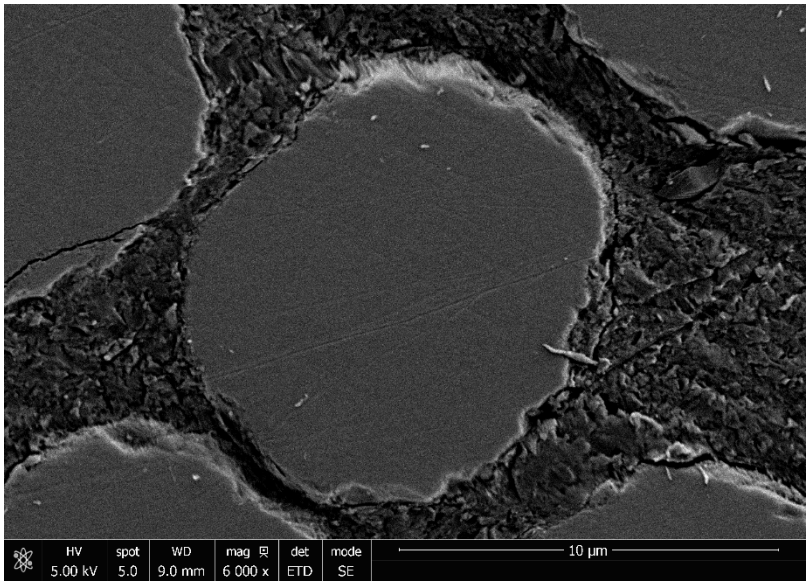


Figure 239 - SEM micrograph of the Hi-Nicalon™ S specimen "Air 3" examining the cross section of the lower portion of a fiber (σ_{cr} = 700 MPa, t_f = 62.5 h).

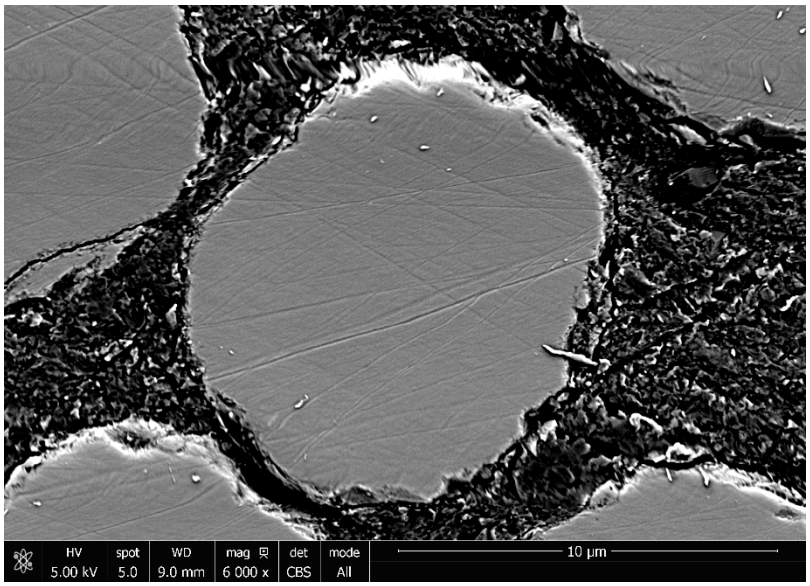


Figure 240 - SEM electron backscatter deflection micrograph of the Hi-Nicalon™ S specimen "Air 3" examining the cross section of the lower portion of a fiber (σ_{cr} = 700 MPa, t_f = 62.5 h).

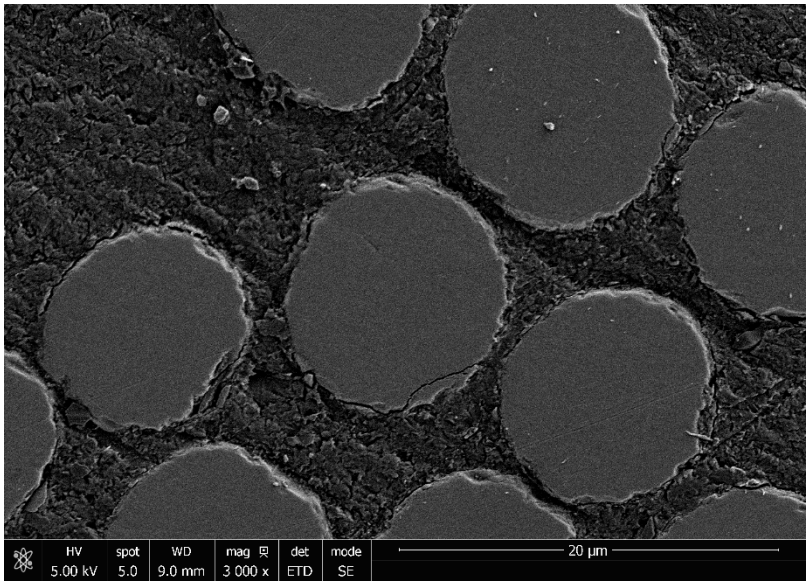


Figure 241 - SEM micrograph of the Hi-Nicalon™ S specimen "Air 3" examining the cross section of the lower portion of a fiber (σ_{cr} = 700 MPa, t_f = 62.5 h).

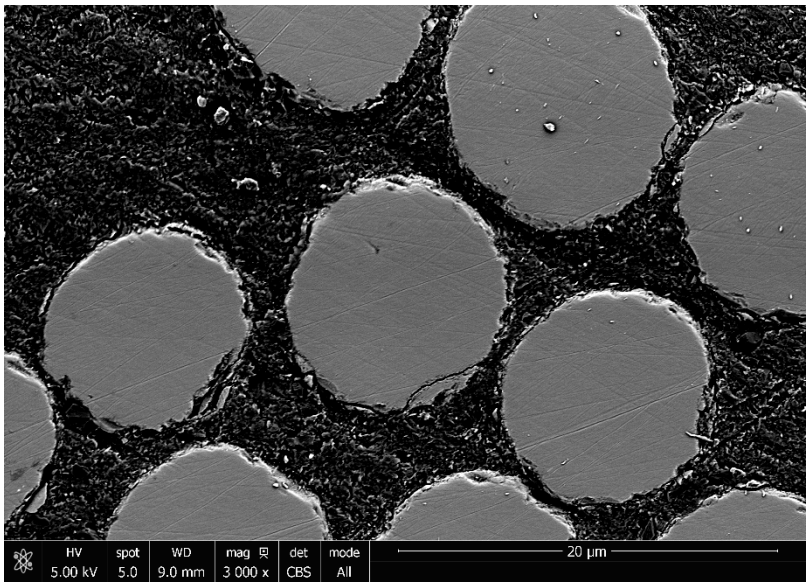


Figure 242 - SEM electron backscatter deflection micrograph of the Hi-Nicalon™ S specimen "Air 3" examining the cross section of the lower portion of a fiber (σ_{cr} = 700 MPa, t_f = 62.5 h).

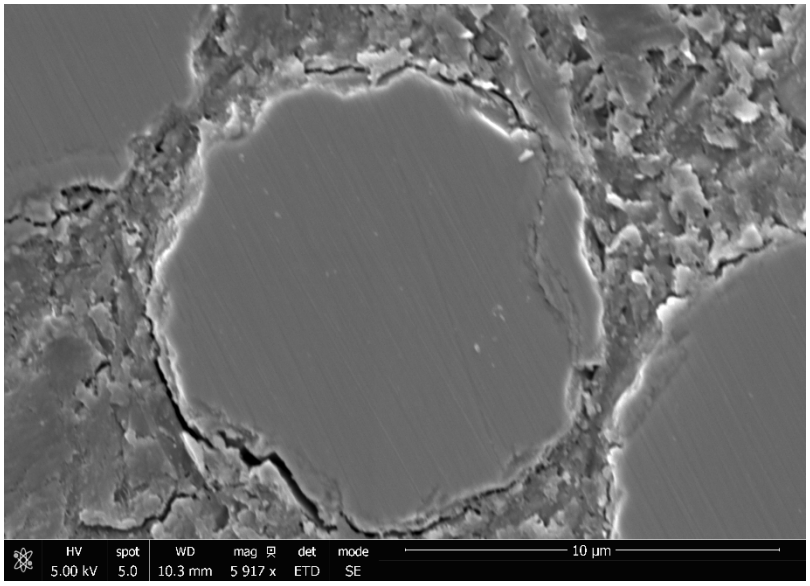


Figure 243 - SEM micrograph of the Hi-Nicalon™ S specimen "Air 10" examining the cross section of the lower portion of a fiber (σ_{cr} = 800 MPa, t_f = 31.0 h).

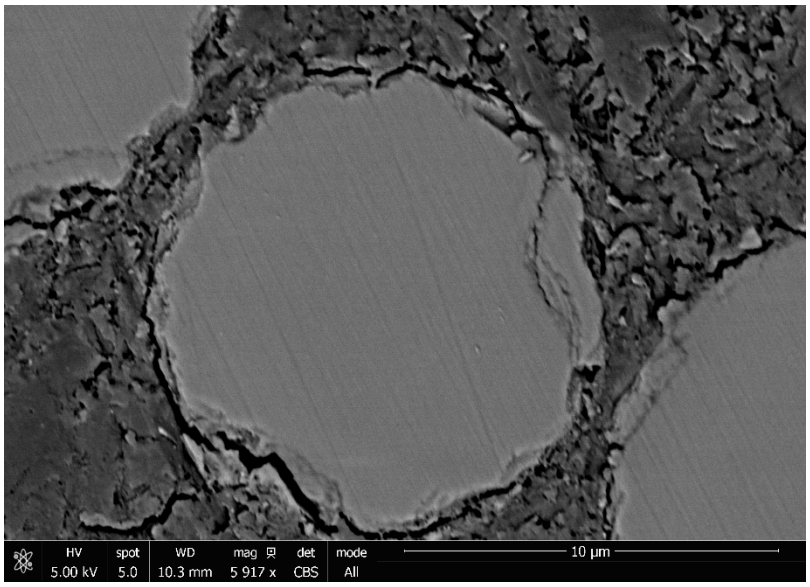


Figure 244 - SEM electron backscatter deflection micrograph of the Hi-Nicalon™ S specimen "Air 10" examining the cross section of the lower portion of a fiber (σ_{cr} = 800 MPa, t_f = 31.0 h).

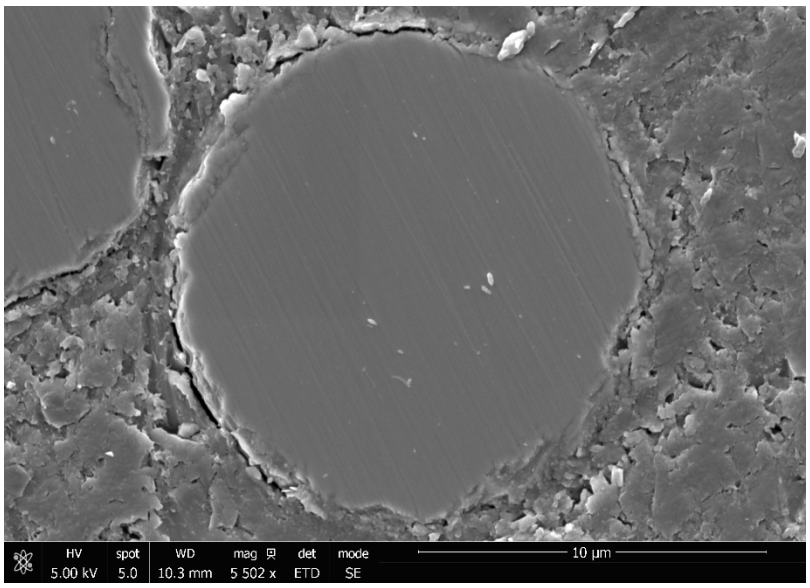


Figure 245 - SEM micrograph of the Hi-Nicalon™ S specimen "Air 10" examining the cross section of the lower portion of a fiber (σ_{cr} = 800 MPa, t_f = 31.0 h).

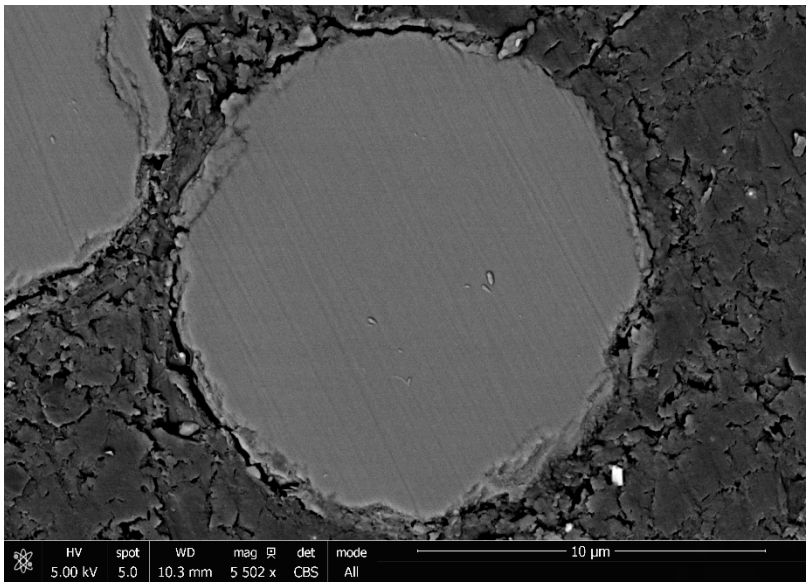


Figure 246 - SEM electron backscatter deflection micrograph of the Hi-Nicalon™ S specimen "Air 10" examining the cross section of the lower portion of a fiber (σ_{cr} = 800 MPa, t_f = 31.0 h).

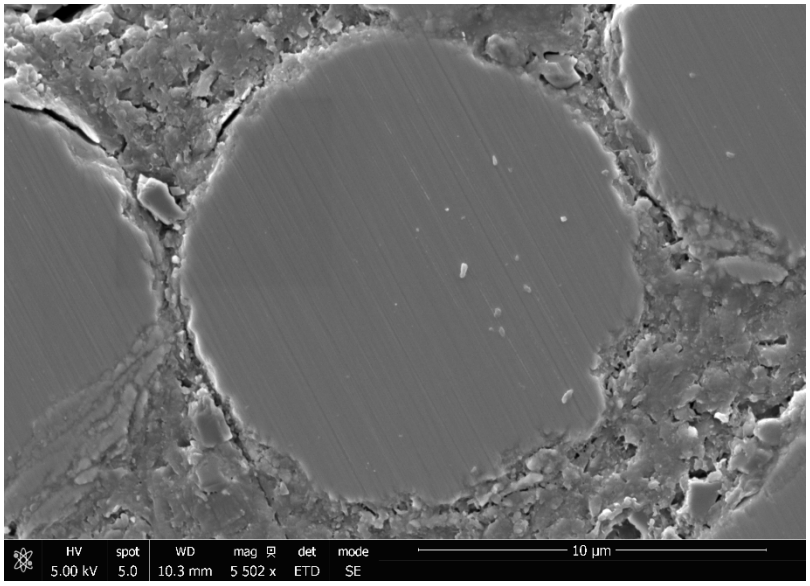


Figure 247 - SEM micrograph of the Hi-Nicalon™ S specimen "Air 10" examining the cross section of the lower portion of a fiber (σ_{cr} = 800 MPa, t_f = 31.0 h).

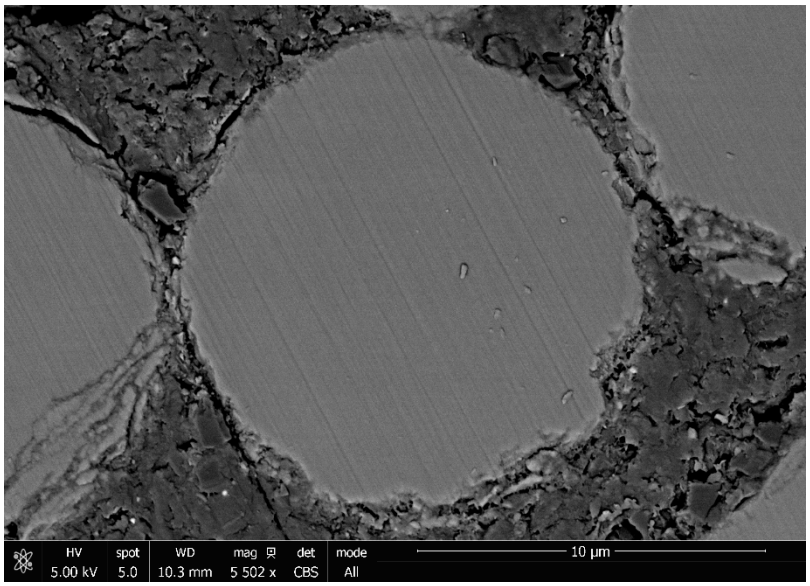


Figure 248 - SEM electron backscatter deflection micrograph of the Hi-Nicalon™ S specimen "Air 10" examining the cross section of the lower portion of a fiber (σ_{cr} = 800 MPa, t_f = 31.0 h).

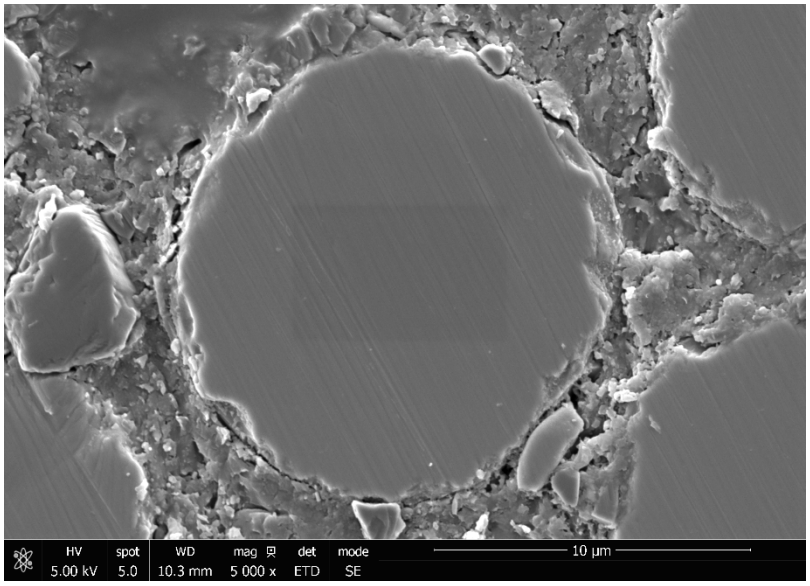


Figure 249 - SEM micrograph of the Hi-Nicalon™ S specimen "Air 10" examining the cross section of the lower portion of a fiber (σ_{cr} = 800 MPa, t_f = 31.0 h).

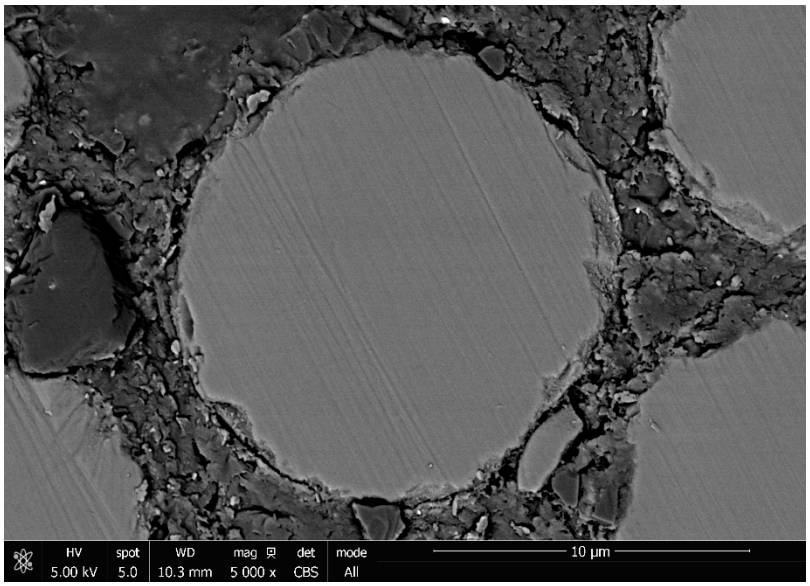


Figure 250 - SEM electron backscatter deflection micrograph of the Hi-Nicalon™ S specimen "Air 10" examining the cross section of the lower portion of a fiber (σ_{cr} = 800 MPa, t_f = 31.0 h).

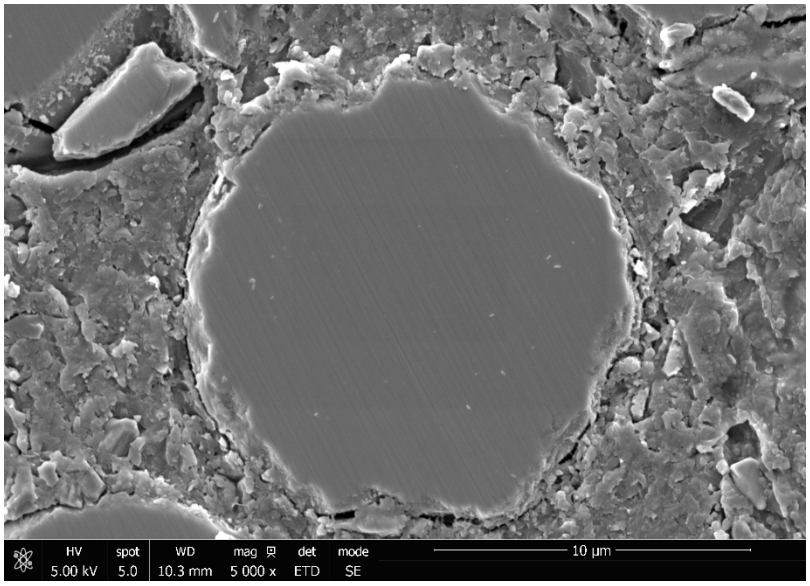


Figure 251 - SEM micrograph of the Hi-Nicalon™ S specimen "Air 10" examining the cross section of the lower portion of a fiber (σ_{cr} = 800 MPa, t_f = 31.0 h).

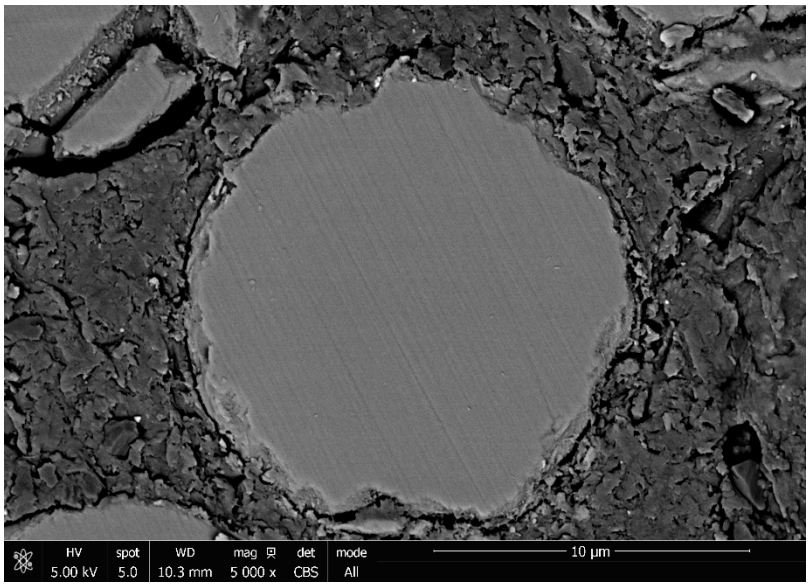


Figure 252 - SEM electron backscatter deflection micrograph of the Hi-Nicalon™ S specimen "Air 10" examining the cross section of the lower portion of a fiber (σ_{cr} = 800 MPa, t_f = 31.0 h).

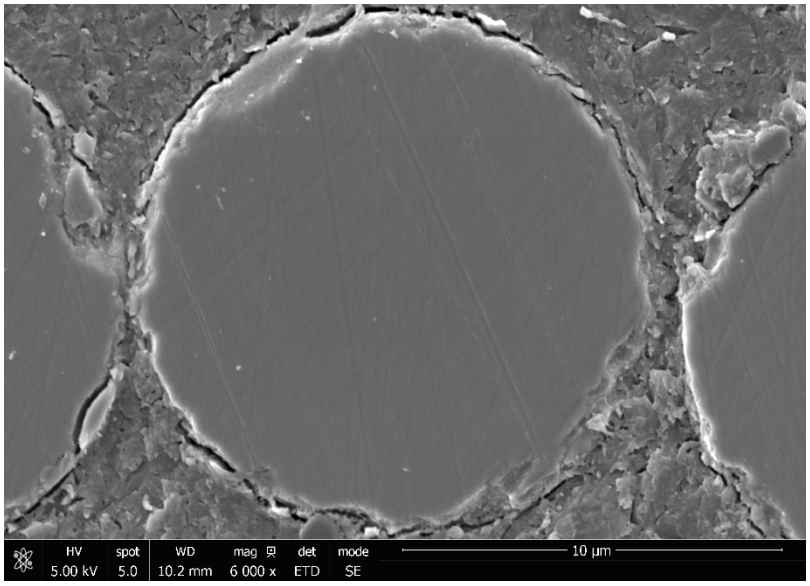


Figure 253 - SEM micrograph of the Hi-Nicalon™ S specimen "Air 10" examining the cross section of the lower portion of a fiber (σ_{cr} = 800 MPa, t_f = 31.0 h).

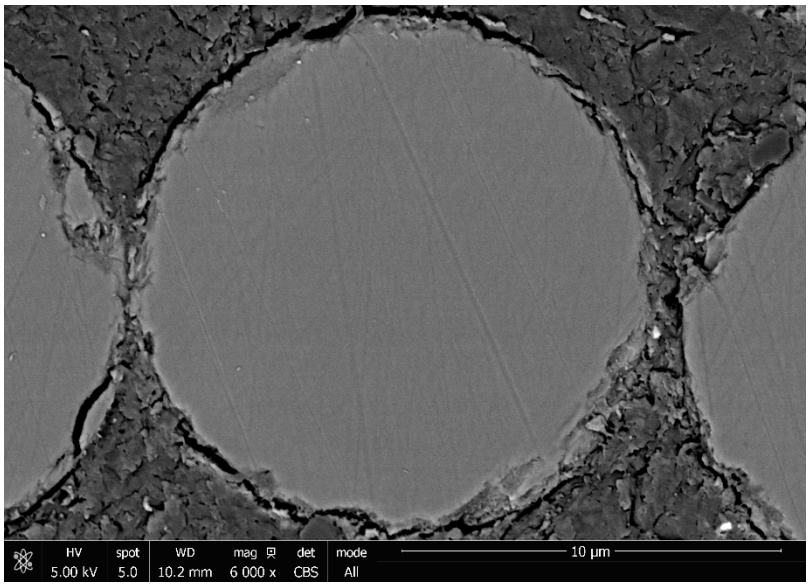


Figure 254 - SEM electron backscatter deflection micrograph of the Hi-Nicalon™ S specimen "Air 10" examining the cross section of the lower portion of a fiber (σ_{cr} = 800 MPa, t_f = 31.0 h).

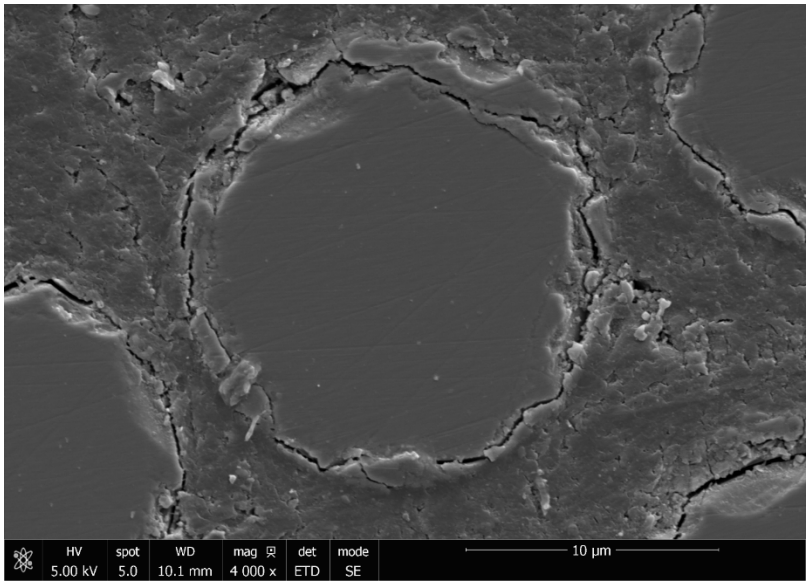


Figure 255 - SEM micrograph of the Hi-Nicalon™ S specimen "Air 10" examining the cross section of the upper portion of a fiber (σ_{cr} = 800 MPa, t_f = 31.0 h).

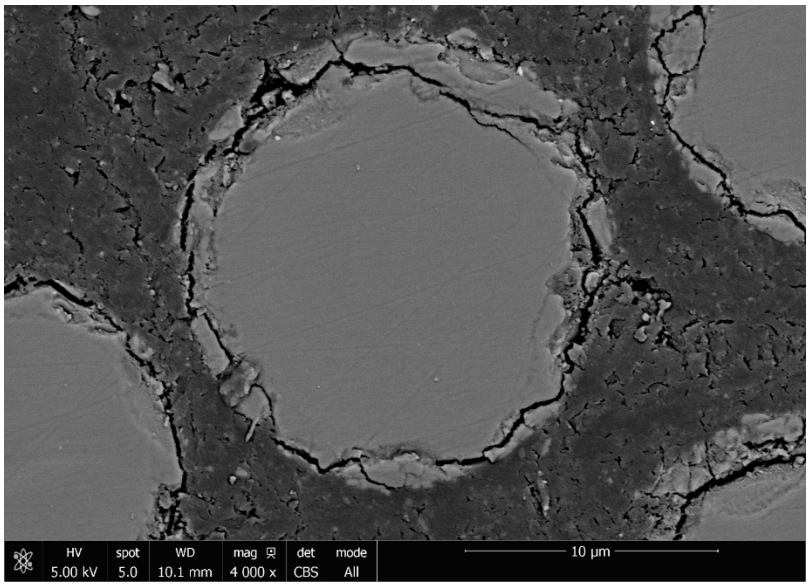


Figure 256 - SEM electron backscatter deflection micrograph of the Hi-Nicalon™ S specimen "Air 10" examining the cross section of the upper portion of a fiber (σ_{cr} = 800 MPa, t_f = 31.0 h).

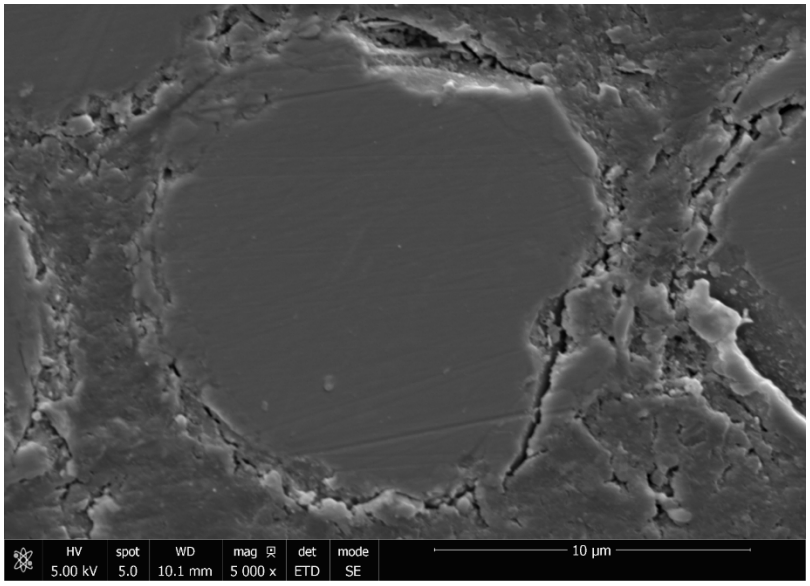


Figure 257 - SEM micrograph of the Hi-Nicalon™ S specimen "Air 10" examining the cross section of the upper portion of a fiber (σ_{cr} = 800 MPa, t_f = 31.0 h).

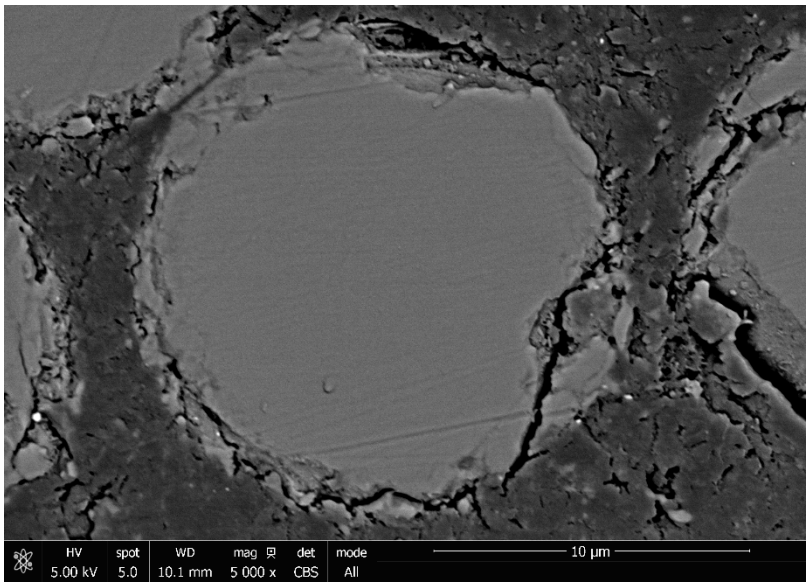


Figure 258 - SEM electron backscatter deflection micrograph of the Hi-Nicalon™ S specimen "Air 10" examining the cross section of the upper portion of a fiber (σ_{cr} = 800 MPa, t_f = 31.0 h).

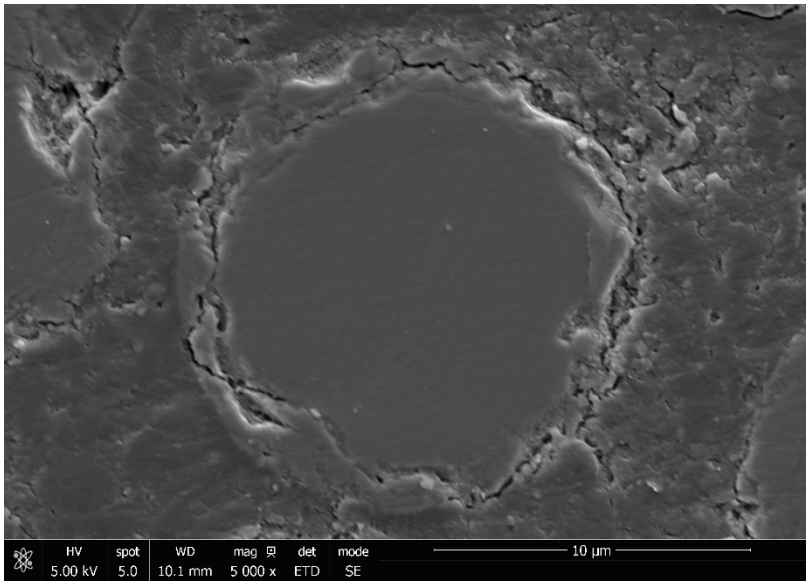


Figure 259 - SEM micrograph of the Hi-Nicalon™ S specimen "Air 10" examining the cross section of the upper portion of a fiber (σ_{cr} = 800 MPa, t_f = 31.0 h).

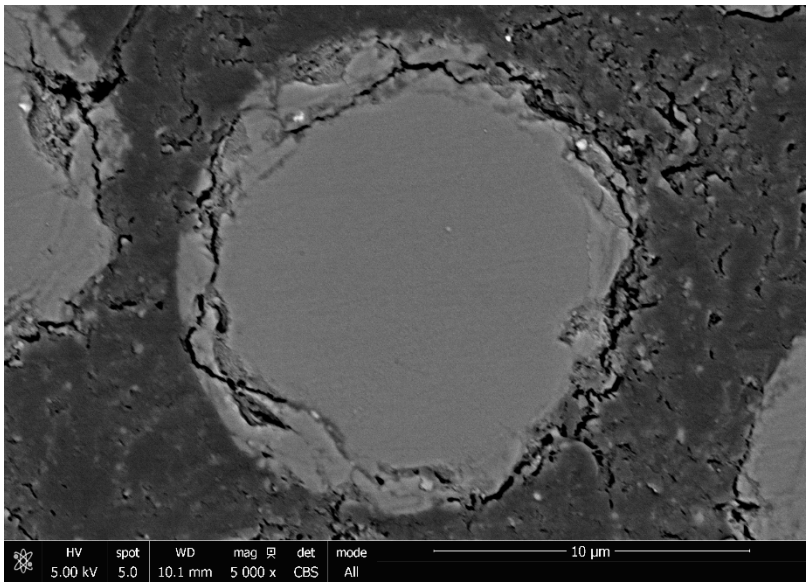


Figure 260 - SEM electron backscatter deflection micrograph of the Hi-Nicalon™ S specimen "Air 10" examining the cross section of the upper portion of a fiber (σ_{cr} = 800 MPa, t_f = 31.0 h).

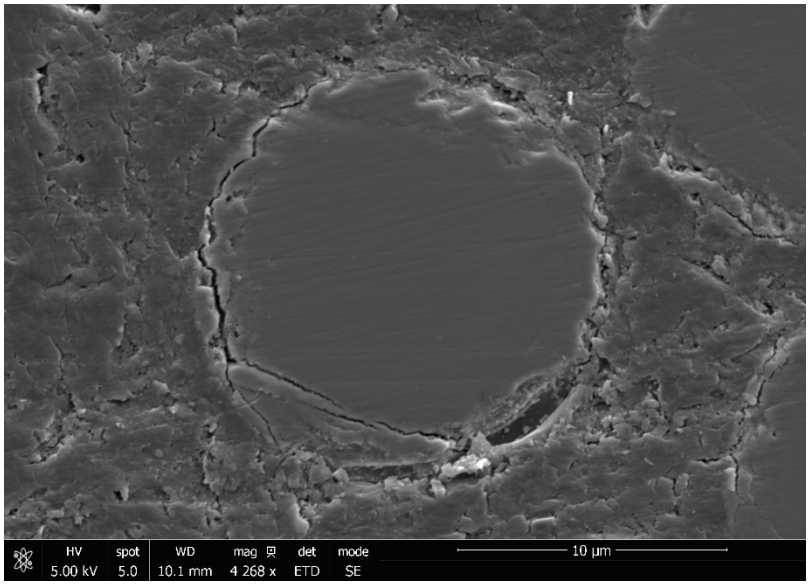


Figure 261 - SEM micrograph of the Hi-Nicalon™ S specimen "Air 10" examining the cross section of the upper portion of a fiber (σ_{cr} = 800 MPa, t_f = 31.0 h).

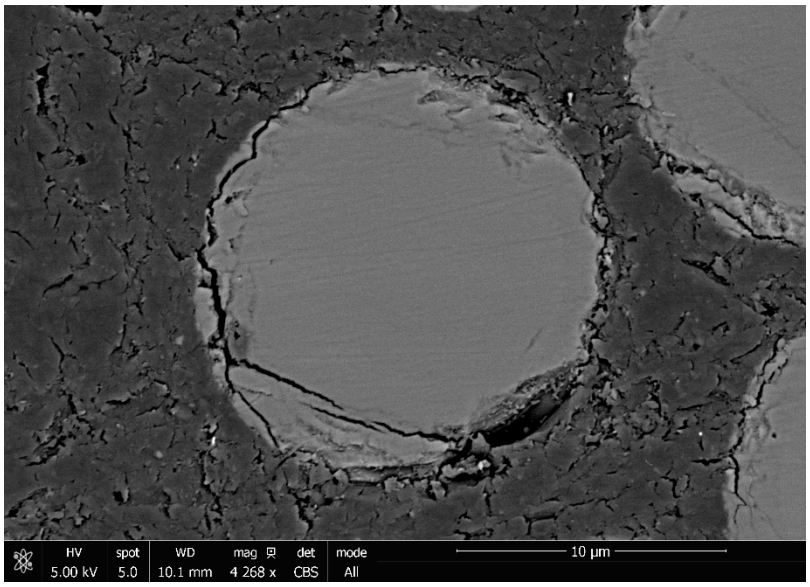


Figure 262 - SEM electron backscatter deflection micrograph of the Hi-Nicalon™ S specimen "Air 10" examining the cross section of the upper portion of a fiber (σ_{cr} = 800 MPa, t_f = 31.0 h).

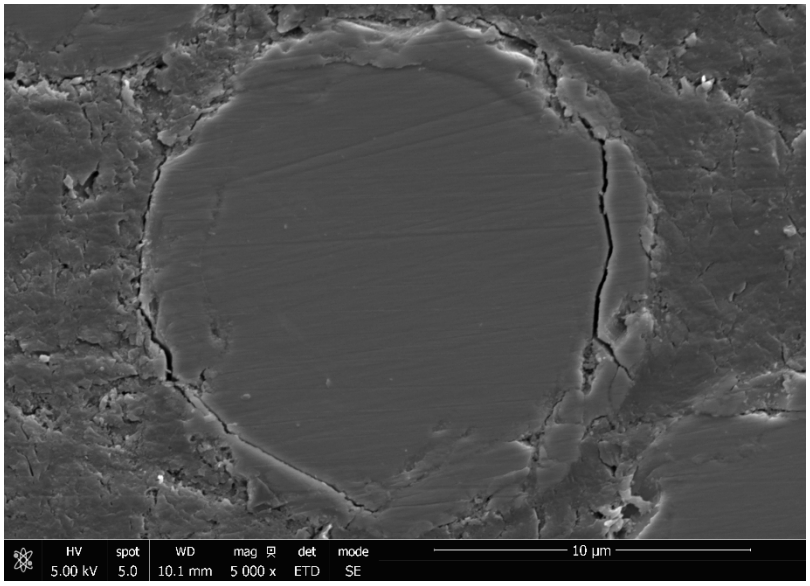


Figure 263 - SEM micrograph of the Hi-Nicalon™ S specimen "Air 10" examining the cross section of the upper portion of a fiber (σ_{cr} = 800 MPa, t_f = 31.0 h).

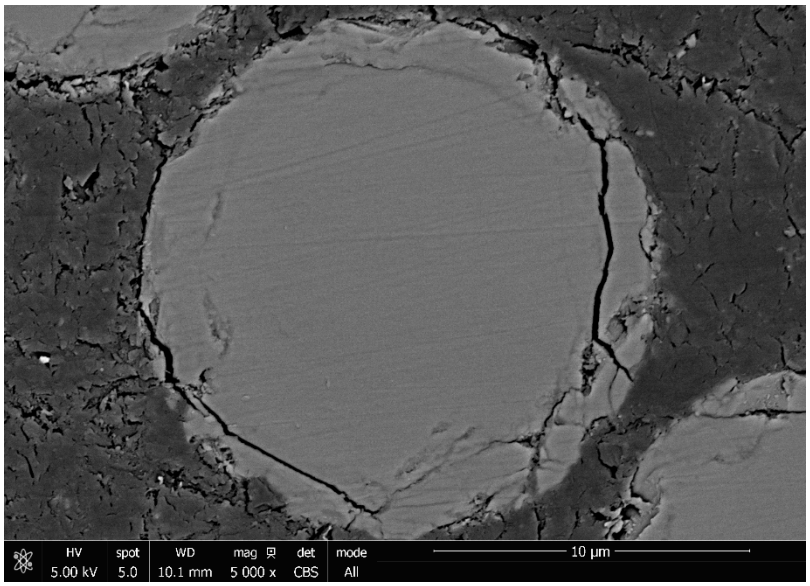


Figure 264 - SEM electron backscatter deflection micrograph of the Hi-Nicalon™ S specimen "Air 10" examining the cross section of the upper portion of a fiber (σ_{cr} = 800 MPa, t_f = 31.0 h).

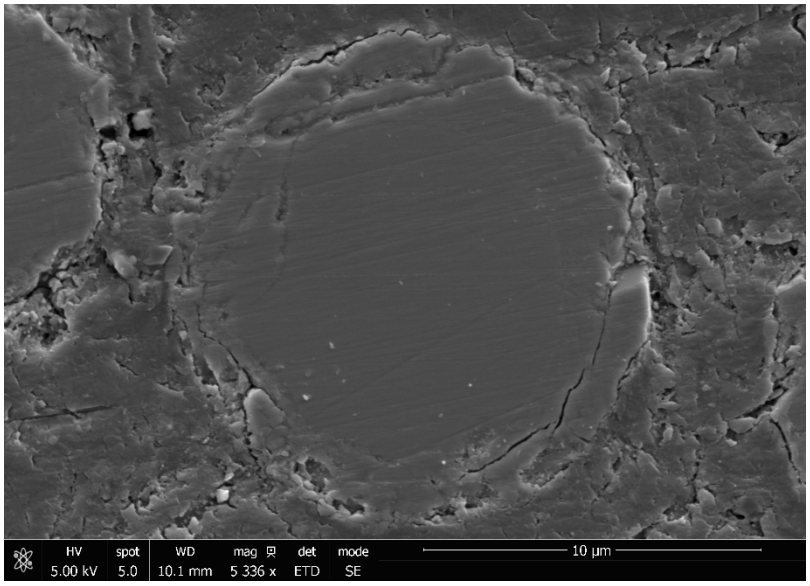


Figure 265 - SEM micrograph of the Hi-Nicalon™ S specimen "Air 10" examining the cross section of the upper portion of a fiber (σ_{cr} = 800 MPa, t_f = 31.0 h).

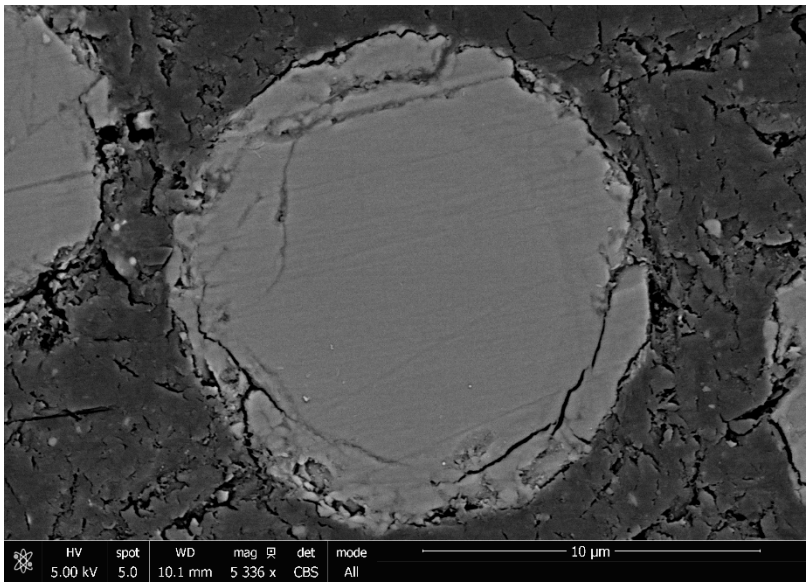


Figure 266 - SEM electron backscatter deflection micrograph of the Hi-Nicalon™ S specimen "Air 10" examining the cross section of the upper portion of a fiber (σ_{cr} = 800 MPa, t_f = 31.0 h).

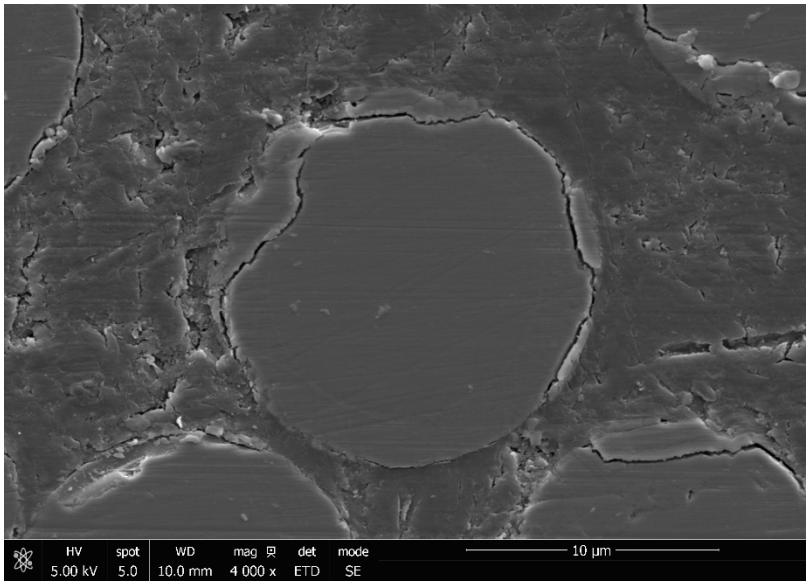


Figure 267 - SEM micrograph of the Hi-Nicalon™ S specimen "Air 10" examining the cross section of the upper portion of a fiber (σ_{cr} = 800 MPa, t_f = 31.0 h).

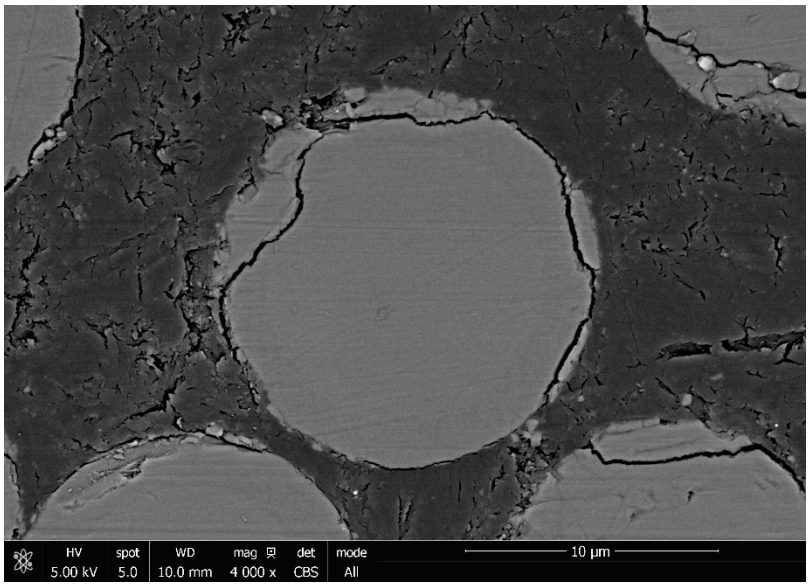


Figure 268 - SEM electron backscatter deflection micrograph of the Hi-Nicalon™ S specimen "Air 10" examining the cross section of the upper portion of a fiber (σ_{cr} = 800 MPa, t_f = 31.0 h).

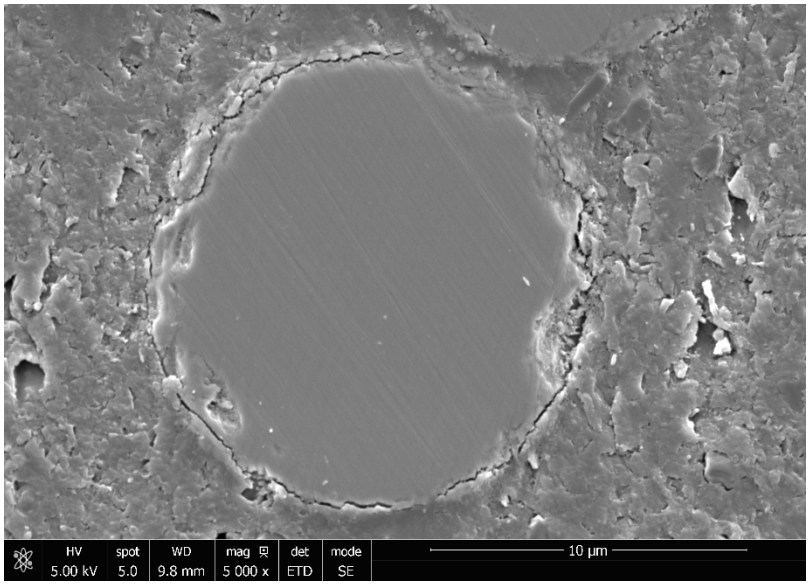


Figure 269 - SEM micrograph of the Hi-Nicalon™ S specimen "Steam 2" examining the cross section at the midpoint of a fiber (σ_{cr} = 3.5 MPa, t_f = 100 h).

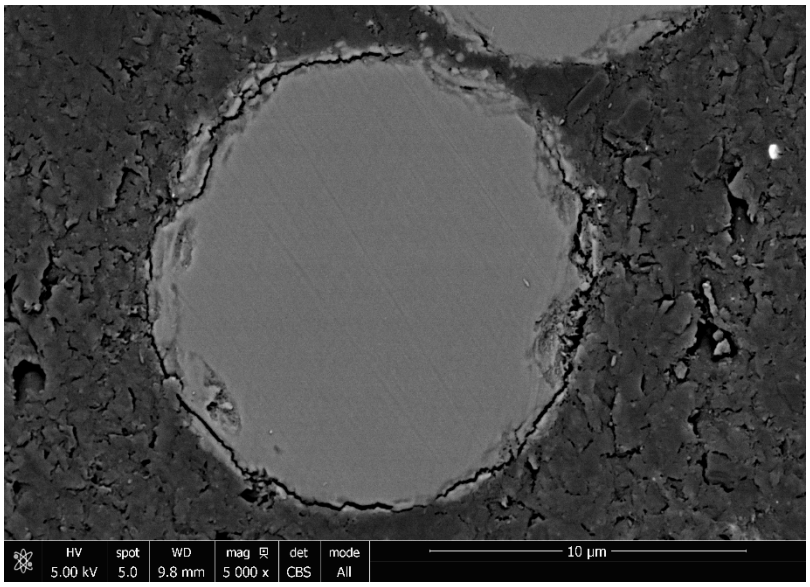


Figure 270 - SEM electron backscatter deflection micrograph of the Hi-Nicalon™ S specimen "Steam 2" examining the cross section at the midpoint of a fiber (σ_{cr} = 3.5 MPa, t_f = 100 h).

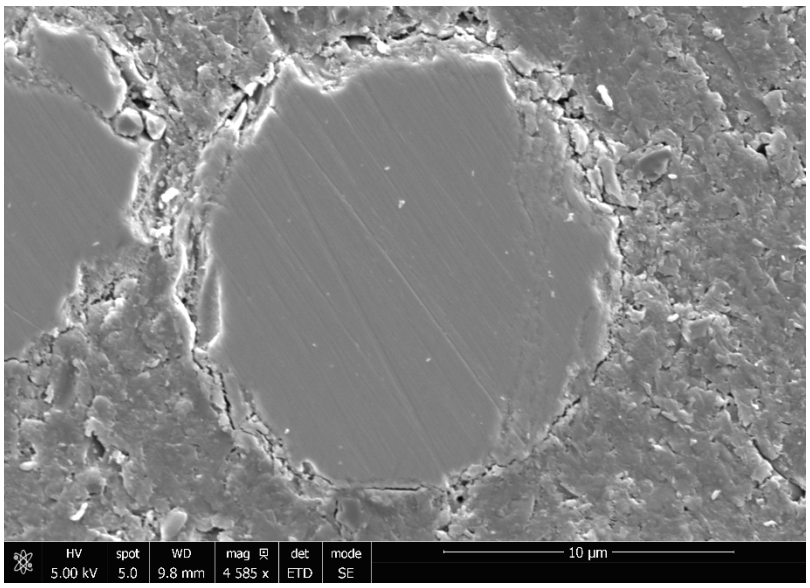


Figure 271 - SEM micrograph of the Hi-Nicalon™ S specimen "Steam 2" examining the cross section at the midpoint of a fiber (σ_{cr} = 3.5 MPa, t_f = 100 h).

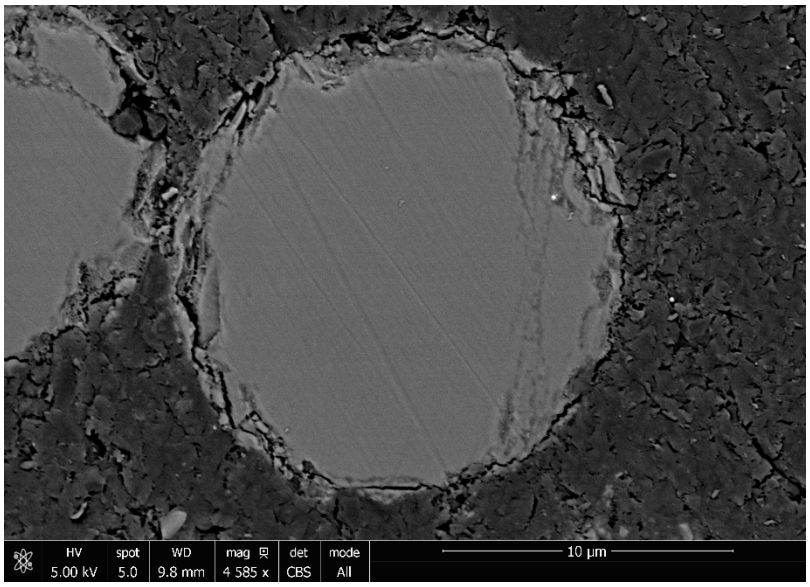


Figure 272 - SEM electron backscatter deflection micrograph of the Hi-Nicalon™ S specimen "Steam 2" examining the cross section at the midpoint of a fiber (σ_{cr} = 3.5 MPa, t_f = 100 h).

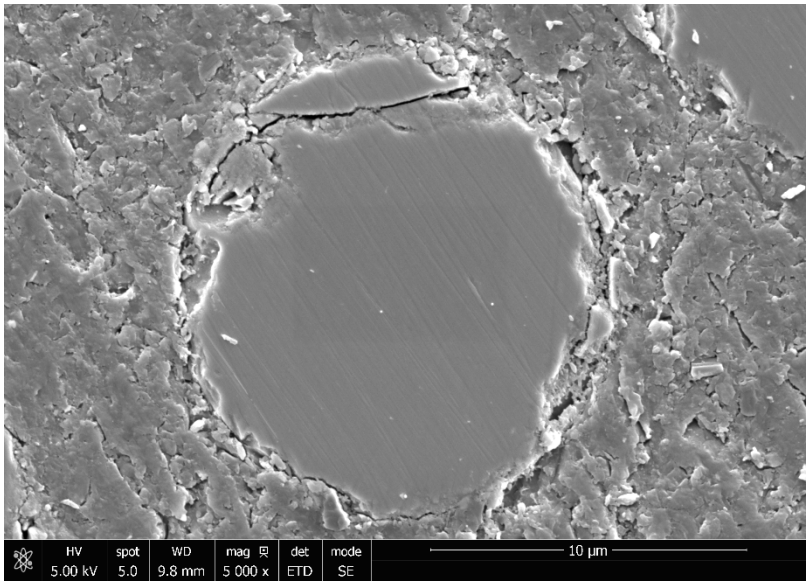


Figure 273 - SEM micrograph of the Hi-Nicalon™ S specimen "Steam 2" examining the cross section at the midpoint of a fiber (σ_{cr} = 3.5 MPa, t_f = 100 h).

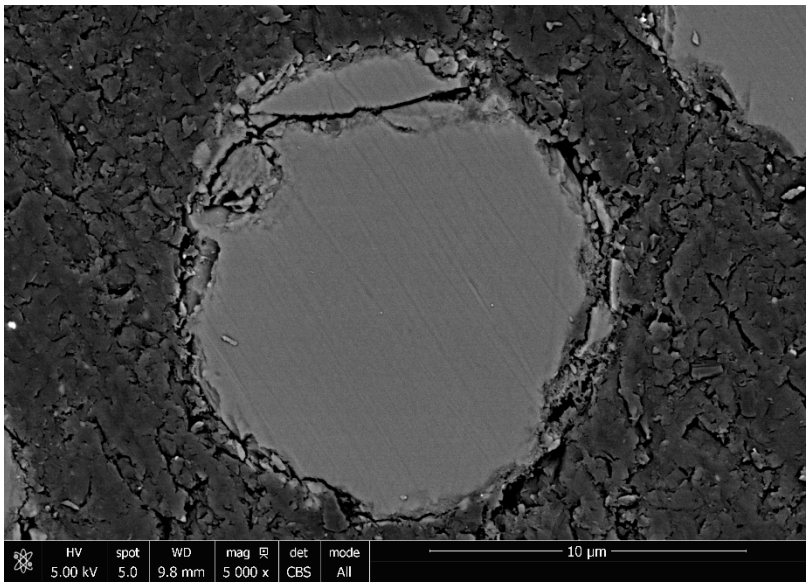


Figure 274 - SEM electron backscatter deflection micrograph of the Hi-Nicalon™ S specimen "Steam 2" examining the cross section at the midpoint of a fiber (σ_{cr} = 3.5 MPa, t_f = 100 h).

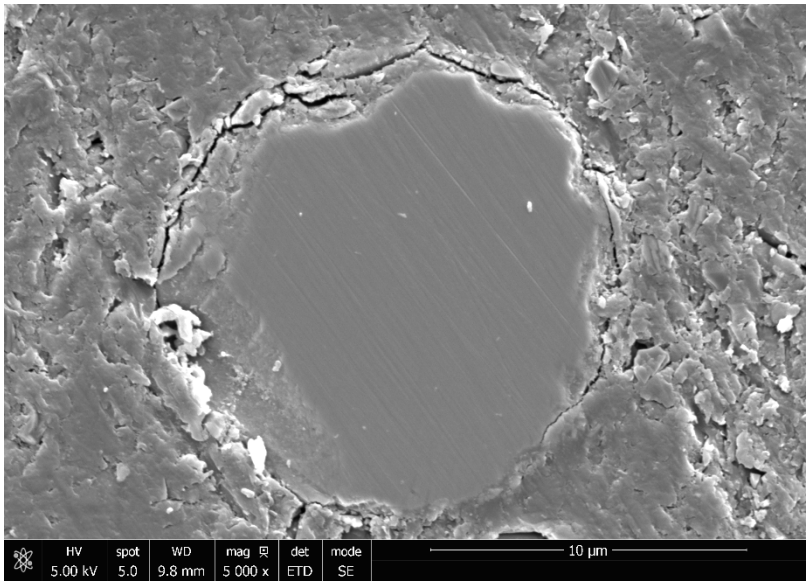


Figure 275 - SEM micrograph of the Hi-Nicalon™ S specimen "Steam 2" examining the cross section at the midpoint of a fiber (σ_{cr} = 3.5 MPa, t_f = 100 h).

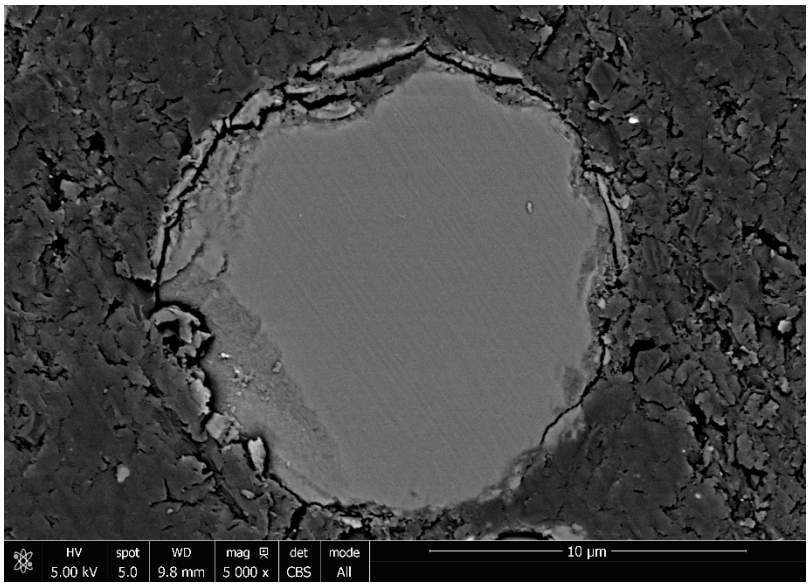


Figure 276 - SEM electron backscatter deflection micrograph of the Hi-Nicalon™ S specimen "Steam 2" examining the cross section at the midpoint of a fiber (σ_{cr} = 3.5 MPa, t_f = 100 h).

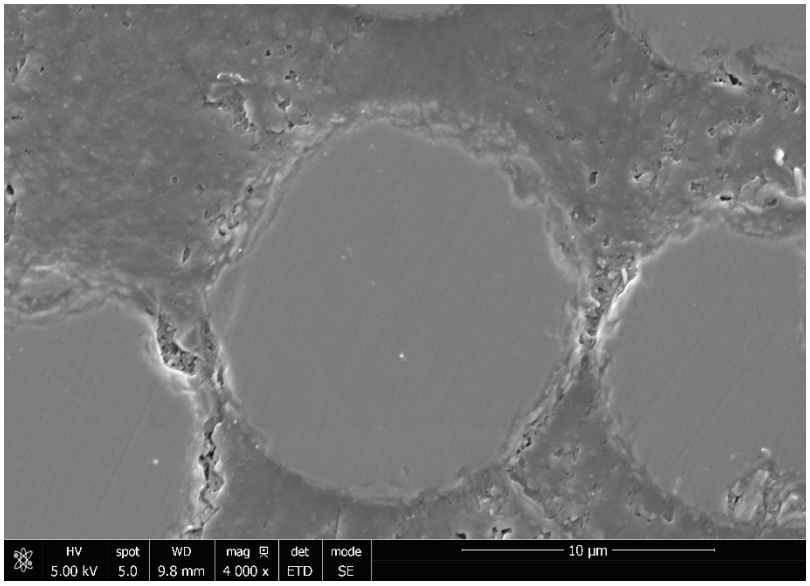


Figure 277 - SEM micrograph of the Hi-Nicalon™ S specimen "Steam 2" examining the cross section at the midpoint of a fiber (σ_{cr} = 3.5 MPa, t_f = 100 h).

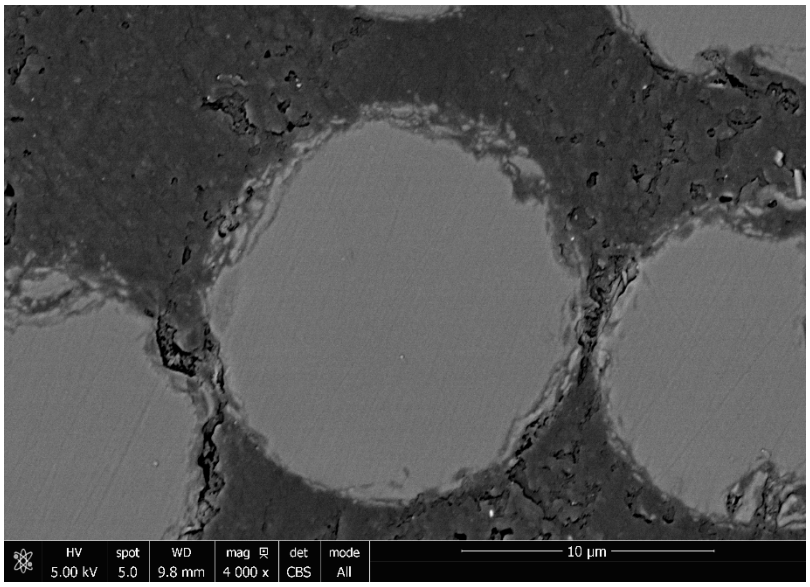


Figure 278 - SEM electron backscatter deflection micrograph of the Hi-Nicalon™ S specimen "Steam 2" examining the cross section at the midpoint of a fiber (σ_{cr} = 3.5 MPa, t_f = 100 h).

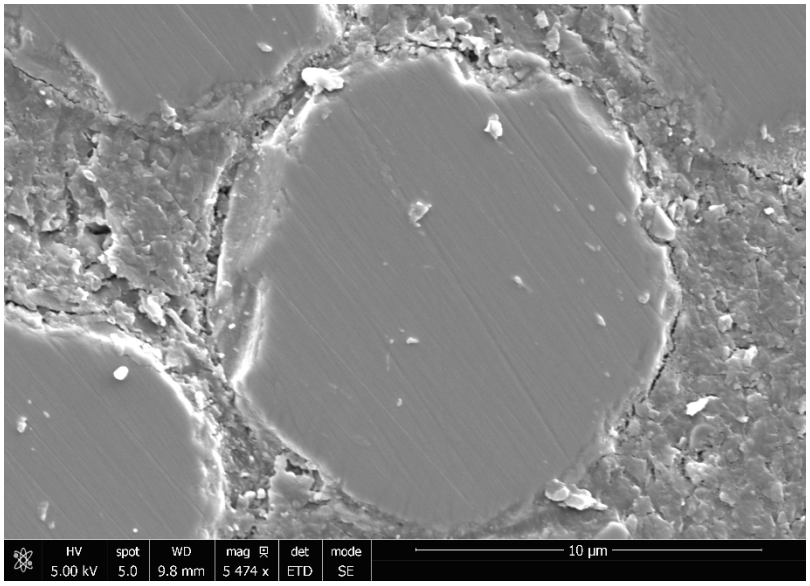


Figure 279 - SEM micrograph of the Hi-Nicalon™ S specimen "Steam 2" examining the cross section at the midpoint of a fiber (σ_{cr} = 3.5 MPa, t_f = 100 h).

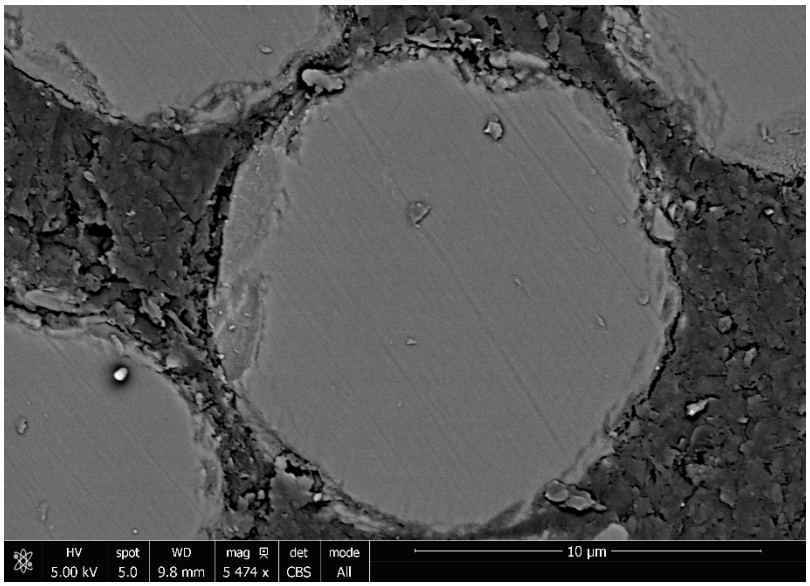


Figure 280 - SEM electron backscatter deflection micrograph of the Hi-Nicalon™ S specimen "Steam 2" examining the cross section at the midpoint of a fiber (σ_{cr} = 3.5 MPa, t_f = 100 h).

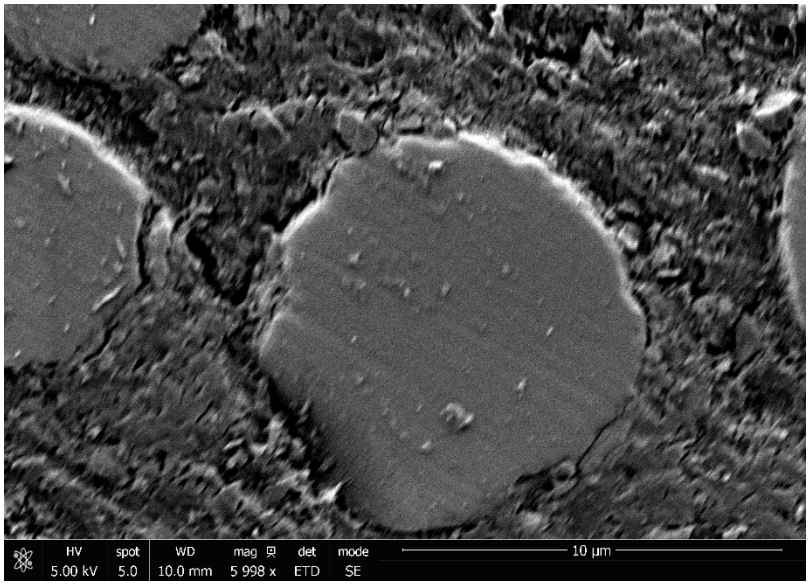


Figure 281 - SEM micrograph of the Hi-Nicalon™ S specimen "Steam 5" examining the cross section the lower portion of a fiber (σ_{cr} = 400 MPa, t_f = 30.83 h).

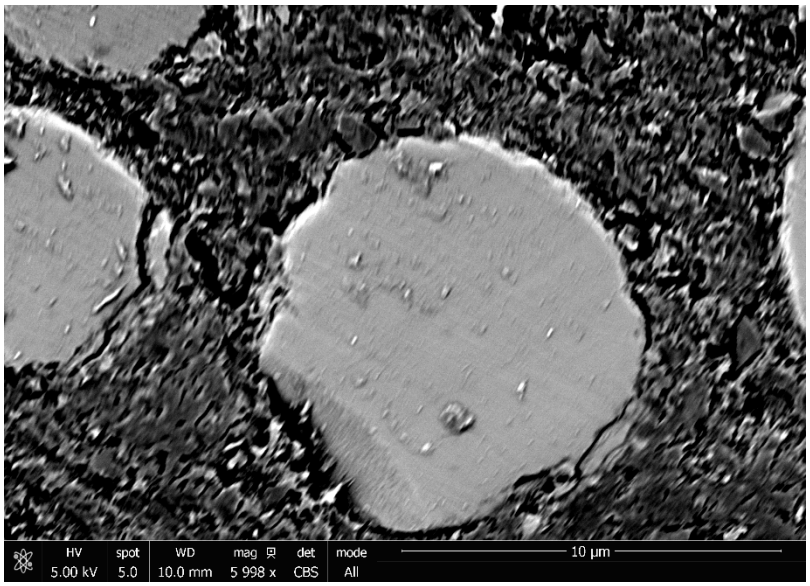


Figure 282 - SEM electron backscatter deflection micrograph of the Hi-Nicalon™ S specimen "Steam 5" examining the cross section the lower portion of a fiber (σ_{cr} = 400 MPa, t_f = 30.83 h).

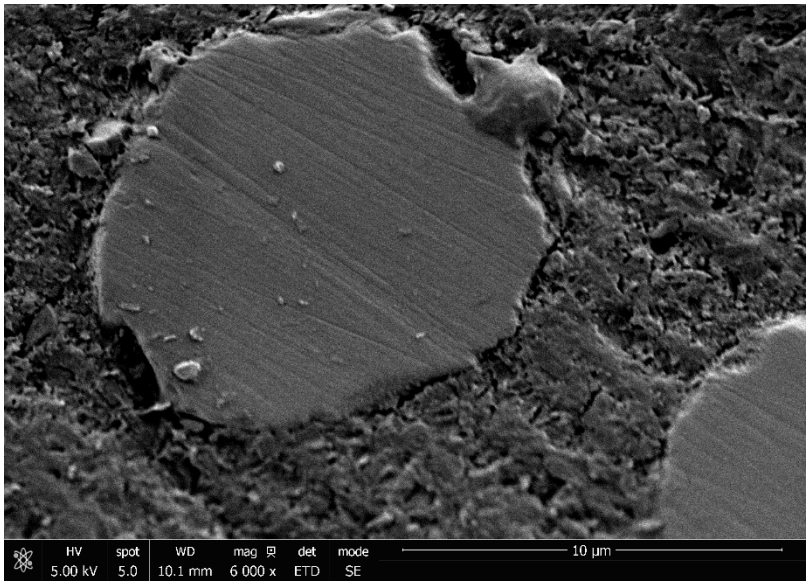


Figure 283 - SEM micrograph of the Hi-Nicalon™ S specimen "Steam 5" examining the cross section the lower portion of a fiber (σ_{cr} = 400 MPa, t_f = 30.83 h).



Figure 284 - SEM electron backscatter deflection micrograph of the Hi-Nicalon™ S specimen "Steam 5" examining the cross section the lower portion of a fiber (σ_{cr} = 400 MPa, t_f = 30.83 h).

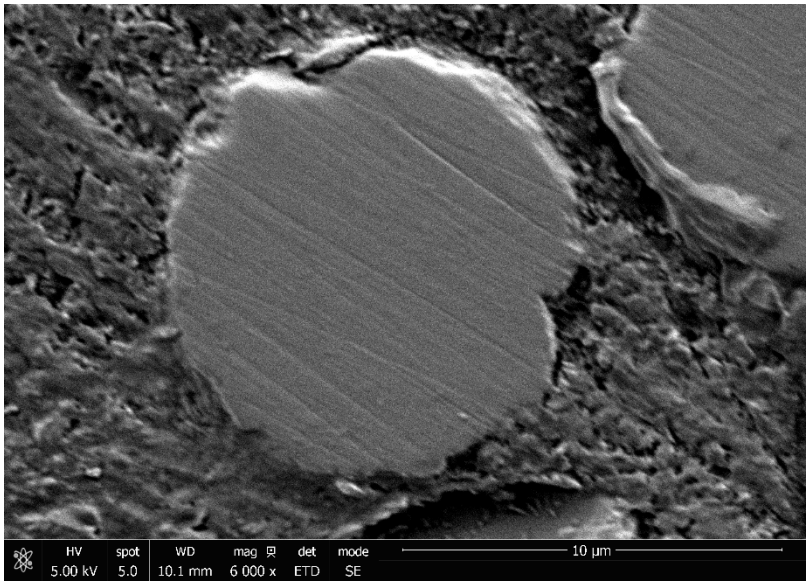


Figure 285 - SEM micrograph of the Hi-Nicalon™ S specimen "Steam 5" examining the cross section the lower portion of a fiber (σ_{cr} = 400 MPa, t_f = 30.83 h).

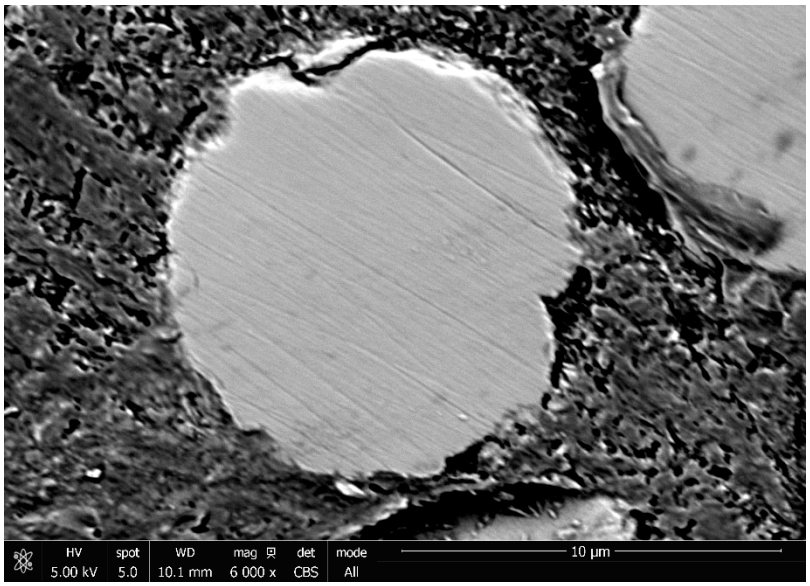


Figure 286 - SEM electron backscatter deflection micrograph of the Hi-Nicalon™ S specimen "Steam 5" examining the cross section the lower portion of a fiber (σ_{cr} = 400 MPa, t_f = 30.83 h).

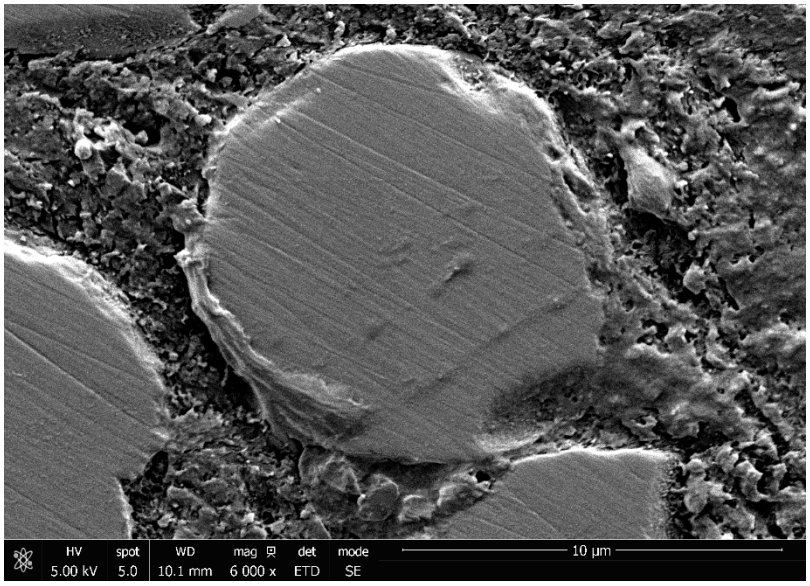


Figure 287 - SEM micrograph of the Hi-Nicalon™ S specimen "Steam 5" examining the cross section the lower portion of a fiber (σ_{cr} = 400 MPa, t_f = 30.83 h).

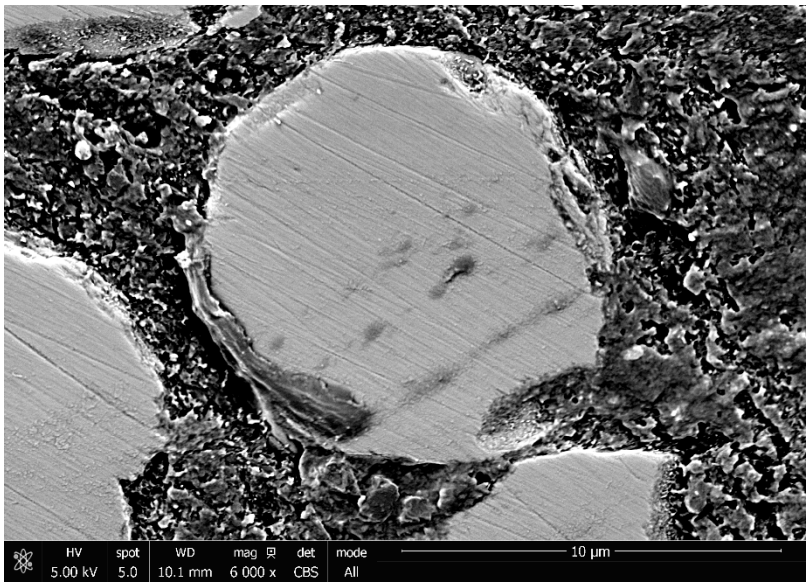


Figure 288 - SEM electron backscatter deflection micrograph of the Hi-Nicalon™ S specimen "Steam 5" examining the cross section the lower portion of a fiber (σ_{cr} = 400 MPa, t_f = 30.83 h).

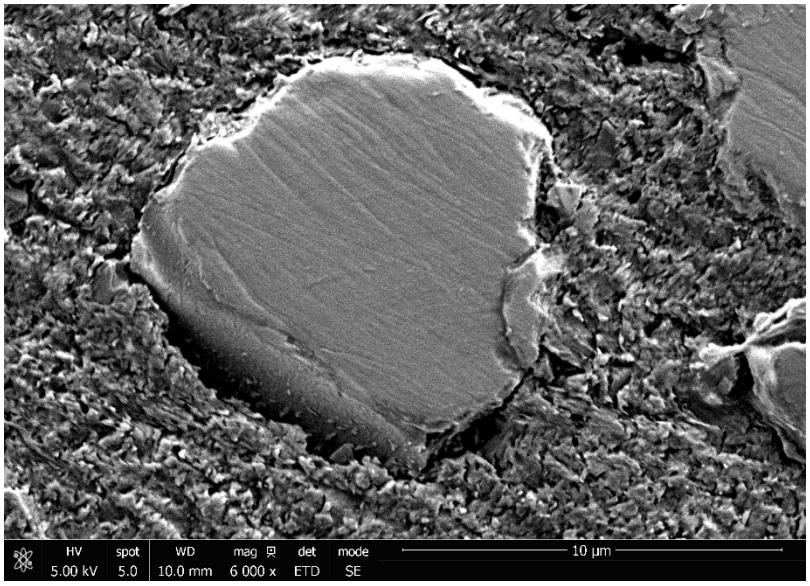


Figure 289 - SEM micrograph of the Hi-Nicalon™ S specimen "Steam 5" examining the cross section the lower portion of a fiber (σ_{cr} = 400 MPa, t_f = 30.83 h).

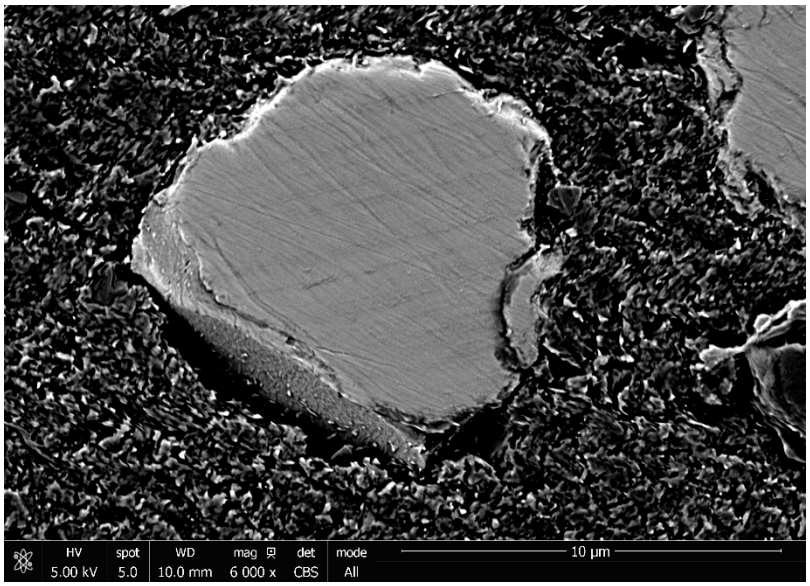


Figure 290 - SEM electron backscatter deflection micrograph of the Hi-Nicalon™ S specimen "Steam 5" examining the cross section the lower portion of a fiber (σ_{cr} = 400 MPa, t_f = 30.83 h).

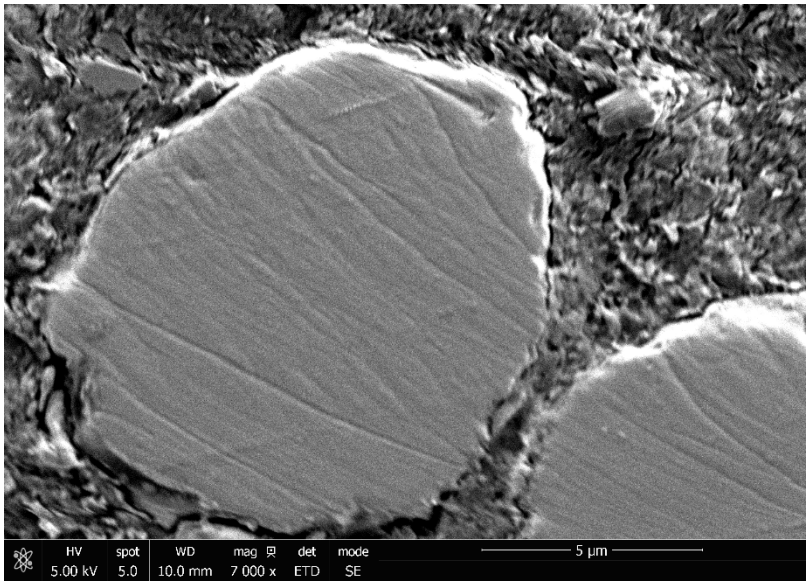


Figure 291 - SEM micrograph of the Hi-Nicalon™ S specimen "Steam 5" examining the cross section the lower portion of a fiber (σ_{cr} = 400 MPa, t_f = 30.83 h).

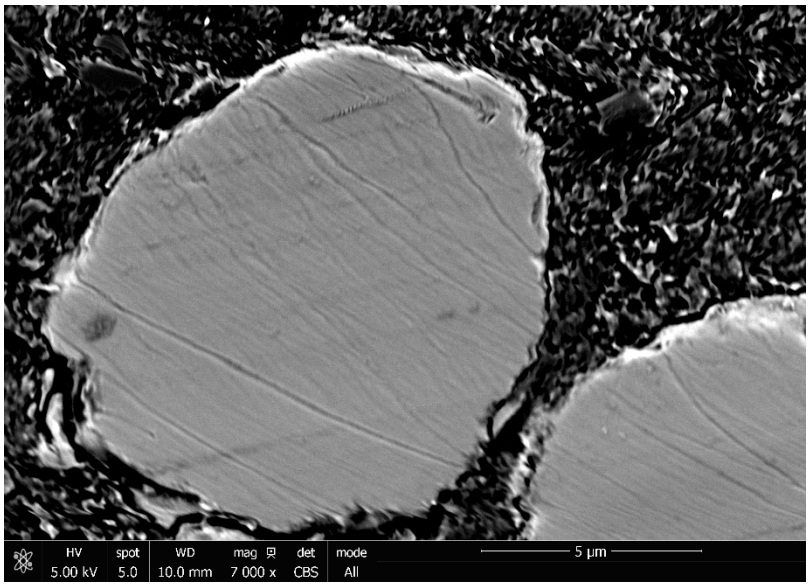


Figure 292 - SEM electron backscatter deflection micrograph of the Hi-Nicalon™ S specimen "Steam 5" examining the cross section the lower portion of a fiber (σ_{cr} = 400 MPa, t_f = 30.83 h).

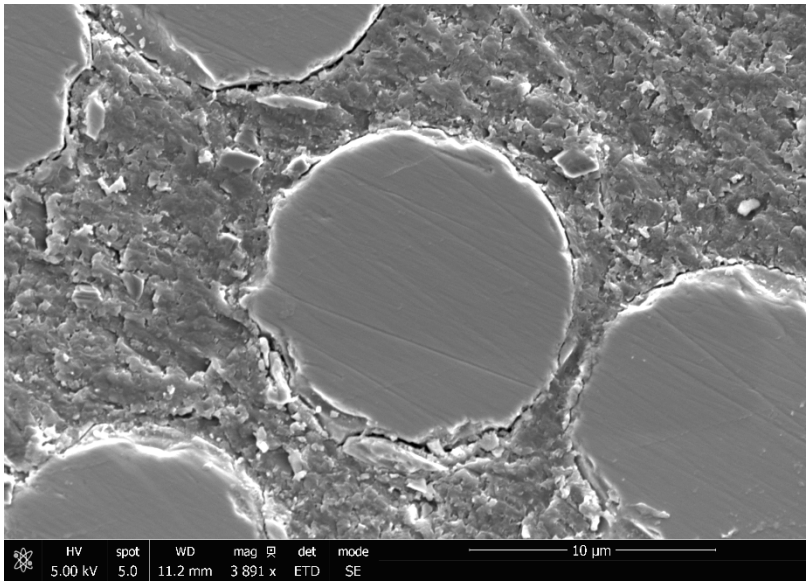


Figure 293 - SEM micrograph of the Hi-Nicalon™ S specimen "Steam 5" examining the cross section the lower portion of a fiber (σ_{cr} = 400 MPa, t_f = 30.83 h).

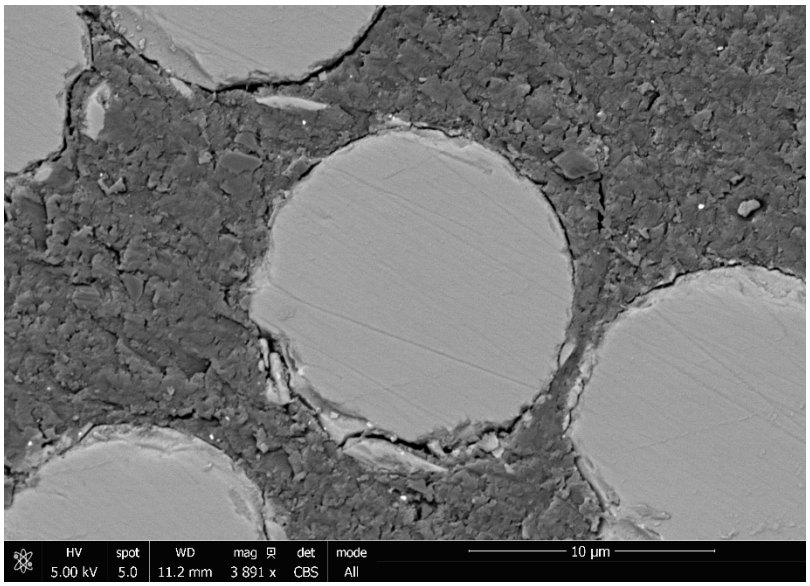


Figure 294 - SEM electron backscatter deflection micrograph of the Hi-Nicalon™ S specimen "Steam 5" examining the cross section the lower portion of a fiber (σ_{cr} = 400 MPa, t_f = 30.83 h).

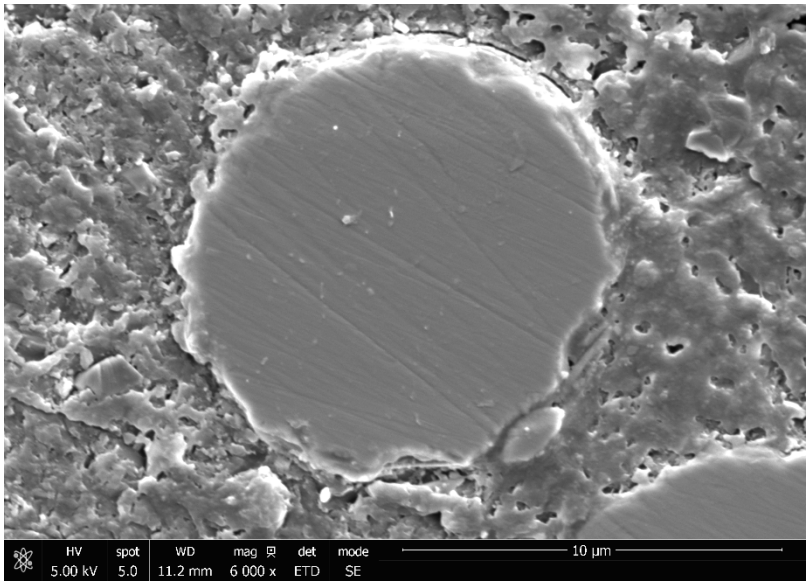


Figure 295 - SEM micrograph of the Hi-Nicalon™ S specimen "Steam 5" examining the cross section the lower portion of a fiber (σ_{cr} = 400 MPa, t_f = 30.83 h).

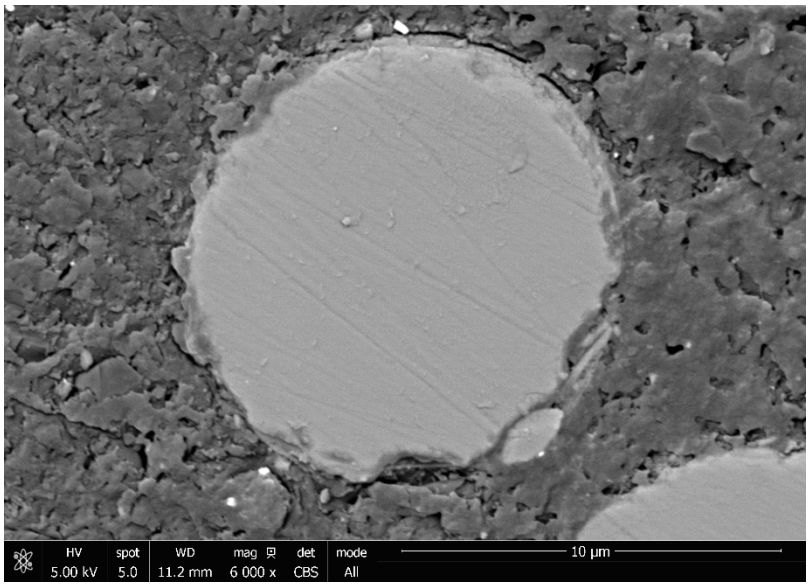


Figure 296 - SEM electron backscatter deflection micrograph of the Hi-Nicalon™ S specimen "Steam 5" examining the cross section the lower portion of a fiber (σ_{cr} = 400 MPa, t_f = 30.83 h).

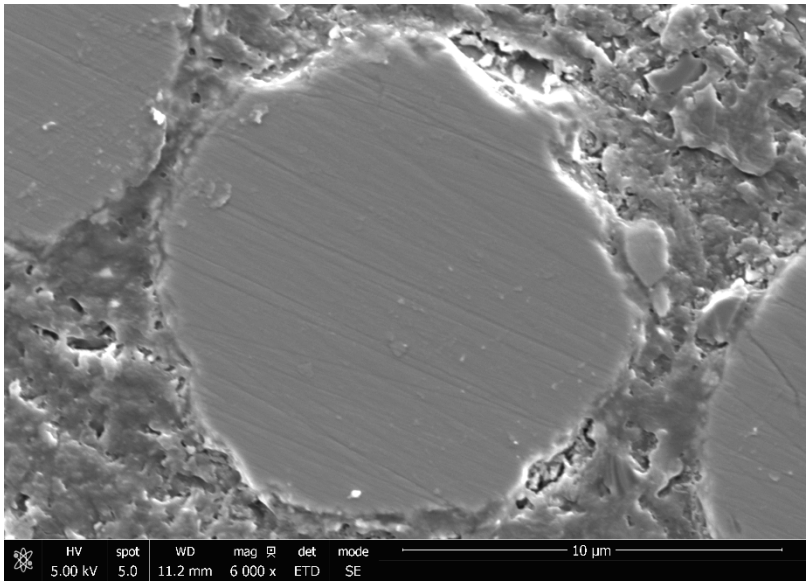


Figure 297 - SEM micrograph of the Hi-Nicalon™ S specimen "Steam 5" examining the cross section the lower portion of a fiber (σ_{cr} = 400 MPa, t_f = 30.83 h).

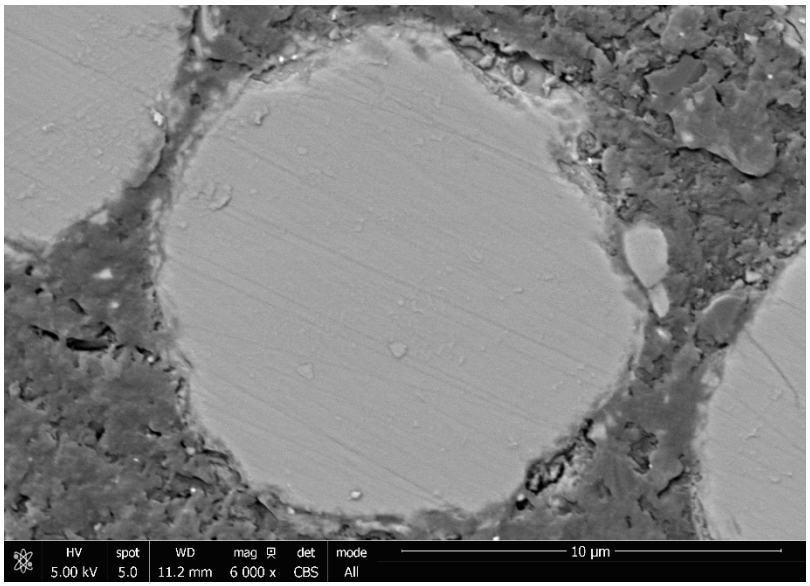


Figure 298 - SEM electron backscatter deflection micrograph of the Hi-Nicalon™ S specimen "Steam 5" examining the cross section the lower portion of a fiber (σ_{cr} = 400 MPa, t_f = 30.83 h).

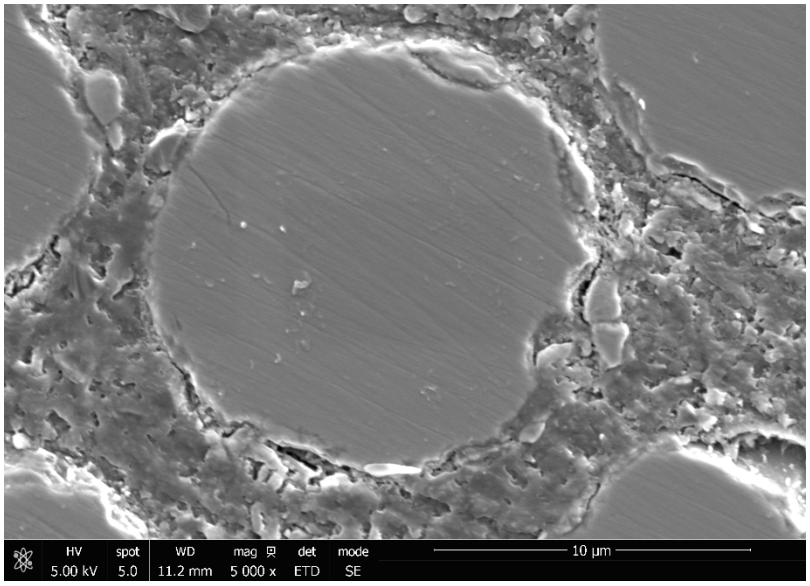


Figure 299 - SEM micrograph of the Hi-Nicalon™ S specimen "Steam 5" examining the cross section the lower portion of a fiber (σ_{cr} = 400 MPa, t_f = 30.83 h).

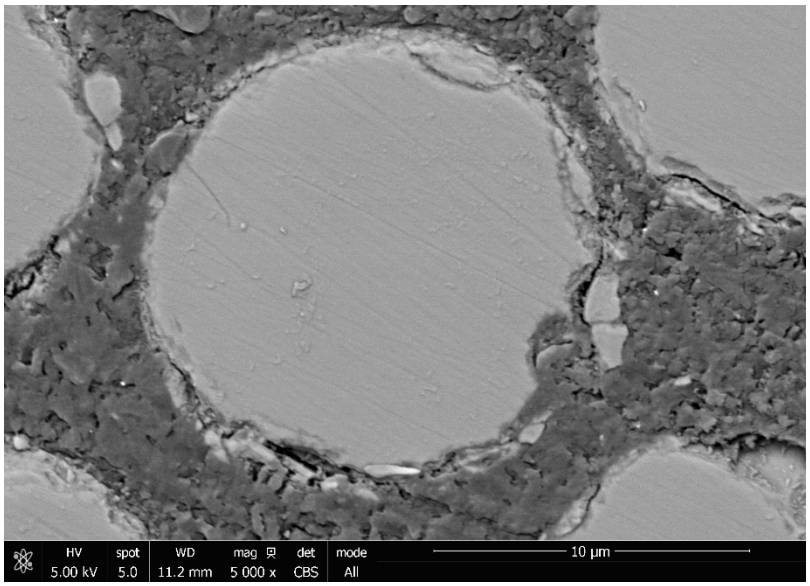


Figure 300 - SEM electron backscatter deflection micrograph of the Hi-Nicalon™ S specimen "Steam 5" examining the cross section the lower portion of a fiber (σ_{cr} = 400 MPa, t_f = 30.83 h).

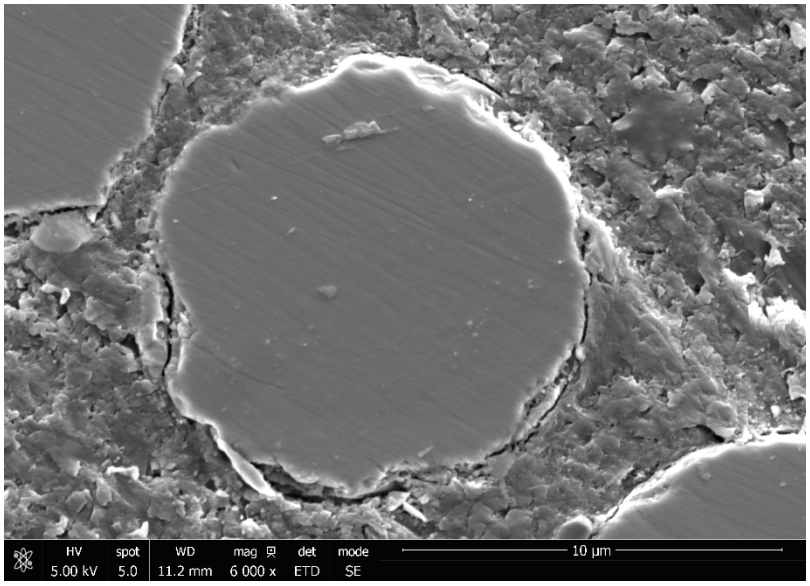


Figure 301 - SEM micrograph of the Hi-Nicalon™ S specimen "Steam 5" examining the cross section the lower portion of a fiber (σ_{cr} = 400 MPa, t_f = 30.83 h).

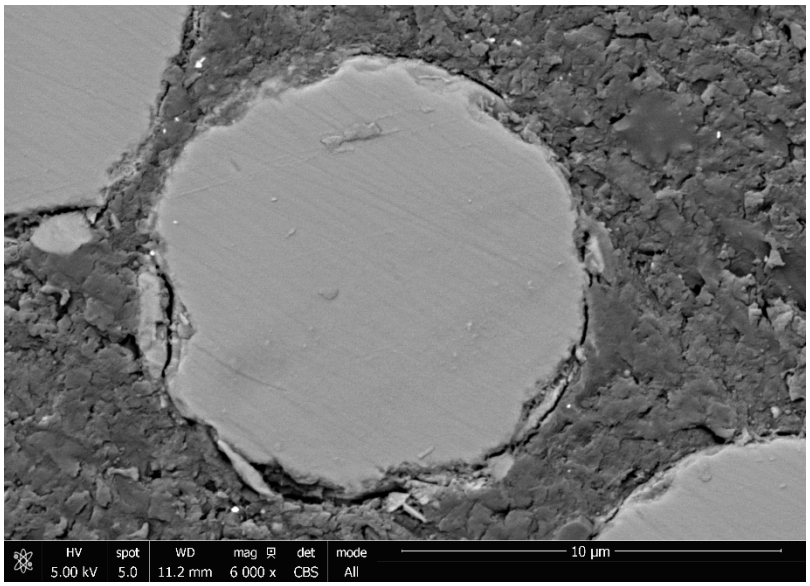


Figure 302 - SEM electron backscatter deflection micrograph of the Hi-Nicalon™ S specimen "Steam 5" examining the cross section the lower portion of a fiber (σ_{cr} = 400 MPa, t_f = 30.83 h).

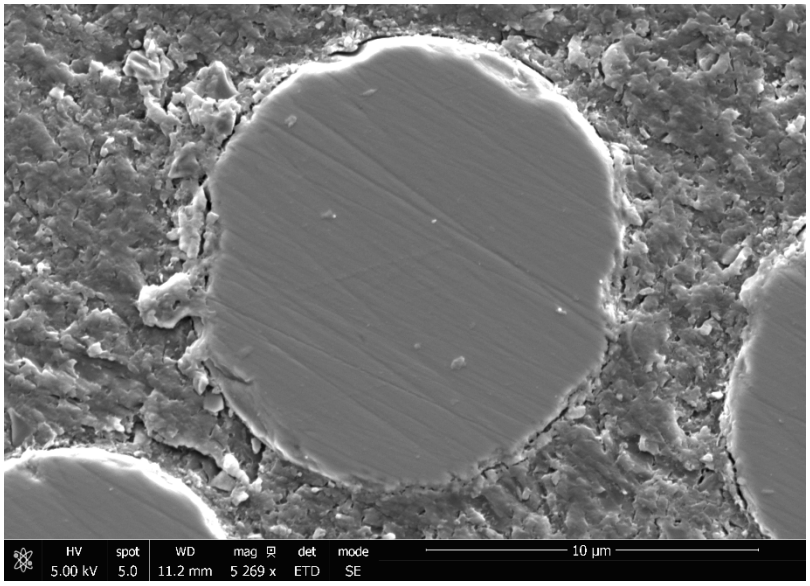


Figure 303 - SEM micrograph of the Hi-Nicalon™ S specimen "Steam 5" examining the cross section the lower portion of a fiber (σ_{cr} = 400 MPa, t_f = 30.83 h).

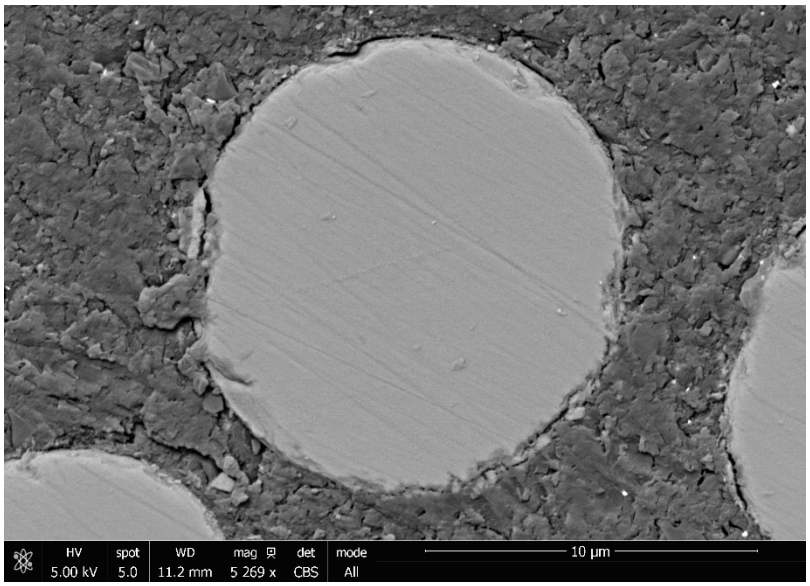


Figure 304 - SEM micrograph of the Hi-Nicalon™ S specimen "Steam 5" examining the cross section the lower portion of a fiber (σ_{cr} = 400 MPa, t_f = 30.83 h).

Bibliography

[1] B. R. Steffens, "Creep of Hi-Nicalon S Ceramic Fiber Tows at Elevated Temperature in Air and in Steam," *MS Thesis. Air Force Institute of Technology (AU), Wright-Patterson Air Force Base,* March 2012.

[2] K. K. Chawla, "Ceramic Matrix Composites," Springer US, New York, 1993.

[3] Department of Defense, "Ceramic Matrix Composites," *Composite Materials Handbook,* vol. 5, pp. 47-67, 2002.

[4] I. M. Daniel and O. Ishai, Engineering Mechanics of Composite Materials, 2nd Ed. ed., New York: Oxford University Press, 2006.

[5] S. Schmidt, H. Knabe, H. Immich, R. Mestring and A. Gessler, "Advanced Ceramic Matrix Composite Material for Current and Future Propulsion Technology Applications," *Acta Astronautica,,* vol. 55, pp. 409-420, 2004.

[6] T. Ishikawa, "Advances in Inorganic fibers," *Polymeric and Inorganic Fibers,* pp. 109-144, 2005.

[7] S. J. Robertson, "Creep of Hi-Nicalon S Ceramic Fiber Tows at Intermediate Temperatures in Air and in Steam," *PhD Dissertation. Air Force Institute of Technology (AU), Wright-Patterson Air Force Base,* (projected for publication in September 2015).

[8] C. J. Armani, "Creep Performance of Oxide Ceramic Fiber Materials at Elevated Temperature in Air and in Steam," *PhD Dissertation. Air Force Institute of Technology (AU), Wright-Patterson Air Force Base,* March 2011.

[9] F. W. Zok, "Developments in Oxide Fiber Composites," *Journal of the American Ceramic Society,* vol. 89, no. 11, pp. 3309-3324, 2006.

[10] A. L. Bunsell and A. Piant, "A review of the development of three generations of small diameter silicon carbide fibres," *Journal of Materials Science,* vol. 41, no. 3, pp. 823-839, 2006.

[11] S. Yajima, J. Hayashi and M. Omori, "Continuous silicon carbide fiber of high tensile strength," *Chemistry Letters,* vol. 4, no. 9, pp. 931-934, 1975.

[12] A. R. Bunsell and M. H. Berger, "Fine diameter ceramic fibres," *Journal of the European Ceramic Society,* vol. 20, pp. 2249-2260, 2000.

[13] K. Okamura, "Ceramic fibres from polymer precursors," *Composites,* vol. 18, no. 2, pp. 107-120, 1987.

[14] H. M. Yun and J. A. DiCarlo, "Thermomechanical Characterization of SiC Fiber Tows and Implications for CMC," Materials Division, NASA Lewis Research Center, Cleveland, OH, 1999.

[15] A. Khan and H. Zhang, "Finite deformation of a polymer: experiments and modeling," *International Journal of Plasticity,* vol. 17, pp. 1167-1188, 2001.

[16] J. B. Wachtman, W. R. Cannon and M. J. Matthewson, Mechanical Properties of Ceramics: Second Edition, John Wiley & Sons, 2009.

[17] J. A. DiCarlo, H. M. Yun and J. B. Hurst, "Fracture mechanisms for SiC fibers and Sic/SiC composites under stress-rupture conditions at high temperatures," *Applied Mathematics and Computation,* vol. 152, pp. 473-481, 2004.

[18] H. M. Yun and J. A. DiCarlo, "Comparison of the Tensile, Creep, and Rupture Strength Properties of Stoichiometric SiC Fibers," in *Journal of the American Ceramic Society*, 1999.

[19] R. Bodet, X. Bourrat, J. Lamon and R. Naslain, "Tensile creep behaviour of a silicon carbide-based fibre with a low oxygen content," *Journal of Materials Science,* vol. 30, no. 3, pp. 661-677, 1995.

[20] S. Bertrand, R. Pailler and J. Lamon, "Influence of Strong Fiber/Coating Interfaces on the Mechanical Behavior and Lifetime of Hi-Nicalon/(PyC/SiC)/SiC Minicomposites," *American Ceramic Society,* vol. 84, pp. 787-794, 2001.

[21] J. A. DiCarlo, "Creep limitations of current polycrystalline ceramic fibers," *Composites Science and Technology,* vol. 51, pp. 213-222, 1994.

[22] J. A. DiCarlo, "Property Goals and Test Methods for High Temperature Ceramic Fiber Reinforcement," *Ceramics International,* vol. 23, no. 4, pp. 283-289, 1997.

[23] J. L. Cédric Sauder, "Tensile Creep Behavior of SiC-Based Fibers With a Low Oxygen Content," *Journal of the American Ceramic Society,* vol. 90, no. 4, p. 10, 2007.

[24] C. Sauder and J. Lamon, "Tensile Creep Behavior of SiC-Based Fibers With a Low," *Journal of the American Ceramic Society,* vol. 90, no. 4, p. 1146–1156, 2007.

[25] K. G. Dassios, M. Steen and C. Filiou, "Mechanical Properties of Alumina Nextel 720 Fibers at Room and Elevated Temperatures: Tensile Bundle Testing," *Materials Science and Engineering,* vol. 349, no. 1-2, pp. 63-72, 2003.

[26] P. Forio, F. Lavaire and J. Lamon, "Delayed Failure at Intermediate Temperatures (600°-700°C) in Air in Silicon Carbide Multifiliment Tows," *Journal of the American Ceramic Society,* vol. 87, pp. 888-893, 2004.

[27] W. Gauthier and J. Lamon, "Delayed Failure of Hi-Nicalon and Hi-Nicalon S Multifiliment Tows and Single Filaments at Intermediate Temperatures (500°-800°C)," *Journal of the American Ceramic Society,* vol. 92, pp. 702-709, 2009.

[28] V. Calard and J. Lamon, "Failure of fiber bundles," *Composites Science and Technology,* vol. 64, pp. 701-710, 2004.

[29] W. Gauthier, F. Pailler, J. Lamon and R. Pailler, "Oxidation of Silicon Carbide Fibers During Static Fatigue in Air at Intermediate Temperatures," *Journal of the American Ceramic Society,* vol. 92, pp. 2067-2073, 2009.

[30] E. J. Opila and R. E. Hann Jr., "Paralinear Oxidation of CVD SiC in Water Vapor," *Journal of the American Ceramic Society,* vol. 80, pp. 197-205, 1997.

[31] T. Shimoo, K. Okamura and Y. Morisada, "Active-to-passive oxidaiton transition for polycarbosilane-derived silicon carbide fibers heared in Ar-O2 gas mixtures," *Journal of Materials Science,* vol. 37, pp. 1793-1800, 2002.

[32] J. P. Viricelle, P. Goursat and D. Bahloul-Hourlier, "Oxidation behaviour of a multi-layered ceramic-matrix composite (SiC) f/C/(SiBC) m.," *Composites Science and Technology,* vol. 61, pp. 607-614, 2001.

[33] J. A. Costello and R. E. Tressler, "Oxidation kinetics of silicon carbide crystals and ceramics: I, in dry oxygen," *Journal of the American Ceramic Society,* vol. 69, pp. 674-681, 1986.

[34] B. E. Deal and A. S. Grove, "General relationship for the thermal oxidation of silicon," *Journal of Applied Physics,* vol. 36, no. 12, pp. 3770-3778, 1965.

[35] Y. Song, S. Dhar, L. C. Feldman, G. Chung and J. R. Williams, "Modified Deal Grove model for the thermal oxidation of silicon carbide," *Journal of Applied Physics,* vol. 95, no. 9, pp. 4953-4957, 2004.

[36] M. H. Jaskowiak and J. A. DiCarlo, "Pressure effects on the thermal stability of silicon carbide fibers," *Journal of the American Ceramic Society,* vol. 72, no. 2, pp. 192-197, 1989.

[37] R. S. Hay, G. E. Fair, R. Bouffioux, E. Urban, J. Morrow and A. a. W. M. Hart, "Hi-Nicalon-S SiC Fiber Oxidation and Scale Crystallization Kinetics," *Journal of the American Ceramic Society,* vol. 94, no. 11, p. 3983–3991, 2011.

[38] R. S. Hay, G. E. Fair, R. Bouffioux, E. Urban, J. Morrow, A. Hart and M. Wilson, "Hi-Nicalon-S Oxidation and Scale Crystallization Kinetics," *Journal of the American Ceramic Society,* vol. 94, pp. 3983-3991, 2011.

[39] R. S. Hay, G. E. Fair, R. Bouffioux, E. Urban, J. Morrow, A. Hart and M. Wilson, "Relationships Between Fiber Strength, Passive Oxidation and Scale Crysallization Kinetics of Hi-Nicalon S SiC Fibers," *Journal of the American Ceramic Society,* vol. 32, pp. 39-54, 2011.

[40] R. S. Hay, G. E. Fair, R. Bouffioux, E. Urban, J. Morrow, A. Hart and M. Wilson, "Relationships Between Fiber Strength, Passive Oxidation and Scale Crystallization Kinetics of Hi-Nicalon™-S SiC Fibers," *Mechanical Properties and Performance of Engineering Ceramics and Composites VI: Ceramic Engineering and Science Proceedings,* vol. 32, pp. 37-51, 2011.

[41] R. S. Hay, G. E. Fair, A. Hart, S. Potticary and R. Bouffioux, "Kinetics of Passive Oxidation of Hi-Nicalon-S SiC Fibers in Wet Air: Relationships between SiO2 Scale Thickness, Crystallization, and Fiber Strength," in *Mechanical Properties and Performance of Engineering Ceramics and Composites VII (eds D. Singh, J. Salem, M. Halbig and S. Mathur)*, Hoboken, NJ, John Wiley & Sons, Inc.,, 2012.

[42] T. A. Parthasarathy, C. P. Przybyla, R. S. Hay and M. K. Cinibulk, "Modeling Environmental Degradation of SiC-Based Fibers," *Journal of the American Ceramic Society,* pp. 1-10, 2016.

[43] R. S. Hay, "Growth stress in SiO2 during oxidation of SiC fibers," *Journal of Applied Physics,* vol. 111, no. 6, p. 063527, 2012.

[44] T. R. Shillig, "Creep of Hi-Nicalon S Ceramic Fiber Tows at Elevated Temeperature in Air and in Steam," *MS Thesis. Air Force Institute of Technology (AU), Wright-Patterson Air Force Base,* March 2013.

[45] K. B. Sprinkle, "Creep of Sylramic-iBN Fiber Tows at Elevated Temperatures in Air and in Silicic Acid-Saturated Steam," *MS Thesis. Air Force Institute of Technology (AU), Wright-Patterson Air Force Base,* June 2015.

[46] M. W. Piper, "Creep of Hi-Nicalon S Ceramic Fiber Tows at 700°C Elevated Temperature in Air and in Steam," *MS Thesis. Air Force Institute of Technology (AU), Wright-Patterson Air Force Base,* March 2016.

[47] R. K. Mitchell, "Creep of Hi-Nicalon S Ceramic Fiber Tows at 700°C Elevated Temperature in Air and in Steam," *MS Thesis. Air Force Institute of Technology (AU), Wright-Patterson Air Force Base,* March 2017.

[48] NGS Advanced Fibers Co., Ltd, "NGS Advanced Fibers," NGS Advanced Fibers Co., Ltd, 2017. [Online]. Available: http://www.ngs-advanced-fibers.com/eng/item/index.html. [Accessed 12 October 2017].

[49] R. M. Morrell, "A Tenile Creep-Testing Apparatus for Ceramic Materials Using Simple Knife-Edge Universal Joints," *Journal of Physics E: Scientific Instruments,* vol. 5, no. 5, pp. 465-467, 1972.

[50] F. A. Kandil and B. F. Dyson, "Tensile Creep of Ceramics: The Development of a Testing Facility," *International Journal of High Technology Ceramics,* vol. 4, no. 2-4, pp. 243-262, 1988.

[51] R. S. Hay and R. J. Chater, "Oxidation kinetics strength of Hi-Nicalon-S SiC fiber after oxidation in dry and wet air," *Journal of the American Ceramics Society,* vol. 100, no. 9, pp. 4110-4130, 2017.

[52] C. Sauder, J. Lamon and R. Pailler, "Thermomechanical properties of carbon fibers at high temperatures (up to 2000°C)," *Composites Science and Technology,* vol. 62, pp. 499-304, 2002.

[53] R. Naslain, "Design, preparation and properties of non-oxide CMCs for application in engines and nuclear reactors: an overview," *Composites Science and Technology,* vol. 64, pp. 155-170, 2004.

[54] R. A. Jurf and S. C. Butner, "Advances in oxide-oxide CMC," in *American Society of Mechanical Engineers*, American Society of Mechanical Engineers, 1999, pp. V004T02A002--V004T02A002.

[55] V. Hammond, "Creep Rupture of an Oxide/Oxide Composite Fiber," University of Virginia, 2001.

REPORT DOCUMENTATION PAGE

Form Approved
OMB No. 0704-0188

The public reporting burden for this collection of information is estimated to average 1 hour per response, including the time for reviewing instructions, searching existing data sources, gathering and maintaining the data needed, and completing and reviewing the collection of information. Send comments regarding this burden estimate or any other aspect of this collection of information, including suggestions for reducing the burden, to Department of Defense, Washington Headquarters Services, Directorate for Information Operations and Reports (0704-0188), 1215 Jefferson Davis Highway, Suite 1204, Arlington, VA 22202-4302. Respondents should be aware that notwithstanding any other provision of law, no person shall be subject to any penalty for failing to comply with a collection of information if it does not display a currently valid OMB control number.

PLEASE DO NOT RETURN YOUR FORM TO THE ABOVE ADDRESS.

1. REPORT DATE *(DD-MM-YYYY)*	2. REPORT TYPE	3. DATES COVERED *(From - To)*
22-03-2018	Master's Thesis	Aug 2016 - Mar 2018

4. TITLE AND SUBTITLE

Creep of Hi-Nicalon™ S Ceramic Fiber Tows at 1000°C In Air and In Silicic Acid-Saturated Steam

5a. CONTRACT NUMBER

5b. GRANT NUMBER

5c. PROGRAM ELEMENT NUMBER

6. AUTHOR(S)

Brian G. Kroeger, Capt, USAF

5d. PROJECT NUMBER

5e. TASK NUMBER

5f. WORK UNIT NUMBER

7. PERFORMING ORGANIZATION NAME(S) AND ADDRESS(ES)

Air Force Institute of Technology
Graduate School of Engineering and Management (AFIT/EN)
2950 Hobson Way
Wright-Patterson AFB, OH 45433-7765

8. PERFORMING ORGANIZATION REPORT NUMBER

AFIT-ENY-18-M-271

9. SPONSORING/MONITORING AGENCY NAME(S) AND ADDRESS(ES)

Air Force Research Laboratory
Dr. Randall S. Hay,
2977 Hobson Way, Building 652
Wright-Patterson AFB, OH 45433
randall.hay@us.af.mil

10. SPONSOR/MONITOR'S ACRONYM(S)

AFRL/RXCCM

11. SPONSOR/MONITOR'S REPORT NUMBER(S)

12. DISTRIBUTION/AVAILABILITY STATEMENT

DISTRIBUTION STATEMENT A:
Distribution Statement A: Approved For Public Release; Distribution Unlimited.

13. SUPPLEMENTARY NOTES

This material is declared a work of the U.S. Government and is not subject to copyright protection in the United States.

14. ABSTRACT

Advanced SiC/SiC ceramic matrix composites (CMCs) are being considered for a variety of applications. Of interest is their ability to withstand exposure to high temperature in an aggressive oxidizing environment. The presence of steam creates such an environment. As steam traverses across a SiC/SiC composite and through cracks in the SiC matrix, it becomes saturated with silicic acid, Si(OH)4. It is essential to understand the long-term impacts and durability of SiC/SiC CMCs that have been exposed to such a demanding environment. The present research investigated creep of Hi-Nicalon™ S SiC fibers at 1000°C in air and in silicic acid saturated steam. The fiber tow consists of 500 fiber filaments with an average diameter of 12 μm. Creep tests were conducted in tension using a dead weight creep test setup. Creep stresses ranged from 3.5 to 800 MPa in air and from 3.5 to 500 MPa in silicic acid saturated steam. Creep run-out was defined as 100 hours under load. Creep run-out was achieved at stresses of 500 MPa in air and 300 MPa in saturated steam. Both primary and secondary creep regimes were observed in all tests with the transition to secondary creep occurring early in the lifetime of each test. Steady-state creep rates were found for each test. The steady-state creep rates in saturated steam were approximately an order of magnitude larger than those in air. Passive oxidation was found on the fibers tested in both environments using scanning electron microscopy (SEM). No evidence was found of active oxidation.

15. SUBJECT TERMS

Creep, SiC, Hi-Nicalon™ S Fiber Tow, Silicic Acid-Saturated Steam, ceramic matrix composite (CMC), oxidation

16. SECURITY CLASSIFICATION OF:			17. LIMITATION OF ABSTRACT	18. NUMBER OF PAGES	19a. NAME OF RESPONSIBLE PERSON
a. REPORT	b. ABSTRACT	c. THIS PAGE			Dr. Marina B. Ruggles-Wrenn, AFIT/ENY
U	U	U	UU	248	19b. TELEPHONE NUMBER *(Include area code)* (937) 255-3636 x1234 Marina.Ruggles-Wrenn@a

Reset

Standard Form 298 (Rev. 8/98)
Prescribed by ANSI Std. Z39.18